Some Explorations in Magneto-Optics and Opto-Magnetics

مقناطیسی نوریات اور نوری مقناطیسیت کے چند گوشے

Ali Akbar

Contents

List of Figures

List of Tables

Abstract

The main focus of this research is to explore magneto-optic phenomena which have been extensively used as a tool for non-destructive, remote characterization of magnetic properties of materials and also demonstrate immense potential in device manufacturing and magnetic recording media. Magneto-optic effects are a manifestation of light-matter interaction in the presence of magnetic field and can be effectively described by the dielectric tensor. The emergence of different asymmetries in different elements of the tensor is dependent upon the direction of the applied magnetic field relative to the wavevector of light. The current work is an amalgamation of theoretical and experimental investigations of these asymmetries—the various forms of birefringence, while both the classical and quantum nature of light is utilized.

The theoretical pursuit involves the description and analysis of magnetic circular birefringence (the Faraday effect), magnetic circular dichroism (the Kerr effect), magnetic linear birefringence (the Voigt effect) and magnetic linear dichroism. The intermixing of these effects present a comprehensive picture of these phenomena. Magnetic birefringence effects are miniscule and require phase sensitive detection. Several experimental techniques have been devised, designed and implemented in order to quantify these asymmetries.

The experimental methods employed in this work encompass diverse kinds of modulation techniques, adapted according to the challenges imposed by the experiment. For example, for measuring the Faraday rotation, modulation is achieved through an ac magnetic field generated by the Helmholtz coils, hence circumventing the need for a large dc field. The Verdet constant for terbium gallium garnet (TGG) crystal is measured by a home-built setup. The analysis for the Kerr effect is based on Jones calculus and modulation is realized through photoelastic modulator. To test the functionality of the setup, ferromagnetic thin films are deposited by magnetron sputtering and subsequently

the absolute Kerr rotation is measured.

The rotation of polarization plane under transverse magnetic fields (the Voigt effect) for TGG crystal is then studied for a wide range of temperatures (8–100 K) by Stokes polarimetry where an optical chopper modulates the polarized beam of light. This particular method utilizes the discrete Fourier transform of polarized light intensity described in terms of the Stokes parameters. The magnitude of rotation and ellipticity are quantified and the Curie-Weiss constant is estimated from the analysis of Voigt coefficients. We consider it the first reported instance where the Curie-Weiss constant is derived from magneto-optic measurements based on the Voigt effect. The Voigt effect, due to its small value, requires ultra-sensitive measurement techniques, and therefore is, otherwise, rarely studied.

With technological advancement in femtosecond laser technology, the conventional role of magneto-optics has been widened from probing to controlling the magnetization of magnetic system. This is dubbed as opto-magnetics. In this context, the response of rare earth-transition metal (RE-TM) alloys and magnetic nano-structures in the form of bilayers, core shell and alloys is simulated, when excited with femtosecond laser pulses. The simulation environment is based on Heisenberg's spin Hamiltonian which then utilizes Monte-Carlo algorithm and Landau-Lifshitz-Gilbert (LLG) in conjunction with two temperature model for investigation of different magnetic properties of the materials.

The simulation results demonstrate the correct estimation of Curie temperatures for well known rare earth and transition metals. Furthermore, all-optical deterministic switching of magnetization is observed for rare earth-transition metal (RE-TM) ferrimagnetic alloys. This switching mechanism operates in the femtosecond timescale. The control of magnetization switching time can be achieved by varying certain parameters, *i.e.*, doping concentration of particular elements in host alloys and variation in laser fluence. These effects are also studied in this work.

The last part of this work reproduces measurements of the earlier chapters using quantum light comprising single photons, generated from a heralded down-conversion nonlinear optical process. The Faraday rotation for quantum light is demonstrated using single photons. The synthesis of polarized single photon states are realized through spontaneous parametric down-conversion and state estimation is performed by quantum state tomography. The tomographic results are then analyzed and various kinds of minimization algorithms are adopted to extract Faraday rotation angles. The extracted Faraday rotation angles from the estimated state are corroborated with the previous experimental findings. Furthermore, our tomographic data is analyzed to assess the ellipticity acquired by single photons while establishing a correspondence with single qubit operations described on the Bloch sphere.

During the course of my doctoral research, I was also part of a collaborative team working on magneto-optic and active optical design of nano-structured devices. This work resulted in some publications which are listed below, but are not a part of this thesis.

List of Publications as primary author

1. Akbar, A., Khalid, M. W., and Anwar, M. S. (2017). "Low temperature Voigt effect in the terbium gallium garnet crystal". *Optics Express*, 25(24), 30550–30559.

2. Akbar, A., Saleem, M., Atiq, S., and Anwar, M. S. (2018). "Magnetic Dynamics and All-Optical Switching in 5 nm Dy–Fe Nanostructures", *IEEE Transactions on Magnetics*, 54(7), 1–6.

3. Akbar, A., Ilahi, E, Faizan., and Anwar, M. S. "Faraday rotation and ellipticity in single photons" (in preparations for *Physics Letters A*).

List of Publications as contributing author

1. Mahmood, N., Kim, I., Mehmood, M.Q., Jeong, H., Akbar, A., Lee, D., Saleem, M., Zubair, M., Anwar, M.S., Tahir, F.A. and Rho, J., (2018). "Polarisation insensitive multifunctional metasurfaces based on all-dielectric nanowaveguides", Nanoscale, 10(38), pp.18323–18330.

2. Fatima, T., Akbar, A., Anwar, M.S. and Tahir, M.N., 2019. "Six new dinuclear Schiff base complexes of Cu (II)/Ln (III) system: Synthesis, characterization and magnetic studies", *Journal of Molecular Structure*, 1184, pp.462–467.

3. Mahmood, N., Jeong, H., Kim, I., Mehmood, M.Q., Zubair, M., Akbar, A., Saleem, M., Anwar, M.S., Tahir, F.A. and Rho, J., 2019. "Twisted non-diffracting beams through all dielectric meta-axicons", *Nanoscale*, 11(43), pp.20571–20578.

4. Abbas, S.K., Akbar, A., Atiq, S., Saleem, M., Iftikhar, M., Rafiq, H.M., Naseem, S. and Anwar, M.S., 2019. "Optimization of DyFe nanostructures using E-beam lithography for magneto-optical applications", *Journal of Magnetism and Magnetic Materials*, 469, pp.196–202.

Chapter 1

Magneto-Optic Effects: An Introduction

The role of magneto-optics in development of modern technology is central [1]. From the discovery of the Faraday effect in 1845 and the Kerr effect in 1875 to the development of devices for optical isolation, optical modulation, polarization control and nonreciprocal phase-shifters manifest the overarching role of these physical phenomena in different forms. Magneto-optic materials offer unique physical properties for device manufacturing with many special functions not possible with other photonic devices [2]. The phenomenological explanation of these effects were completed with Maxwell's electromagnetic theory but the microscopic origin was not established until 1896 by the discovery of the Zeeman effect and explained by Lorentz in terms of classical electron theory [3].

The change in optical response of a medium in the presence of magnetic field is referred to as magnetic birefringence, ascribed to the asymmetry and anisotropy introduced by magnetic field. The induced birefringence results in the rotation of plane of polarization of the incident polarized light and association of ellipticity to the light coming out of magnetically active medium. Depending on the relative orientation between applied magnetic field and propagation vector, magnetically induced birefringence phenomena are categorized as *circular* and *linear* birefringence. In addition, further classification of magneto optic effects arises from the perspective of geometry. For example, in the

reflection geometry, the leading magneto optic effect is called the Kerr effect (which will also be discussed in the current Chapter). In the transmission mode, we can identify two variations as depicted in the Fig. 1.1.

1. The Faraday geometry (circular birefringence): Applied magnetic field **B** is parallel to the propagation vector of light **k**, *i.e.*, **B** ∥ **k**. The effect is proportional to **B**.

2. The Voigt geometry (linear birefringence): Light travels perpendicular to the direction of applied magnetic field, *i.e.* **B** ⊥ **k**. The effect is proportional to B^2.

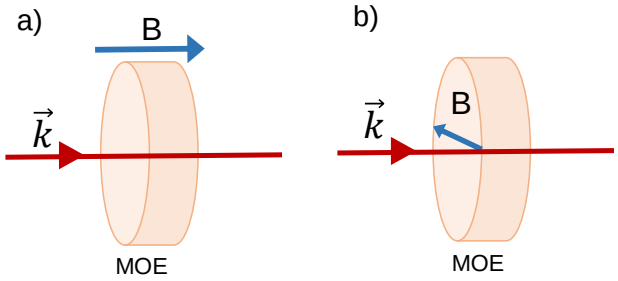

Figure 1.1: The applied magnetic field **B** is a) parallel (the Faraday geometry) and b) perpendicular (the Voigt geometry) to the propagation vector **k**. **MOE** refers to a magneto-optic element.

These magneto-optical effects are also classified respectively as linear and quadratic showing their respective dependence on the order of magnetization. The most straightforward and useful effect is the Faraday effect due to its potential applications in optical isolators, magneto-optic modulators, current and magnetic field sensation devices and spatial light modulators [4]. The next chapter deals completely with quadratic magneto-optic effect, however, we discuss the Faraday effect in this Chapter.

From discovery of gravitational waves, manipulation of quantum bits in ion trapped quantum computing, photonic quantum bits, magnetic state reversal, light has played a central role for the demonstration of these far reaching

discoveries in science. One of the major advantages for using light is that optical manipulation is robust and less affected by noise (shot noise, noise due to electrical power etc.) which are more pronounced in alternative approaches such as electrical measurement or vibrating magnetometer devices. In recent years, the burgeoning interest in all optical magnetic switching and control of magnetization is another key aspect of magneto-optic effects.

In one of the kinds of such experiments, ultra-short (femtosecond scale) pulses of polarized light can result in precessional switching of the magnetization even in the absence of an external field. This all-optical switching is enabled by the increase in temperature of the spin system due to the femtosecond laser pulse. Consequently, magnetization of the system relaxes to a direction opposite to prior. This method promises magnetization switching at an unprecedent rate in the femtosecond— the ultrafast regime. In another experiment, helicity dependent magnetic switching is attributed to inverse Faraday effect in rare-earth transition metal GdFeCo alloy [5]. In chapter 3, we explore this particular aspect of ultrafast magnetization switching in detail.

Coming back to some of the interesting explorations of the Faraday effect, it can also be used in paramagnetic resonance experiments to measure the saturation of spin levels under steady and perturbed states for investigation of spin-lattice relaxation times [6, 7]. In addition, Crooker *et.al* [8] described a method of time-resolved Faraday rotation to study the dynamic spin behavior of both photoinjected excitons and of the embedded magnetic sublattice.

The non-reciprocal nature of the Faraday effect allows its use as an optical isolator. Non-reciprocity means that if linearly polarized material is subjected through a medium in a magnetic field, the sense of rotation reverses for light traveling parallel or antiparallel to the field. A great deal of scientific effort is spent in the search of suitable Faraday devices (FDs) for high power laser system. Faraday devices are used in laser systems particularly for the multi-pass amplification and regenerative amplifiers as well as for optical isolation

of one part of the system from another by eliminating possible harmful back-reflections [9]. Additionally due to the inherited dependence on temperature and wavelength, only few of the magneto-optic materials covers the complete spectral range (UV-IR).

The desirable feature for a Faraday material to be used as an optical isolator are high Verdet constant and high thermal conductivity. The Verdet constant signifies the amount of polarization rotation with respect to **B**. Some promising materials for FDs are orthoferrites with the general formula $RFeO_3$ and paramagnetic rare earth garnets especially terbium gallium garnet doped with rare earth ions, titatnium doped terbium aluminum garnet (Ti:TAG) [10], terbium scandium aluminum garnet (TSAG) [11] and Tb doped yttrium oxide [12], which have been extensively studied and reported over wide temperature ranges [13]. Further, garnets based ceramics have enabled the researcher to develop large aperture components unlike single crystals.

In addition to rotation of plane of polarization of light, another pertinent effect is ellipticity which arises due to ever present absorption inside the medium. For room temperature measurement, the magnitude of ellipticity is usually small, however for cryogenic temperatures, the magnitude become considerably large affecting the output state of emerging light, hence, altering the capabilities of an optical isolator. The mathematical background presented in this chapter also encompasses polarization rotation in conjunction with ellipticity imparted to the light due to circular dichroism and linear magneto optic effects.

We setup the discussion by reviewing Maxwell's equations and polarized light in terms of Jones calculus. Then follows the discussion for basic framework of magnetic circular birefringence (the Faraday effect), magnetic circular dichroism (the Kerr effect) and devise experimental techniques for measurements of these MO effects. We will also accurately define what is meant by circular and linear birefringence, dichroism effects etc.

1.1 Maxwell's Equations

Maxwell's equations provide the basic constitutive framework for magneto-optical phenomenon. In free space, Maxwell's equations are [2, 14]

$$\nabla \times \mathbf{E} = -\mu_0 \frac{\partial \mathbf{H}}{\partial t} \qquad (1.1a) \qquad \nabla \cdot \mathbf{H} = 0 \qquad (1.1b)$$

$$\nabla \times \mathbf{H} = \varepsilon_0 \frac{\partial \mathbf{E}}{\partial t} \qquad (1.2a) \qquad \nabla \cdot \mathbf{E} = 0 \qquad (1.2b)$$

where ε_0 and μ_0 are electric permittivity and magnetic permeability of free space. They constitute a set of first order partial differential coupled equations and can be decoupled by applying the curl operator to Eq. (1.1a), resulting in the wave equation [15]

$$\nabla^2 \mathbf{E} = -\frac{1}{c^2} \frac{\partial^2 \mathbf{E}}{\partial t^2} \qquad (1.3)$$

where $c^2 = 1/\sqrt{\mu_0 \varepsilon_0}$ is the speed of light. One of the remarkable features of Maxwell's theory is that the speed of light can be determined from experiments based on force between condensor plates or current carrying wire, which do not seem to be connected to light [15]. Any function that satisfies Eq. (1.3) is an electromagnetic wave. One possible solution to Eq. (1.3) is

$$\mathbf{E}(\mathbf{r}, t) = \mathbf{E_0} e^{i(\mathbf{k}\cdot\mathbf{r} - \omega \mathbf{t})}$$

where $\mathbf{E_0}$ entails the information of amplitude and phase of the electromagnetic (EM) wave [14]. In a non conducting medium, two additional vector fields are required, electric displacement $\mathbf{D}(\mathbf{r}, t)$ and magnetic flux density $\mathbf{B}(\mathbf{r}, t)$. Maxwell's equations are now written as

$$\nabla \times \mathbf{E} = -\frac{\partial \mathbf{B}}{\partial t} \qquad (1.4a) \qquad \nabla \cdot \mathbf{B} = 0 \qquad (1.4b)$$

$$\nabla \times \mathbf{H} = \frac{\partial \mathbf{D}}{\partial t} \qquad (1.5a) \qquad \nabla \cdot \mathbf{D} = 0. \qquad (1.5b)$$

The relationship between electric displacement and electric field is determined by electric properties of the medium, characterized by the polarization density

P, macroscopic sum of the electric dipole moments induced by the electric field [16]. Similarly, magnetic flux density and magnetic field depends on the magnetic properties of medium, embodied in the magnetization density **M**, volume density of magnetic moments [16]. The corresponding relations between flux densities and the fields are

$$\mathbf{D} = \varepsilon_0 \mathbf{E} + \mathbf{P} \tag{1.6}$$

$$\mathbf{B} = \mu_0 \mathbf{H} + \mathbf{M}. \tag{1.7}$$

For linear homogeneous medium, $\mathbf{D} = \varepsilon \mathbf{E}$ where $\varepsilon = \varepsilon_0(1 + \chi)$ is a scalar quantity called the electric permittivity and χ is the medium's electric susceptibility. A similar relation holds for the magnetic field and magnetic flux density

$$\mathbf{B} = \mu \mathbf{H}$$

where μ is called the magnetic permeability of the medium. For an optically anisotropic medium, the relation between **P** and **E** depends on the direction of vector **E**,

$$P_i = \sum_j \varepsilon_0 \chi_{ij} E_j, \quad i, j = x, y, z.$$

Consequentially the relation between electric displacement **D** and **E** follows

$$D_i = \sum_i \varepsilon_{ij} E_j \tag{1.8}$$

where χ_{ij} and ε_{ij} now represent the electric susceptibility and electric permittivity tensors. Similarly, the magnetic susceptibility tensor χ_m can be defined to describe the magnetization either intrinsic or induced by a magnetic field

$$M_i(\omega) = \sum_i (\chi_m)_{ij}(\omega) H_j \quad \text{and} \qquad H_i(\omega) = \sum_i \frac{1}{\mu_{ij}(\omega)} B_j. \tag{1.9}$$

However $\chi_m = 0$ and $\mu = \mu_0$ at optical frequencies [2]. Therefore, the response of material to an optical field at a frequency ω, irrespective of whether it is magnetic or non-magnetic, is fully characterized by its electric susceptibility $\chi(\omega)$ and equivalently by its electric permittivity $\varepsilon(\omega)$ [2]. The electric susceptibility and electric permittivity at an optical frequency thus become a function

of magnetic field **H**. Therefore, magneto-optic effects are completely characterized by the permittivity tensor. This implies that if a dielectric medium is symmetric $\varepsilon_{ik} = \varepsilon_{ki}$ at $H = 0$, it will be anti-symmetric $\varepsilon_{ik}(H) = \varepsilon_{ki}(-H)$ in the presence of a magnetic field.

In general, these effects are weak perturbations to the optical properties of material. The first order or linear magneto-optic effect is characterized by a linear dependence of ε on **H** or **M** and the second order or quadratic magneto-optic effects results from a quadratic dependence of ε on **H** or **M**. A phenomenological expression for the dielectric tensor capturing magneto-optic effects for an isotropic medium magnetized in an arbitrary direction is [17]

$$\varepsilon_{MO} = \varepsilon_0 \begin{pmatrix} n_o^2 & -iA_1M_z & iA_1M_y \\ iA_1M_z & n_o^2 & -iA_1M_x \\ -iA_1M_y & iA_1M_x & n_o^2 \end{pmatrix} + A_2 \begin{pmatrix} M_x^2 & M_xM_y & M_xM_z \\ M_xM_y & M_y^2 & M_yM_z \\ M_xM_z & M_yM_z & M_z^2 \end{pmatrix}. \tag{1.10}$$

The tensor is decomposed into terms that are respectively linear and quadratic in the magnetization. The magnetization has components M_x, M_y and M_z. Furthermore n_o is the isotropic refractive index and $A_1(\omega)$ and $A_2(\omega)$ are frequency-dependent empirical constants. Generally $A_2 \ll A_1$. Other physical effects which need be considered from a crystal symmetry perspective while discussing magneto-optic effects are given below.

1. **Space Inversion Symmetry**. Dielectric medium with inversion symmetry, *i.e.*, the properties of the medium are not changed under the transformation **r** $\rightarrow$ **-r**, are centrosymmetric [2]. No spontaneous polarization occurs in such materials, hence there can be no first order electro-optic effect. However, this does not imply any constraint for the observation of linear magneto-optic effects. The difference arises due to odd and even symmetry of vector **E** and **H** respectively, under parity transformation.

$$\mathcal{P}f(\mathbf{E}, \mathbf{H}) = f(-\mathbf{E}, \mathbf{H}) \tag{1.11}$$

where $\mathcal{P}$ is the parity operator.

2. **Time Reversal Symmetry**. Time reversal symmetry implies the conservation of energy of the system if direction of time is reversed **t**→**-t**. Dielectric media with time reversal symmetry are considered lossless and reciprocal. Time reversal symmetry breaks when a dielectric medium has loss or gain, or subjected to an external magnetic field. In an optical system, reciprocity is manifested as the interchange of source and detector without altering the reality of physics [2].

Note that in vacuum, Maxwell's equations are parity and time invariant.

1.1.1 Boundary Conditions

When an electromagnetic wave travels from one medium to other medium with different refractive indices, whether it is reflected or transmitted, the kind and strength of interaction depends on the electrodynamics boundary conditions. For a linear, homogeneous dielectric medium, in the absence of free charges and currents, the tangential components of **E** and **H** and the normal components of **D** and **B** must be continuous which is symbolized as [15]

$$\epsilon_1 E_1^{\perp} = \epsilon_2 E_2^{\perp}, \qquad E_1^{\parallel} = E_2^{\parallel}, \tag{1.12}$$

$$B_1^{\perp} = B_2^{\perp} \qquad \text{and} \qquad \frac{1}{\mu_1} H_1^{\parallel} = \frac{1}{\mu_2} H_2^{\parallel}. \tag{1.13}$$

1.2 Polarization of Light

The electromagnetic nature of light is a well established concept which captures the oscillating electric and magnetic field vectors, mutually perpendicular to each other and the direction of propagation of light. Polarization specifies the direction of the electric field vector in a plane perpendicular to the direction of electromagnetic wave's propagation. Figure 1.2 illustrates different polarization states of light.

Consider a monochromatic plane wave with frequency ω traveling in the z-direction

$$\mathbf{E}(\mathbf{r}, t) = \mathbf{E_0} e^{i(kz - \omega t)} \tag{1.14}$$

Only the real part of Eq. (1.14) is physically relevant. Here $\mathbf{E_0} = E_x\hat{x}+E_y\hat{y}$ is a complex vector indicating the polarization vector. In general, the relationship between E_x and E_y defines the polarization of light. For example, if $E_y = 0$, the light is said to be linearly polarized along the x-direction. Expressing $E_x = E_{0x}\exp i\phi_x$ and $E_y = E_{0y}\exp i\phi_y$ in terms of their magnitude and complex phases and substituting in (1.14) we get

$$E_x = E_{0x}\cos(kz - \omega t + \phi_x)$$

and

$$E_y = E_{0y}\cos(kz - \omega t + \phi_y)$$

which further reduces to the parametric equation for an ellipse [1]

$$\frac{E_x^2}{E_{0x}^2} + \frac{E_y^2}{E_{0y}^2} - 2\frac{E_xE_y}{E_{0x}E_{0y}}\cos\phi = \sin^2\phi \tag{1.15}$$

where $\phi = \phi_y - \phi_x$ is the phase difference. The shape of the polarization ellipse is determined by the amplitude and relative phase between electric field vector which is characterized by two angles defined in Fig. 1.2(d). The angle θ represents the direction of the major axis a with respect to the horizontal and the angle χ stands for the ratio of minor to major axis, $\tan(\chi) = \pm b/a$, known as the ellipticity (χ), where b is the semi-minor axis [18]. The relationships between electric field vector components and the rotation θ and ellipticity χ relevant to the polarization ellipse are [16]

$$\tan 2\theta = \frac{2r}{1-r^2}\cos\phi \tag{1.16}$$

and

$$\sin 2\chi = \frac{2r}{1+r^2}\sin\phi \tag{1.17}$$

where $r = E_{0y}/E_{0x}$.

As a plane wave is completely characterized by its complex envelope of the x and y components of the electric field vector, a more useful mathematical representation of plane wave is given by the Jones vector [18]. For a plane

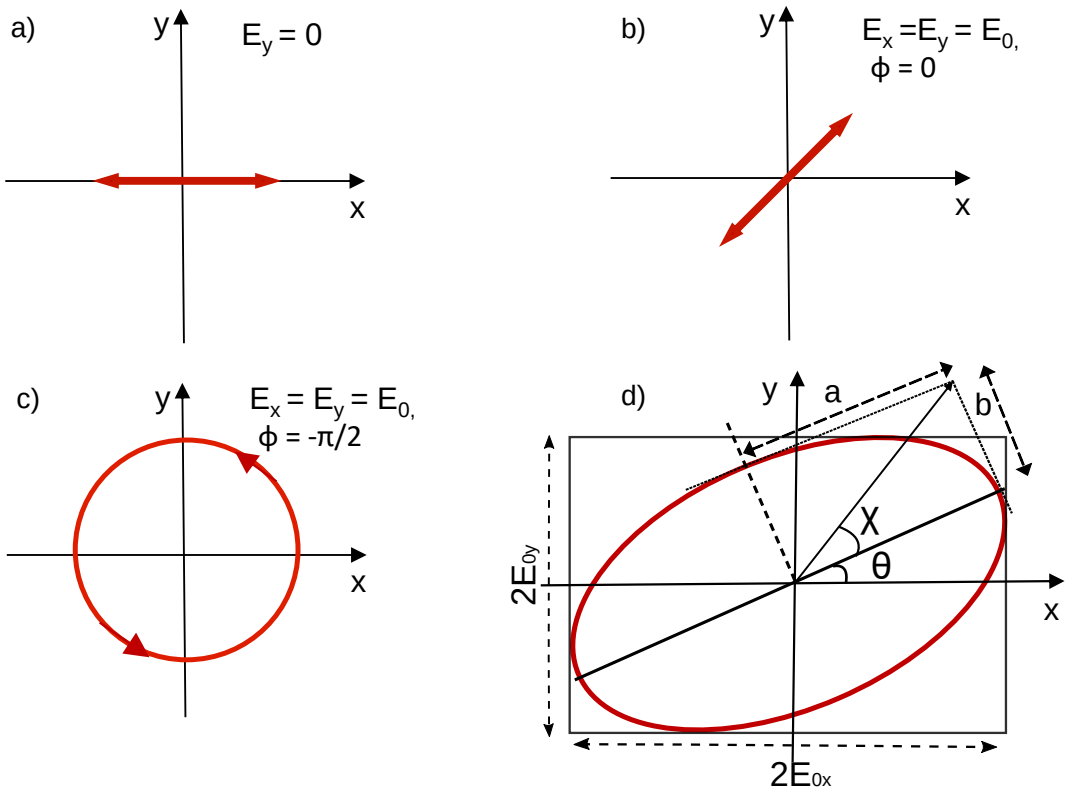

Figure 1.2: a) Linearly polarized light along the x-direction, b) plane polarized light at an angle 45^0 w.r.t. the horizontal, c) left circularly polarized light seen as wave approaches the observer and d) elliptically polarized light where the size of ellipse represents the intensity of light.

wave described by Eq. (1.14), the Jones vector is defined, after suppressing the time dependent exponent, as

$$\mathbf{J} = \begin{bmatrix} \mathbf{A}_x \\ \mathbf{A}_y \end{bmatrix}, \tag{1.18}$$

where $\mathbf{A}_x$ and $\mathbf{A}_y$ are complex amplitudes. For a given $\mathbf{J}$, the total intensity of polarized light can be determined by $I = \sqrt{A_x^2 + A_y^2}$, the ratio of the amplitudes $r = E_{0y}/E_{0x} = |A_y|/|A_x|$ determines the size and shape of the polarization ellipse and also determines the Stokes parameters [16]. The polarization state of light is represented by 2×1 column vector *i.e.*, the Jones vector, whereas polarization modifying optical elements are represented by 2×2 matrix *i.e.*, the Jones matrices. The Jones vectors and matrices for particular polarization and birefringent elements are given in Table 1.1.

Table 1.1: Jones vector representation of polarization states and optical elements.

Horizontally polarized light	$\begin{pmatrix} 1 \\ 0 \end{pmatrix}$
Right (+) and left (-) circularly polarized	$\frac{1}{\sqrt{2}} \begin{pmatrix} 1 \\ \pm i \end{pmatrix}$
Polarizer with transmission axis at an angle β	$\begin{pmatrix} \cos^2\beta & \sin\beta\cos\beta \\ \sin\beta\cos\beta & \sin^2\beta \end{pmatrix}$
Retarder with fast axis oriented along the horizontal	$\begin{pmatrix} e^{i\phi/2} & 0 \\ 0 & e^{-i\phi/2} \end{pmatrix}$

With discussion on Jones calculus, we conclude this section which lays the foundation of basic framework for our mathematical analysis in the forthcoming sections. The next section deals with birefringence introduced in a medium by a magnetic field and will explore how different types of MO effects including circular and linear birefringence and dichroism affect the polarization state of the electromagnetic wave.

1.3 The Faraday Effect

1.3.1 Magnetic Circular Birefringence

We set up the discussion by reviewing the basics of magneto-optic effect in an isotropic paramagnetic crystal. This discussion is based upon the work [19] earlier published by our research group and merely reproduces and expands the calculation therein. The permittivity tensor (2.1) in the presence of an applied magnetic field applied $\mathbf{B} = (0, 0, B)$ is modified as

$$\varepsilon_{MO} = \varepsilon_0 \begin{pmatrix} n^2 & -iQ & 0 \\ iQ & n^2 & 0 \\ 0 & 0 & n^2 \end{pmatrix} \tag{1.19}$$

The diagonal term in the tensor corresponds to refractive indices for isotropic medium and off-diagonal terms proportional to Q, are responsible for magneto

optical activity of the medium. Comparing with Eq. (2.1), we have $Q = A_1 M_z$ and $M_x = M_y = 0$. For the current discussion, we assume Q to be real which determines the strength of magneto-optical interaction. A real Q represents what is called *pure* magnetic circular birefringence as we explain shortly.

By solving Eq. (1.19) for its eigenvalues, plane wave normal modes for magneto optic system turn out to be left and right circularly polarization states, $\hat{e}_-$ and $\hat{e}_+$ respectively, where $e_\pm = (\hat{x} \pm i\hat{y})/\sqrt{2}$. The respective refractive indices are $n_+ = \sqrt{n^2 + Q}$ and $n_- = \sqrt{n^2 - Q}$. The relationship between the wavecetors and their respective refractive indices is given by

$$\beta_\pm = \frac{\omega_\circ}{c}(n_\pm). \tag{1.20}$$

Since $Q \neq 0, n_+ \neq n_-$, this difference in refractive indices for the two kinds of *circular* polarization states leads to the terminology magnetic *circular* birefringence and can be written as

$$\Delta\beta = \frac{\omega_\circ}{c}\Delta n. \tag{1.21}$$

where $\Delta n = n_+ - n_-$. For linearly polarized light along the horizontal traveling in the z-direction through a magneto optical element of length d, the output polarization state would be

$$\begin{aligned}
\mathbf{E}\big|_d &= \frac{E_0}{\sqrt{2}}(\hat{e}_+ e^{-i\beta_+ d} + \hat{e}_- e^{-i\beta_- d}) \\
&= \frac{E_0 e^{-\beta_0 d/2}}{\sqrt{2}}(\hat{e}_x \cos\Delta\beta d/2 + \hat{e}_y \sin\Delta\beta d/2) \\
&= \frac{E_0 e^{-\beta_0 d/2}}{\sqrt{2}} \begin{pmatrix} \cos\Delta\beta d/2 \\ \sin\Delta\beta d/2 \end{pmatrix}
\end{aligned} \tag{1.22}$$

Hence the Faraday rotation angle extracted from equation (1.16) will take the form

$$\theta = \frac{\Delta\beta d}{2} = \frac{\omega_\circ}{2c}(n_+ - n_-)d \approx \frac{\omega_\circ}{2c} nQd. \tag{1.23}$$

1.3.2 Combined Magnetic Circular Birefringence and Dichroism

If a magneto-optic media exhibits absorption, the plane wave normal modes, RCP and LCP will encounter different absorption coefficients, hence the output polarization state will be elliptically polarized. This is called magnetic circular dichroism (MCD). In the previous section 1.3.1 we assumed the variable Q to be real but with the introduction of the absorption inside the medium, Q becomes complex *i.e.*, $Q = Q' - iQ''$. Dichroism can be introduced into the system by making the wavevector complex *i.e.* $k_\pm = \beta_\pm - i\alpha_\pm$ where $\alpha_\pm$ represents the absorption coefficients for different normal modes $\hat{e}_+$ and $\hat{e}_-$ respectively. Now this modifies the expression (1.21) as

$$\Delta\beta - i\Delta\alpha = \frac{\omega_\circ}{c}(\Delta n) \tag{1.24}$$

where $\Delta\beta$ is ascribed to MCB and $\Delta\alpha$ (change in absorption coefficients *i.e.*, $\Delta\alpha = \alpha_+ - \alpha_-$) accounts for MCD. The electric field vector (polarized along the horizontal) after passing through an optical medium which exhibits both MCB and MCD will be

$$\begin{aligned}\mathbf{E}\big|_d &= \frac{E_0}{\sqrt{2}}\left(\hat{e}_+ e^{-i(\beta_+ - i\alpha_+)d} + \hat{e}_- e^{-i(\beta_- - i\alpha_-)d}\right) \\ &= \frac{E_0 e^{-i\beta d/2} e^{-i\alpha d/2}}{\sqrt{2}}\Bigg(\hat{e}_x \cosh[i(\Delta\beta d/2 + i\Delta\alpha d/2)] \\ &\qquad - i\hat{e}_y \sinh[i(\Delta\beta d/2 + i\Delta\alpha d/2)]\Bigg).\end{aligned} \tag{1.25}$$

Note the presence of hyperbolic trigonometric functions instead of ordinary trigonometric functions. For linearly polarized light along y-axis, a similar calculation can be performed and finally the transfer matrix for a medium with both MCB and MCD can be written as

$$T = \begin{pmatrix} \cosh[i(\Delta\beta d/2 + i\Delta\alpha d/2)] & -i\sinh[i(\Delta\beta d/2 + i\Delta\alpha d/2)] \\ i\sinh[i(\Delta\beta d/2 + i\Delta\alpha d/2)] & \cosh[i(\Delta\beta d/2 + i\Delta\alpha d/2) \end{pmatrix}. \tag{1.26}$$

Ignoring global phase factor in expression (1.25), it is clearly seen that $E_y = \cosh[i(\Delta\beta d/2 + i\Delta\alpha d/2)]$ and $E_x = \sinh[i(\Delta\beta d/2 + i\Delta\alpha d/2)]$. Using this

formulation and after trigonometric manipulation, the angles for rotation θ and ellipticity χ can be extracted using equations (1.16) and (1.17) and yield

$$\tan 2\theta = \frac{\sqrt{\cosh^2(\Delta\alpha d) - \cos^2(\Delta\beta d)}}{\cos(\Delta\beta d)} \cos\phi \tag{1.27}$$

$$= \tan(\Delta\beta d) \tag{1.28}$$

$$\sin 2\chi = \frac{\sqrt{\cosh^2(\Delta\alpha d) - \cos^2(\Delta\beta d)}}{\cosh(\Delta\alpha d)} \sin\phi \tag{1.29}$$

$$= \tanh(\Delta\alpha d) \tag{1.30}$$

$$\begin{aligned}\phi &= \phi_y - \phi_x \\ &= \tan^{-1}\left(\frac{\sin(\Delta\beta d)e^{-\Delta\alpha d}}{1+\cos(\Delta\beta d)e^{-\Delta\alpha d}}\right) - \tan^{-1}\left(\frac{1-\cos(\Delta\beta d)e^{-\Delta\alpha d}}{\sin(\Delta\beta d)e^{-\Delta\alpha d}}\right).\end{aligned} \tag{1.31}$$

We first assume the case of pure magnetic linear birefringence (the nominal Faraday effect), *i.e.*, $\Delta\alpha = 0$. For incident light polarized along the horizontal, Eq. (1.27) will reduce to $\tan(2\theta) = \tan(\Delta\beta d)$ which is identical to Eq. (1.23). This further implies that rotation angle is a linear function of circular birefringence $\Delta\beta$, as shown in Fig. 1.3.

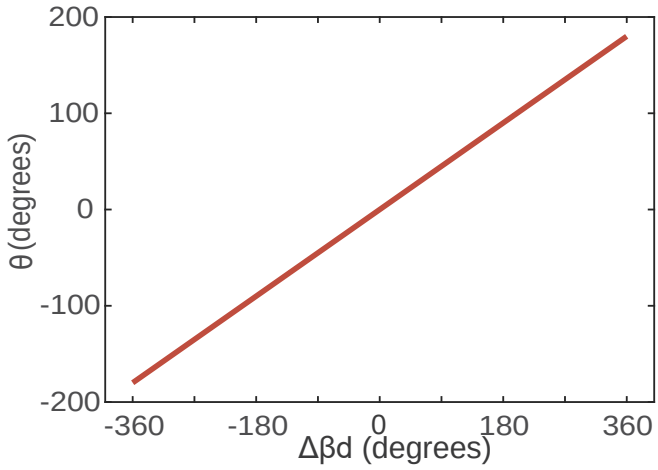

Figure 1.3: Angle of rotation as a function of magnetic circular birefringence.

For the other extreme, we have pure circular dichroism, *i.e.*, $\Delta\beta = 0$ and $\Delta\alpha \to \infty$, the phase difference turns out to be $\phi = -90^o$. It immediately

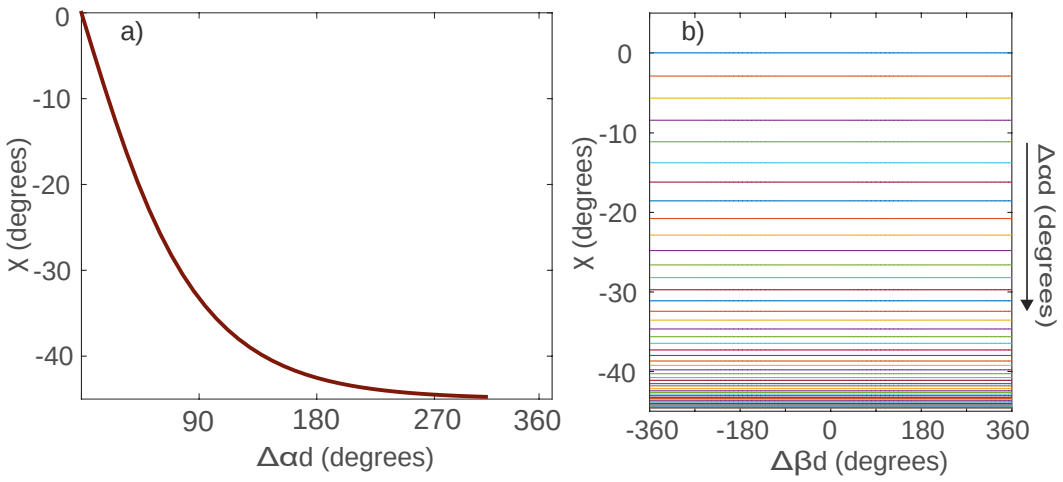

Figure 1.4: Angle of ellipticity as a function of (a) magnetic circular dichroism and (b) magnetic circular birefringence for different values of MCD.

follows from Eqns. (1.27) and (1.29) that

$$\tan 2\psi = 0 \tag{1.32}$$

$$\sin 2\chi = \sin\phi \rightarrow \chi = -45^{\circ} \tag{1.33}$$

the output light is left circularly polarized but the rotation of plane of polarization (the Faraday rotation) will be zero in a pure absorptive medium. Fig. 1.4(a) illustrates the non linear variation of ellipticity as a function of magnetic circular dichroism.

In the limit of small MCD, *i.e.*, $\Delta\alpha \ll 1$ ellipticity is linear as $\tanh(\Delta\alpha d/2) \approx \Delta\alpha d/2$ and $\sinh 2\chi \approx 2\chi \approx \Delta\alpha d/2$. Figure 1.4(b) displays the angle of ellipticity for different values of MCD iterated in steps of 0.1 rad from top to bottom of plot.

The discussion of MCB and MCD complements the observation that ellipticity is entirely caused by magnetic circular dichroism and the rotation is an artifact of pure magnetic circular birefringence. Next section deals with another interesting magneto optic effect, *i.e.*, magnetic linear birefringence combined with MCB.

1.3.3 Combined Magnetic Circular and Linear Birefringence

Magnetic linear birefringence (MLB) arises when the externally applied static magnetic field is perpendicular to the wavevector of electromagnetic wave passing through the magneto-optic medium or paramagnetic crystal. In liquids, MLB is generally referred to the Cotton-Mouton effect whereas in crystalline solids, MLB is known as the Voigt effect. These effects for a terbium gallium garnet crystal are thoroughly discussed in the next chapter over a wide range of temperatures. Here we discuss the MCB in the presence of MLB (irrespective of the origin of MLB) and the consequence on the rotation and ellipticity of polarization state of the output electromagnetic wave.

In the presence of pure magnetic linear birefringence, the diagonal elements of the magneto optical tensor (1.34) are asymmetric, *i.e.*, $n_x^2 = \varepsilon_{xx} \neq n_y^2 = \varepsilon_{yy} \neq n_z^2 = \varepsilon_{zz}$ and off diagonal terms are zero. However, in the combined presence of magnetic linear and circular birefringence, the magneto-optical tensor in Eq. (1.19) takes the form

$$\varepsilon_{MO} = \varepsilon_0 \begin{pmatrix} n_x^2 & -iQ & 0 \\ iQ & n_y^2 & 0 \\ 0 & 0 & n_z^2 \end{pmatrix} \tag{1.34}$$

where MLB is quantified by $\varepsilon_{xx} - \varepsilon_{yy} = \varepsilon_0(n_x^2 - n_y^2)$. Generally, MLB is a much smaller effect than magnetic circular birefringence quantified by $Re(Q)$. The relative strengths of MCB and MLB are captured by the angle ξ defined as $\tan\xi = Q/\varsigma$ where $\varsigma = (\varepsilon_{xx} - \varepsilon_{yy})/2$. Solving the wave equation (1.3) and assuming only plane wave solutions propagating in the z-direction, the normal modes are given by

$$\beta_\pm = \frac{\omega^2}{2c_0^2}\left[(\varepsilon_{xx} + \varepsilon_{yy}) \pm \sqrt{(\varepsilon_{xx} - \varepsilon_{yy})^2 + 4Q^2}\right] \tag{1.35}$$

and the wave vectors for these normal modes are

$$\hat{v}_+ = \begin{pmatrix} 1 \\ i\frac{\varepsilon_{yy} - \varepsilon_{xx} + \sqrt{(\varepsilon_{xx} - \varepsilon_{yy})^2 + 4Q^2}}{2Q} \end{pmatrix}, \tag{1.36}$$

and

$$\hat{v}_- = \begin{pmatrix} 1 \\ -i\frac{\varepsilon_{xx}-\varepsilon_{yy}+\sqrt{(\varepsilon_{xx}-\varepsilon_{yy})^2+4Q^2}}{2Q}a \end{pmatrix}. \tag{1.37}$$

Eqns. (1.36) and (1.37) can be simplified by defining the following variables and identities

$$\gamma_+^2\gamma_-^2 = -Q^2 \qquad \gamma_+^2 + \gamma_-^2 = 2\xi \tag{1.38}$$

$$\frac{\gamma_+^4 - Q^2}{\gamma_+^4 - Q^2} = \frac{\gamma_-^2}{\gamma_+^2} \qquad \gamma_+^2 - \gamma_-^2 = 2\sqrt{\xi^2 + Q^2} \tag{1.39}$$

where $\gamma_\pm^2 = \varsigma \pm \sqrt{\varsigma^2 + Q^2}$. With these substitutions, the normal mode wave vectors will be transformed to

$$\hat{v}_+ = C_1 \begin{pmatrix} 1 \\ i\frac{Q}{\gamma_-^2} \end{pmatrix} \tag{1.40}$$

and

$$\hat{v}_- = C_1\left(\frac{\gamma_+}{\gamma_-}\right) \begin{pmatrix} 1 \\ -i\frac{Q}{\gamma_-^2} \end{pmatrix}. \tag{1.41}$$

The coefficient C_1 is a normalization constant. These wave-vectors can be transformed into their corresponding rectilinear coordinates. The transformation is

$$\begin{pmatrix} \hat{e}_x \\ \hat{e}_y \end{pmatrix} = \mathbf{M} \begin{pmatrix} \hat{v}_+ \\ \hat{v}_- \end{pmatrix}$$

where

$$\mathbf{M} = \frac{\gamma_-^2}{C_1(\gamma_-^2 - \gamma_+^2)} \begin{pmatrix} 1 & -\frac{\gamma_+}{\gamma_-} \\ \frac{\gamma_+}{\gamma_-} & 1 \end{pmatrix}. \tag{1.42}$$

For input light polarized along the x-direction, $E_0\hat{e}_x$ can be rearranged in superposition states of RCP and LCP as

$$E_0\hat{e}_x = E_0\frac{\gamma_-^2}{(\gamma_-^2 - \gamma_+^2)}\left(\hat{v}_+ + \frac{\gamma_+}{\gamma_-}\hat{v}_-\right) \tag{1.43}$$

which upon passing through magneto-optical element of length d, will take the form

$$E_0\frac{\gamma_-^2}{(\gamma_-^2 - \gamma_+^2)}\left(\hat{v}_+ e^{-i\beta_+ d} + \left(\frac{\gamma_+}{\gamma_-}\right)\hat{v}_- e^{-i\beta_- d}\right). \tag{1.44}$$

Substituting the values of normal modes from (1.35), we get

$$E_0 \frac{\gamma_-^2}{(\gamma_-^2 - \gamma_+^2)} \begin{pmatrix} \gamma_-^2 e^{-i\beta_+ d} - \gamma_+^2 e^{-i\beta_- d} \\ iQ\left(e^{-i\beta_+ d} - e^{-i\beta_- d}\right) \end{pmatrix}. \tag{1.45}$$

In a similar manner, if the input light is vertically polarized, $E_0\hat{e}_y$, the output is

$$E_0 \frac{\gamma_-^2}{(\gamma_-^2 - \gamma_+^2)} \begin{pmatrix} iQ\left(e^{-i\beta_+ d} - e^{-i\beta_- d}\right) \\ \gamma_+^2 e^{-i\beta_+ d} - \gamma_-^2 e^{-i\beta_- d} \end{pmatrix}. \tag{1.46}$$

Implying trigonometric identities and mathematical manipulation, the transfer matrix for a magneto-optic medium exhibiting both MCB and MLB can finally be written as

$$\mathbf{T_2} = \begin{pmatrix} \cos(\Delta\beta d/2) + i\cos(\xi)\sin(\Delta\beta d/2) & -\sin(\xi\sin(\Delta\beta d/2) \\ \sin(\xi\sin(\Delta\beta d/2) & \cos(\Delta\beta d/2) - i\cos(\xi)\sin(\Delta\beta d/2) \end{pmatrix} \tag{1.47}$$

where $\Delta\beta = \beta_+ - \beta_-$. The transfer matrix is sufficient to determine the output polarization state properties. Finally, the azimuthal rotation θ and ellipticity χ are respectively found out to be

$$\tan(2\theta) = \frac{\sin\xi\sin(\Delta\beta d)}{\cos^2(\Delta\beta d/2) + \cos(2\xi)\sin^2(\Delta\beta d/2)}, \tag{1.48}$$

$$\sin(2\chi) = \sin(2\xi)\sin^2(\Delta\beta d/2). \tag{1.49}$$

Analyzing the expressions (1.48) and (1.49) reveals interesting effects. For the limiting case of pure circular birefringence, $\xi = 90^o$ and the Faraday rotation is $\theta = \Delta\beta d/2$ while $\chi = 0$ as expected. On other extreme, for pure linear birefringence, $\xi = 0^o$. This condition results in the complete preservation of the input state since $\theta = \chi = 0$. This is expected as the input light is horizontally polarized which is a normal mode of a magneto-optic system possessing pure MLB.

Figure 1.5 shows the Faraday rotation variation with Q, the magneto-optic parameter which varies from zero to a maximum value of $\lambda_\circ$ where $\lambda_\circ = 785$ nm represents the typical wavelength used in the experiments and $n = 1.9535$ is the refractive index for paramagnetic crystal TGG as reported in the reference [20]. Figure 1.5 also iterates the fact that relationship between rotation

and Q becomes nonlinear as a small magnetic linear birefringence is introduced in the system and χ becomes smaller than 90°, but still greater than 45°. It is also noticeable that the magnitude of Faraday rotation angle increases despite lowering the strength of pure circular birefringence. This effect is more pronounced at $\xi = 50°$.

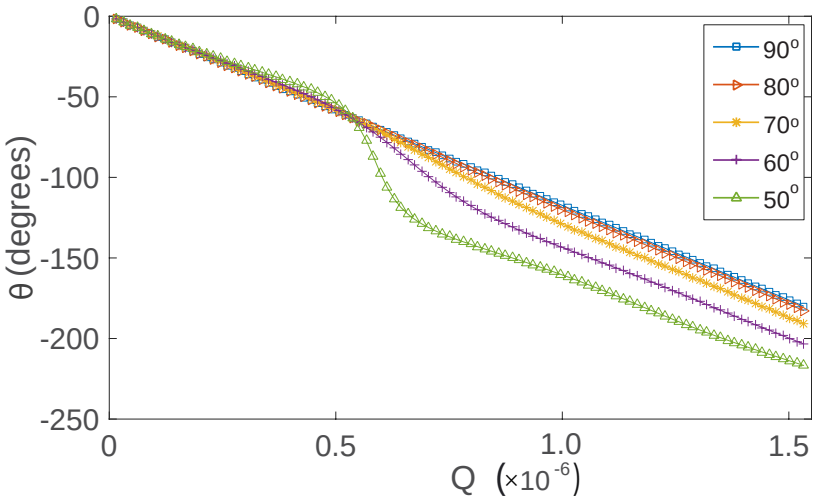

Figure 1.5: Angle of rotation as a function of magneto optic parameter Q for different values of ξ. The non-linearity in rotation angle θ increases as relative strength between MCB and MLB, *i.e.*, ξ is varied from 90° to 50°.

The second term in the denominator of equation (1.48) changes sign between $\xi \in [0°, 45°]$ and $\xi \in [45°, 90°]$. For smaller values of ξ, the effect of linear birefringence dominates and results in the oscillatory and non monotonic behavior of rotation angle as described in Figure 1.6(a). The rotation changes sign with the transition from negative to positive being more pronounced around $\xi = 45^o$ as depicted in Figure 1.6(b). For smaller values of ξ, *i.e.*, $\xi \ll 1$, Eq. (1.48) can be simplified as

$$\tan 2\psi \approx 2\psi \approx \xi \sin(\Delta\beta d) \tag{1.50}$$

which constrains the rotation within the range $\pm\xi/2$. Furthermore, there also exists nodal points where the rotation is completely zero, where $\Delta\beta$ is an integral multiple of π/d.

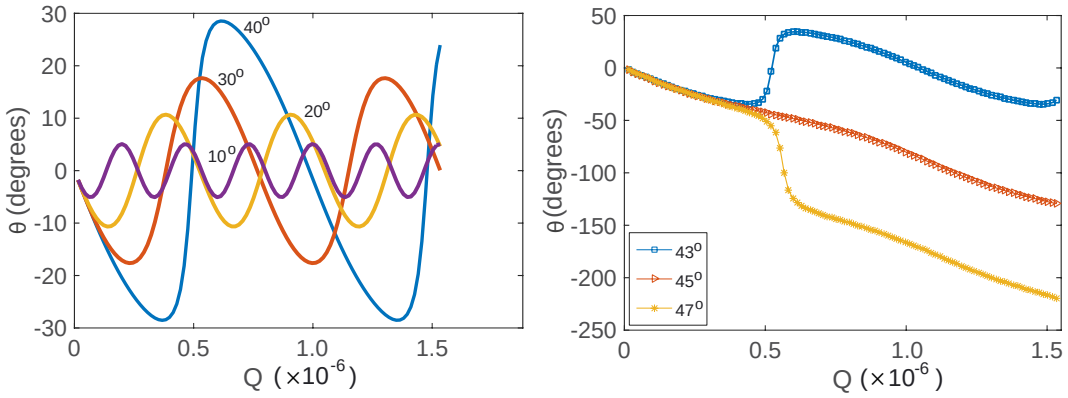

Figure 1.6: (a) Oscillatory behavior of the Faraday rotation angle for different strength of ξ, (b) variation of angle of rotation around $\xi = 45°$, showing the switching of the sense of rotation.

The addition of magnetic linear birefringence certainly imparts ellipticity to the output light which deteriorates the quality of polarization. The alternation of angle of ellipticity with magneto optical parameter for different values of ξ is illustrated in Fig. 1.7. For pure magnetic circular birefringence, the Faraday effect $\xi = 90^o$, ellipticity is zero as shown in Figure 1.7(b). As the strength of MLB increases, the response becomes oscillatory. For the dominating condition of MLB, equation (1.49) can be modeled to a good approximation as

$$\sin 2\chi \approx 2\chi \approx 2\xi \sin^2(\Delta\beta d/2) \tag{1.51}$$

where maximum allowed values are $\chi = \pm\xi$.

The preceding discussion describes the polarization properties of light through pure circular birefringence (MCB) intermixed with magnetic linear birefringence (MLB). The detailed analysis revealed interesting properties of the emergent light such as periodic variation in ellipticity and rotation angle and the complementary and indispensable role of ellipticity measurements. The calculations also highlight the interdependency of rotation and ellipticity. However, the description of magneto-optic effects is still incomplete without the discussion of magnetic linear and circular dichroism combined with MCB and MLB. This discussion will be continued in the next Chapter.

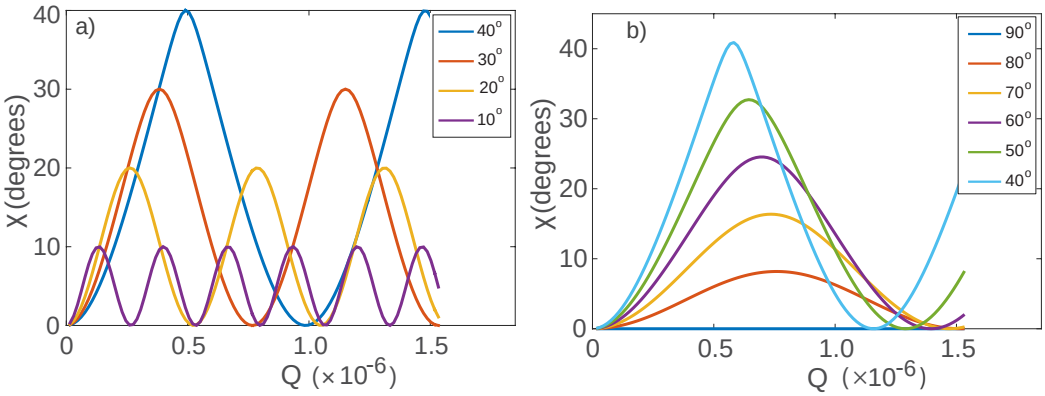

Figure 1.7: Ellipticity as a function of magneto optic parameter for relative strengths of MCB and MLB with a) and b) showing different ranges of the relative MLB and MCB strength quantified by the angle ξ.

Another important part of this chapter is to introduce the reader with an experimental arrangement for the measurement of Faraday rotation angle and the ellipticity. The Faraday rotation angles and ellipticities are usually very small and prone to electrical and thermal noises. In the following Section, we discuss a detection technique which is useful in determining the signal of interest obscured by noise. We will use these techniques to describe our experimental work conducted as part of this dissertation.

1.3.4 Experimental Scheme for Measuring Faraday Rotation

In any physical experiment, there is an uncertainty associated with the measurement. These uncertainties could be the result of limitation of the measuring device or maybe random in nature. In case of electrical measurement, there are different types of noises, *e.g.*, white noise, shot noise and flicker noise etc. The credibility of a measurement is highly dependent on the size and magnitudes of these errors. Very often the signal of interest, in our case the Faraday rotation angle, which is minuscule and may be of the order of nanoradians is buried under noise. In these cases, phase sensitive detection provides the tool to detect and measure extremely small signals hidden inside noise.

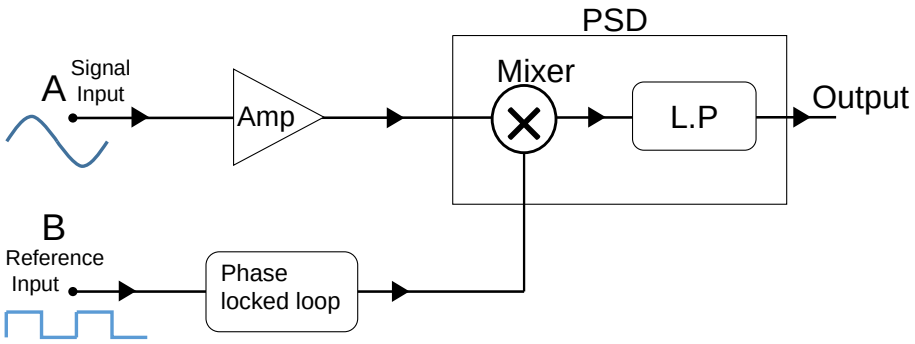

Figure 1.8: Block Diagram of phase sensitive detection. **Amp**= amplifier and **PSD**= phase sensitive detection box and **L.P**= low pass filter.

1.3.5 Phase Sensitive Detection

Phase sensitive detection relies on measurement of that component of the signal which is around a specific frequency or possesses a specific phase. Noise signals, other than within a narrow band around specified frequency are rejected and do not affect the measurement [21]. The steps involved in this phase sensitive detection are depicted in Fig. 1.8 and are mostly implemented by an instrument called lockin amplifier.

A lockin amplifier has two ac input signals, *i.e.*, signal input **A** and reference input **B** as shown in Fig. 1.8. The desired signal ($\omega_\circ$) which is to be measured is given at input A and input B (reference input) is excited with a reference signal with a particular frequency ω_r. This reference signal could be the sync output of an optical chopper or a function generator. The input signal A is first amplified prior to multiplication with the reference signal at mixer. The product signal from the mixer consists of a dc component and and high frequency harmonics. This signal is then allowed to pass through a low pass filter which rectifies the higher harmonics from the output signal and completes the PSD operation. The preceding discussion can also be understood mathematically in the following way.

Consider a sinusoidal input signal with amplitude A and frequency $\omega_\circ$

$$V_{in} = A\sin(\omega_\circ t) \tag{1.52}$$

and reference signal with amplitude B, frequency ω_r and phase ϕ relative to the input signal

$$V_{ref} = B\sin(\omega_r t + \phi). \tag{1.53}$$

The mixer multiplies the signals and the output will be

$$V_{psd} = AB\sin(\omega_\circ t)\sin(\omega_r t + \phi) \tag{1.54}$$

$$= \frac{AB}{2}\Big(\cos((\omega_\circ - \omega_r)t + \phi) - \cos((\omega_\circ + \omega_r)t + \phi)\Big). \tag{1.55}$$

The output signal V_{psd} comprises of two ac signals, one at the difference of frequencies $(\omega - \Omega)$ and the other at the sum frequency $(\omega + \Omega)$. For a special case when input signal frequency matches the reference frequency, *i.e.*, $\omega_\circ = \omega_r$, Eq. (1.54) can be rewritten as

$$V_{psd} = \frac{AB}{2}\Big(\cos(\phi) + \cos(2\omega_r t + \phi)\Big) \qquad \omega_\circ = \omega_r \tag{1.56}$$

Now if this output from the mixer is allowed to pass through a low pass filter with a cutt-off frequency $\omega_c = \omega_\circ$, the sinusoidal component of the equation (1.56) will be removed and the output signal will be

$$V_{psd} = \frac{AB}{2}\cos\phi \tag{1.57}$$

Note the presence of phase component ϕ in Eq. 1.57 which can be adjusted to give a clean DC signal proportional to the amplitude of input signal. The relevance of this phase component can be explained graphically.

Fig. 1.9 displays three different possibilities depending on the relative phase ϕ between reference and input signal which are 0°, 90° and 180°. Let's consider the first case when the reference and input signal are in phase, the output from mixer is a positive quantity (voltage or current). The output remains positive even for the negative half cycle of the reference wave. Hence the output from

mixer is a full wave rectified sinusoid whose DC component is proportional to the input signal. For th second case, *i.e.* $\phi = 90°$, the time average of the output is zero whereas for $\phi = 180°$, the output is simply the negative value of the DC signal and is affirmed by the Eq. (1.57).

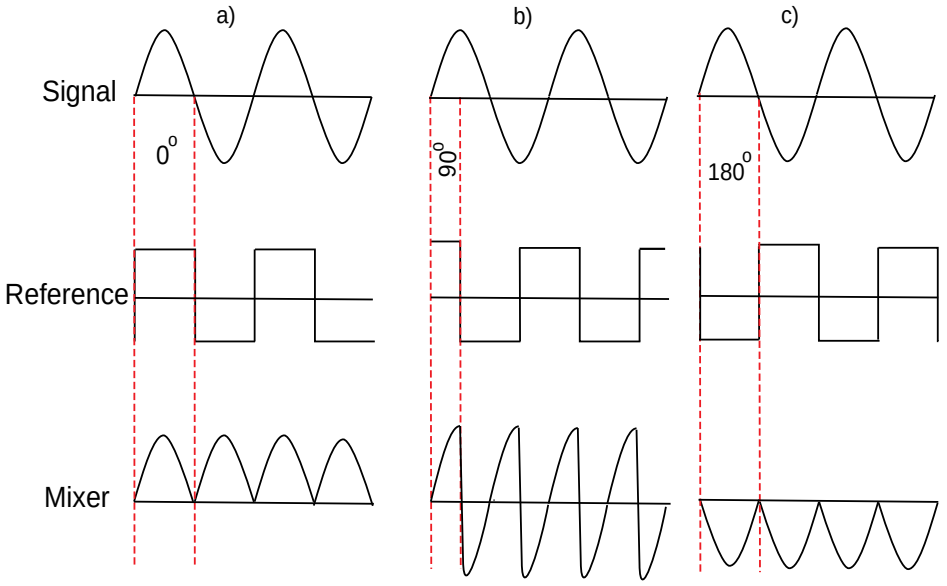

Figure 1.9: Reference and input signal are a) in phase, the mixer output is positive, b) at 90°, the mixer output is zero and c) out of phase, the output is negative.

The signal to noise ratio can be further improved by narrowing the bandwidth of the low pass filter. In the next section, we will discuss the experiment in which we detect the signal of interest extracting the Verdet constant based on this phase sensitive detection technique.

1.3.6 Determination of the Verdet Constant

The strength of the Faraday material is characterized usually by a more meaningful quantity called the Verdet constant. The Verdet constant is basically the measure of the Faraday rotation θ per unit length per unit field. Magneto optic materials with high Verdet constant are highly desirable from device

manufacturing point of view. In this section, we buildup a theoretical background of our experimental setting followed by describing the procedure for determining the Verdet constant. We will use the delineated technique in our subsequent work, in particular the magneto-optic measurements described in Chapters 2 and 4.

The relationship between the Faraday rotation angle θ and the Verdet constant is given by

$$\theta = VBd \tag{1.58}$$

where V represents the Verdet constant which depends on wavelength, temperature and properties of the medium. Different methods for measurement of Verdet constant are outlined by several authors [22, 23] which make use of large dc magnetic field produced by bulky and heavy solenoids and susceptible to electrical noise. In this work we instead follow a phase sensitive detection technique with ac field modulation.

The schematic arrangement of our experimental setup is illustrated in Figure 1.10. Light from a laser source is polarized by a polarizer and passes through the magneto-optic medium placed inside a set of home-built Helmholtz coils. After the coils, the light passes through another polarizer, often called the analyzer. Finally, it impinges on a photodetector which produces a current proportional to the input light intensity. A transimpedance amplifier (TIA) can be used to convert this photocurrent into a voltage before feeding into a lockin amplifier.

For maximum sensitivity of our experimental setup, we ought to find the optimum relative angle between polarizer and analyzer. A linearly polarized light along the horizontal after passing through the Faraday crystal is rotated by an angle θ and Jones vector (suppressing the exponent part) of light is as follows

$$A \begin{pmatrix} \cos\theta \\ \sin\theta \end{pmatrix}, \tag{1.59}$$

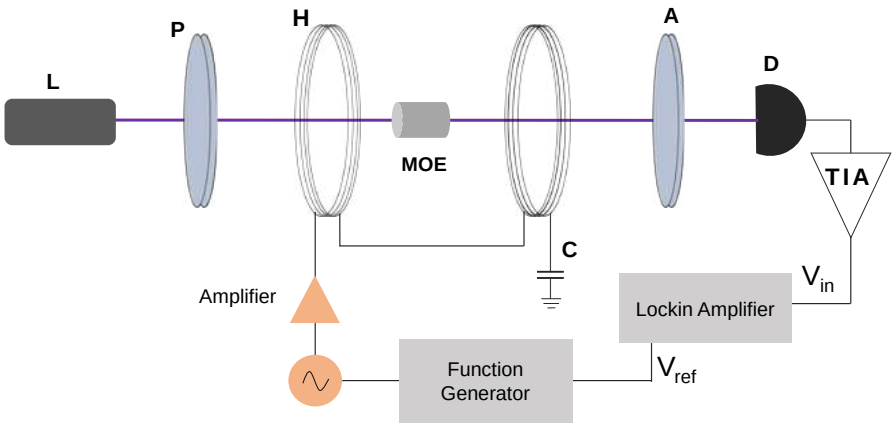

Figure 1.10: The experimental arrangement includes **L**=laser, **P**=polarizer, **MOE**= magneto optic element, **A**= analyzer, **D**= photodetector, **C**= capacitor, **H**= Helmholtz coils and **TIA**= transimpedance amplifier. The perceived beam path is shown in purple.

where A is some constant. After passing through analyzer oriented at angle α relative to polarizer, the electric field vector is given by

$$\mathbf{E} = A \begin{pmatrix} \cos(\alpha - \theta)\cos\alpha \\ \cos(\alpha - \theta)\sin\alpha \end{pmatrix} \tag{1.60}$$

Therefore, the intensity expression for this electric field vector is

$$I = \mathbf{E}^*\mathbf{E} = |A|^2 \cos^2(\alpha - \theta). \tag{1.61}$$

Double differentiating equation (1.61) will help us determine the optimum relative angle between polarizer and analyzer. In other words, $dI/d\alpha$ will be maximum when

$$\alpha - \theta = 45^\circ$$

This equation states that relative angle between polarizer and analyzer must be adjusted to 45° for maximum sensitivity of the setup to measure the Faraday rotation θ. Now if an ac current of frequency Ω was driven through the Helmholtz coils, it generates an oscillatory magnetic field $B = B_\circ \sin\Omega t$. In response to this field, the Faraday rotation angle also becomes a function of time, $\theta = \theta_\circ \sin\Omega t$ with $\theta_\circ = VB_\circ d$. For $\alpha = 45^\circ$ and assuming θ to be small,

equation (1.61) will become

$$I = |A|^2\left(\frac{1 + 2\theta_\circ \sin \Omega t}{2}\right). \tag{1.62}$$

The intensity at photodetector is converted to an electrical current comprising of dc and ac components, i_{dc} and i_{ac} which are given by

$$i_{dc} = \frac{|A|^2}{2}$$

and

$$i'_{ac} = |A|^2\theta_\circ \sin \Omega t$$

As far as the lockin is concerned, it measures the rms component of i_{ac} which is $i_{ac} = i'_{ac}/\sqrt{2}$.

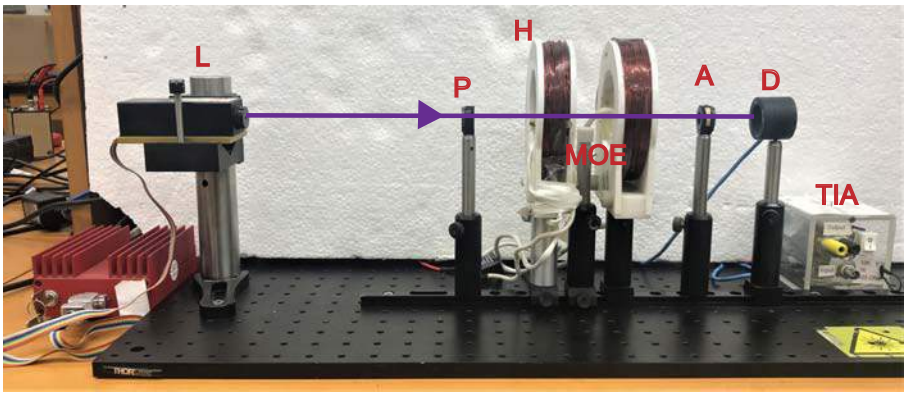

Figure 1.11: Experimental arrangement of the Faraday setup. The light exiting the source passes through the optical element before hitting the photodetector. Where **L**=laser, **P**=polarizer, **H**= Helmholtz coils, **MOE**= magneto-optic element, **A**= analyzer, **TIA**= trans-impedance amplifier and **D**= photodetector

The dc signal refers to the intensity in the absence of a magnetic field. The Faraday rotation angle can be extracted by taking the ratio of ac and dc components.

$$\theta_\circ = \frac{i_{ac}}{\sqrt{2} i_{dc}} \tag{1.63}$$

$$\theta_{rms} = \frac{\theta_\circ}{\sqrt{2}}. \tag{1.64}$$

For measurement of these rotation angles, we employed phase sensitive detection technique through a lockin amplifier (Stanford Research System, SR-830).

The procedural steps for measurement of i_{dc} and i_{ac} are enlisted in the following section.

1.3.7 Experimental Results on Faraday Rotation

A linearly polarized light of wavelength 405 nm from a laser source (B & W TEK-40 mW) is allowed to fall on the cross-sectional area of a magneto-optical element placed at the center of Helmholtz coils. The inductance and resistance of the coils are measured using an LCR meter, are found to be 15 mH and 3.0 ohm, respectively. Before hitting the surface of photodetector (Newport SLS-818), light passes through an analyzer oriented at 45° relative to the polarizer. The detector converts the light intensity to electrical current which serves as an input signal to lockin amplifier.

The pair of Helmholtz coils[1] presents an RLC series circuit whose resonant frequency is given by $f_r = 1/2\pi\sqrt{LC}$, where L is the inductance and C is the capacitance of the series connected capacitor. The resonance frequency f_r is determined by varying the frequency while current through the coils is being measured. At resonant frequency, the strength of inductive and capactive reactances are equal and out of phase, hence the coils become purely resistive and the current through the coils is maximized, which also maximizes the magnetic field.

An ac signal at the resonant frequency $f_r = 820$ Hz is generated by a function generator (BK-precision) is split into two parts. One is used as a reference for lockin amplifier and the other as input to Audio amplifier (150 W) which is connected to the Helmholtz coils for producing an oscillating magnetic field.

Furthermore, prior to conducting the optical measurement, the magnitude of magnetic field produced by the Helmholtz coils is measured using Gaussmeter (Lakeshore-410). We measure different values of i_{ac} as strength of magnetic

[1]Inner and outer diameter of coils are 10.2 cm and 6.5 cm, respectively. No. of turns for each coil is 324 with a resistance of 1.5 Ohm and total inductance $L = 7$ mH.

field is varied by changing the magnitude of current through the Helmholtz coils.

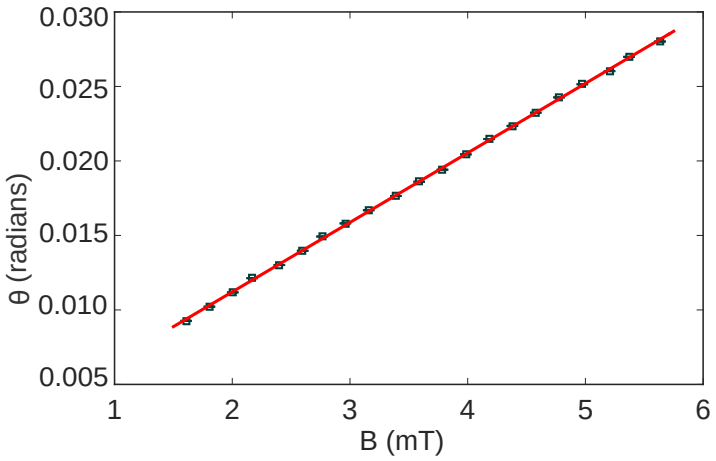

Figure 1.12: Least square curve fitted graph for the Faraday rotation angle θ vs magnetic field B_{rms}. Verdet constant is extracted from the slope of the graph in accordance with Eq. (1.58).

The measured ratio of intensities (1.64), θ is plotted against the magnetic field in Figure 1.12. The dc signal i_{dc} is measured at zero field by using an IV converter of known transimpedance gain. The complete arrangement of the experimental setup is illustrated in Fig. 1.11. The Verdet constant at room temperature for TGG crystal is then estimated by least squares curve fitting of the graph and equals $V = (470 \pm 9)$ rad/T-m at the wavelength 405 nm. This result corroborates with another published value of Verdet constant for TGG which is 463 rad/T-m [24] at $\lambda = 405$ nm.

In another collaborative work carried out by our lab, we also investigated the magneto optic properties of zinc oxide ZnO thin films irradiated with Ni^{+2} ions at different fluence. The results for the Verdet constant measurement are illustrated in Fig. 1.13. The maximum value of Verdet constant is obtained for pristine ZnO thin film which is 53 rad/T-m. The detailed discussion can be found in the published article [25].

Our experimental setup is capable of measuring the Faraday rotation at room

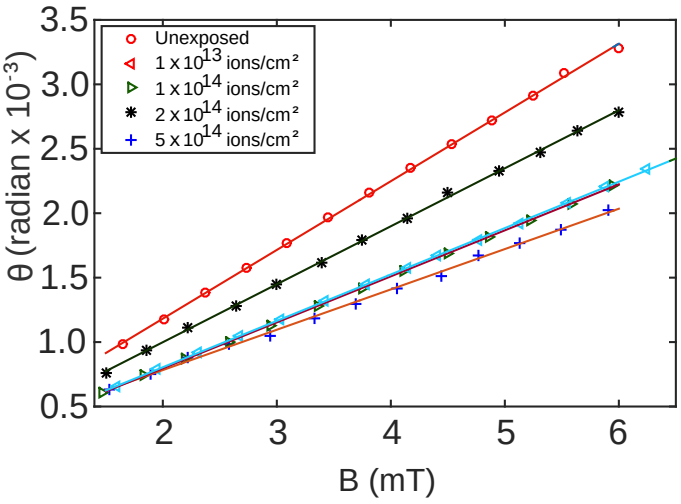

Figure 1.13: The Faraday rotation measurement of pristine and Ni^{+2} irradiated ZnO thin films with different ion fluence. Optical rotation are plotted against the applied magnetic field B.

temperature and it can be also extended to low temperature measurement in a cryogenic chamber equipped with an optical window. As the temperature of the paramagnetic crystals is lowered, the magnetization of the material increases. Consequentially, the Voigt parameter Q, the off-diagonal term in equation (1.19) manifests as the rotation of plane of polarization, is directly proportional to magnetization $\mathbf{M}$. Hence the magnitude of the Faraday rotation increases which could go upto as high as 300° [24]. We describe these low temperature measurements in the next Chapter.

1.4 Magneto Optical Kerr Effect

In the previous section we have discussed magneto-optical effects in the transmission geometry. Its counterpart in reflection geometry is known as magneto optical Kerr effect (MOKE). In Kerr effect, the plane of polarization of rotation of incident light is rotated similar to the Faraday effect but the underlying mechanism for this rotation is somewhat different. In Faraday effect, magnetic circular birefringence is considered the main cause for rotation whereas in Kerr effect it is magnetic circular dichroism which leads to different absorption spectra for left and right circularly polarized light [2, 26]. Polar MOKE was first

used in 1985 for the optical readout of magneto-optic recording devices but the idea of MO storage devices was superseded by advancement in Hard Disk Drive (HDD) technology.

1.4.1 Uses of MOKE in Physics

MOKE is most commonly used in research settings to characterize the electronic and magnetic properties of materials such as the magnetic domain structure, spin density of states, and magnetic phase transition dynamics. We cannot present a comprehensive survey review here. Rather, we like to mention some of the application we've studied (and even attempted, albeit unsuccessfully) in the course of the current doctoral work.

Recent experimental progress on high-quality nanostructures and 2D materials (*e.g.*, transition metal dichalcogenides, graphene, topological insulators) [27] promises to harness these magneto-optic effects for enhanced control of light at the nanoscale for integrated photonic [28] or spintronics devices [29].

Magnetic anisotropy of thin films can be estimated using longitudinal and polar MOKE (we will explain kinds of MOKE shortly). Additionally, in the emergent field of spintronics, one manipulates the spin degree of freedom resulting in spin-polarized currents or pure spin currents and their interaction with lattice, orbital and magnetic moments of the crystal. In a ferromagnetic structure, a spin current can be initialized either by electronic current or applying a thermal gradient to the magnetized sample. The latter comes under the realm of spin caloritronics and is called the spin Seebeck effect [30, 31]. The direct detection of these spin currents is not possible and alternatively, spin currents are converted to charge current by the inverse spin Hall effect [30, 32].

However the detection is encountered with certain limitations due to diminutive size of spin diffusion length and very often the detected signal is contaminated by noise due to different mechanisms such as proximity effect [33], Planar Nernst effects [34], thermoelectric and magnetothermal noises [35–37].

The MOKE technique offers a non-invasive method for detection of these spin currents and was beautifully demonstrated by Ryan *et.al* [38] providing a quantitative description of Kerr rotation due to spin accumulation. In another experiment, the generation of spin orbit torque in a heavy metal(HM)/ferromagnetic metal(FM) bilayer structures due to spin orbit coupling and Rashba effect is detected and quantified by using different geometries of the Kerr effect [39, 40]. Furthermore, detection of spin Hall effect was realized in ferromagnetic semiconductors by making use of MOKE [41].

1.4.2 MOKE Microscopy

Similarly, MOKE microscopy provides the opportunity to observe the dynamic behavior of ferromagnetic domains and domain wall motion [42, 43]. The observation of magnetic domains in ferromagnetic materials by MOKE microscopy is first established in the 1950's [26]. The reflected light from a ferromagnetic film determines the the magnitude of the rotation which is proportional to the local magnetization. The Kerr rotation can determine the orientation and magnitude of the local magnetic domain.

In contemporary physics, MOKE is well established as a cornerstone for investigation of magnetization dynamics and offers a distinctive, robust, noise-free and unique tool for understanding and unraveling the fundamental physical processes involved at nanoscale and ultrafast timescales. The polar, longitudinal and transverse MOKE effects have been exploited in magnetometry and imaging measurements performed upon magnetic thin films [3,5,6].

With technological development, time resolved MOKE microscopy has enabled the researchers to observe the evolutionary behavior of magnetization in the sub-picosecond time regime. Time-resolved MOKE measurements can be used to study electronic relaxation processes and lifetimes of spin populations. A polarized pump pulse initializes the population of spin states. Then a probe pulse measures the strength of the MOKE signal. The relaxation and lifetime

of spin states can be examined by time dependence of population states [44]. A pump-probe MOKE investigation demonstrated the first ever spin dynamics in ultrafast regime by Beaurepaire *et. al.* [45] and initiated a chain reaction of research and exploration in the ultrafast regime. One particular topic in the realm of ultrafast all-optical switching will be discussed in detail in Chapter 3.

MOKE is particularly favored for the non-invasive evaluation of samples and devices that are spatially inhomogeneous, and for in-situ measurements within growth chambers. The additional use of an ultrafast laser source allows high frequency magnetisation dynamics to be probed and imaged [10–16]. The principal limitation of the magneto-optical probe is the finite spatial resolution associated with the optical diffraction limit.

Over the course of this PhD work, we have attempted several experiments revolving around MOKE. The purpose for developing MOKE setup (apart from pedagogical reasons) in our research group is to observe the spin currents generated by thermal gradients in magnetic thin films—the spin Seebeck effect. We first attempted the electrical detection of these spin currents which involves the development and optimization of different components of apparatus required for the desired task, *i.e.*, deposition of thin films, the design and construction of thermo-spin generator, measurement and control of temperature gradients, interfacing of equipments with the computer and MOKE setup. A great deal of time and effort was rendered for this purpose but the attempts to measure the spin current optically were outstripped by another research group [38]. Nevertheless, we learned and developed some key projects during the course of these ventures. Here we'll discuss one of them—magneto-optic Kerr effect.

1.4.3 Geometries of MOKE

MOKE has been classified into three categories based on different orientations of the magnetization of the medium with respect to the incident plane and are depicted in Fig. 1.14.

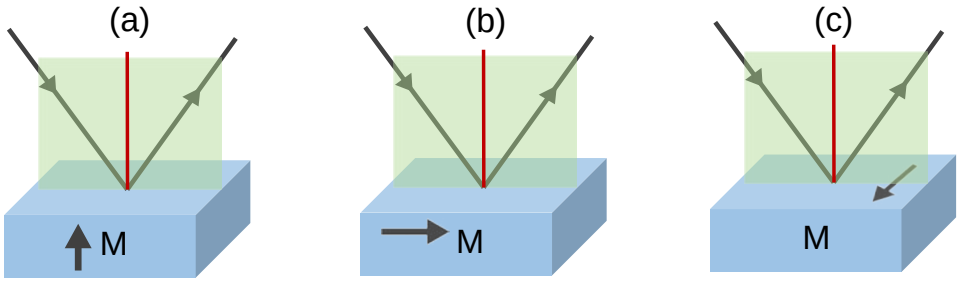

Figure 1.14: Different orientations of magnetization vector with plane of incidence corresponds to different geometries of the Kerr effect: a) polar Kerr effect, b) longitudinal Kerr effect and c) transverse Kerr effect.

1. Longitudinal: The magnetization of the medium is in plane and parallel to incident plane of light.

2. Polar: Magnetization vector is perpendicular to the plane of medium and parallel to plane of incidence.

3. Transverse Kerr effect: Magnetization of the medium is in plane but perpendicular to the plane of incidence.

In each geometry, Kerr effect varies strongly with the angle of incidence. In longitudinal geometry, the magneto optic Kerr effect is zero for normal incidence whereas in the polar Kerr effect, the signal is maximum at normal incidence [46]. Furthermore, polar Kerr effect is almost one order of magnitude larger than longitudinal. The transverse Kerr effect is fundamentally different from longitudinal and polar configuration as it depends on the nature of polarization of incident light. In this configuration, for s-polarized light, there is no interaction between magnetic moment of the sample and incident light. However, for incident p-polarization, the intensity of the reflected light changes but no rotation of polarization plane occurs.

1.4.4 Jones Calculus for Kerr Effect

Here we present the phenomenological description of Kerr effect based on Jones calculus. The schematics of MOKE setup is displayed in Fig. 1.15 and the Jones matrices for the various optical elements are presented below. For the

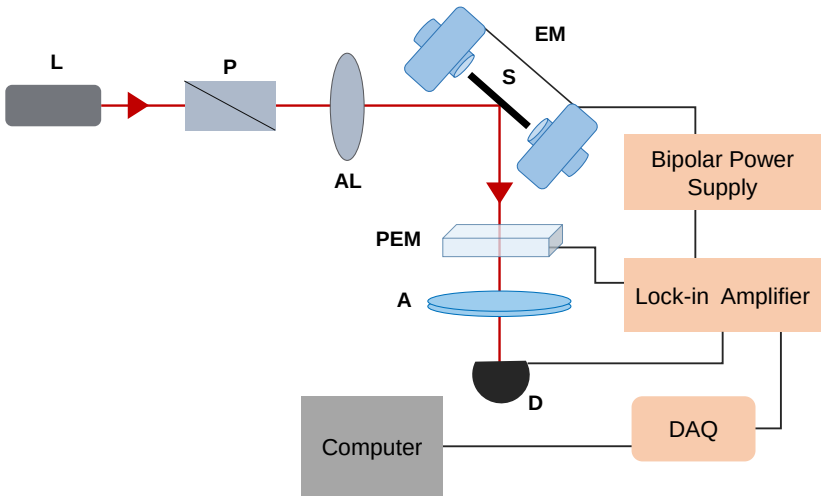

Figure 1.15: The experimental arrangement for longitudinal MOKE including **L**=laser, **P**=Glan-Thompson polarizer, **S**= sample, **PEM**=photoelastic modulator, **A**= analyzer, **D**= photodetector, **DAQ**= data acquisition device, **EM**= electromagnet. The perceived beam path is shown in red.

initial polarizer oriented at an angle β with respect to horizontal, we have

$$P = \begin{pmatrix} \cos^2\beta & \sin\beta\cos\beta \\ \sin\beta\cos\beta & \sin^2\beta \end{pmatrix}, \tag{1.65}$$

and for the analyzer at an angle α

$$A = \begin{pmatrix} \cos^2\alpha & \sin\alpha\cos\alpha \\ \sin\alpha\cos\alpha & \sin^2\alpha \end{pmatrix}. \tag{1.66}$$

Magneto optic Kerr effect is relatively weaker effect than Faraday, which necessitates the use of phase sensitive detection technique, which can be employed by several methods. For example, light modulation can be achieved with optical chopper or magnetic field (discussed in the Section 1.3.7). However we adopted the light polarization modulation technique with photoelastic modulator. The working principle of the photoelastic modulator is the photoelastic effect, *i.e.*, the change in optical properties of the dielectric medium when subjected to mechanical stress. The stress is imposed by a piezoelectric transducer operated at a frequency tuned to the natural frequency of the dielectric which is fused silica The matrix for the photoeleastic modulator is given by

$$M = \begin{pmatrix} e^{i\phi/2} & 0 \\ 0 & e^{-i\phi/2} \end{pmatrix} \tag{1.67}$$

where $\phi = \phi_\circ \sin(\omega t)$ is the periodic retardation imposed by an electric field. The magnetic sample has the matrix of the following form

$$R = \begin{pmatrix} \tilde{r}_p & \tilde{r}_{ps} \\ \tilde{r}_{sp} & \tilde{r}_s \end{pmatrix} \tag{1.68}$$

where diagonal terms are normal Fresnel reflection coefficients and are independent of magnetization similar to the dielectric tensor, defined earlier in Section 1.3.1. The off-diagonal terms describes the coupling strength between s and p polarization components. The magnitudes of $\tilde{r}_{sp}$ and $\tilde{r}_{ps}$ are proportional to magnetization and are linearly dependent on $\mathbf{M}$, consequently they change sign upon the reversal of magnetization of the medium. These co-efficients also reflect the ability of the medium to change an incident p-polarized light to reflected s-polarized light and vice versa. For example, for linearly vertically polarized incident light, the action of the sample matrix will be

$$\begin{pmatrix} \tilde{r}_p & \tilde{r}_{ps} \\ \tilde{r}_{sp} & \tilde{r}_s \end{pmatrix} \begin{pmatrix} 0 \\ 1 \end{pmatrix} = \begin{pmatrix} \tilde{r}_{ps} \\ \tilde{r}_s \end{pmatrix}. \tag{1.69}$$

The off-diagonal terms are given as $\tilde{r}_{ps} = r_{ps} e^{i\delta_{ps}} = -\tilde{r}_{sp} = -r_{sp} e^{i\delta_{sp}}$. The terms δ_i are the corresponding phase angles. Following the schematic arrangement shown in Figure 1.15, the output electric field vector after exiting through analyzer can be computed as

$$\begin{pmatrix} E_p \\ E_s \end{pmatrix}_r = A\, M\, R\, P \begin{pmatrix} E_p \\ E_s \end{pmatrix}_i, \tag{1.70}$$

where r and i represents reflected and incident Jones vectors. The polarizer is used to control the incident beam polarization, the PEM easy axis is along x-direction (lab frame) while the analyzer angle can be varied to obtain the maximum sensitivity for the signal. The Jones calculus for this particular arrangement of elements with polarizer kept at $\beta = 90°$ is computed as

$$\begin{pmatrix} E_p \\ E_s \end{pmatrix}_r = \begin{pmatrix} \cos^2\alpha & \sin\alpha\cos\alpha \\ \sin\alpha\cos\alpha & \sin^2\alpha \end{pmatrix} \begin{pmatrix} e^{i\phi/2} & 0 \\ 0 & e^{-i\phi/2} \end{pmatrix} \begin{pmatrix} \tilde{r}_p & \tilde{r}_{ps} \\ \tilde{r}_{sp} & \tilde{r}_s \end{pmatrix} \begin{pmatrix} 0 \\ 1 \end{pmatrix} \tag{1.71}$$

$$= \begin{pmatrix} e^{-\frac{i\phi}{2}} \cos(\alpha) \left(e^{i\phi} \cos(\alpha) r_{\mathrm{ps}} + \sin(\alpha) r_s \right) \\ e^{-\frac{i\phi}{2}} \sin(\alpha) \left(e^{i\phi} \cos(\alpha) r_{\mathrm{ps}} + \sin(\alpha) r_s \right) \end{pmatrix}. \tag{1.72}$$

The intensity received at the photodetector is

$$\begin{aligned} I \propto \mathbf{E}_\mathbf{r}^* \mathbf{E}_\mathbf{r} &= |E_r|^2 \\ &= K\big[\cos^2\alpha\big[|r_{ps}|^2\cos^2\alpha + |r_s|^2\sin^2\alpha + 2\tilde{r}_s^*\tilde{r}_{ps}\cos(\alpha)\sin(\alpha) \\ &\times e^{-i\phi_\circ\sin(\omega t)} + 2\tilde{r}_{ps}^*\tilde{r}_s\cos(\alpha)\sin(\alpha)e^{-i\phi_\circ\sin(\omega t)}\big] \end{aligned} \tag{1.73}$$

$$= K\big[|r_{ps}|^2\cos^2\alpha + |r_s|^2\sin^2\alpha + r_{ps}r_s\sin(2\alpha)\cos\big(\phi_\circ\sin(\omega t + \delta_{ps} - \delta_s)\big)\big] \tag{1.74}$$

The constant K represents the conversion of electric field squared to intensity units. The last term in expression (1.74) can be further simplified using the Jacobi-Anger expansion [47] which states that

$$\cos(z\sin\theta) = J_0(z) + 2\sum_{n=1}^{\infty} J_{2n}(z)\cos(2n\theta) \tag{1.75}$$

$$\sin(z\sin\theta) = 2\sum_{n=1}^{\infty} J_{2n-1}(z)\sin\big(2n-1\big)(\theta) \tag{1.76}$$

where $J_\zeta(\phi)$ is the Bessel function of first kind and ζ is an integer. The Bessel function is defined as

$$J_\zeta(z) = \sum_{m=0}^{\infty} \frac{(-1)^m}{m!\,\Gamma(m+\zeta+1)!}\left(\frac{z}{2}\right)^{2m+\zeta} \tag{1.77}$$

where Γ is the gamma function $\Gamma(n) = (n-1)!$ [47]. Hence the general expression for intensity can be rewritten as

$$\begin{aligned} \frac{I}{K} &= |r_{ps}|^2\cos^2\alpha + |r_s|^2\sin^2\alpha + 2J_0(\phi_\circ)r_s r_{ps} \times \cos(\delta_s - \delta_{ps})\sin\alpha\cos\alpha \\ &+ 4J_1(\phi_\circ)r_s r_{ps}\sin(\omega t)\sin(\delta_s - \delta_{ps})\sin\alpha\cos\alpha \\ &+ 4J_2(\phi_\circ)\cos(2\omega t)r_s r_{ps}\cos(\delta_s - \delta_{ps})\sin\alpha\cos\alpha + \cdots . \end{aligned} \tag{1.78}$$

Let's analyze this expression for various orientations of the analyzer angle α. For $\alpha = 0$, $I/K = |r_{ps}|^2$ showing that the intensity directly determines the magnitude of the Fresnel coefficients, *i.e.*, $|r_{ps}|^2$. Similarly for $\alpha = 90^o$, the expression (1.78) is simplified to $I/K = |r_s|^2$. However for $\alpha = 45^o$ and $\alpha = 135^o$, the intensity expression comprise the sum of the magnitude of Fresnel coefficients (steady component) and time varying component which are given by

$$\begin{aligned} \frac{I}{K} &= \frac{1}{2}|r_{ps}|^2 + \frac{1}{2}|r_s|^2 + J_0(\phi_0)r_s r_{ps}\cos(\delta_s - \delta_{ps}) + 2J_1(\phi_0)r_s r_{ps}\sin(\omega t) \\ &\times \sin(\delta_s - \delta_{ps}) + 2J_2(\phi_0)\cos(2\omega t)r_s r_{ps}\cos(\delta_s - \delta_{ps}) + \cdots \end{aligned} \tag{1.79}$$

and

$$\frac{I}{K} = \frac{1}{2}|r_{ps}|^2 + \frac{1}{2}|r_s|^2 - J_0(\phi_0) r_s r_{ps} \cos(\delta_s - \delta_{ps}) - 2J_1(\phi_0) r_s r_{ps} \sin(\omega t) \times \sin(\delta_s - \delta_{ps}) - 2J_2(\phi_0) \cos(2\omega t) r_s r_{ps} \cos(\delta_s - \delta_{ps}) + \cdots \quad (1.80)$$

respectively.

We strive to find the angle of rotation and ellipticity specified by the general expressions (1.16) and (1.17) for a polarization ellipse. In the present case, $r = \tilde{r}_s/\tilde{r}_{ps}$, therefore the rotation angle and ellipticity can be redefined in terms of the Fresnel coefficients as

$$\tan 2\theta_k \approx 2\theta_k = \frac{r_{ps}}{r_s} \cos\delta \quad (1.81)$$

$$\sin 2\chi_k \approx 2\chi_k = \frac{r_{ps}}{r_s} \sin\delta \quad (1.82)$$

where $\delta = \delta_s - \delta_{ps}$ and subscript k is attributed to the Kerr effect. Using equations (1.81) and (1.82) and algebraic manipulation, the intensity (1.79) can be rewritten as

$$\frac{I}{K} = 1 + \frac{|r_{ps}|^2}{2|r_s|^2} + J_0(\phi_0)\theta_k + 4J_1(\phi_0)\chi_k \sin(\omega t) + 4J_2(\phi_0) \cos(2\omega t)\theta_k + \cdots . \quad (1.83)$$

Equation (1.83) corresponds to two different frequencies (ωt) and ($2\omega t$), which are called first and second harmonics in addition to a dc value.

$$\tilde{I}_0 = 1 + \frac{|r_{ps}|^2}{2|r_s|^2} + J_0(\phi_0)\theta_k \quad (1.84)$$

$$I_\omega = 4J_1(\phi_0)\chi_k \quad (1.85)$$

$$I_{2\omega} = 4J_2(\phi_0)\theta_k \quad (1.86)$$

In our experimental scheme, we have chosen the value of $\phi_0 = 108^o$ which renders $J_0(\phi_0) = 0$. Furthermore, $r_{ps} \ll r_s$, hence $r_{ps}^2/r_s^2 \approx 0$, which reduces $\tilde{I}_0 = I_0 = (1/2)r_s^2$. It is also obvious that rotation angle can be extracted from equation (1.86) as

$$\theta_k = \frac{\sqrt{2} I_{2\omega}}{4J_2(\phi_0) I_0} \quad (1.87)$$

where $\sqrt{2}$ comes from the fact that the lockin amplifier outputs the rms value. We conclude this section with the comment that the measurement of the Kerr rotation angle requires the second harmonic measurement which can be performed by phase sensitive detection as described earlier in Section 1.3.5. The next section lays out the experimental details and implementation of PSD for the Kerr measurements performed in our lab.

1.4.5 Experimental Method for MOKE Studies

The experimental method is based on phase sensitive detection where modulation is achieved by a photoeleastic modulator as described previously [48–51]. A photograph showing the experimental arrangement of all optical elements is shown in Figure 1.16.

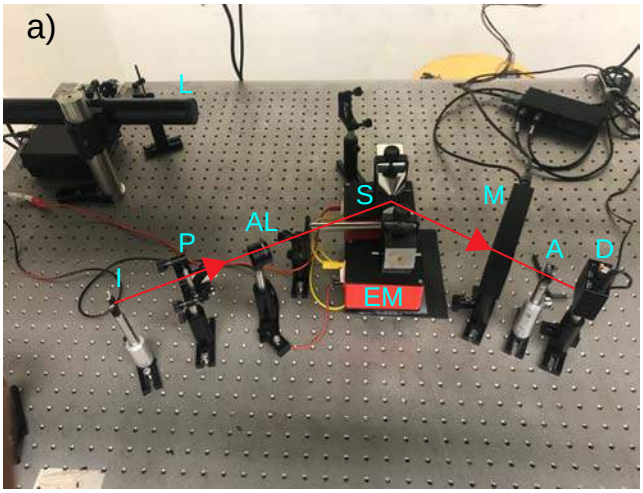

Figure 1.16: Experimental arrangement of optical elements for polar MOKE. The percieved beam path is highlighted in red where **L**=laser, **I**= iris diaphragm, **P**=polarizer, **S**= magnetic thin film, **PEM**= photoelastic modulator, **A**= analyzer, **D**= photodetector and **EM**= electromagnet.

Since Kerr rotation and ellipticity are usually small in magnitude $\approx 10^{-3}$ rad, suitable arrangement of optical elements is crucial to achieve high signal to noise ratio.

For a high degree of polarization, the light from He-Ne laser ($\lambda = 632.8$ nm)

passes through a Glan-Thompson polarizer (Thorlabs GTH10-A) with an extinction ratio of 10^6:1. An aspheric lens of focal length $f = 250$ mm is used to focus the light on the sample surface. The reflected light is then modulated sinusoidally by the photoelastic modulator (Hinds Instrument, PEM-100) operated at 50 kHz. The modulation signal is also used as a reference for the lockin amplifier (Stanford Reasearch System, SR-830). The modulated beam traverses through the analyzer (Thorlabs, LPVIS050-A) to reach a high speed photodetector (Hinds Instruments, DET-200).

The sample is placed between the poles of an electromagnet (GMW-3470) which is driven by a bipolar power supply (KEPCO). The strength of the magnetic field is measured with a Gaussmeter (Lakeshore-410) against the input current. For convenience, this graph is stated as calibration curve and is presented in Fig. 1.17 (we will explain shortly how this calibration curve is used in our measurements). The slope of the graph yields the magnitude of magnetic field per unit current which is (45 ± 1) mT/A. The complete MOKE setup is integrated and interfaced with computer in Labview environment (A.1.1) through a data acquisition device (National Instruments, USB-6001).

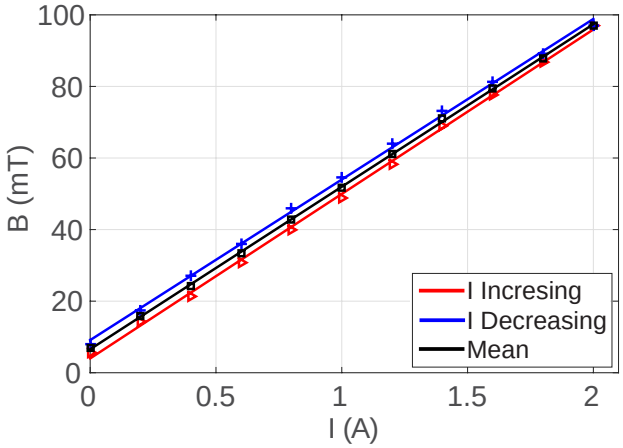

Figure 1.17: Magnitude of magnetic field produced between the poles of the electromagnet against the input current. The data is curve fitted linearly and shown as solid lines.

This concludes the discussion of experimental details on MOKE. For testing the capabilities of our experimental setup, we obtained standard samples, *i.e.*, ferromagnetic thin films, from Durham Magneto Optics with known values of the Kerr rotation. In addition, we also deposited ferromagnetic thin films using magnetron sputtering. The next section introduces the reader to this topic in particular.

1.4.6 Thin Film Deposition by Magnetron Sputtering

Sputtering is a physical vapor deposition technique for thin film deposition. This involves the generation of a plasma inside a vaccum chamber and positively charged ions and electrons are accelerated by high voltage imposed upon the plasma. The accelerated ions strike the negative electrode with sufficient energy to dislodge and eject atoms from the target. These atoms will be ejected in a typical line-of-sight cosine distribution from the face of the target and will get deposited to a substrate placed in close proximity of the sputtering cathode. The sputtering process is illustrated in Figure 1.18.

The target material of which the thin film is desired is placed inside a vacuum chamber. Once the desired vacuum has been achieved, the sputter gas (argon, oxygen, nitrogen etc.) is introduced in the chamber at constant pressure using a mass flow controller. The sputtering is initialized by applying high voltages which ionizes the sputter gas and creates a plasma inside the chamber. These positive ions are attracted towards the negatively biased target material at high velocities that sputters off atomic size particles from the surface of the target source material due to the momentum of the collisions. These particles cross the vacuum deposition chamber of the sputter coater and are deposited as a thin film of material on the surface of the substrate to be coated.

The sputtering process can be distinguished as DC or RF sputtering depending on the type of applied potential difference. Metallic target can be sputtered by direct current power supply (DC-sputter) and insulators are deposited by using radio frequency power supply (RF-sputter). Further, the application of

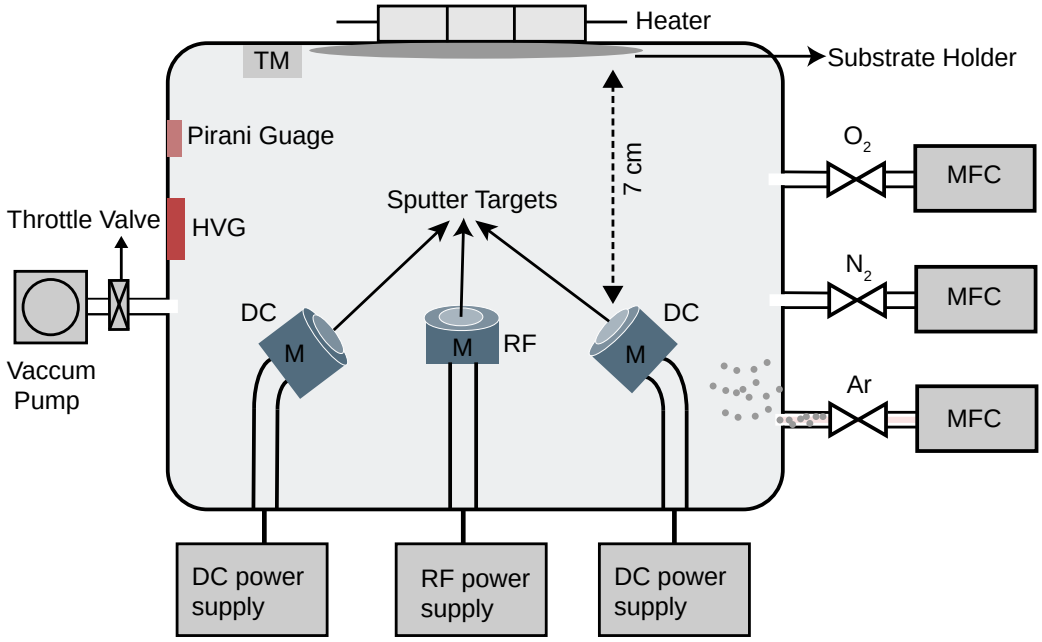

Figure 1.18: The schematic illustration of the mechanical and electrical components involved in magnetron sputtering process. Here **HVG**= high vacuum gauge, **M**= cylindrical magnets below the sputter targets, **MFC**= mass flow controller and **TM**= thickness monitor.

magnetic field can be used to trap ions and electrons which in turns enhances the efficiency of ionization process and allow the plasma to be generated at lower pressure. This kind of sputtering is often referred to "magnetron" sputtering.

The number of atoms ejected or "sputtered off" from the target or source material is called the sputter yield. The sputter yield can be controlled by many key parameters, *e.g.*, base pressure, substrate temperature, target to substrate distance, applied voltages and more importantly sputter gas pressure. The sputter gas pressure increases the rate at which atoms are ejected from the target surface and results in non uniform clusteral growth of target material on the substrate. Further, the substrate temperature is quite crucial for nucleation of atoms being deposited on substrate which in turns affect the uniformity of thin films. The optimization of these key parameters is an iterative process and it may take several weeks to obtain desired results.

In our case thin films have been deposited by using the magnetron sputtering unit (VTS Korea DaON 1000s), equipped with an RF and two DC power supplies. Before deposition, we followed the standard protocol for cleaning the substrate which is essential for deposition of good quality thin films. The substrate were first dipped in acetone and placed in an ultrasonic bath for 15 minutes. The same procedure is followed with iso-propanol and distilled water. The process may be repeated if any dust residue remained on the surface.

Table 1.2: Optimized parameters for magnetron sputtering of magnetic thin films.

Base Pressure	1.0×10^{-6} Torr
Ar Pressure	4.8 mTorr
Ar flow rate	50 sccm
RF power	100 Watt
Substrate temperature	25°C
Target to substrate distance	7 cm

We have optimized the sputter parameters for deposition of magnetic thin films of permalloy $Ni_{80}Fe_{20}$, Nickel (Ni), permendur ($Co_{50}Fe_{50}$) on silicon (Si) and sapphire (Al_2O_3) substrates and are listed in Table 1.2. To minimize the lattice mismatch, we deposited a buffer layer of thickness 2 nm of platinum (Pt) between substrate and magnetic thin film. The thickness of thin films is estimated by analyzing the cross-sectional image of thin film using scanning electron microscope. Moreover, the surface analysis is also performed to determine the quality of sputtered thin films. The results of SEM are presented in the Appendix A.1.

1.4.7 MOKE Results for Ferromagnetic Thin Films

A set of ferromagnetic thin films have been utilized to study the magnetization response and accuracy of the MOKE setup. The scheme for measuring the Kerr response is as follows. All optical elements are arranged according to MOKE measurement geometry, *i.e.*, L or P-MOKE. We intend to measure the change in intensity of the reflected light as the magnetic field at the sample is

varied. This is achieved by sweeping current I which is manifested as a change in magnetic field.

It is pertinent to mention two important points while setting the sweep frequency for current I. First, the sweep signal must be slow enough to sample that magnetization remains in quasi-equilibrium state. Second, the sweep frequency and lockin integration time constant must be adjusted in a way that lockin must register the change in intensity before the current changes to a new value. For this purpose, we simulated a triangular wave of frequency 0.01 Hz in a Labview program which is fed to the bipolar power supply (KEPCO, BOP-50-8D) through the analog output channel of the DAQ. This in turns drives the stipulated current through the coil of electromagnet. In response to the variation of magnetic field, the intensity measured at lockin amplifier is read out by analog inputs of DAQ with an integration time constant of 300 ms, unless stated otherwise.

The Labview program registers the data in the computer which contains the column vectors for current and lockin intensity. The current is multiplied with the calibration factor calculated from the slope of Fig. 1.17 to accurately estimate the magnitude of magnetic field at the sample. The Labview program for MOKE setup is given in the Appendix A.1.1.

Figure 1.19 illustrate the results of MOKE measurement of ferromagnetic permalloy thin film sputtered on silicon and sapphire substrates. Fig. 1.19(a-b) show the 1st and 2nd harmonic longitudinal MOKE response of Si/Pt/NiFe thin film, respectively. Further, Fig. 1.19(c) depicts only the first harmonic of sapphire/Pt/NiFe thin film whereas Fig. 1.19(d) shows the polar MOKE of Si/Pt/NiFe. The graphs are plotted for the lockin intensity against the magnetic field. The soft magnet behavior of NiFe can be clearly seen in the figure and depicts the magnetization easy axis lying in the plane of thin film. In the case of permalloy grown on sapphire substrates, a slight increase in coercivity is observed.

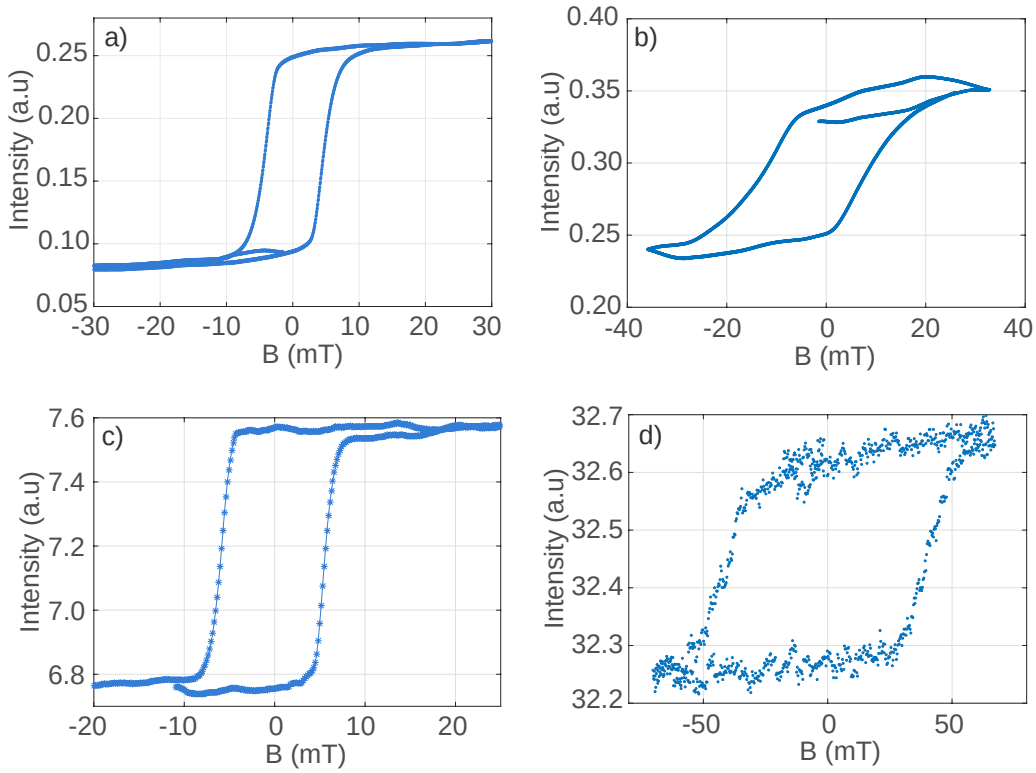

Figure 1.19: a) First harmonic of longitudinal MOKE (L-MOKE) performed on Si/Pt/NiFe and b) second harmonic measurement of permalloy thin film on silicon substrate using L-MOKE. c) First Harmonic of L-MOKE of Al_2O_3/Pt/NiFe thin film and d) polar MOKE (P-MOKE) of Si/Pt/NiFe thin film.

To calculate the absolute Kerr rotation of the samples, we measured the dc value of light intensity at photodetector in the absence of magnetic field. Different methods can be used to measure the dc component given in equation (1.84), however we employed the optical shutter (Stanford Research System, SR-470) in the beam path just before the photodetector in the experimental arrangement 1.15. The optical shutter blocks/unblocks the laser light mechanically. This is operated at a frequency of 100 Hz and the rms output is measured by the lockin amplifier in the absence of magnetic field.

The ratio of intensities according to equation (1.87) yields the magnitude of

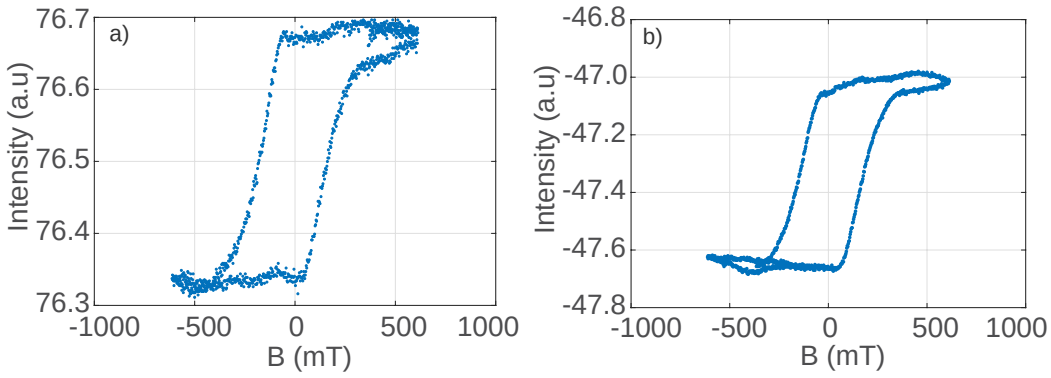

Figure 1.20: a) First harmonic and b) second harmonic polar MOKE measurement of Ta/Pt/CoFeB/Pt thin film. The data presented here is averaged over 14 run.

the Kerr rotation $\theta_k \approx 14$ mdeg in case of Si(substrate)/Pt(8 nm)/NiFe(20 nm) sample.

Similarly Figure 1.20 presents the first and second harmonic measurements for ultrathin film Si(substrate)/Ta(4 nm)/Pt(10 nm)/CoFeB(0.6 nm)/Pt(2 nm) obtained from Durham Magneto-optics for testing purpose. The Kerr rotation angle measured for this thin film is 23 mdeg which is comparable to the reported rotation of 25 mdeg.

The foregoing results completes the discussion of the first order magneto-optic effects, the Faraday and the Kerr effect. This chapter establishes the basic theoretical ground for magneto-optic investigation and measurement techniques for their measurements. The next chapter deals with the second order magneto-optic effects, *i.e.*, the Voigt effect, its measurements and techniques establishing low-temperature magneto optic studies of the terbium gallium garnet crystal.

References

[1] A. Zvezdin and V. Kotov, "Magnetooptical effects," *Modern Magnetooptics and Magnetooptical Materials*, pp. 33–58, 1997.

[2] J. Liu, *Photonic Devices*. Cambridge University Press, 2009.

[3] M. Freiser, "A survey of magnetooptic effects," *IEEE Transactions on Magnetics*, vol. 4, no. 2, pp. 152–161, 1968.

[4] R. I. Hunter, D. A. Robertson, P. Goy, and G. M. Smith, "Design of high-performance millimeter wave and sub-millimeter wave quasi-optical isolators and circulators," *IEEE Transactions on Microwave Theory and Techniques*, vol. 55, no. 5, pp. 890–898, 2007.

[5] S. Mangin, M. Gottwald, C. Lambert, D. Steil, V. Uhlíř, L. Pang, M. Hehn, S. Alebrand, M. Cinchetti, G. Malinowski, *et al.*, "Engineered materials for all-optical helicity-dependent magnetic switching," *Nature Materials*, vol. 13, no. 3, p. 286, 2014.

[6] K. E. Rieckhoff and D. Griffiths, "Optical Faraday rotation studies of paramagnetic resonance in neodymium ethylsulphate," *Canadian Journal of Physics*, vol. 41, no. 1, pp. 33–45, 1963.

[7] D. J. Griffiths and H. Glättli, "Optical Faraday rotation studies of paramagnetic resonance and relaxation in praseodymium ethylsulphate," *Canadian Journal of Physics*, vol. 43, no. 12, pp. 2361–2373, 1965.

[8] S. Crooker, D. Awschalom, J. Baumberg, F. Flack, and N. Samarth, "Optical spin resonance and transverse spin relaxation in magnetic semiconductor quantum wells," *Physical Review B*, vol. 56, no. 12, p. 7574, 1997.

[9] D. Vojna, O. Slezák, A. Lucianetti, and T. Mocek, "Verdet constant of magneto-active materials developed for high-power Faraday devices," *Applied Sciences*, vol. 9, no. 15, p. 3160, 2019.

[10] H. Furuse, R. Yasuhara, K. Hiraga, and S. Zhou, "High Verdet constant of ti-doped terbium aluminum garnet (tag) ceramics," *Optical Materials Express*, vol. 6, no. 1, pp. 191–196, 2016.

[11] U. V. Valiev, J. B. Gruber, G. W. Burdick, I. Igor'A, D. Fu, V. O. Pelenovich, and N. I. Juraeva, "Optical and magnetooptical properties of terbium–scandium–aluminum and terbium-containing (gallates and aluminates) garnets," *Journal of Luminescence*, vol. 176, pp. 86–94, 2016.

[12] W. Crossley, R. Cooper, J. Page, and R. Van Stapele, "Faraday rotation in rare-earth iron garnets," *Physical Review*, vol. 181, no. 2, p. 896, 1969.

[13] O. Slezák, R. Yasuhara, D. Vojna, H. Furuse, A. Lucianetti, and T. Mocek, "Temperature-wavelength dependence of Verdet constant of dy 2 o 3 ceramics," *Optical Materials Express*, vol. 9, no. 7, pp. 2971–2981, 2019.

[14] D. Griffiths, *Introduction to Electrodynamics*. Pearson International Edition, Prentice Hall, 1999.

[15] M. Ware and J. Peatross, *Physics of Light and Optics (Black & White)*. Brigham Young University, Department of Physics, 2015.

[16] B. E. Saleh and M. C. Teich, *Fundamentals of Photonics*. John Wiley & Sons, 2019.

[17] A. Akbar, M. W. Khalid, and M. S. Anwar, "Low temperature Voigt effect in the terbium gallium garnet crystal," *Optics Express*, vol. 25, no. 24, pp. 30550–30559, 2017.

[18] D. Clarke and J. Grainger, *Polarized Light and Optical Measurement*. International Encyclopedia of Pharmacology and Therapeutics, Elsevier Science & Technology, 1971.

[19] M. S. Anwar, H. Majeed, and A. Shaheen, "Analyzing combinations of circular birefringence, linear birefringence, and elliptical dichroism in magneto-optical rotators," *Journal of Modern Optics*, vol. 62, no. 1, pp. 75–84, 2015.

[20] U. Schlarb and B. Sugg, "Refractive index of terbium gallium garnet," *Physica Status Solidi (b)*, vol. 182, no. 2, pp. K91–K93, 1994.

[21] M. L. Meade, *Lock-in amplifiers: principles and applications*. No. 1, Mike Meade, 1983.

[22] M. Basharat, M. Ding, H. Cai, Y. Li, and J. Fang, "A comparative study on the measurement of Verdet constant of magneto-optic glass by different techniques," in *2018 15th International Bhurban Conference on Applied Sciences and Technology (IBCAST)*, pp. 55–62, IEEE, 2018.

[23] O. Brevet-Philibert, R. Brunetton, and J. Monin, "Measuring the Verdet constant: a simple, high precision, automatic device," *Journal of Physics E: Scientific Instruments*, vol. 21, no. 7, p. 647, 1988.

[24] A. Shaheen, H. Majeed, and M. S. Anwar, "Ultralarge magneto-optic rotations and rotary dispersion in terbium gallium garnet single crystal," *Applied Optics*, vol. 54, no. 17, pp. 5549–5554, 2015.

[25] M. F. Khan, K. Siraj, M. Anwar, M. Irshad, J. Hussain, H. Faiz, S. Majeed, M. Dosmailov, J. Patek, J. Pedarnig, *et al.*, "700 kev ni+ 2 ions induced modification in structural, surface, magneto-optic and optical properties of zno thin films," *Nuclear Instruments and Methods in Physics Research Section B: Beam Interactions with Materials and Atoms*, vol. 368, pp. 45–49, 2016.

[26] N. Spaldin, *Magnetic Materials: Fundamentals and Applications*. Cambridge University Press, 2010.

[27] S. Das, J. A. Robinson, M. Dubey, H. Terrones, and M. Terrones, "Beyond graphene: progress in novel two-dimensional materials and van der waals solids," *Annual Review of Materials Research*, vol. 45, pp. 1–27, 2015.

[28] T. Loughran, P. Keatley, E. Hendry, W. Barnes, and R. Hicken, "Enhancing the magneto-optical Kerr effect through the use of a plasmonic antenna," *Optics Express*, vol. 26, no. 4, pp. 4738–4750, 2018.

[29] D. Allwood, G. Xiong, M. Cooke, and R. Cowburn, "Magneto-optical Kerr effect analysis of magnetic nanostructures," *Journal of Physics D: Applied Physics*, vol. 36, no. 18, p. 2175, 2003.

[30] K. Uchida, S. Takahashi, K. Harii, J. Ieda, W. Koshibae, K. Ando, S. Maekawa, and E. Saitoh, "Observation of the spin seebeck effect," *Nature*, vol. 455, no. 7214, p. 778, 2008.

[31] J. Xiao, G. E. Bauer, K.-c. Uchida, E. Saitoh, S. Maekawa, *et al.*, "Theory of magnon-driven spin seebeck effect," *Physical Review B*, vol. 81, no. 21, p. 214418, 2010.

[32] K.-i. Uchida, H. Adachi, T. Ota, H. Nakayama, S. Maekawa, and E. Saitoh, "Observation of longitudinal spin-seebeck effect in magnetic insulators," *Applied Physics Letters*, vol. 97, no. 17, p. 172505, 2010.

[33] S.-Y. Huang, X. Fan, D. Qu, Y. Chen, W. Wang, J. Wu, T. Chen, J. Xiao, and C. Chien, "Transport magnetic proximity effects in platinum," *Physical Review Letters*, vol. 109, no. 10, p. 107204, 2012.

[34] A. Avery, M. Pufall, and B. L. Zink, "Observation of the planar nernst effect in permalloy and nickel thin films with in-plane thermal gradients," *Physical Review Letters*, vol. 109, no. 19, p. 196602, 2012.

[35] S. Huang, W. Wang, S. Lee, J. Kwo, and C. Chien, "Intrinsic spin-dependent thermal transport," *Physical Review Letters*, vol. 107, no. 21, p. 216604, 2011.

[36] I. Soldatov, N. Panarina, C. Hess, L. Schultz, and R. Schäfer, "Thermoelectric effects and magnetic anisotropy of gamnas thin films," *Physical Review B*, vol. 90, no. 10, p. 104423, 2014.

[37] M. Schmid, S. Srichandan, D. Meier, T. Kuschel, J.-M. Schmalhorst, M. Vogel, G. Reiss, C. Strunk, and C. H. Back, "Transverse spin seebeck effect versus anomalous and planar Nernst effects in permalloy thin films," *Physical Review Letters*, vol. 111, no. 18, p. 187201, 2013.

[38] R. McLaughlin, D. Sun, C. Zhang, M. Groesbeck, and Z. V. Vardeny, "Optical detection of transverse spin-seebeck effect in permalloy film using sagnac interferometer microscopy," *Physical Review B*, vol. 95, no. 18, p. 180401, 2017.

[39] X. Fan, H. Celik, J. Wu, C. Ni, K.-J. Lee, V. O. Lorenz, and J. Q. Xiao, "Quantifying interface and bulk contributions to spin–orbit torque in magnetic bilayers," *Nature Communications*, vol. 5, p. 3042, 2014.

[40] X. Fan, A. R. Mellnik, W. Wang, N. Reynolds, T. Wang, H. Celik, V. O. Lorenz, D. C. Ralph, and J. Q. Xiao, "All-optical vector measurement of spin-orbit-induced torques using both polar and quadratic magneto-optic Kerr effects," *Applied Physics Letters*, vol. 109, no. 12, p. 122406, 2016.

[41] Y. K. Kato, R. C. Myers, A. C. Gossard, and D. D. Awschalom, "Observation of the spin Hall effect in semiconductors," *Science*, vol. 306, no. 5703, pp. 1910–1913, 2004.

[42] W. Jiang, P. Upadhyaya, Y. Fan, J. Zhao, M. Wang, L.-T. Chang, M. Lang, K. L. Wong, M. Lewis, Y.-T. Lin, *et al.*, "Direct imaging of thermally driven domain wall motion in magnetic insulators," *Physical Review Letters*, vol. 110, no. 17, p. 177202, 2013.

[43] T. Koyama, Y. Nakatani, J. Ieda, and D. Chiba, "Electric field control of magnetic domain wall motion via modulation of the Dzyaloshinskii-Moriya interaction," *Science Advances*, vol. 4, no. 12, p. eaav0265, 2018.

[44] K. Lee, J. Kim, J. Jeong, D. Kim, S. Shin, K. Hong, Y. S. Lee, C. H. Nam, M. H. Son, and S. W. Hwang, "Femtosecond pump-probe moke microscopy for an ultrafast spin dynamics study," *Journal-Korean Physical Society*, vol. 49, no. 6, p. 2402, 2006.

[45] E. Beaurepaire, J.-C. Merle, A. Daunois, and J.-Y. Bigot, "Ultrafast spin dynamics in ferromagnetic nickel," *Physical Review Letters*, vol. 76, no. 22, p. 4250, 1996.

[46] M. Mansuripur, *Classical Optics and its Applications*. Cambridge University Press, 2002.

[47] G. Arfken, H. Weber, and F. Harris, *Mathematical Methods for Physicists: A Comprehensive Guide*. Elsevier Science, 2013.

[48] K. Sato, "Measurement of magneto-optical Kerr effect using piezo-birefringent modulator," *Japanese Journal of Applied Physics*, vol. 20, no. 12, p. 2403, 1981.

[49] S. Jasperson and S. Schnatterly, "An improved method for high reflectivity ellipsometry based on a new polarization modulation technique," *Review of Scientific Instruments*, vol. 40, no. 6, pp. 761–767, 1969.

[50] P. Nederpel and J. Martens, "Magneto-optical ellipsometer," *Review of Scientific Instruments*, vol. 56, no. 5, pp. 687–690, 1985.

[51] W. Kim, M. Aderholz, and W. Kleemann, "Calibration of polar Kerr rotation and ellipticity measurements," *Measurement Science and Technology*, vol. 4, no. 11, p. 1275, 1993.

Chapter 2

Magneto-Optic Rotations under Transverse Magnetic Fields—the Voigt Effect

The previous chapter discussed the mainstream magneto-optic effects, the Faraday and the Kerr, which are important for their widespread utilization in device manufacturing, technological advancement and role in magnetic characterization. In this chapter, we will discuss the relatively lesser known magneto optic effect (the Voigt effect). We set up the discussion by invoking a phenomenological description of Voigt effect based on the Jones calculus as outlined in the previous chapter. Then follows the discussion of Stokes vector and polarimetry. Afterwards, we describe the experimental arrangement for measurement in the Voigt geometry and present our experimental results.

2.1 Background and Motivation

A magnetic field induces a magnetization **M** inside a paramagnetic material changing its response to polarized light; qualifying as a preliminary investigation in the realm of magneto-optics [1]. The response manifests as a rotation θ and ellipticity χ imparted to the outgoing beam. The orientation of **M** relative to the wave vector **k** determines the nature, amplitude, reciprocity and order of magneto-optic activity. The strongest of these effects, and the most prominently studied, is undoubtedly the Faraday rotation which is observed when $\mathbf{M}\|\mathbf{k}$. The effect is first order in **M**, originates from magnetic circular

birefringence (MCB), and is non reciprocal, $\theta(-\mathbf{k}) = -\theta(\mathbf{k})$ as discussed in detail in the previous Chapter.

In paramagnetic crystals, there also exists a much smaller effect called the Voigt [2] or Cotton-Mouton effect [3] which registers when the magnetization is perpendicular to the wave vector, $\mathbf{M} \perp \mathbf{k}$. The phenomenon is reciprocal, $\theta(-\mathbf{k}) = +\theta(\mathbf{k})$ and quadratic, i.e., $\propto |\mathbf{M}|^2$. The Voigt effect originates from magnetic linear birefringence (MLB) and magnetic linear dichroism (MLD) which are defined shortly. Briefly these correspond to the real and imaginary values of the asymmetry in refractive indices $\Delta n = n_1 - n_2$ where n_1 and n_2 are defined for polarizations parallel and perpendicular to the magnetization. The smallness of the effect can be gauged from some typical values. For example, the asymmetry is reported at a mere $(6.7 \pm 0.5) \times 10^{-15}$ for water vapor [4] at room temperature and 1 T and $\approx -5 \times 10^{-4}$ for the terbium aluminate garnet $Tb_3Al_5O_{12}$ at 4.2 K and 4 T [5]. Clearly sensitive techniques are required for recording these asymmetries.

For conductive and semiconducting materials, however relatively larger effects can be observed. For example we deduce a value of $\approx 3 \times 10^{-4}$ from the data provided on the doped dilute magnetic semiconductor $(Ga_{0.98}Mn_{0.02})As$ [6]. For conductive media, the effective permittivity tensor $\tilde{\varepsilon}$ includes the conductivity tensor σ at optical frequency ω and is given by $\tilde{\varepsilon} = \varepsilon_b + i\sigma/\omega$. In these materials, the magneto-optic rotations are dominated by the field-dependent terms in σ rather than the non-conductive background part ε_b. This effect has been used to reveal magnetic anisotropies related to structural patterning in Co films [7], spin-orbit torques transferred across interfaces [8] and magnetization dynamics in Huesler compounds [9].

The Voigt studies of non-conducting garnet crystals are however less common [3, 5, 10]. In the present work, we report systematic investigations of MLB and MLD for terbium gallium garnet $Tb_3Ga_5O_{12}$ (TGG) at cryogenic temperatures (8–100 K) and variable dc magnetic fields. Although crystalline

TGG has been extensively studied in the Faraday configuration from room temperatures all the way down to cryogenic temperatures [11] but measurements in the Voigt geometry are lacking. The material's prominence owes to some highly desirable features such as large Verdet constants, high thermal conductivity [12] and high damage threshold [13] making it into an almost archetypal material.

Furthermore, the Voigt effect offers an invaluable tool for the investigation of antiferromagnets (AFs). Antiferromagnetic materials lack the macroscopic magnetization due to the antiparallel alignment of neighbouring spins in a crystal. The magnetic field required for reorientation of AFs could reach tens or hundreds of Tesla. In addition, the AFs materials are much difficult to access by first order magneto-optic phenomena. However, MLB and MLD are both quadratic with respect to M, antiparallel magnetization vectors will both give additive rotations which can be analyzed by means of the expression derived above. Hence by rotating the crystal, or the input polarization, it is possible to measure δ and hence the orientation of the Néel vector. Indeed this has been beautifully demonstrated in the reference [14] and evokes exciting possibilities for studying antiferromagnets [15, 16]. In another experiment, ultrafast spin dynamics in antiferromagnet NiO has been attributed to the inverse Voigt effect [17].

Additionally, interesting quantum phenomena have also been detected in TGG which include the obsevation of the phonon Hall effect [18], excitation of magnetic resonances at THz [19] and microwave frequencies [20], and the observation of the inverse Faraday effect [21]. The present work complements previous studies and introduces an altogether new perspective for TGG crystals to be used in the unusual Voigt geometry, providing quantitative data on the magnetic field induced asymmetries in the refractive index, Δn, from which temperature dependent coefficients can also be deduced. The theoretical background is presented in Section 2.2 and Section 2.3 describes the experimental work.

2.2 Theory

2.2.1 Phenomenological Description of the Voigt Effect

The dielectric tensor capturing magneto-optic effects is represented by equation (1.34) and is reproduced here

$$\varepsilon_{MO} = \varepsilon_0 \begin{pmatrix} n_x^2 & -iQ & 0 \\ iQ & n_y^2 & 0 \\ 0 & 0 & n_z^2 \end{pmatrix}. \tag{2.1}$$

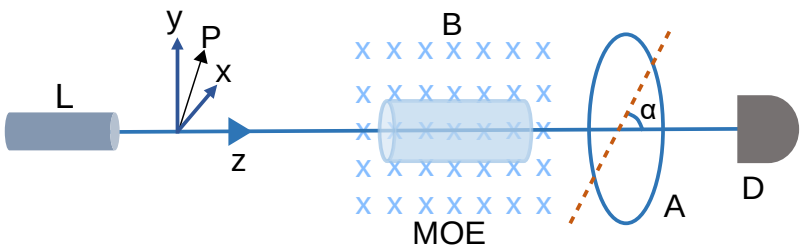

Figure 2.1: The Voigt effect geometry. **P** denotes the light polarized in the x-y plane transverse to the propagation direction z-axis, **MOE** = magneto-optic element, **B** = magnetic field applied into the page, **A** = analyzer at an angle α and **D** = photodetector.

Magnetic circular birefringence (MCB) and magnetic circular dichroism (MCD) relate to the off-diagonal whereas magnetic linear birefringence (MLB) and magnetic linear dichroism (MLD) relate to the diagonal terms. The latter two are the main theme of the present Chapter. For a cubic crystal we have $n_x = n_y = n_z = n$ where n represents the refractive index in the absence of magnetization. Here we assume that the radiation is propagating along the $\hat{z}$ direction and is polarized inside the transverse ($\hat{x}$-$\hat{y}$) plane as depicted in Fig. 2.1.

Let's first assume $Q = 0$ which which corresponds to the axial magnetization $M_z = 0$. Without loss of generality we also assume that $M_y = 0$ and $M_x = M$ (i.e. the sample is magnetized along $\hat{x}$). The magnetic field lifts the $n_x = n_y$ degeneracy introducing an asymmetry Δn and the induced refractive indices become $n_x = n + \Delta n/2$ and $n_y = n - \Delta n/2$. By solving Eq. (2.1), the

normal modes of the tensor are the *linear* polarization states $E_o\hat{x}$ and $E_o\hat{y}$. The wave vectors for the normal modes are given by $\omega/c(n \pm \Delta n/2)$ where ω and c represent the angular frequency and speed of light.

The asymmetry $\Delta n = \Delta n' - i\Delta n''$ is a complex number, its real ($\Delta n'$) and imaginary ($\Delta n''$) components are designated MLB and MLD respectively. Even though these terms show a *quadratic* dependence on M_{xy}, the terms are classified *linear* ascribed to their linear normal modes. In order to probe Δn with maximal sensitivity, we input light that is an equal superposition of the normal modes and in Jones notation

$$E_1 = \frac{E_o}{\sqrt{2}}\big(\hat{x} + \hat{y}\big). \tag{2.2}$$

After emerging from a crystal of axial length d the state becomes

$$E_o \frac{e^{ik_o nd}}{\sqrt{2}}\left(e^{i\Delta\beta' d/2}\hat{x} + e^{-i\Delta\beta'' d/2}\hat{y}\right). \tag{2.3}$$

For convenience, we have defined $\Delta\beta' = k_o\Delta n'$ and $\Delta\beta'' = k_o\Delta n''$ and $k_o = \omega/c$. The polarization angle θ (with respect to the $\hat{x}$ axis) and the ellipticity $\chi \in [-\pi/4, \pi/4]$ can be immediately extracted from the complex elements in the Jones vector (2.3). For a Jones vector with elements $\left(|E_x|e^{i\phi_x}, |E_y|e^{i\phi_y}\right)^T$, the angles are given by equations (1.16) and (1.17), defined earlier in the previous chapter. Due to the explicit use in the forthcoming sections, we reiterate these angles here as

$$\tan 2\theta = \frac{2r}{1-r^2}\cos\phi \tag{2.4}$$

$$\sin 2\chi = \frac{2r}{1+r^2}\sin\phi. \tag{2.5}$$

where $r = |E_y|/|E_x|$ and $\phi = \phi_y - \phi_x$. Applying these equations to the state in (2.3), we obtain closed form expressions for the angles

$$\tan 2\theta = -\frac{\cos\left(\Delta\beta' d\right)}{\sinh\left(\Delta\beta'' d\right)} \tag{2.6}$$

$$\sin 2\chi = \frac{\sin\left(\Delta\beta' d\right)}{\cosh\left(\Delta\beta'' d\right)}. \tag{2.7}$$

Hence the net magneto-optic rotation affected by the element will be $|\theta - \pi/4|$ (since the initial polarization is $\pi/4$). In the limit of small MLD and MLB, $\Delta\beta' d, \Delta\beta'' d \ll 1$, we deduce

$$\tan 2\theta \approx -1/(\Delta\beta'' d), \quad \text{and} \tag{2.8}$$

$$\sin 2\chi \approx \Delta\beta' d, \tag{2.9}$$

indicating that the rotation is exclusively caused by MLD and ellipticity by MLB. Interestingly, this is opposite to what is observed in conventional Faraday rotation experiments wherein the rotation is caused by MCB (i.e. Q') and the ellipticity originates from MCD (i.e. Q'') as derived in the Sections 1.3.1 and 1.3.2 of the previous chapter, respectively. Equations (2.8) and (2.9) indeed quantify the rotation and variation in the ellipticity caused by the Voigt effect but the discussion will be incomplete without investigating the intermixing of these effects. The next section will investigate the intermixing of linear birefringence and dichroism.

2.2.2 Intermixing of Magnetic Linear Birefringence and Dichroism Effects

Following the experimental geometry illustrated in the Fig. 2.1, we can pass the state in (2.3) through an analyzer oriented at an angle α with respect to $\hat{x}$ and measure the signal on a subsequently placed detector. Using Jones calculus we predict an output intensity

$$I(\alpha) = I_o\Big(\cosh(\Delta\beta'' d) + \sinh(\Delta\beta'' d)\cos(2\alpha) + \cos(\Delta\beta' d)\sin(2\alpha)\Big) \tag{2.10}$$

where I_o is a proportionality factor measured at zero magnetic field and $\alpha = 0$. The terms $\Delta\beta' d$ and $\Delta\beta'' d$ represents the magnetic linear birefringence and dichroism respectively. The form of the intensity shows that MLD and MLB are intertwined with one another. It is relevant to point the reader towards two important corollaries. First, suppose the input polarization makes an angle of $(\pi/4 + \delta)$ with the magnetization which could arise due to the slight misalignment of polarizer or birefringence of optical elements, thereby modifying the input field, (2.2) to

$$E_1 = E_o\big(\cos(\pi/4 + \delta)\hat{x} + \sin(\pi/4 + \delta)\hat{y}\big). \tag{2.11}$$

Following an analogous calculation based on Jones analysis, the output intensity is determined as

$$I(\alpha) = I_o\Big(\cosh(\Delta\beta'' d)\left\{1 - \sin(2\delta)\cos(2\alpha)\right\} + \sinh(\Delta\beta'' d) \times \left\{\cos(2\alpha) - \sin(2\delta)\right\} + \cos(\Delta\beta' d)\sin(2\alpha)\left\{cos(2\delta)\right\}\Big) \tag{2.12}$$

where the modified terms are highlighted through their placement inside curly brackets. As a verification, expression (2.10) is correctly reproduced for $\delta = 0$. This scenario is highly relevant to probing the magnetic structure of antiferromagnets, which by virtue of their compensated magnetization, have largely remained elusive for magneto-optic investigations.

The second corollary is the presence of circular effects concomitant with the linear ones. In the previous chapter, Section 1.3.3 elaborated the intermixing of pure magnetic circular and linear birefringence. Here, we further extend the analysis to a more general case where linear and circular magneto-optic effects merges with the linear and circular dichroism.

2.2.3 Intermixing of Linear and Circular Effects

Clearly a nonzero axial magnetization ($M_z \neq 0, Q \neq 0$) modifies the results discussed so far. For example, this scenario can arise out of a stray component in the axial direction. For the complete solution to the full tensorial problem we observe that the normal modes of the magneto-optic tensor are the elliptically polarized states,

$$\vec{w}_1 = \frac{1}{\sqrt{2}}\Big(-i(1+\sin\xi), \cos\xi\Big)^T \quad \text{and} \quad \vec{w}_2 = \frac{1}{\sqrt{2}}\Big(\cos\xi, -i(1+\sin\xi)\Big)^T \tag{2.13}$$

with the respective refractive indices

$$\gamma_1 = \left(n^2 + \sqrt{Q^2+\zeta^2}\right)^{1/2} \quad \text{and} \quad \gamma_2 = \left(n^2 - \sqrt{Q^2+\zeta^2}\right)^{1/2}. \tag{2.14}$$

In (2.13), we have defined the parameter $\zeta = (n_1^2 - n_2^2)/2 \approx n\Delta n$ which characterizes the asymmetry in the linear direction and $\tan\xi = \zeta/Q$ which

determines the mixing of the linear and circular effects. The input state (2.2) can now be resolved into the eigenmodes, (2.13), each mode picks up a phase $e^{ik_o\gamma_i d}, (i = 1, 2)$ inside the crystal and the output electric field vector in $\{\vec{w}_1, \vec{w}_2\}$ basis will be

$$E_o\big|_{\vec{w}_1,\vec{w}_2} = \begin{pmatrix} \big(\sqrt{1-\sin\xi} + i\sqrt{1-\sin\xi}\big)e^{ik_\circ\gamma_1 d} \\ \big(\frac{\cos\xi}{\sqrt{1-\sin\xi}} - i\frac{\cos\xi}{\sqrt{1+\sin\xi}}\big)e^{ik_\circ\gamma_2 d} \end{pmatrix}. \tag{2.15}$$

Implying a similar approach we used earlier in conjunction with Eq. (1.26), this state can be transformed back to the rectilinear coordinates by a transfer matrix P given by

$$P = \frac{1}{2}\begin{pmatrix} -i\sqrt{1+\sin\xi} & \frac{i\cos\xi}{\sqrt{1+\sin\xi}} \\ \sqrt{1-\sin\xi} & \frac{\cos\xi}{\sqrt{1-\sin\xi}} \end{pmatrix}. \tag{2.16}$$

Consequently, the state in equation (2.15) will get transformed as

$$E_o\big|_{\hat{x},\hat{y}} = PE_o\big|_{\vec{w}_1,\vec{w}_2} \tag{2.17}$$

$$= \frac{1}{2}\begin{pmatrix} -i\sqrt{1+\sin\xi} & \frac{i\cos\xi}{\sqrt{1+\sin\xi}} \\ \sqrt{1-\sin\xi} & \frac{\cos\xi}{\sqrt{1-\sin\xi}} \end{pmatrix}\begin{pmatrix} e^{i\tan^{-1}(f)}e^{ik_\circ\gamma_1 d} \\ e^{i\tan^{-1}(\frac{1}{f})}e^{ik_\circ\gamma_2 d} \end{pmatrix} \tag{2.18}$$

where $f = \big(1+\sin\xi\big)/\cos\xi$. After some algebra it can be shown that the emergent state in the $\hat{x}$, $\hat{y}$ basis is

$$E_o\big|_{\hat{x},\hat{y}} = \frac{1}{2}\frac{1}{\sqrt{1+\sin\xi}}\begin{pmatrix} -ie^{i\theta_1}(1+\sin\xi) + e^{i\theta_2}\cos\xi \\ e^{i\theta_1}\cos\xi + -ie^{i\theta_2}(1+\sin\xi) \end{pmatrix}, \tag{2.19}$$

where $\theta_1 = \tan^{-1}(f) + k_o\gamma_1 d$, $\theta_2 = \tan^{-1}(1/f) + k_o\gamma_2 d$. This form does not provide much physical insight in a straightforward way but becomes the basis for calculating the rotation and ellipticity. Subsequently, the components of output electric field can be readily obtained by implying trigonometric manipulations on equation (2.19) and are given by

$$|E_{\circ x}| = \frac{1}{\sqrt{2}}\left(\sqrt{1-\cos\xi\cos\big(\tan^{-1}(f) - \tan^{-1}(\frac{1}{f}) + k_\circ(\gamma_1-\gamma_2)d\big)}\right) \tag{2.20}$$

$$|E_{\circ y}| = \frac{1}{\sqrt{2}}\left(\sqrt{1+\cos\xi\cos\big(\tan^{-1}(f) - \tan^{-1}(\frac{1}{f} + k_\circ(\gamma_1-\gamma_2)d\big)}\right) \tag{2.21}$$

Hence the rotation θ and ellicpticty angle χ is calculated using the recipe in (2.4) and (2.5).

$$\tan 2\,\theta = \frac{\cot(\theta_1-\theta_2)}{\cos\xi} \tag{2.22}$$

$$\sin 2\,\chi = -\sin\xi\sin(\theta_1-\theta_2). \tag{2.23}$$

These expressions provide a quantitative relationship for the magnitude of angle of rotation θ and elliptcity χ when a medium exhibits all of these magneto optic effects i.e., MLD, MLB, MCD and MCB. It also highlights the fact that these effects are inextricably linked together and jointly determine the rotation and ellipticity.

This completes the discussion of intermixing of linear and circular effects. The next task is to measure the rotation and ellipticity angles in the Voigt geometry. The measurement of magnetic linear birefringence (the Voigt effect) can be approached in several ways outlined by several authors [1, 22] but we adopted a more comprehensive approach (which we will discuss shortly) based on the measurement of the Stokes vector.

2.2.4 The Stokes Vector

For perfectly polarized light, Jones calculus suffices the need for determination of characteristics of polarization ellipse as discussed in the previous Chapter (section 1.2). However, Jones vectors cannot be used to describe partially polarized beam of light. Another set of parameters is required for the description of partially polarized light, a combination of totally polarized and unpolarized components, which could encompass the complete characterization of polarizaiton ellipse. The Stokes vector (I, M, C, S) constitute such a set of parameters [22]. The Stokes parameters provides the advantage and convenience of polarization measurement as each parameter corresponds to measurable intensities. The Stokes parameters in a fixed basis are given by

$$\begin{aligned} I &= \langle E_x^2 \rangle + \langle E_y^2 \rangle \\ M &= \langle E_x^2 \rangle - \langle E_y^2 \rangle \\ C &= \langle E_d^2 \rangle - \langle E_a^2 \rangle \\ S &= \langle E_l^2 \rangle - \langle E_r^2 \rangle \end{aligned} \tag{2.24}$$

where the subscripts represent different bases, $\hat{x}, \hat{y}$ are the Cartesian axes, $\hat{b}, \hat{a}$ are the Cartesian axes rotated by $\pm 45°$ and the circular bases are defined by

$\hat{l} = (\hat{x} + i\hat{y})/\sqrt{2}$ and $\hat{r} = (\hat{x} - i\hat{y})/\sqrt{2}$. For convenience, the Stokes parameters are represented by a column vector

$$\begin{pmatrix} I \\ M \\ C \\ S \end{pmatrix}. \tag{2.25}$$

The first parameter I represents the total intensity of the beam, M describes the degree of polarization with respect to the two orthogonal axes, x and y axes and parameter C embodies the plane polarization oriented at 45° with respect to the x-axis and S shows the degree of circular polarization, i.e., $S = -1$ for left circular polarization and $+1$ for right ciruclar polarization. It is pertinent to note that for perfectly polarized light, only three parameters are independent since the relation

$$I^2 = M^2 + C^2 + S^2 \tag{2.26}$$

holds true for completely polarized light. Whereas for partially polarized light $I^2 \geq M^2 + C^2 + S^2$ wherein the inequality arises due to the presence of unpolarized components of light[1].

Therefore for completely unpolarized components of light, the Stokes vector can takes the form

$$\begin{pmatrix} 1 \\ 0 \\ 0 \\ 0 \end{pmatrix}. \tag{2.27}$$

Since the Stokes parameters are dependent on the choice of axes [23], there must exist some rotation matrix which transforms the Stokes vector from one coordinate system to another. The transformation can be written as

$$\begin{pmatrix} I' \\ M' \\ C' \\ S' \end{pmatrix} = R \begin{pmatrix} I \\ M \\ C \\ S \end{pmatrix} \tag{2.28}$$

[1]In Chapter 4, we'll change gears to using another definition of Stokes parameters wherein $I \leftrightarrow S_\circ$, $M \leftrightarrow S_3$, $C \leftrightarrow S_1$ and $S \leftrightarrow S_2$. This is to conform to a quantum mechanical description which matches the conventional Bloch sphere representation of quantum states.

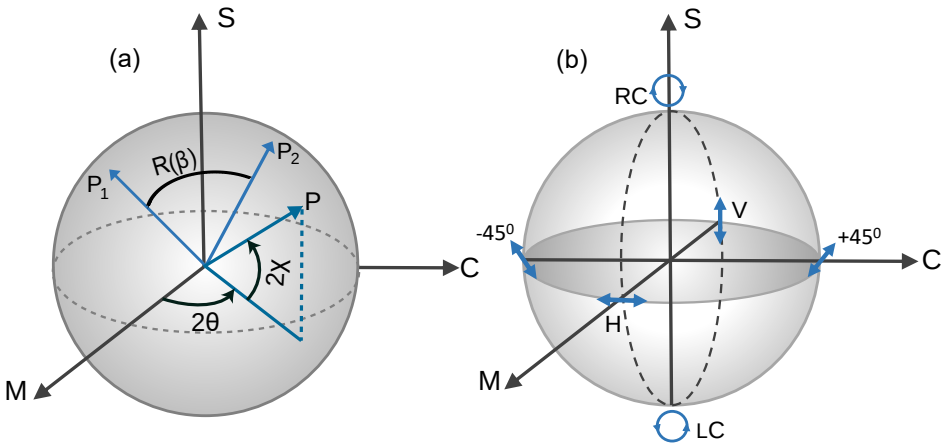

Figure 2.2: The description of Poincare sphere where a) a transfer matrix R(β) rotates the point P$_1$(M, C, S) to another point P$_2$(M', C', S') by an angle β and b) the illustration of different commonly encountered polarization states on the sphere.

where the transformation matrix R

$$R(\beta) = \begin{pmatrix} 1 & 0 & 0 & 0 \\ 0 & \cos 2\beta & \sin 2\beta & 0 \\ 0 & -\sin 2\beta & \cos 2\beta & 0 \\ 0 & 0 & 0 & 1 \end{pmatrix}, \tag{2.29}$$

and β is the rotation angle. The rotation in the opposite sense changes the sign of the sine function.

Furthermore, Eq. (2.26) represents an equation for a sphere of radius I with co-ordinate axes M, C and S. This scenario is visualized in Fig. 2.2. The three dimensional graphical approach offers a more convenient method for the description and manipulation of polarized light and is known as the Poincare sphere [22]. Each point on the surface of Poincare sphere represents a polarization state with particular Stokes parameters (M, C, S). The action of the rotation matrix (2.29) for an arbitrary polarization state can be visualized by means of Poincare sphere and is illustrated in Fig. 2.2(a) where a point P_1 with particular set of Stokes parameter, is being rotated through an angle β to another point on the Poincare sphere.

All linear polarization states lie on the equator and circularly polarized states are listed at the poles as depicted in the Fig. 2.2(b). Whereas intermediate elliptical states are continuously distributed between the equator and the poles. Any two orthogonal states are represented on the antipodal points of Poincare sphere[2].

The relationship between the Stokes vector and spherical orientation and ellipticity, θ and χ, can be obtained by the projection of point P on the coordinate axis of the Poincare sphere as depicted in the Fig. 2.2(a) and is given by [1]

$$M = I\cos 2\chi \cos 2\theta \tag{2.30}$$

$$C = I\cos 2\chi \sin 2\theta \tag{2.31}$$

$$S = I\sin 2\chi \tag{2.32}$$

The characteristics of polarization ellipse, from the Poincare representation of Stokes vector is given by [22]

$$\theta = \frac{1}{2}\tan^{-1}\left(\frac{C}{M}\right) \qquad 0 \leq \theta \leq \pi \tag{2.33}$$

$$\chi = \frac{1}{2}\sin^{-1}\left(\frac{S}{I}\right) \qquad -\frac{\pi}{4} \leq \chi \leq \frac{\pi}{4} \tag{2.34}$$

The shape of the ellipse is given by S/I and handedness can be inferred from the sign of S [24].

The aim of this discussion was to familiarize the reader with the Stokes vector which form the bases of our experimental investigation and how they are related to our variables of interest, i.e., rotation θ and ellipticity χ. Once the Stokes vector are determined, the estimation of rotation and ellipticity is straight forward, as dictated by equations (2.33) and (2.34). The next section will lay the theoretical background for the Stokes vector estimation from the intensity measurement of light.

[2]In Chapter 4, we employ the Bloch sphere, sometimes also called the polarization sphere [24], in line with quantum terminology.

2.2.5 Stokes Polarimetry

For measurement of the Stokes vector, the intensity measurement needs to be determined at different orientations of polarimetry elements. We setup the discussion with the experimental arrangement as illustrated in the Fig. 2.3. In this configuration, for polarized light impinging on a retarder with fast axis at angle δ with the x-axis, followed by an analyzer at an angle α, the intensity measured at the detector can be determined by Mueller's calculus [22]

$$\begin{pmatrix} I' \\ M' \\ C' \\ S' \end{pmatrix} = A\, R(\alpha - \beta)\, \delta\, R(\beta) \begin{pmatrix} I \\ M \\ C \\ S \end{pmatrix} \tag{2.35}$$

where $R(\beta)$ is given by Eq. (2.29) which transform the Stokes vector (I, M, C, S) to the retarder frame of reference and δ captures the effect of retarder and P is the polarizer. The transformation back to the analyzer frame of reference is achieved by the rotation matrix $R(\alpha - \beta)$. The Mueller matrices for the retarder δ and the polarizer A are given by

$$\delta = \begin{pmatrix} 1 & 0 & 0 & 0 \\ 0 & 1 & 0 & 0 \\ 0 & 0 & \cos 2\delta_r & \sin 2\delta_r \\ 0 & 0 & -\sin 2\delta_r & \cos 2\delta_r \end{pmatrix} \quad \text{and} \quad A = \begin{pmatrix} 1 & 1 & 0 & 0 \\ 1 & 1 & 0 & 0 \\ 0 & 0 & 0 & 0 \\ 0 & 0 & 0 & 0 \end{pmatrix}. \tag{2.36}$$

The emerging intensity to be measured is given by

$$\begin{aligned} I'_{out}(\alpha, \beta, \delta_r) = \frac{1}{2}\Big(& I + [M \cos 2\beta + C \sin 2\beta] \cos 2(\alpha - \beta) \\ & + [(C \cos 2\beta - M \sin 2\delta_r) \cos \delta_r + S \sin \delta_r] \times \sin 2(\alpha - \beta) \Big). \end{aligned} \tag{2.37}$$

Eq. (2.37) is a general intensity expression which can be utilized in several configurations, facilitating an experimenter with various degrees of freedom to choose from. Different approaches used for the Stokes parameter estimation are enumerated in [22], however, we adopted a fixed analyzer and rotating retarder (QWP) technique presented in [25]. For a rotating retarder, Eq. (2.37) can be

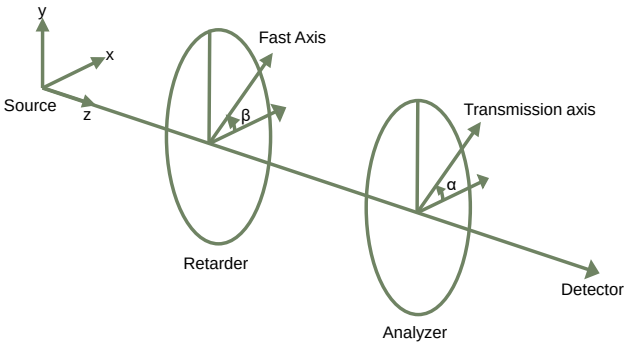

Figure 2.3: The experimental arrangement for the determination of Stokes parameters.

rewritten as

$$I'_{out}(\alpha,\beta,\delta_r) = \frac{1}{2}\Big[I + \big(\frac{M}{2}\cos 2\alpha + \frac{C}{2}\sin 2\alpha\big)\Big] + \frac{1}{2}\Big[S\sin\delta\sin(2\alpha - 2\beta) + \frac{1}{4}[(M\cos 2\alpha - C\sin 2\alpha)\cos 4\beta + (M\sin 2\alpha + C\cos 2\alpha) \times \sin 4\beta](1-\cos\delta)\Big], \tag{2.38}$$

where the retardation plate angle $\beta = \omega t$. Here ω represents the angular velocity of the retarder and t is the time.

It can be clearly seen that Eq. (2.38) represents a Fourier series of the form given by

$$I'(\beta) = C_\circ + C_2\cos 2\beta + C_4\cos 4\beta + S_2\sin 2\beta + S_4\sin 4\beta \tag{2.39}$$

which can be inverted in a finite and discrete Fourier transform. The relationship between the Fourier coefficients $C_\circ, C_2, C_4, S_4$ and the measured intensity at the detector, for even number of data points, i.e., $N = 2L$ (36 in our case) is given by [25]

$$C_{\omega k} = \frac{2}{N}\frac{1}{1+\delta_{k,0}+\delta_{k,L}}\sum_1^N I_i'(\beta)\cos(\omega_k\beta_i), \tag{2.40}$$

$$C_{\omega k} = \frac{2}{N}\frac{1}{1+\delta_{k,0}+\delta_{k,L}}\sum_1^N I_i'(\beta)\sin(\omega_k\beta_i), \tag{2.41}$$

where $k = 0, 1 \cdots, L$ and $\delta_{k,j}$ are Kronecker delta functions and

$$\omega_k = \frac{2\pi}{N}.\frac{k}{\Delta\beta} \quad \text{and} \quad \beta_i = (i-1)\Delta\beta.$$

Here $\Delta\beta$ is the step size for the rotating QWP. Once the Fourier coefficients are extracted from the measured intensity, the determination of Stokes parameters from the coefficients is straightforward and can be readily obtained by [25]

$$I = C_o - \frac{1+\cos\delta_r}{1-\cos\delta_r}[C_4\cos(4\alpha+4\beta_o) + S_4\sin(4\alpha+4\beta_o)] \tag{2.42}$$

$$M = \frac{2}{1-\cos\delta_r}[C_4\cos(2\alpha+4\beta_o) + S_4\sin(2\alpha+4\beta_o)] \tag{2.43}$$

$$C = \frac{2}{1-\cos\delta_r}[S_4\cos(2\alpha+4\beta_o) - C_4\sin(2\alpha+4\beta_o)] \tag{2.44}$$

$$S = \frac{-S_2}{\sin\delta_r\cos(2\alpha+4\beta_o)} \tag{2.45}$$

where β_o is the initial angle between the fast axis of the retarder and the x-axis.

The envisaged scheme for Stokes polarimetry can be understood in the following steps. Linearly polarized light is subjected to pass through a magneto optical element (TGG crystal). The radiation is then followed by a retarder (QWP) and for a known value of analyzer angle α, the intensity variation is measured as the QWP is being rotated in steps of size $\Delta\beta$, which are a small fraction of 360°. The measured intensity is processed through discrete Fourier transform to extract the Stokes vector. Finally, the rotation θ and ellitpcitiy angle χ are determined using equations (2.33) and (2.34), respectively.

As stated earlier in Section 2.1, magnetic *linear* birefringence is a weaker effect than *circular* and the rotation caused by pure linear birefringence is usually very small. One possible way to address this problem is to increase the local magnetization of the medium in conjunction with the phase sensitive detection scheme discussed earlier in the first Chapter. This can be achieved either by increasing the magnitude of applied magnetic field B or by decreasing the temperature of the magneto optic medium. For all practical purposes, the magnitude of magnetic field required is too high to be implemented. Therefore we adopted the latter approach and the following section will discuss the

experimental scheme for determination of Stokes parameters and details for achieving the cryogenic temperatures.

2.3 Experimental Setup

The experimental setup can be divided into two components: the mechanical and optical. The mechanical part of the setup is solely comprised of instruments necessary for achieving cryogenic temperatures. The system is called a closed cycle helium refrigeration system and is illustrated in Fig. 2.4. The optical part includes the light source, detectors, polarizers, waveplates mounted in rotation stages and home-built stages for optical elements housing designed according to the constraint imposed by measurement geometry.

2.3.1 Refrigeration Cycle

The block diagram of the mechanical part of the setup is shown in Figure 2.4. The major components of the closed cycle cryostat are the expander, compressor, vacuum-pump station, and radiation shield. The expander (Janis, CS-350S), commonly referred to as the coldhead, is where the Gifford-McMahon refrigeration cycle takes pace. It is connected to a compressor by two gas lines and an electrical power cable. One of the gas lines supplies high pressure helium gas to the expander, the other gas line returns low pressure helium gas from the cold head.

The compressed helium is allowed to expand which provides cooling to the two stage refrigeration cycle. The vacuum shroud surrounds the cold end of the expander in a vacuum limiting the heat load on the expander, caused by conduction and convection. The radiation shield is actively cooled by the first stage of the expander and insulates the second stage from the room temperature thermal radiation being emitted from the vacuum shroud [26]. The vacuum chamber is fitted with non-magnetic quartz windows.

The heat generated by the compressor is carried by the cooled water supplied by the chiller (Polyscience, 6550) at 4.2 liter per minute (lpm). For optimum

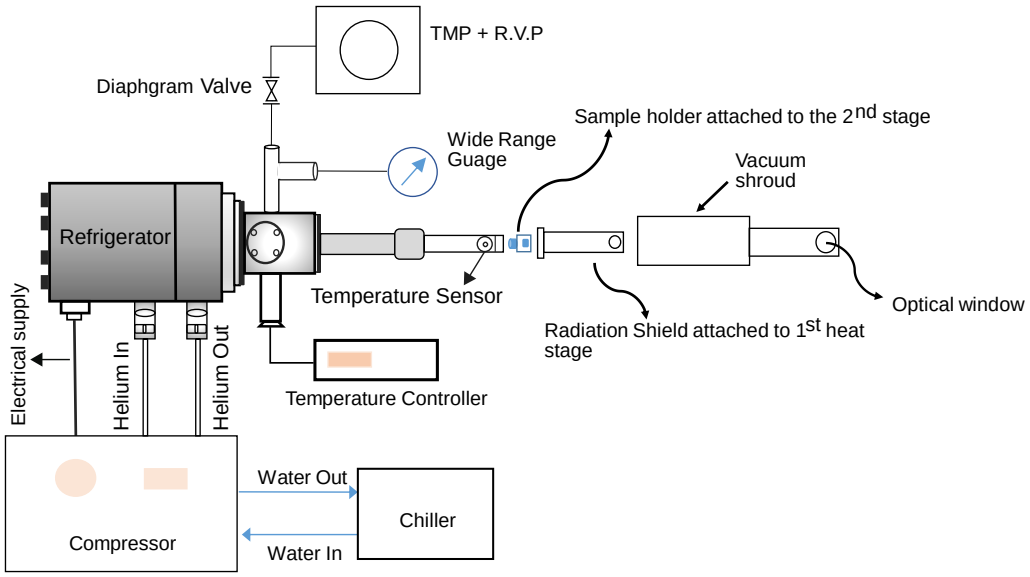

Figure 2.4: Block diagram of the mechanical setup for achieving cryogenic temperatures. **TMP**= turbo molecular pump and **RVP** = rotary vane pump.

performance of this whole setup, the ambient temperature must not exceed 20° and so these experiments are always carried out in an air conditioned environment. The cryostat assembly is fixed on the optics table. For purpose of microscopy, G-M cryo-coolers are not suitable as the vibration produced by them are of the order of 5 microns perpendicular to the cold head. However, the magnitudes of these vibrations are marginal in our case. The complete mechanical setup is depicted in Fig. 2.5.

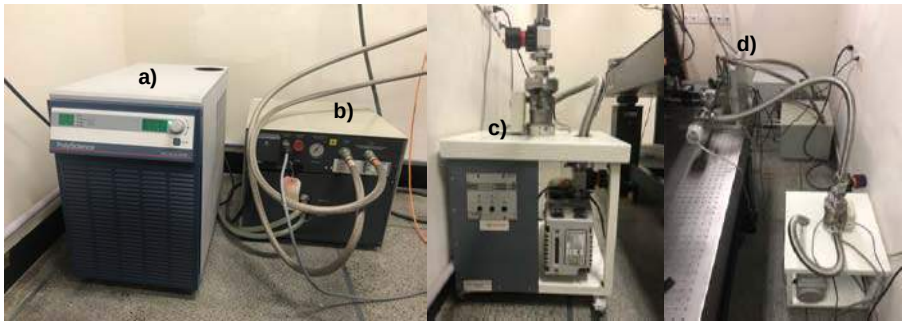

Figure 2.5: a) Chiller b) compressor c) rotary vane pump and turbo molecular pump unit d) the complete cryostat assembly placed alongside the optical table.

2.3.2 Temperature Measurement

Traditional silicon diodes for temperatures below 60 K are not suitable when magnetic fluxes are involved. Therefore, we mounted a specialized GaAlAs diode sensor (temperature range 1.4-500 K) at the cold finger surrounded by low temperature thermal grease (Apiezon) for good thermal contact. The voltages across the four terminals of diode sensor are read by a temperature controller (Model 331, LakeShore). A 25 W heater installed inside the cryostat is also controlled by the temperature controller which implements a PID control to vary the temperature.

The cryostat is connected with a flange line to the turbo molecular pump (TMP) which is backed by a rotary vane pump (Edwards RV-8) as depicted in Fig.2.5(b). The pressure is measured by wide range pressure guage (Edwards-WRG) installed at the junction of flange line connecting the TMP with cryostat. The pressure inside the cryostat during the experiment is well below 10^{-6} torr. The minimum temperature achieved inside the cryostat was 7 K.

2.3.3 Sample Holder

For mounting the crystal we devised a clamping assembly made out of 99.9 percent pure copper due to high thermal conductivity. The picture of the designed sample holder is shown in the Figure 2.6. A cylindrically shaped TGG crystal of width 3 mm and length 1 cm is acquired. Its long axis lies along the [111] crystallographic direction and is mounted inside the cryostat. TGG crystal is mounted on the sample holder using a homebuilt clamp as shown in the Fig. 2.6. The design and dimensions of the sample holder assembly are listed in the Appendix B.1.2.

2.3.4 Electromagnets

For generation of uniform magnetic field transverse to the propagating light, an electromagnet (GMW-3470) is used. The magnitude of magnetic field is changed by varying the current through the electromagnet coils with current

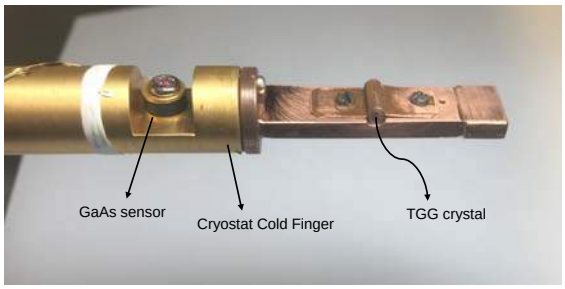

Figure 2.6: Home-built sample holder assembly attached to the cryostat cold finger.

controlled power supply. The distance between the poles is adjusted to accommodate the optical window of cryostat which is 40 mm wide.

The magnetic field strength is determined ex-situ and measured by a Gaussmeter (410-SCT, LakeShore). Figure 2.7 represents the graph for B vs I. The maximum field produced by the magnets is 250 mT for a current of 5 A and calibration factor estimated by linear curve fitting is (50 ± 0.5) mT/A.

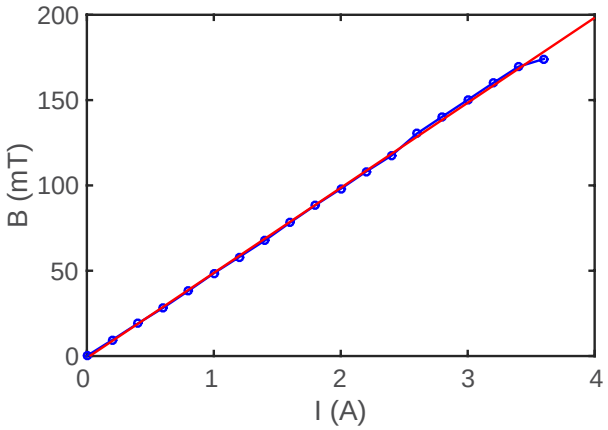

Figure 2.7: Current through electromagnet coils vs magnetic field produced. The slope is found by linear curve fitting.

2.3.5 Optical Setup

The schematic of optical part of setup is displayed in the Figure 2.8, whereas Fig. 2.9 illustrates the optical components arranged in the experimental setup

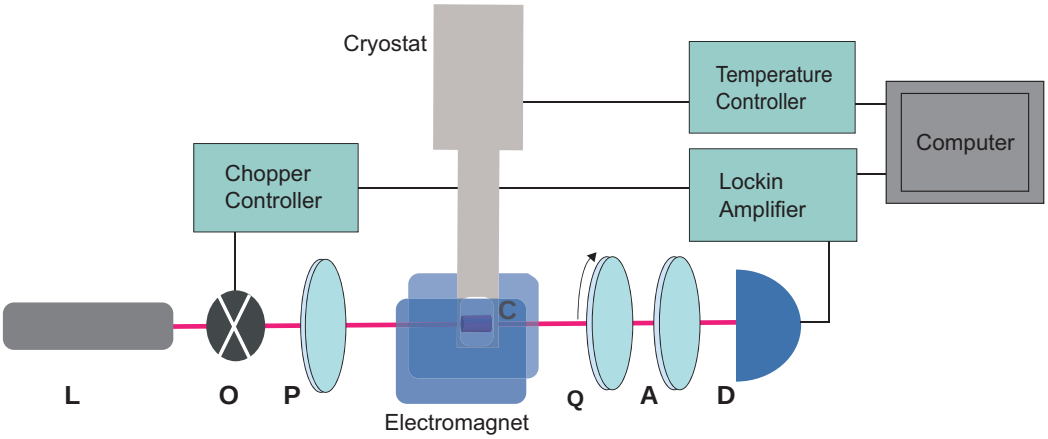

Figure 2.8: The experimental arrangement including **L** = laser, **O** = optical chopper, **P** = polarizer, **C**= crystal, **Q** = quarter waveplate, **A** = analyzer, **D** = photodetector. The perceived beam path is shown in red.

for Stokes polarimetry. This completes the discussion of experimental section and the next section enumerates the steps for Stokes parameters estimation.

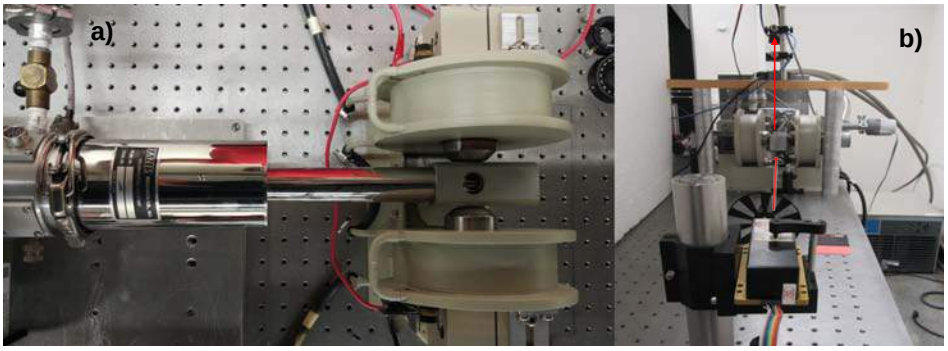

Figure 2.9: The optical setup displaying a) the cryostat placed between the poles of electromagnet and b) the path of light beam highlighted in the red.

The entirety of the experiment, lockin signal outputs, control of the rotational stages mounting the quarter wave plate and analyzer and current driven through the electromagnetic coils, is integrated and interfaced with computer within Labview environment (**??**). We have utilized data acquistion card (National Instruments, PCI-6221) for digitization of analog input and for generating the output signal.

2.3.6 Determination of the Stokes Vector

A helium-neon laser beam of wavelength 633 nm passes the optical window of the cryostat and makes normal incidence on the cross sectional face of TGG. A 633 nm quarter wave plate (WPMQ05M-633, Thorlabs) was used as the retarder Q mounted in a precision motorized rotation stage (PRM1/MZ8E, Thorlabs) allowing the angular displacement β to be varied with a resolution better than 0.1^o. The retardation δ_r at 633 nm was pre-determined as follows: I_T vs β was measured for light with known Stokes parameters, the Fourier coefficients for the data were determined and δ_r was calculated using Eq. (9) [25]. The transmission axis of the analyzer A was fixed at $\alpha = 0$.

The transmitted intensity I_T of the laser, after passing through all the aforementioned components, was measured by a silicon photodetector. The signal from photodetector was connected to the input of a lock-in amplifier (SR830, Stanford Research Systems) allowing phase sensitive detection. The data was taken over a wide range of temperature 8–100 K. To avoid any temperature gradient at the crystal, we allowed the system to equilibrate at each temperature for 20 min prior to the intensity measurement from photodetector.

The Stokes parameters (I, M, C, S) are extracted from the Fourier decomposition of the detected intensity signal from Eqs. (2.42)–(2.45), as a quarter wave plate inserted before the analyzer is synchronously rotated in a motorized stage. The angular displacement for the retarder in one set of measurement is π with equal step size, i.e., $\Delta\beta = 5$.

The foregoing discussion is important as Stokes parameters estimation is imperative to the measurement of signal of interest, i.e., rotation θ and ellipticity angle χ which will be discussed in the next section. To give the reader an overview of the data processing involved we have plotted the measured Stokes parameters against the applied magnetic field in the Fig. 2.10 and Matlab codes are presented in Appendix B.1.1. Furthermore, virtual program written for Stokes polarimetry, realized in Labview environment, is given in the

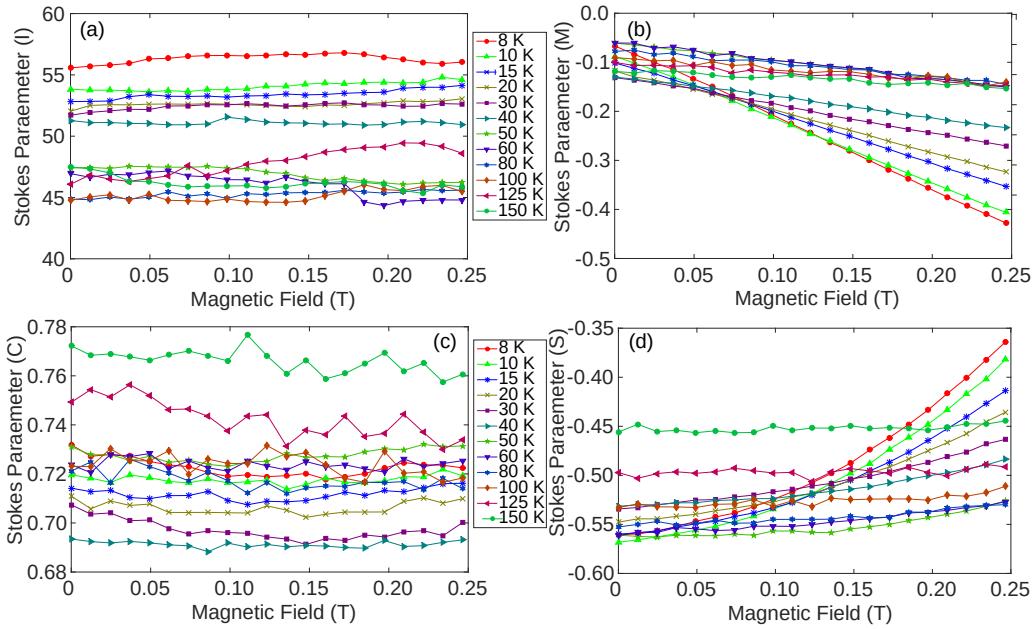

Figure 2.10: The Stokes parameters a) I, b) M, c) C and S extracted from the discrete Fourier transform of measured intensity.

Appendix B.1.

2.4 Results and Discussion

The rotation θ and ellipticity angle χ are determined by Equations (2.33) and (2.34) respectively. Equation (2.9) predicts a quadratic dependence of the ellipticity on the field. Indeed this is the observed behavior and is elucidated in Fig. 2.11(a). The ellipticity is measured to be $\approx 7°$ at 250 mT and 8 K. Using Eqs. (2.8) and (2.9), we can also deduce the magnetically induced asymmetries Δn enabling quantitative estimates of MLB and MLD. The estimates of MLB, $\Delta n'$, are simply proportional to χ and are therefore identified on the right axis of Fig. 2.11(a). These asymmetries are of the order 10^{-6}, and increase by increasing B and lowering T.

Similarly Fig 2.11(b) shows the variation of the polarization angle θ. For zero field, all curves coincide at $\theta = 45°$ which is a control baseline. The overall rotations can approach $\approx 12°$ for fields of 250 mT at a temperature of

8 K. Nonetheless, the rotations are indeed much smaller than the conventionally observed for Faraday rotation which could approach $\approx 300°$ under similar conditions [11].

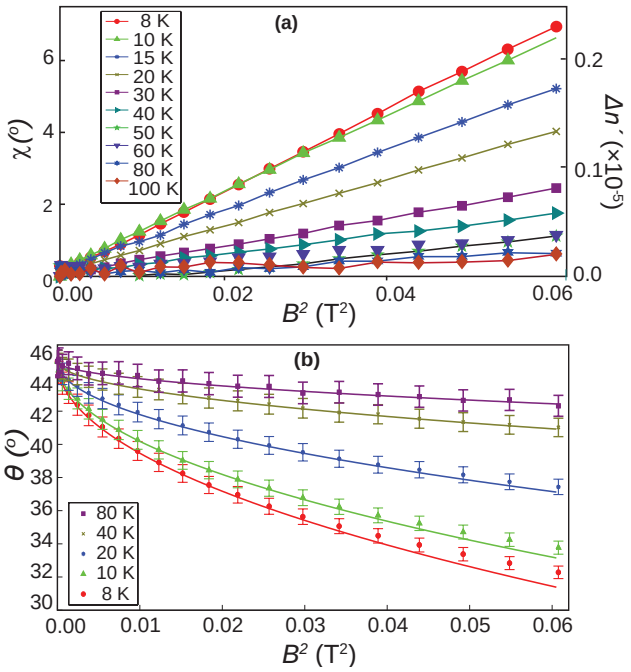

Figure 2.11: (a) The ellipticity χ and magnetic linear birefringence $\Delta n'$ with respect to the square of magnetic field. (b) Angle θ plotted with respect to the square of magnetic field showing correspondence with the theoretical predictions (solid lines) based on intertwined linear and circular birefringence. Uncertainties in angles θ are of the order of $\pm 0.6°$ and solid lines are guide to the eye.

Similar amplitudes are measured for the MLD as well and are illustrated in Fig. 2.12. The phase sensitive measurement technique is capable of revealing these minute asymmetries whose magnitudes are in close agreement with similar paramagnetic materials [3, 5]. Furthermore, the method for estimation of uncertainties is outlined in the supplementary information 2.6.1.

We also notice that for θ, we obtain a quadratic dependence on B only for temperatures ≥ 30 K. These results are explicable by the intermixing of the strong circular components due to tiny misalignments of the applied field away

from the Voigt, and towards the Faraday geometry. The effect is accentuated at lower temperatures and stronger magnetic fields when the Faraday rotation, even stemming from slight axial components can leave a significant impact on the observed rotation angle. In fact, equation (2.23) describes the presence of concomitant circular effects.

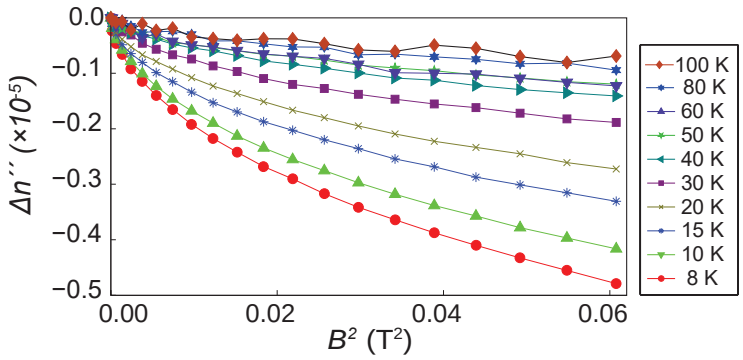

Figure 2.12: Magnetic linear dichroism, $\Delta n''$ plotted with respect to the square of magnetic field B^2. Solid lines are only visual guides

.

The experimental data is fit to this expression and drawn as solid lines in the Figure. Suppose the field's skew angle is θ_s away from the $\hat{x}$-$\hat{y}$ plane and towards the axial direction. The component $B\sin\theta_s$ causes Faraday rotation due to MCB; is proportional to B, and gives rise to $Q = Q_o(B\sin\theta_s)$ where $Q_o = 2\theta_f/(Bk_od)$ is a constant derived from the Faraday angles θ_f determined in other experiments [11]. The other parameter required in the analysis is $\zeta = n\Delta n = \zeta_o(B\cos\theta_s)^2$ which, originating from MLB and MLD, shows a quadratic dependence on B. Here $n = 1.9535$ is the isotropic refractive index of TGG.

A nonlinear fitting procedure determines best estimates of ζ_o and the skew angles, and the former are in excellent agreement with our measurements of MLB and MLD. The data is presented in Table 2.1 and for a single experimental setting, provides an estimate of the skew angle: $(3.0 \pm 0.5)°$. Furthermore, Fig. 2.13 elucidates the intermixing of circular and linear effects where angle of rotation θ given by Eq. (2.23) is simulated against the applied magnetic

Table 2.1: Data showing the temperatures T, asymmetries Q_0 and values of the fitted parameters ζ_o and θ_s.

T (K)	Q_o ($\times 10^{-4}$ rad T^{-1})	ζ_o ($\times 10^{-6}$ T^{-2})	θ_s ($^\circ$)
8	5.6	7.8	3.4
10	4.3	7.3	3.7
20	2.6	4.7	3.6
40	1.4	1.7	2.5
80	0.6	0.6	2.5

field $\mathbf{B}$ and square of the magnetic field $\mathbf{B}^2$ for different temperatures.

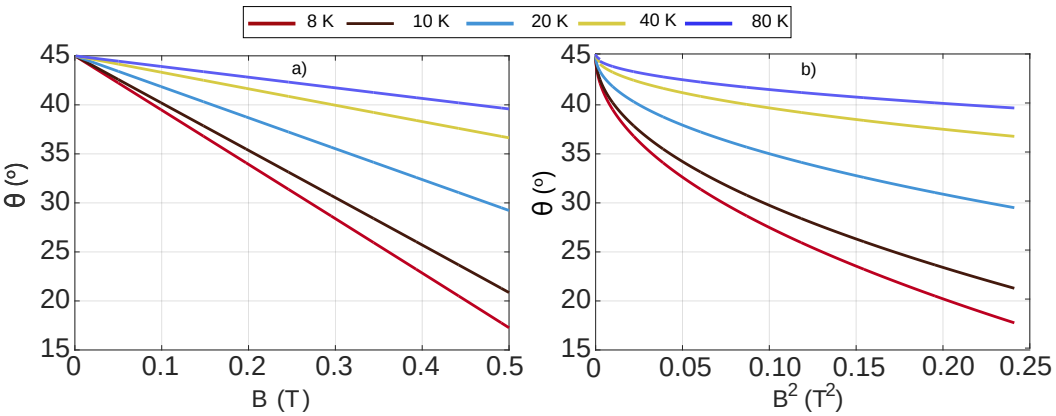

Figure 2.13: Eq. (2.23) is plotted in Matlab for temperature dependent angle of rotation against a) magnetic field $\mathbf{B}$ and b) square of the magnetic field $\mathbf{B}^2$. The strength of different parameters used are enumerated in Table 2.1.

The field independent temperature dependence of the polarization angles can in fact be captured by defining the coefficients, $V_\chi = \Delta n'/B^2$ and $V_\theta = \Delta n''/B$. For TGG, these coefficients respectively approach values of 4×10^{-5} T^{-2} and -1.7×10^{-6} T^{-1} at 8 K and their complete temperature dependence can be seen in Fig. 2.14(a) and (b). These coefficients are estimated through the slopes of the χ versus B^2 (Fig. 2.11(a)) and θ versus B (Fig. 2.15(b)).

For completeness, Fig. 2.15(a) depicts the variation of χ with the magnetic field B. The coefficient V_θ is predominantly caused by the strong Faraday rotation and is similar to the Verdet constant though intermixed with a minute

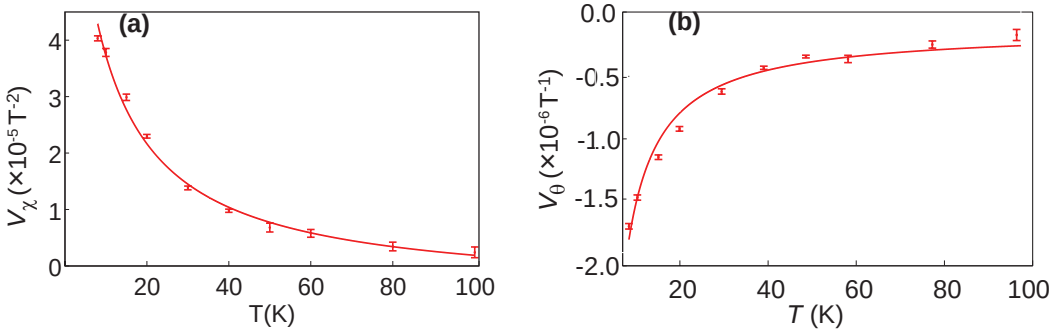

Figure 2.14: Temperature dependence of the Voigt coefficients (a) V_χ and (b) V_θ. The solid lines are fits to hyperbolic curves showing an inverse temperature dependence.

Voigt component. The smallness of the MLB that gives rise to the coefficient V_χ, for example, can be appreciated from the guesstimate that achieving a birefringence of 1% in TGG at 8 K would require a magnetic field of strength 200 T. The inverse temperature relationship indicates proportionality with the paramagnetic nature of the magnetic susceptibility of TGG [27].

Fitting the two kinds of Voigt coefficients to the Curie-Weiss law $V = C/(T - T_W)$ also yields Curie-Weiss constant T_W estimates of -8.7 K and -7.3 K which are in excellent agreement with data acquired by magnetic susceptibility [27] or pure Faraday effect measurements [28]. Furthermore, $|T_W| > T_N = 0.35$ K also corroborates the existence of a strongly frustrated spin system inside the TGG crystal for the temperature range $[T_N, |T_W|]$ where T_N is the Neél temperature. We consider this being the first reported instance of the Curie-Weiss constant derived from magneto-optic measurements based on the Voigt effect.

Finally Figure 2.16 depicts the temperature dependence of the angles of the polarization ellipse at values of B. The rotation and ellipticity are relatively small at temperatures above 30 K and become pronounced only at low temperatures and strong fields. For example, no detectable rotation and ellipticity were observed at room temperature up to fields of 1 T.

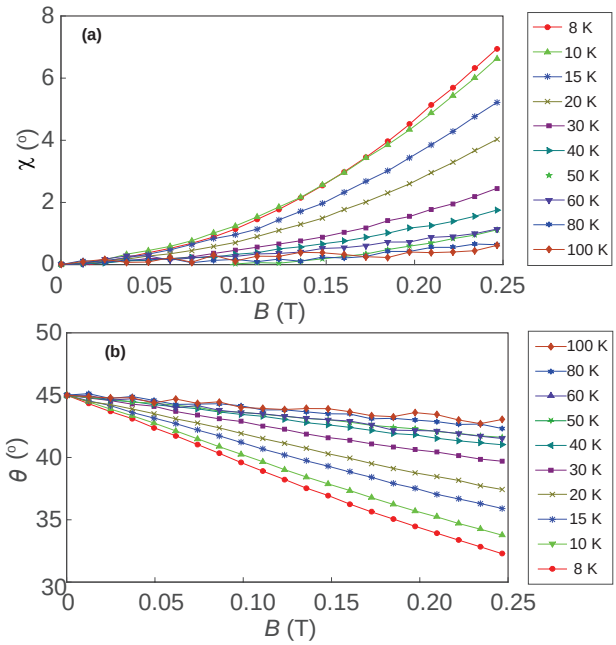

Figure 2.15: The polarization angles (a) χ and (b) θ determined from Stokes polarimetry are plotted as function of the magnetic field B whereas in the main text, we choose to plot these angles as functions of B^2.

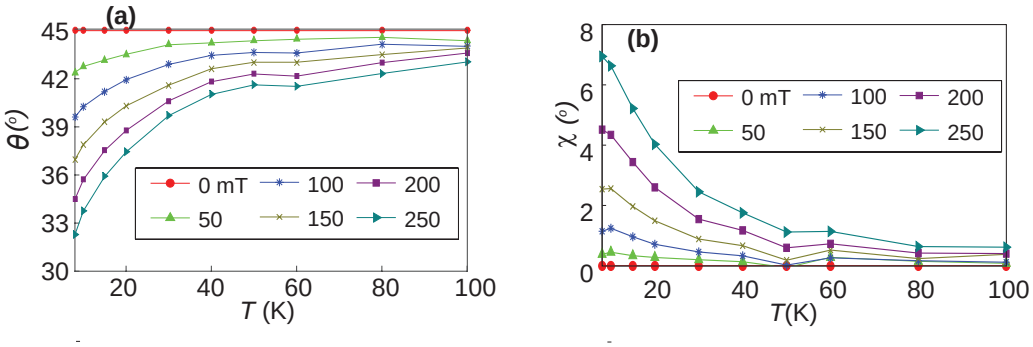

Figure 2.16: Temperature dependence of (a) angle of the polarization ellipse θ and (b) ellipticity χ versus temperature. Solid lines are only visual guides. Data is shown for various settings of the magnetic field.

2.5 Conclusion

We have conducted a complete characterization for magneto-optical effects for TGG in the Voigt geometry. With the help of a Fourier decomposition of the signal and phase-sensitive detection it is possible to detect minute asymmetries in the refractive indices. In particular, we show that ideally MLB imparts el-

lipticity to the emergent light while MLD rotates the polarization ellipse. The simple decoupling of rotation and ellipticity, however, breaks down in the presence of circular magneto-optic effects. This intertwining can be tackled from a theoretical perspective and our experimental data is systematically analyzed and seen to corroborate theoretical predictions. We can perform temperature dependent measurements of the polarization ellipse, helping us to quantify coefficients for ellipticity and rotation in the Voigt geometry, determining the Curie-Weiss constant as well as the direction of a magnetic field misaligned from the nominal.

Applying uniform axial fields as in the Faraday configuration, may sometimes become restrictive with magnet pole pieces intervening the optical beam path. Furthermore, in the area of integrated magneto-photonic circuits, single-sided magnetic geometries, or on-chip surface coils are preferred. The Voigt configuration may become useful in these scenarios and especially when reciprocal and non-reciprocal components are integrated for building optical circulators or polarization preserving isolators. But at the same time, we should be wary that the ellipticity is large and comparable to the rotations, which limits the usefulness of this geometry for practical applications [29]. Several other useful ideas, however, have been surveyed in this Chapter. The recent study determining the Néel vector in an antiferromagnet through MLD could reinvigorate the practical utilization of the Voigt effect [14].

2.6 Supplementary Information

2.6.1 Method for calculation uncertainties in the FFT data, Stokes parameters and angles of the polarization ellipse

We outline the method employed to quantify uncertainties from intensity of light, collected at the photodetector after emerging from some birefringent element, in our case the TGG crystal. Following the experimental scheme visualized in Fig. 2.8, the polarization state of transmitted intensity of light can be completely characterized by Stokes parameters (I, M, C, S) [25]. The transmitted intensity I_T is given by [22, 25]

$$\begin{aligned} I'_{out}(\alpha,\beta,\delta_r) = \frac{1}{2}\big[I + \big(\frac{M}{2}\cos 2\alpha + \frac{C}{2}\sin 2\alpha\big)\big] + \frac{1}{2}\big[S\sin\delta\sin(2\alpha-2\beta) \\ + \frac{1}{4}[(M\cos 2\alpha - C\sin 2\alpha)\cos 4\beta + (M\sin 2\alpha + C\cos 2\alpha) \\ \times \sin 4\beta](1-\cos\delta)\big], \end{aligned} \tag{2.46}$$

where α is the analyzer angle, β is the retarder angle of QWP and δ is the retardation. By virtue of the discrete FFT, the uncertainty propagates from the intensity I_T into each Fourier coefficient, and hence into the Stokes parameters and derived quantities, including θ and χ. The uncertainties in the Fourier coefficients labeled C_k and S_k are (using the notation Δx for the uncertainty in x)

$$\begin{aligned} \Delta C_k = \frac{2}{N}\frac{1}{1+\delta_{k,0}+\delta_{k,L}}\Big(&(\Delta I_{T_1}\cos(\omega_k\beta_1))^2 \\ &+ (\Delta I_{T_2}\cos(\omega_k\beta_2))^2 + \ldots + (\Delta I_{T_N}\cos(\omega_k\beta_N))^2\Big)^{1/2} \end{aligned} \tag{2.47}$$

$$\begin{aligned} \Delta S_k = \frac{2}{N}\frac{1}{1+\delta_{k,0}+\delta_{k,L}}\Big(&(\Delta I_{T_1}\sin(\omega_k\beta_1))^2 \\ &+ (\Delta I_{T_2}\sin(\omega_k\beta_2))^2 + \ldots + (\Delta I_{T_N}\sin(\omega_k\beta_N))^2\Big)^{1/2} \end{aligned} \tag{2.48}$$

where $\beta_i = (i-1)\Delta\beta$ and $\omega_k = \frac{2\pi k}{N\Delta\beta}$, and $\Delta\beta$ is the step size of the rotating QWP. We are particularly interested in the coefficients $(C_0, C_2, C_4, S_2, S_2)$.

Subsequently, the uncertainties in the Stokes parameters I, M, C, S are given by

$$\Delta M = \frac{2}{1-\cos\delta}\sqrt{\left(C_4\cos(2\alpha+4\beta_o)\Delta C_4\right)^2+\left(S_4\cos(2\alpha+4\beta_o)\Delta S_4\right)^2} \quad (2.49)$$

$$\Delta C = \frac{2}{1-\cos\delta}\sqrt{\left(C_4\cos(2\alpha+4\beta_o)\Delta C_4\right)^2+\left(S_4\cos(2\alpha+4\beta_o)\Delta S_4\right)^2} \quad (2.50)$$

$$\Delta S = \sqrt{\left(\frac{1}{\sin\delta\cos(2\alpha+4\beta_o)}\Delta S_4\right)^2} \quad (2.51)$$

$$\Delta I = \left(\Delta {C_o}^2+\left(\frac{1+\cos\delta}{1-\cos\delta}\right)^2\left(C_4\cos(2\alpha+4\beta_o)\Delta C_4\right)^2 + \left(S_4\cos(2\alpha+4\beta_o)\Delta S_4\right)^2\right)^{1/2} \quad (2.52)$$

Finally, the uncertainties in rotation θ and ellipticity χ of the light are determined as,

$$\Delta\theta = \sqrt{\left(\frac{-0.5C}{C^2+M^2}\right)^2+\left(\frac{0.5M}{C^2+M^2}\right)^2} \quad (2.53)$$

$$\Delta\chi = \frac{1}{(C^2+M^2+S^2)}\left(\left(0.5\sqrt{C^2+M^2}\Delta S\right)^2+\left(\frac{0.5MS}{\sqrt{C^2+M^2}}\Delta M\right)^2 + \left(\frac{-0.5CS}{\sqrt{C^2+M^2}}\Delta C\right)^2\right)^{1/2} \quad (2.54)$$

$$\Delta\tan(2\theta) = \frac{C}{M}\sqrt{\left(\frac{\Delta C}{C}\right)^2+\left(\frac{\Delta M}{M}\right)^2}. \quad (2.55)$$

2.6.2 Supplementary Experimental Data

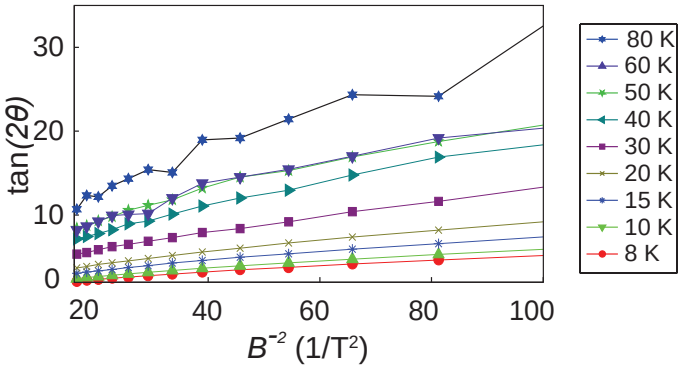

Figure 2.17: Plot of $\tan(2\theta)$ as a function of B^{-2} showing correspondence of experimental data with (2.8)

.

References

[1] A. Zvezdin and V. Kotov, "Magnetooptical effects," *Modern Magnetooptics and Magnetooptical Materials*, pp. 33–58, 1997.

[2] W. Voigt, *Magneto-und Elektrooptik*, vol. 3. BG Teubner, 1908.

[3] K. Cho, S. P. Bush, D. L. Mazzoni, and C. C. Davis, "Linear magnetic birefringence measurements of Faraday materials," *Physical Review B*, vol. 43, no. 1, p. 965, 1991.

[4] F. Valle, A. Ejlli, U. Gastaldi, G. Messineo, E. Milotti, R. Pengo, L. Piemontese, G. Ruoso, and G. Zavattini, "Measurement of the Cotton Mouton effect of water vapor," *Chem. Phys. Lett*, vol. 592, pp. 288–291, 2013.

[5] N. Vedernikov, A. Zvezdin, R. Levitin, and A. Popov, "Magnetic linear birefringence in rare earth garnets," *Zhurnal Ehksperimental'noj i Teoreticheskoj Fiziki*, vol. 93, no. 12, pp. 2161–2178, 1987.

[6] A. Kimel, G. Astakhov, A. Kirilyuk, G. Schott, G. Karczewski, W. Ossau, G. Schmidt, L. Molenkamp, and T. Rasing, "Observation of giant magnetic linear dichroism in (Ga,Mn)As," *Physical Review Letters*, vol. 94, no. 22, p. 227203, 2005.

[7] M. A. Arranz and J. M. Colino, "Magnetooptical Voigt effect in rippled polycrystalline co films," *Journal of Physics D: Applied Physics*, vol. 49, no. 40, p. 405306, 2016.

[8] X. Fan, A. R. Mellnik, W. Wang, N. Reynolds, T. Wang, H. Celik, V. O. Lorenz, D. C. Ralph, and J. Q. Xiao, "All-optical vector measurement of spin-orbit-induced torques using both polar and quadratic magneto-optic Kerr effects," *Applied Physics Letters*, vol. 109, no. 12, p. 122406, 2016.

[9] D. Steil, O. Schmitt, R. Fetzer, T. Kubota, H. Naganuma, M. Oogane, Y. Ando, A. Suszka, O. Idigoras, G. Wolf, *et al.*, "Ultrafast magnetization

dynamics in co-based heusler compounds with tuned chemical ordering," *New Journal of Physics*, vol. 16, no. 6, p. 063068, 2014.

[10] N. Kolmakova, R. Levitin, A. Popov, N. Vedernikov, A. Zvezdin, and V. Nekvasil, "Magnetic linear birefringence in rare-earth garnets: Crystal-field effects and the Judd-Ofelt approximation," *Physical Review B*, vol. 41, no. 10, p. 6170, 1990.

[11] H. Majeed, A. Shaheen, and M. S. Anwar, "Complete Stokes polarimetry of magneto-optical Faraday effect in a terbium gallium garnet crystal at cryogenic temperatures," *Optics Express*, vol. 21, no. 21, pp. 25148–25158, 2013.

[12] R. Yasuhara, S. Tokita, and J. Kawanaka, "Measurement of magneto-optical property and thermal conductivity on tgg ceramic for Faraday material of high-peak and high average power laser," *Reza Kenkyu*, vol. 35, no. 12, pp. 806–810, 2007.

[13] R. Yasuhara, H. Nozawa, T. Yanagitani, S. Motokoshi, and J. Kawanaka, "Temperature dependence of thermo-optic effects of single-crystal and ceramic tgg," *Optics Express*, vol. 21, no. 25, pp. 31443–31452, 2013.

[14] V. Saidl, P. Němec, P. Wadley, V. Hills, R. Campion, V. Novák, K. Edmonds, F. Maccherozzi, S. Dhesi, B. Gallagher, *et al.*, "Optical determination of the Néel vector in a cumnas thin-film antiferromagnet," *Nature Photonics*, vol. 11, no. 2, p. 91, 2017.

[15] D. Bossini, A. Kalashnikova, R. Pisarev, T. Rasing, and A. Kimel, "Controlling coherent and incoherent spin dynamics by steering the photoinduced energy flow," *Physical Review B*, vol. 89, no. 6, p. 060405, 2014.

[16] J. Zhao, A. V. Bragas, D. J. Lockwood, and R. Merlin, "Magnon squeezing in an antiferromagnet: reducing the spin noise below the standard quantum limit," *Physical Review Letters*, vol. 93, no. 10, p. 107203, 2004.

[17] C. Tzschaschel, K. Otani, R. Iida, T. Shimura, H. Ueda, S. Günther, M. Fiebig, and T. Satoh, "Ultrafast optical excitation of coherent magnons in antiferromagnetic NiO," *Physical Review B*, vol. 95, no. 17, p. 174407, 2017.

[18] C. Strohm, G. Rikken, and P. Wyder, "Phenomenological evidence for the phonon Hall effect," *Physical Review Letters*, vol. 95, no. 15, p. 155901, 2005.

[19] R. Mikhaylovskiy, E. Hendry, F. Ogrin, and V. Kruglyak, "Low-temperature time-domain terahertz spectroscopy of terbium gallium garnet crystals," *Physical Review B*, vol. 87, no. 9, p. 094414, 2013.

[20] N. Kostylev, M. Goryachev, P. Bushev, and M. E. Tobar, "Electromagnetic properties of terbium gallium garnet at millikelvin temperatures and low photon energy," *Applied Physics Letters*, vol. 111, no. 5, p. 052402, 2017.

[21] R. Mikhaylovskiy, E. Hendry, and V. Kruglyak, "Ultrafast inverse Faraday effect in a paramagnetic terbium gallium garnet crystal," *Physical Review B*, vol. 86, no. 10, p. 100405, 2012.

[22] D.-G. CLARKE, "Jf polarized light and optical measurement. 1. vyd," 1971.

[23] W. H. McMaster, "Polarization and the Stokes parameters," *American Journal of Physics*, vol. 22, no. 6, pp. 351–362, 1954.

[24] E. Collett, *Field Guide to Polarization.* Field Guide Series, SPIE Press, 2005.

[25] H. G. Berry, G. Gabrielse, and A. Livingston, "Measurement of the Stokes parameters of light," *Applied Optics*, vol. 16, no. 12, pp. 3200–3205, 1977.

[26] G. Claudet, R. Lagnier, and A. Ravex, "Closed cycle liquid helium refrigerators," *Cryogenics*, vol. 32, pp. 52–55, 1992.

[27] U. Löw, S. Zvyagin, M. Ozerov, U. Schaufuss, V. Kataev, B. Wolf, and B. Lüthi, "Magnetization, magnetic susceptibility and ESR in terbium gallium garnet," *The European Physical Journal B*, vol. 86, no. 3, p. 87, 2013.

[28] O. Slezák, R. Yasuhara, A. Lucianetti, and T. Mocek, "Temperature-wavelength dependence of terbium gallium garnet ceramics Verdet constant," *Optical Materials Express*, vol. 6, no. 11, pp. 3683–3691, 2016.

[29] A. R. Taussig, G. F. Dionne, and C. Ross, "Dependence of Faraday rotation and magneto-optical figure of merit on dielectric tensor elements in materials with uniaxial symmetry," *Physical Review B*, vol. 77, no. 1, p. 012407, 2008.

Chapter 3

Ultrafast Magnetization Dynamics

In the first two chapters, we have investigated how polarized light can be used to probe magnetization. This interaction is the standard magneto-optic phenomenon. In the current chapter, we explore another facet of this discipline, *i.e.*, how light can be used as a control switch to steer the magnetization. The considered physical system is a nanostructured composite of a rare-earth and transition metal element which exemplifies these *opto-magnetic* dynamics, whose typical timescales are found to be in the femtosecond to picosecond timescale—hence the name 'ultrafast magnetization dynamics'. These studies have immense technological importance as we will describe.

3.1 Introduction

The manipulation of spin and charge degrees of freedom has been an active area of research since decades and is essential for data storage and information processing. A bit of information is rewritten when the magnetization of a recording unit is reversed by 180°. The ultimate limit for the magnetization reversal in recording media and the underlying physical processes are also of prime importance from a technological point of view. The quest for high density and fast speed recording media have triggered new frontiers in condensed matter physics. Some examples of the phenomena being investigated include magnetization control with spin polarized currents [1], current pulses [2], temperature gradients [3], spin-orbit torque induced switching [4]

and more recently THz switching [5, 6]. These proposed methods operate at different timescales and involve different physical mechanisms for magnetization switching. Magnetization control can be achieved by various methods but the distinction based on the underlying physical mechanisms are depicted in Fig. 3.1 and can be explained as follows.

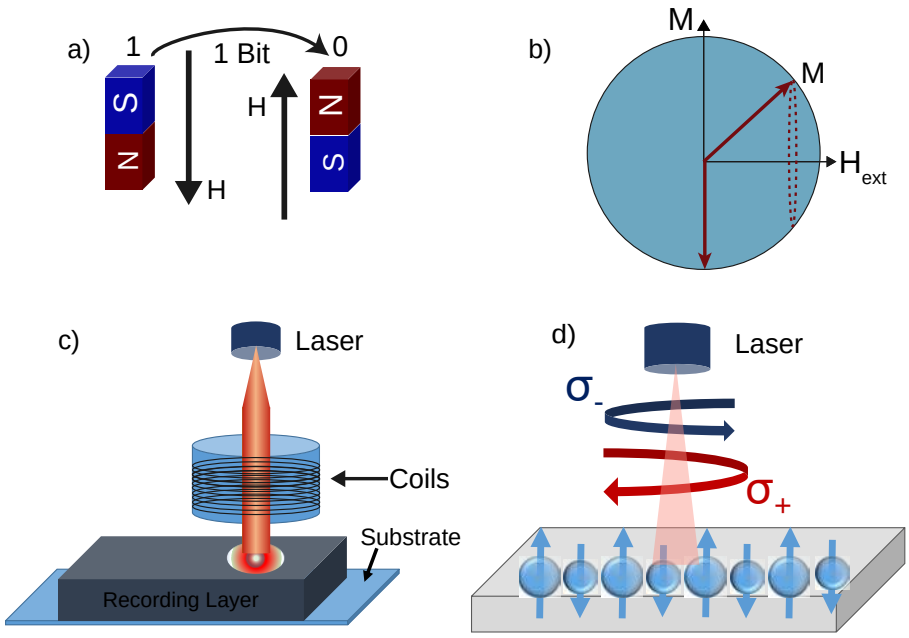

Figure 3.1: Various methods for the manipulation of magnetization which include a) conventional method by applying magnetic field antiparallel to the magnetization direction, b) precessional switching where magnetic field is applied perpendicular to the magnetization vector, c) thermomagnetic switching which is realized by femtosecond laser in conjunction with applied magnetic field and d) all optical helicity dependent switching where σ_+ and σ_- represents right and left circularly polarized light, respectively.

1. Magnetic field induced magnetization reversal is one of the earliest methods in which the magnetic state of the medium remains in a quasistatic equilibrium and magnetization control is achieved by means of an applied magnetic field as depicted in Fig. 3.1(a). The magnetic system follows the minimization of energy by aligning itself in the direction of applied field and is evidenced by hysteresis previously discussed and demonstrated in the Section 1.4.7.

2. Precessional switching presents an alternative to quasistatic switching which has pushed the magnetization switching time into the picosecond regime [7, 8]. Precessional switching is still triggered by external stimuli such as magnetic field, yet the route taken for magnetization reversal is slightly different than that of quasistatic switching mechanism and is shown in Fig. 3.1(b). The underlying mechanism for precessional switching is spin-lattice interaction and a phenomenological description is based on Landau-Lifshitz-Gilbert equation which will be discussed in the forthcoming Section. The ultimate limit for precessional switching lies between 100 ps–10 ns [8].

3. Thermomagnetism offers the data writing on a timescale of 1–100 ps [9]. In this technique, a permanent magnet is heated locally with optical means to reduce the coercivity of the medium. Once the nucleation starts, the new state of equilibrium magnetization opposite to the prior direction is favored by the application of a bias magnetic field. Electron-phonon, phonon-phonon and spin-lattice interactions prevail at this timescale. A similar approach is employed in heat assisted magnetic recording (HAMR) technology [10]. The schematic of thermomagnetic switching is shown in Fig. 3.1(c).

4. Photo-induced effects utilizes ultrashort laser pulses for the manipulation of spin. The category is further sub-divided into opto-magnetism (all-optical helicity dependent switching) and femto-magnetism (all-optical switching). All-optical helicity dependent (AO-HDS) [11] and all-optical switching (AOS) [12] magnetization reversal involves altogether different mechanism. In AO-HDS, circularly polarized light interacts with atoms via first order magneto-optic effect (the inverse Faraday effect or magnetic circular dichroism) as shown in Fig. 3.1(d), whereas femtosecond laser generated thermal non-equilibrium processes (electron-electron and electron-phonon interactions) are at play in the case of AOS. The present chapter investigates the latter phenomenon.

Thermally induced magnetic switching by laser in synthetic materials is now a topic of extraordinary importance due to its practical applications in magnetic recording media [13–16]. A femtosecond pulsed laser can switch or alter the magnetic states of a material by thermally induced ultrafast changes in spin states without any applied external magnetic field [17, 18]. In addition, laser induced thermal heating is a non-destructive route for magnetic switching in nanostructures having potential utilization [19, 20]. This makes the mechanism of ultrafast magnetic switching a hot topic of discussion.

GdFeCo or GdFe alloys are considered trademark composites for the investigation of all optical magnetization switching phenomenon AO-HDS was first observed in 2007 when Stanciu *et.al* demonstrated the magnetization switching in GdFeCo alloy with femtosecond circularly polarized light [21]. The magnetization switching is dependent on the helicity of incident light, hence the name all-optical helicity dependent switching. The quest for finding new synthetic materials for AO-HDS is a hot topic of contemporary research [22–25].

Later on, Radu *et.al* [26] showed the deterministic reversal of magnetization in GdFeCo and GdFe alloys with femtosecond linearly polarized light in a pump probe experiment, circumventing the helicity dependence of incident femtosecond light. This in turns raised the question of how and how fast, the magnetization can be reversed. It was generally assumed that heating alone (a scalar field) cannot result in deterministic switching of magnetization, however it may assist the reversal process [27]. Several phenomena attributed to the magnetization reversal include the inverse Faraday effect [28], symmetry breaking [29] and transfer of angular momentum between electron and spin reservoirs [26]. However, the microscopic origin of deterministic switching of magnetization is still under debate and requires a tangible explanation.

It is well established that the size, design, type and composition of a material are directly associated with which ultrafast magnetic switching mechanism is actualized [30–33]. In this context, the systems of binary alloys optimized by

using transition metals (TM) with minute concentration of rare earth (RE) elements could be potentially investigated to work at room temperature (RT) for data storage applications [34–37]. For example, by suitably optimizing the concentration content of RE metals in these binary alloys, efficient systems for ultrafast thermally induced magnetic switching systems could promise to fulfill the future demands.

The present chapter describes the simulation work for magnetic nanostructures performed on an opensource software Vampire which utilizes a finite element approach [38]. The dynamical simulation is based on the classical spin Hamiltonian and makes use of Landau-Lifshitz-Gilbert equation to predict magnetization, hysteresis loop, a Monte-Carlo algorithm for equilibrium magnetization (Curie temperature over a dynamic temperature range) and the two temperature model to study the response of magnetic system when excited with ultra-short laser pulses.

The present work is built upon two of our previously published articles. In one of works [39], we studied the DyFe magnetic nanostructures with concentration of 5 % Fe in Dy element in the form of bilayer, coreshell and random alloy. However the temperature dependent magnetization investigations revealed a lack of magnetization at room temperature for this particular composition of materials, which is an essential characteristic for efficient and economically viable magnetic recording media. These results will be discussed in context of our experimental investigation of DyFe bilayer nanostructures in the Section 3.4. Consequentially, here we alter the composition of nanocomposites with varying content of Dy concentration % in host element Fe and compute the temperature dependent magnetization and ultrafast magnetization dynamics. We investigate and analyze the magnetic dynamics, demagnetization time and thermally induced magnetic switching in these nanostructures.

Furthermore, we start off with the assumption that concentration of RE ions in the host TM could alter the magnetization switching time as exchange con-

stant are different for RE and TM lattices. For this purpose, we also perform atomistic spin model simulations of novel RE-Fe alloys (RE= Tb, Gd) for different concentration of RE ions and peak electron bath temperature in order to manipulate the switching time.

The present chapter is divided into the following sections. Section 3.2 introduces the reader with different types of magnetic materials which is imperative to understand the origin of magnetism and interactions among magnetic entities which further lead to the actualization of magnetic recording media. This section also elaborates the emergence of different magnetic quantities (magnetic anisotropy, uni-axial magnetic anisotropy) and interactions (exchange interaction) which form the basis of our atomistic spin simulation. Section 3.3 is based on the phenomenological description of Landau-Lifshitz-Gilbert (LLG) equation and also discusses the dynamics of atomistic spin simulator we have employed in our work. Finally, we present the results for our simulative investigations followed by a discussion in Section 3.4.

3.2 Types of Magnetism

The most primitive unit of magnetism is magnetic dipole moment—an idea which stems from the efforts of scientist of to understand the magnetic forces at the atomic level. A magnetic dipole moment $\boldsymbol{\mu}$ is associated with an electron orbiting around a nucleus, *i.e.*, $\boldsymbol{\mu} = I\mathbf{A}$ where I is the current and $\mathbf{A}$ is the area of the loop. It is straightforward to derive the relationship between magnetic moment and angular momentum and is given by [40]

$$\boldsymbol{\mu} = \frac{q}{2m_e}\mathbf{L}.$$

A similar relation $\boldsymbol{\mu} = (e/m_e)\mathbf{S}$ also holds for spin angular momentum $\mathbf{S}$ and magnetic moment. In the presence of magnetic field $\mathbf{H}$, the energy of the magnetic moment is given by the expression $E = -\boldsymbol{\mu} \cdot \mathbf{H}$. The minimization of energy gives rise to a torque which is perpendicular to both $\boldsymbol{\mu}$ and $\mathbf{H}$ and tends to align the magnetic moment in the direction of applied field. The

torque acting on a magnetic dipole moment in a magnetic field is given by [41]

$$\boldsymbol{\tau} = \boldsymbol{\mu} \times \mathbf{H}. \tag{3.1}$$

The sum of all magnetic moments taken over the volume of magnetic solid is called the magnetization $\mathbf{M}$ [41]. We have already explored the relationship between applied magnetic field $\mathbf{H}$ and magnetization $\mathbf{M}$ in the Section 4.7 of first Chapter. Additionally, for a linear and homogeneous magnetic material $\mathbf{M} = \chi\mathbf{H}$, where χ is the magnetic susceptibility and for this special case, magnetic flux density $\mathbf{B}$ and magnetic field $\mathbf{H}$ are also related by the constitutive relationship

$$\mathbf{B} = \mu_\circ(1 + \chi)\mathbf{H}, \tag{3.2}$$

where $\mu_\circ$ is the permeability of free space. The classification of magnetic materials is based upon the interaction of these magnetic moments inside a material in conjunction with temperature effects. The commonest types of magnetic materials are depicted in Fig. 3.2 and can be enumerated as diamagnetic, paramagnetic, ferromagnetic, antiferromagnetic and ferrimagnetism.

Diamagnetism is attributed to the change in orbital motion of electrons due to an applied magnetic field. It is rather a weak effect and occurs in all atoms but is often overshadowed by the presence of much stronger effects [41]. Magnetic susceptibility for diamagnetic material is negative, *i.e.,* $\chi < 0$ and is largely independent of temperature [42].

Paramagnetism corresponds to the presence of a net magnetic moment inside a material. However the magnetic moments are randomly oriented due to thermal fluctuations and either independent (isolated) or only weakly coupled to each other. Magnetic susceptibility for paramagnetic materials is positive ($\chi > 1$) and temperature dependence is generally captured by the famous Curie law, *i.e.,* $\chi = C/T$, where C is the Curie constant and T is the temperature [43]. As the temperature is lowered the magnetic susceptibility increases and below a certain critical temperature, a paramagnetic material undergoes a phase transition—*para* to *ferro*.

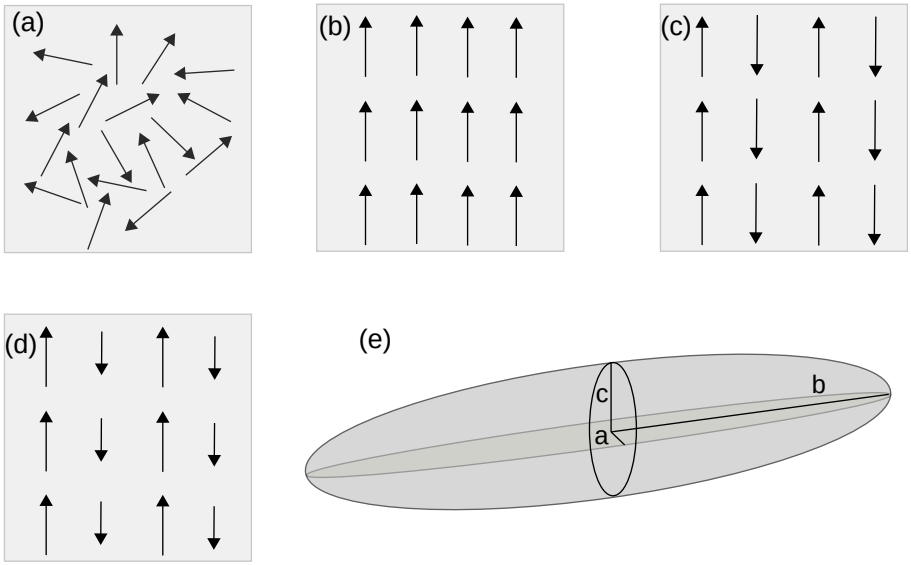

Figure 3.2: An illustration of different orientations of magnetic dipole moments in a) paramagnetic, b) ferromagnetic, c) antiferromagnetic and d) ferrimagnetic materials whereas e) represents an ellipsoid system with magnetization along the long axis.

Ferromagnetic materials possess a spontaneous magnetization even in the absence of magnetic field and are distinguished by high and positive magnetic susceptibility ($\chi \gg 1$). The presence of spontaneous magnetization was first explained in terms of mean field which aligns the magnetic moments parallel to each other [41], whereas in antiferromagnetic material, this molecular field tends to align the neighbouring magnetic moments in an antiparallel configuration as depicted in Fig. 3.2(c). The magnitude of magnetic moments are equal but opposite hence the spontaneous magnetization in antiferromagnetic materials is completely washed out. Ferrimagnetic materials refer to a similar class yet a non-zero net magnetization arises due to the unequal magnitudes of the oppositely oriented magnetic moments [42].

The presence of spontaneous magnetization can be explained by intrinsic fields $\mathbf{H_i}$ and $\mathbf{B_i}$ inside a magnetizable media. This in turns require a careful differentiation between the applied field $\mathbf{H_a}$ and magnetic field inside a material $\mathbf{H_i}$. In the special case of an ellipsoid, when the applied field lies along the principal

axis b as shown in Fig. 3.2(e), the relationship between applied and intrinsic field can be expressed through the equation

$$\mathbf{H_i} = \mathbf{H_a} - N\mathbf{M}. \tag{3.3}$$

The correction term here represents a demagnetizing field, *i.e.,* $\mathbf{H_d} = -N\mathbf{M}$ which plays an important role in determining the magnetization state of magnetic medium with susceptibilities $\chi \gg 1$. The materials with spontaneous magnetization (ferro or ferri-magnetic) are central to the upcoming discussions in the chapter, therefore for historical perspective and pedagogical reasons it is important to take a closer look at the interactions among magnetic moments inside a ferromagnetic materials. The next section discusses this particular aspect, *i.e.,* exchange interaction which is responsible for long range ordering in ferromagnets.

3.2.1 Exchange Interaction

In 1907, Weiss presented a phenomenological model for ferromagnetism which assumes the presence of a molecular field $\mathbf{B_{mf}} = \lambda\mathbf{M}$, arises out of the strong interaction between localized moments in a ferromagnet and responsible for the magnetization of substance even in the absence of external magnetic field [41]. Here λ parameterize the strength of molecular field as a function of magnetization. However, the value of constant λ needs to be very large to agree with large values of T_c for materials like Fe ($T_c = 1043$ K) and Co ($T_c = 1390$ K). Even though, the Weiss theory agrees with experimental results in some cases yet the origin of this molecular field remained ambiguous until Heisenberg explained the phenomenon in terms of a quantum mechanical exchange interaction [42].

The exchange interaction is a direct consequence of Pauli's exclusion principle and symmetrization postulates [43]. In plain words, the origin of exchange interaction is coulombic interaction between electrons [44]. The exchange energy Hamiltonian for a system of interacting spin moments is given by [42]

$$\mathbf{H_{exc}} = -\sum_{i \neq j} J_{ij}\mathbf{S_i} \cdot \mathbf{S_j}. \tag{3.4}$$

where J_{ij} is the exchange interaction, $\mathbf{S_i}$ and $\mathbf{S_j}$ are spin moments of atoms at i'th and j'th site, respectively. If J_{ij} is positive, then exchange energy will be minimum when spins are parallel, which leads to ferromagnetic order of the system. If J_{ij} is negative then an antiparallel alignment of spins will lower the energy, hence antiferromagnetic ordering. In most of the cases, J_{ij} is considered isotropic, *i.e.,* interaction between spin depends only on relative orientation, not their direction. In case of anisotropic exchange interaction, J_{ij} is represented by a tensor [38]

$$J_{ij} = \begin{bmatrix} J_{xx} & J_{xy} & J_{xz} \\ J_{yx} & J_{yy} & J_{yz} \\ J_{zx} & J_{zy} & J_{zz}, \end{bmatrix} \tag{3.5}$$

where exchange tensor components can be obtained phenomenologically or via ab initio methods [38]. For a magnetic system having z nearest neighbours, the exchange constant (measure of the strength of coupling between neighbouring magnetic moments) is given by [38, 41, 45]

$$J_{ij} = \frac{3k_B T_c}{\varepsilon z} \tag{3.6}$$

where T_c is the Curie temperature, k_B is Boltzmann's constant and ε is a correction factor emerging from the mean field expression [45].

At this juncture, we would like to address another relevant phenomenon which determines the suitability of a magnetic material in a particular application. All magnetic moments in an isolated environment respond identically to the applied magnetic field. However in a crystal lattice, these magnetic moments may tend to align in a preferred direction and give rise to an anisotropy. We have already discussed the optical anisotropies (MCB, MLB, MCD and MLD) induced by the extrinsic agent (magnetic field) in the first two chapters. Here we discuss the magnetic analogue of anisotropy which has its origin in energy minimization, shape and environment of crystal lattice or can be induced extrinsically by careful conditioning of magnetic materials—magnetic anisotropy.

3.2.2 Magnetic Anisotropy

Magnetic anisotropy is the energy required to rotate the magnetization direction from the preferred direction (easy axis) to the hard direction. For a cubic crystal, the anisotropy energy E_{ani} can be expanded as direction cosines α_i, where α_i are the angles between saturation magnetization and crystal axes and is given by [42]

$$E_{ani} = K_1\left(\alpha_1^2\alpha_2^2 + \alpha_2^2\alpha_3^2 + \alpha_3^2\alpha_1^2\right) + K_2\left(\alpha_1^2\alpha_2^2\alpha_3^2\right) + \cdots . \tag{3.7}$$

For hexagonal structure with single easy axis (c-axis) oriented at an angle θ with respect to the magnetization vector M, anisotropy energy is given by [41, 44]

$$E_{ani} = K_1(\sin^2\theta) + K_2(\sin^4\theta) + K_3(\sin^6\theta) + \cdots , \tag{3.8}$$

where $K_i (i = 1, 2, 3\cdots)$ are anisotropy constants with dimensions of energy per unit volume. It is also customary to represent the anisotropy energy E_{ani} with an effective magnetic field H_{ani} to simulate the effect of magnetic anisotropy and will be actualized in the forthcoming section 3.3.

The first order term K_1 in both Eqns. (3.7) and (3.8) can be represented as $K_1 = K_u + K_s$, where K_u and K_s are magnetocrystalline and shape anisotropies, respectively. In case of thin films, if $(K_u + K_s) > 0$, the film will preferentially get magnetized perpendicular to its plane. For $(K_u + K_s) < 0$, the easy axis will be in plane. These scenarios are often called out-of-plane and in-plane magnetizations.

Shape anisotropy arises due to structural constraint of the system and its origin is magnetostatic. Magnetocrystalline anisotropy is the spin system's tendency to align itself in a preffered crystallographic orientation. When an external field is applied to reorient the direction of spin in the system, electron orbit must also be reoriented due to the coupling between spin and angular momentum, called the spin-orbit coupling.

The exchange field does not act on the orbital moment or on the nuclear magnetic moment. This is of great importance because in the presence of the exchange interaction, the spin system still remains independent from the orbital angular momentum which is locked to the crystal lattice [44]. Once the magnetization is established by the exchange interaction, the coupling of the spin moment to the orbital moment is mediated through the weaker spin–orbit interaction. It is this coupling which leads to the magnetocrystalline anisotropy by locking the spin to the orbital moment which itself is locked to the lattice [8, 44]. In solids, the spin–orbit interaction determines the magnetocrystalline anisotropy [44]. This scenario is highly relevant with the MOKE study of permalloy thin film in Section 1.4.7. It is worth mentioning here that area of the hysteresis loop[1] for $Ni_{80}Fe_{20}$ is different for L and P-MOKE which marks the presence of an easy axis inside the material. *i.e.*, magnetocrystalline anisotropy.

Uniaxial anisotropy refers to the magnetic moment's preference to align in one single direction, the easy axis. An anisotropy field H_{ani} needed to saturate the material in the hard direction is given by [43]

$$H_{ani} = 2\frac{K_u}{M_s} \tag{3.9}$$

where K_u is usually derived experimentally from a typical ferromagnetic resonance experiment [41].

This concludes our survey about different types of magnetism and the interactions between magnetic moments. The next section deals with the phenomenological description of the mathematical equations which govern the evolution of magnetization in a magnetic medium when subjected to an external stimuli such as dc magnetic field. The interactions are important parameters of the system determining the specifics of the magnetization in dynamics.

[1] Area of hysteresis loop determines the work done required to magnetize or demagnetize a ferromagnetic material.

3.3 Magnetization and Spin Dynamics

3.3.1 Landau-Lifshitz-Gilbert Equation

A magnetic moment $\boldsymbol{\mu}$ placed inside a magnetic field $\mathbf{H}$ experiences a torque given by Eq. (3.1). According to Newton's classical equation of motion, torque can be defined in terms of of rate of change of angular momentum, *i.e.*, $\boldsymbol{\tau} = d\mathbf{S}/dt$. Therefore Eq. (3.1) can be rewritten

$$\frac{d\boldsymbol{\mu}}{dt} = -\gamma \boldsymbol{\mu} \times \mathbf{H}, \tag{3.10}$$

which governs the precession of magnetic moment around the magnetic field. Here γ represents the gyromagnetic ratio. It is important to mention here that we have only assumed that spin angular momentum $\mathbf{S}$ contributes to the magnetic moment. The rationale for this assumption has its origin in the quenching of orbital angular momentum in transition metals (TM) due to crystal field effect [45].

Assuming $\mathbf{H}$ to be spatially uniform and taking the volume average of all magnetic moments in a system, Eq. (3.10) further simplifies to give Bloch equation which represents the trajectory of an uncoupled and undamped magnetization of the system as

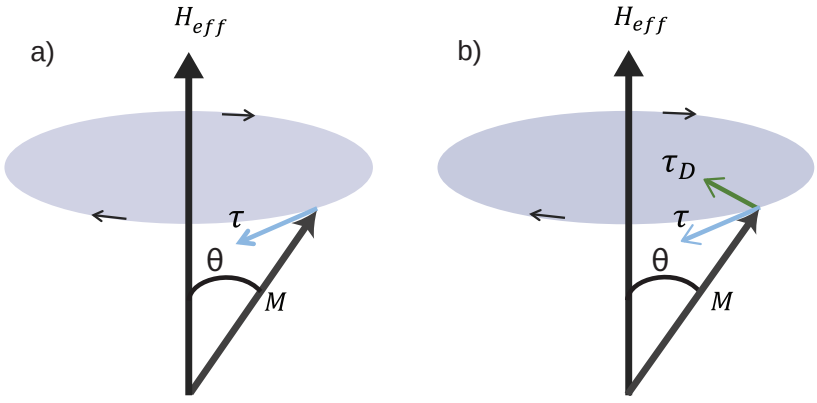

Figure 3.3: (a)Bloch Equation which predicts the presence of precessional torque which acts perpendicular to both $\boldsymbol{\mu}$ and $\mathbf{M}$. (b) Landau-Lifshitz equation explains the existence of an additional damping torque which tends to align the magnetization in the applied field direction.

$$\frac{d\mathbf{M}}{dt} = -\gamma \mathbf{M} \times \mathbf{H}. \tag{3.11}$$

The equation predicts the continuous precession of magnetization vector $\mathbf{M}$ around the magnetic field $\mathbf{H}$. Fig. 3.3(a) shows the dynamics of $\mathbf{M}$ oriented at an angle θ with an effective magnetic field $\mathbf{H}_{\text{eff}}$. The motion of magnetic moment around magnetic field is called precession. There is no reason at all why magnetization should align with $\mathbf{H}_{\text{eff}}$ which is the actual observation. Consequentially in 1935, Landau and Lifshitz proposed a correction to the Bloch equation on an entirely phenomenological basis. The correction term introduces a damping torque τ_D which tends to align the magnetization vector in the applied field as shown in Fig. 3.3(b). The Landau-Lifshitz (LL) equation can be written as

$$\frac{d\mathbf{M}}{dt} = \gamma \Bigg(\mathbf{M} \times \Big(\mathbf{H}_{\text{eff}} + \frac{\lambda'}{M_s} (\mathbf{M} \times \mathbf{H}_{\text{eff}}) \Big) \Bigg), \tag{3.12}$$

where damping torque τ_D is given by the term

$$\tau_D = \frac{\gamma \lambda'}{M_s} \big(\mathbf{M} \times (\mathbf{M} \times \mathbf{H}_{\text{eff}}) \big),$$

and $\mathbf{H}_{\text{eff}}$ is the sum of all the magnetic fields (intrinsic or extrinsic) present in the medium

$$\mathbf{H}_{\text{eff}} = \mathbf{H}_{\text{ext}} + \mathbf{H}_{\text{exch}} + \mathbf{H}_{\mathbf{d}} + \mathbf{H}_{\text{ani}}. \tag{3.13}$$

The term $\mathbf{H}_{\text{ext}}$ is an externally applied magnetic field, $\mathbf{H}_{\text{exch}}$ is exchange interaction field, $\mathbf{H}_{\mathbf{d}}$ is the demagnetization field and $\mathbf{H}_{\text{ani}}$ is the anisotropy field. Eqn. (3.12) can only be used for small damping and refers only to intrinsic contribution (spin-lattice and spin-electron interactions) to the relaxation mechanism. In 1955, Gilbert suggested to add a correction term to LL equation for a strongly damped system and Eq. (3.12) then takes the form

$$\frac{d\mathbf{M}}{dt} = \frac{\gamma}{1+\alpha^2} (\mathbf{M} \times \mathbf{H}_{\text{eff}}) + \frac{\gamma \alpha}{(1+\alpha^2) M_s} \big(\mathbf{M} \times (\mathbf{M} \times \mathbf{H}_{\text{eff}}) \big), \tag{3.14}$$

where α is phenomenological Gilbert damping parameter (10^{-3}–10^{-1}) related to both intrinsic and extrinsic (surface inhomogeneties, doping, demagnetization field) relaxation mechanisms [7]. This equation describes the evolution of magnetization $\mathbf{M}$ and referred to as Landau-Lifshitz-Gilbert equation (LLG).

Eqn. (3.12) and (3.14) are similar from a mathematical point of view and produce identical results for small damping parameters ($\alpha, \lambda' \rightarrow 0$) as they belong to same class of damped gyromagnetic precession equations [7]. The difference in the predicted dynamics of both LL and LLG equation is amplified when larger damping terms are considered.

The LLG equation can be decomposed into its rectangular components as follows:

$$(1+\alpha^2)\left(\frac{d\mathbf{M_x}}{dt}\right) = \gamma(m_y H_z - m_z H_y) + \frac{\alpha\gamma}{m}\big(m_x m_y H_y + m_x m_z H_z - H_x m_z^2 - H_x m_y^2\big) \quad (3.15)$$

$$(1+\alpha^2)\left(\frac{d\mathbf{M_y}}{dt}\right) = \gamma(m_z H_x - m_x H_z) + \frac{\alpha\gamma}{m}\big(m_x m_y H_x + m_y m_z H_z - H_y m_x^2 - H_y m_z^2\big) \quad (3.16)$$

$$(1+\alpha^2)\left(\frac{d\mathbf{M_z}}{dt}\right) = \gamma(m_x H_y - m_y H_x) + \frac{\alpha\gamma}{m}\big(m_x m_z H_x + m_y m_z H_y - (m_x^2 + m_y^2) H_z\big), \quad (3.17)$$

where $\mathbf{H} = (H_x, H_y, H_z)$ and $\mathbf{m} = (m_x, m_y, m_z)$ are vector fields. The equations (3.15)–(3.17) present a set of coupled non-linear differential equations. For a magnetic field applied in the z-direction $(0, 0, H_z)$, the equations can be further simplified and take the form

$$(1+\alpha^2)\left(\frac{d\mathbf{M_x}}{dt}\right) = \gamma(m_y H_z) + \frac{\alpha\gamma}{m}\big(m_x m_z H_z\big), \quad (3.18)$$

$$(1+\alpha^2)\left(\frac{d\mathbf{M_y}}{dt}\right) = -\gamma m_x H_z + \frac{\alpha\gamma}{m}\big(m_y m_z H_z\big), \quad (3.19)$$

$$(1+\alpha^2)\left(\frac{d\mathbf{M_z}}{dt}\right) = -\frac{\alpha\gamma}{m}\big(m_x^2 + m_y^2\big) H_z. \quad (3.20)$$

Figure 3.4 represents the temporal evolution of magnetization vector components simulated in Matlab for different damping coefficients α with different initial conditions such as magnetization vector and strength of magnetic field. Fig. 3.4(a) and (b) draw a comparison between heavily and lightly damped system. The time taken by magnetization to get aligned in the direction of applied field are 3 ps and 14 ps respectively. For a negative damping parameter, the magnetization switches to the direction antiparallel to the applied

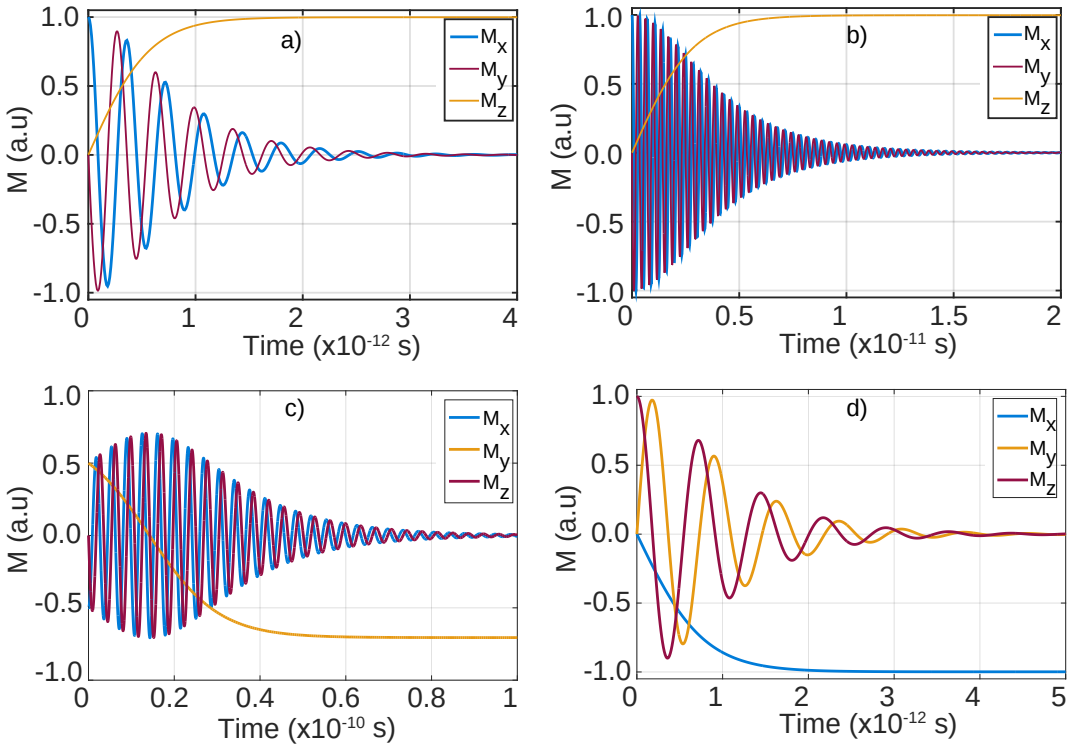

Figure 3.4: The evolution of different components of magnetization according to LLG equation for different initial conditions such as damping parameter, magnetization vector and different strengths and directions of applied magnetic field where a) $\alpha = 0.1$, $\mathbf{m} = (1, 0, 0)$ and $H_z = 100$ T, b) $\alpha = 0.02$, $\mathbf{m} = (1, 0, 0)$ and $H_z = 100$ T, c) $\alpha = -0.1$, $\mathbf{m} = (0.5, 0.5, 0)$ and $H_y = 5$ T and d) a heavily damped system, $\alpha = 0.15$, $\mathbf{m} = (0, 0, 1)$ and $H_z = 50$ T.

magnetic field as shown in Fig.3.4(c), a phenomenon known as precessional switching. A clearer picture for precessional switching of magnetization vector $\mathbf{M}$ is presented in Fig. 3.5 where magnetization components are plotted on unit magnetization sphere with similar parameters used previously for the Fig. 3.4. The role of demagnetizing field, anisotropy field in precessional switching can be understood in the following discussion.

3.3.2 Few Words on Precessional Switching

In our previous discussion on the LLG equation, we have already seen how the magnetization can switch its direction. We explore this concept further here. Precessional switching of magnetization can be initiated in two ways.

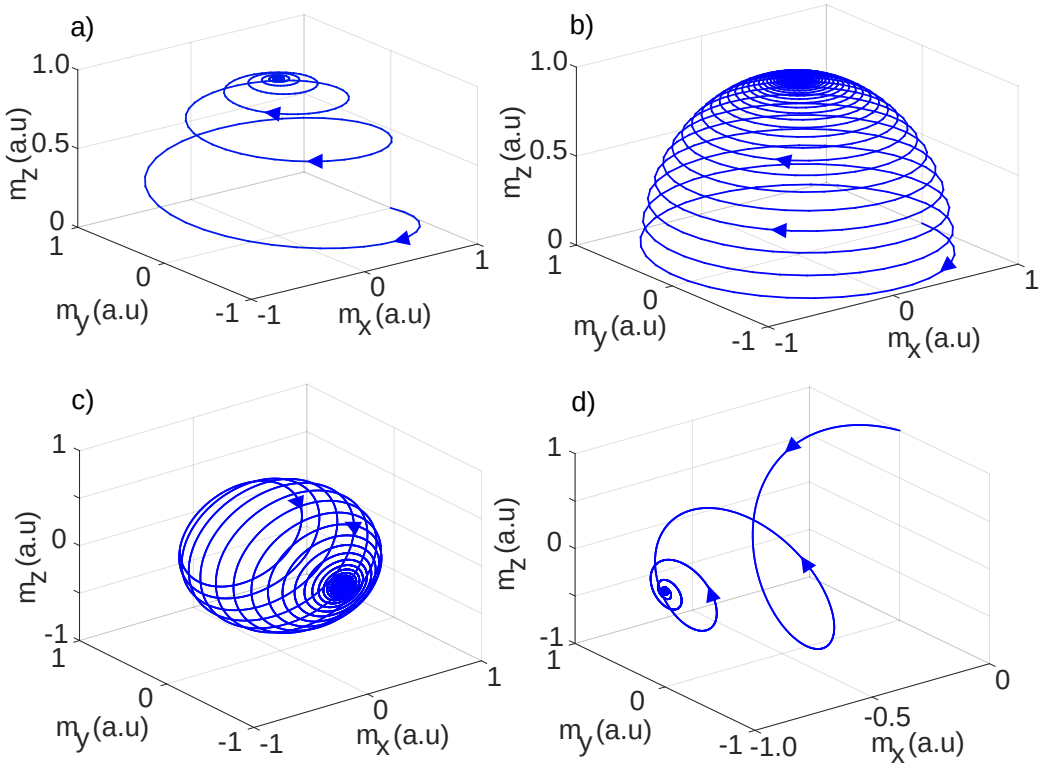

Figure 3.5: A simulation of LLG equation for evolution of magnetization vector on a unit magnetization sphere. The initialization parameters are similar to what were used in Fig. 3.4 in the respective order.

One method is to apply a magnetic pulse antiparallel to the prior state of magnetization [46]. However the second method has proven to be more efficient in terms of energy and time which involves the application of a magnetic pulse *perpendicular* to the magnetization. We'll discuss the second approach in the following discussion. The mechanism for precessional switching can be explained on the basis of three step model.

For simplicity, we limit our discussion only to uniaxial magnetic thin films where the magnetization easy axis lies in the plane of the film. For a thin film placed in a co-ordinate system x-y plane, we assume that the magnetization easy axis is parallel to x-axis. The z-axis is perpendicular to the plane of film and an external magnetic field $\mathbf{H_{ext}}$ is applied in the $-y$ direction. As the pulse arrives, magnetic moment starts recessing out of the film plane due to the torque defined by Eq. (3.1) and is illustrated in Fig. 3.6(a). In the second

step, **M** start precessing about the demagnetization field which is generated due to out of plane component of magnetization and **M** follows the direction of demagnetizing field by traversing through an angle ϕ. In the last step, as depicted in Fig. 3.6(c), the anisotropy field (which lies in-plane) comes at play and **M** starts oscillations about the anisotropy field given by Eq. (3.9) before getting aligned in the $-x$-axis direction, hence completing the precessional switching mechanism [44, 47].

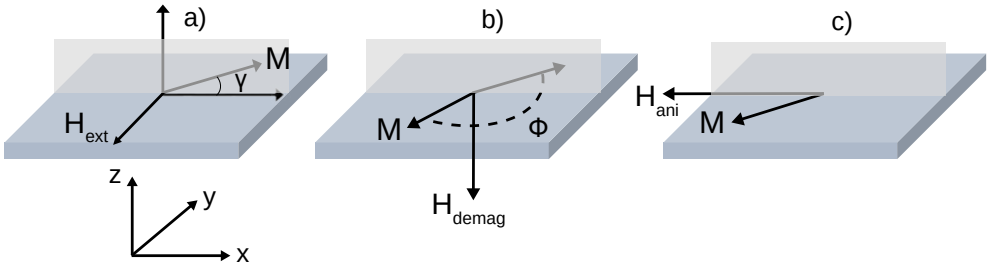

Figure 3.6: Three step model for precessional switching a) In response to an external magnetic field pulse H_{ext}, magnetization **M** start precessing at angle γ given by $\gamma = \omega t$ where t is the duration of pulse, b) **M** traverses an angle ϕ due to the demagnetization field and c), finally the anisotropy fields aligns the magnetization **M** antiparallel to the prior state.

Apparently, the LLG equation explains the evolution of macro-magnetization **M** of the system but doesn't incorporate temperature effects which are crucial for determining the magnetic state of the system. This particular aspect is explored in the following section which will provide the reader a general overview of the implementation of LLG equation and other schemes in atomistic spin simulation software for determination of temperature dependent magnetization in a magnetic medium.

3.3.3 Dynamics of Atomistic Spin Simulator—Vampire

This section is based on the popular atomistic spin simulation software Vampire[2] developed by Evans et.al [38]. A typical atomistic spin dynamic software generally utilizes the LLG equation to simulate magnetization dynamics as

[2] https://vampire.york.ac.uk/

a function of magnetic field and ultrafast changes in the magnetization and a Monte-Carlo based approach for modeling of magnetization with temperature. We will skim through the assumptions and key features of the simulation whereas the detailed discussion can be found here [38].

As stated earlier, the LLG equation explains the evolution of macro magnetization dynamics where damping parameter α captures both intrinsic (spin-lattice and spin-electron interactions) and extrinsic (spin-spin interaction arising due to demagnetizing field, surface defects and doping) contributions. Our choice of software applies the LLG on atomic spin moment. Without any loss of generality, Eq. (3.14) can be rewritten for the spin magnetic moments as [38]

$$\frac{d\mathbf{S_i}}{dt} = \frac{\gamma}{1+\lambda^2}(\mathbf{S_i} \times \mathbf{H}_{\text{eff}}) + \frac{\gamma\lambda}{(1+\lambda^2)}\big(\mathbf{S_i} \times (\mathbf{S_i} \times \mathbf{H}_{\text{eff}})\big), \tag{3.21}$$

where $\mathbf{S_i}$ represent a unit vector for spin magnetic moment at site i which interacts with an effective field $\mathbf{H}_{\text{eff}}$ and damping coefficient is re-defined as λ, merely to differentiate from Gilbert damping parameter α [38]. Furthermore, the temperature dependent effects can be efficiently included in the LLG equation by introducing a stochastic thermal field $\mathbf{H_{th}}$ to the $\mathbf{H}_{\text{eff}}$ in Eq. (3.13). The stochastic thermal field H_{th} has the form [38]

$$H_{th} = \Lambda\sqrt{\frac{2\lambda k_B T}{\gamma \mu_s \Delta t}}, \tag{3.22}$$

where λ is microscopic damping parameter, T is the temperature, k_B is the Boltzmann's constant, γ is gyromagnetic ratio, μ_s is the magnitude of atomic magnetic moment, Δt is the integration time step and Λ represents thermal fluctuations by a three-dimensional Gaussian distribution [38]. This in turns modifies the effective field to $\mathbf{H}_{\text{eff}} \rightarrow \mathbf{H}_{\text{eff}} + \mathbf{H_{th}}$.

The LLG equation can be analytically solved only in a handful of few special cases, however numerical methods have been extensively employed to obtain the solution for physical systems. The presence of the stochastic thermal field in LLG makes it a Langevin dynamics problem which can be solved with Stratonovich calculus. However any numerical method opted to solve LLG

must obey the underlying physics and keep the properties realizable, particularly the modulus of the magnetization must remain constant. Vampire uses the Heun corrector-predictor scheme [38, 48, 49] to solve stochastic LLG which ensures the convergence to Stratonovich solution. However, the Heun scheme does not preserve the spin length which necessitates to renormalize the spin unit vector length $\mathbf{S_i}$ after both the predictor and corrector steps [38].

Furthermore, vampire utilizes LLG with Heun integration scheme in conjunction with two temperature model to simulate the ultrafast magnetization dynamics of magnetic nanostructures. The next section will present a brief review of the two temperature model.

3.3.4 Two Temperature Model

All optical switching mechanism involves non-equilibrium transport and temperature dynamics of electrons and lattice degree of freedoms. The dynamics of electrons and phonons are based on the two temperature model which consists of two stages. The first stage is the absorption of laser energy by electron-phonon interaction. The temperature of the electron system reaches a maximum T_e depending on the laser fluence within ≈ 0.3 ps. The temporal dynamics is also illustrated in Fig. 3.7.

The second stage involves the transfer of heat energy to the lattice through electron-phonon interaction. The electron and phonon temperature equilibrates within 1–2 ps. Two temperature model is valid only for low laser fluences in which the electronic temperature does not crosses the threshold 0.1 T_f, where T_f is the Fermi temperature (typical range for metals, $T_f > 20000$ K) [50]. The mathematical expressions for the two temperature model has the following form:

$$C_e \frac{\partial T_e}{\partial t} = -G(T_e - T_p) + S(r,t), \tag{3.23}$$

$$C_p \frac{\partial T_p}{\partial t} = G(T_e - T_p), \tag{3.24}$$

where T_e and T_p represent the instantaneous temperatures for electrons and phonons (crystal lattice degree of freedom) and C_e and C_p are electron and phonon heat capacities, respectively, while G is the electron-phonon coupling constant. The term $S(r,t)$ represent the heat flux which is added only to the Eq. 3.23 as thermal energy is directly transferred only to the electron system.

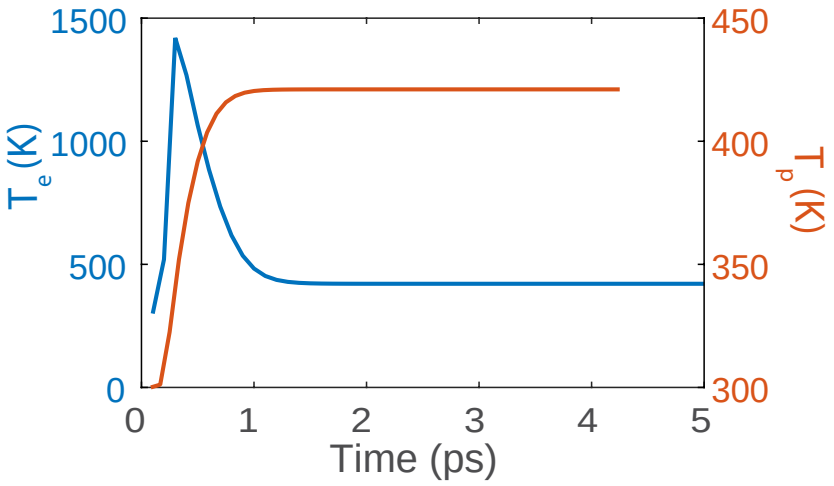

Figure 3.7: Temporal evolution of electron T_e and phonon temperature T_p in response to a laser pulse of 50 fs. The data presented here is taken from one of the simulation we performed on Vampire for ultrafast magnetization.

Furthermore, in order to characterize the temperature dependent magnetization of the magnetic sub-systems, our choice of software Vampire uses a Monte Carlo (MC) algorithm to measure the observable, *i.e.,* magnetization and the Curie temperature T_c. To measure the Curie temperature, the program performs a step-wise loop over temperature, performing equilibration and averaging steps and calculating the mean magnetization before incrementing the temperature. As the system experiences a change in temperature, it takes a finite amount of time (integration steps in the case of Monte Carlo integration) to reach thermal equilibrium. It is therefore important to make sure that thermal equilibrium is reached before taking an average of the magnetization

In Vampire, the Curie temperature program includes both equilibration and

averaging loops variables to ensure the thermodynamic equilibrium. Additionally, the use of MC instead of LLG equation for temperature dependent magnetization is motivated due to the advantage of reduced computational effort. The detailed discussion about Monte Carlo method is beyond the scope of this thesis and can be found elsewhere [38, 51]. We end this discussion with a short note on the specification of key parameters to be parsed to the software for initialization.

3.3.5 Running the Vampire Software

Input parameters are drafted in two different files to be utilized by Vampire: a) a Material file and b) an Input file. The material file contains the information of elements, exchange energies, anisotropy energies and initial state of the system (randomly oriented spins or aligned in a specific direction). It also incorporates the doping percentage and structural information for a proposed hetero-structure. The input file, on the other hand, consists of boundary conditions, type and dimensions of crystal structure. It also registers the data for magnetic measurement to be performed on the structure proposed in the material file. The choice of simulation algorithm and integrator (LLG-Heun for magnetic hysteresis and Monte Carlo for equilibrium magnetization M-T curve) or ultra-fast thermally induced magnetization switching dynamics parameters are also accommodated in the input file.

The preceding discussion covers the theoretical basis which is employed in determining different magnetization dynamics. The next section discusses simulation results for temperature dependent magnetization studies of different materials and alloys. First we performed the simulation for transition metals, rare-earth elements and alloys to corroborate with the experimental findings. These results also offer a testing ground for the correct estimation of the exchange energy constant J_{ij} which will be utilized in the subsequent measurements and analysis of magnetization dynamics in the forthcoming sections. Subsequently, we present the results for RE-TM alloys where RE= Tb,

Gd and finally describe the temperature dependent magnetization curves for the proposed DyFe magnetic nanostructures.

3.4 Results and Discussion

For an alloy or a nanostructure based on more than two constituent elements, one of which for example is Fe, Eq. (3.4) will be modified as

$$\begin{aligned}\mathcal{H} = -\sum_{i\neq j} J_{X-X}\mathbf{S_i}\cdot\mathbf{S_j} - \sum_{i\neq j} J_{X-Fe}\mathbf{S_i}\cdot\mathbf{S_j} - \sum_{i\neq j} J_{Fe-Fe}\mathbf{S_i}\cdot\mathbf{S_j} \\ -(K_X^u\sum_i(\mathbf{S_i}\cdot\mathbf{e})^2 - (K_{Fe}^u\sum_i(\mathbf{S_i}\cdot\mathbf{e})^2\end{aligned} \tag{3.25}$$

where X = RE or TM, J_{X-Fe} describes the exchange interaction between element X and Fe and K_X^u represents the uniaxial magnetic anisotropy constant for the element X. The input parameters for the crystal structure and lattice parameters for the respective elements are tabulated in Table 3.1.

We performed the field cooled magnetization vs temperature simulation of the native rare earth, native transition metals and the alloys ($Ni_{80}Fe_{20}$, $Co_{35}Fe_{65}$) to corroborate simulated results with experimental data. The volume of the

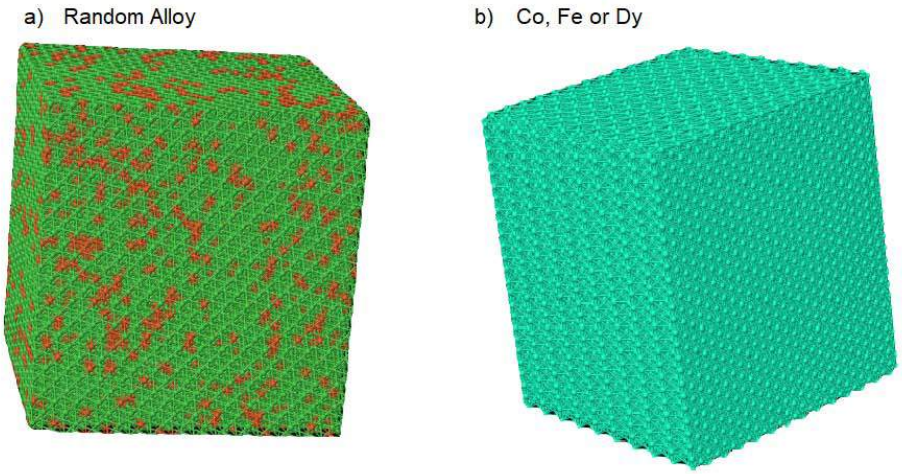

Figure 3.8: The crystal structure data generated by the Vampire is visualized in the JMOL software. a) Random alloy for $Ni_{80}Fe_{20}$ and $Co_{35}Fe_{65}$ b) Co, Fe, Dy magnetic structures.

Table 3.1: Input File parameters for rare earth, transition metals and alloys.

Element	Crystal Structure	Lattice Parameters (Å)
Dy	hcp	$a = 3.58$, $c = 5.65$
Co	hcp	$a = 3.58$, $c = 4.069$
Fe	bcc	$a = 2.86$
Ni	fcc	3.524
Ho	hcp	$a = 3.58$, $c = 5.62$
Gd	hcp	$a = 3.64$, $c = 5.78$
Tb	hcp	$a = 3.60$, $c = 5.69$
$Ni_{80}Fe_{20}$	fcc	a=3.524
$Co_{35}Fe_{65}$	bcc	a=2.856

magnetic structures for these analysis was kept constant at 25 nm^3 and exchange energy J_{ij} is estimated by mean field expression Eq. (3.6). The applied magnetic field strength is 1 T and the effective damping constant value is 1. [13, 15, 38]. Field cooled **M**-T curve for various materials and alloys are shown in Fig. 3.9 and Curie temperatures are estimated by least square curve fit of equation [40]

$$m(T) = (1 - \frac{T}{T_c})^{\beta} \tag{3.26}$$

where $m(T)$ is the normalized magnetization T_c is the Curie temperature and β is the critical exponent. The estimated Curie temperatures are in excellent agreement with experimentally known results.

For Permalloy ($Ni_{80}Fe_{20}$) and permendur ($Co_{35}Fe_{65}$), an additional exchange interaction occurs between Ni-Co and Fe-Co elements in their respective alloys and is denoted by J_{X-Fe} in Table 3.2. The sign of J_{X-Fe}, positive in the current case illustrating that the coupling between elements in an alloy is ferromagnetic. This results in higher Curie temperatures for $Ni_{80}Fe_{20}$ and $Co_{35}Fe_{65}$.

This brings us to our next topic of discussion which deals with the magnetization of rare earth-transition metal (RE-TM) alloys as a function of temperature, similar to several extensive studies done by various groups due to their distinctive magnetic properties [7, 29, 38, 52–54]. For a magnetic composite to

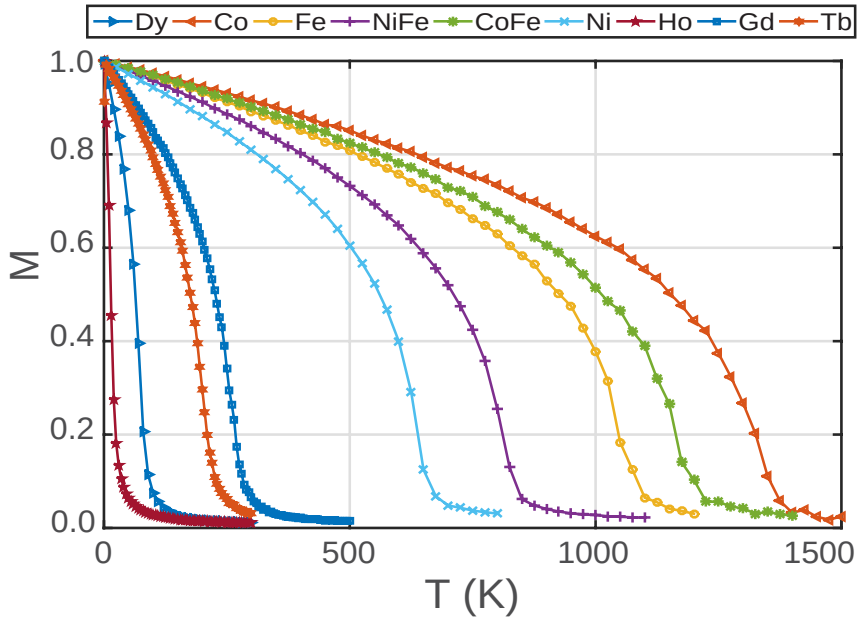

Figure 3.9: Field cooled temperature dependent magnetization curves for different transition metals and alloys.

Table 3.2: Parameters for materials file and Curie temperature calculated from M-T curves where J_{exc} and K_u denotes the exchange and anisotropy energy, respectively.

Element	J_{exc} (J/link)	K_u (J/atom)	J_{X-Fe} (J/link)	T_c (K)
Dy	1.6×10^{-23}	1.58×10^{-23}	-	90
Fe	7.050×10^{-21}	5.65×10^{-25}	-	1043
Co	11.2×10^{-21}	6.69×10^{-24}	-	1388
$Ni_{80}Fe_{20}$	-	-	4.5×10^{-21}	843
$Co_{35}Fe_{65}$	-	-	7.5×10^{-21}	1210

be used in magnetic recording media, one of the essential properties for a material is to possess magnetization at room temperature, *i.e.*, $T_c > 300$ K. This analysis will help us choose the right composition of alloys or nanocomposites for ultrafast magnetic switching.

3.4.1 Curie and Compensation Temperature

RE-Fe alloys (with RE = Tb, Gd) are ferrimagnetic in nature, *i.e.*, the two metals with distinct magnetic moments are coupled antiferromagnetically which has its origin in the hybridization of 5d and 3d orbitals of the constituent el-

ements [55], respectively. We first report results of an atomistic simulation obtaining field cooled M-T curves for different concentration of RE (Gd,Tb) in the host element Fe.

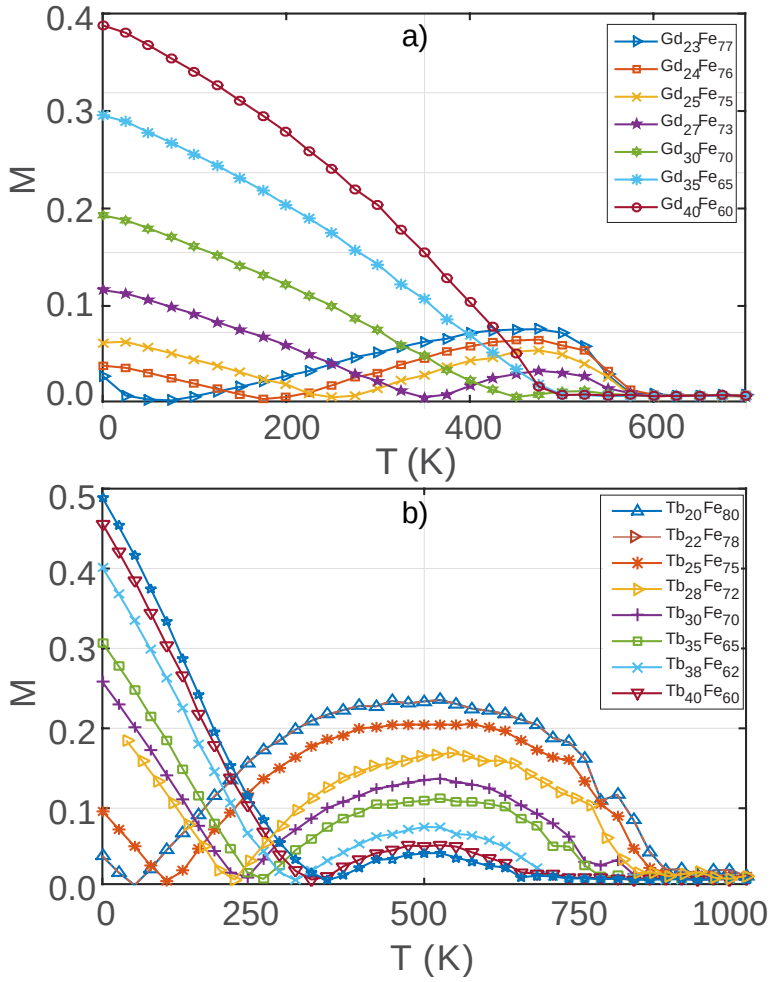

Figure 3.10: Temperature dependent magnetization curves for different concentration of a) Gd ions in GdFe alloy and b) Tb ions in TbFe alloy. Solid lines are guide to the eye.

We have used the same exchange parameters for RE and TM ions as reported in Section 3.4 which predict the accurate Curie temperatures for respective elements. The exchange value for inter-sublattice exchange J_{X-Fe} is optimized to reproduce the key static magnetic properties, *i.e.*, temperature dependent magnetization. The values for inter sublattice exchange coupling are $J_{Gd-Fe} = -1.09 \times 10^{-21}$ and $J_{Tb-Fe} = -1.25 \times 10^{-21}$ (J/link). The magnitudes of magnetic moments are 7.6 μ_B, 9.21 μ_B and 2.21 μ_B for Gd, Tb and Fe ions,

respectively [43]. The crystal structure dimension along each axis is 5 nm with periodic boundaries.

Fig. 3.10(a) illustrates the magnetization curves with temperature for varying Gd concentrations in the range of 20 to 40 %. A similar simulation is performed for Tb-Fe alloys for different concentrations of Tb ions in the host element Fe and results are depicted in the Fig. 3.10(b).

It is evident from Figures. 3.10(a) and (b) that the normalized magnetization approaches zero at two distinct temperatures. The first point at lower temperatures where magnetization meets the temperature axis is referred as the compensation temperature where the net magnetization due to the oppositely aligned RE and Fe magnetic moments is zero. The second point at higher temperatures is attributed to the Curie temperature where material undergoes a transition from *ferro* to *para*.

The temperature dependence of the compensation temperature and Curie temperature on Gd and Tb ion concentrations are summarized in Fig. 3.11. With the increase of RE concentration, the magnetization follows a decrease in the Curie temperature T_c which is attributed to magnetic softening due to addition of more RE nearest neighbors as RE-RE has a smaller exchange coupling as compared to Fe-Fe [55]. For small changes in Gd concentration, variance in Curie temperature is almost negligible as shown in Fig. 3.11. Meanwhile for Tb, T_c decreases monotonically.

Additionally, the compensation points T_m shift towards higher temperature with the increase in RE ions concentration. However, for a critical value of RE concentration, *i.e.*, 30% for Gd and 45% for Tb, no compensation point was observed. The reason for this behavior is the contest between inter sublattice exchange coupling. As the RE concentration increases, more atoms contribute to the net magnetization of RE sublattice, hence net magnetization is greater than Fe [55].

Figure 3.12 shows a similar behavior for Dy-Fe alloy for the range 20–40 % Dy ion concentration in the host element Fe. No compensation point was observed however for Dy ion concentration less than 24%.

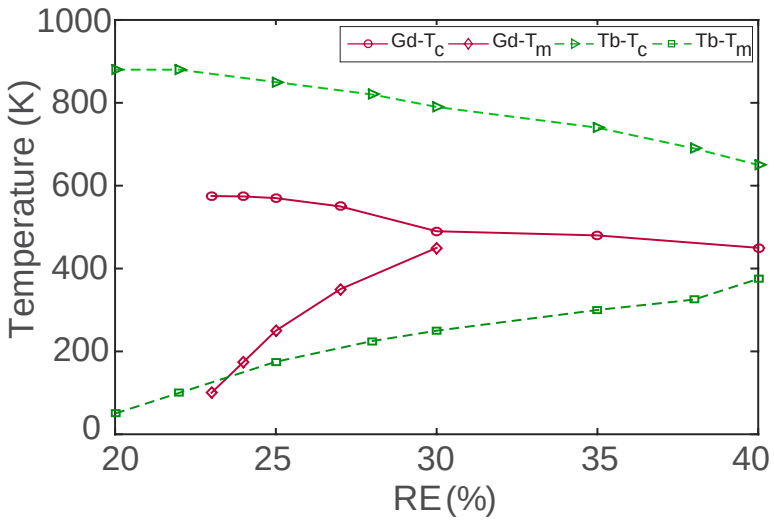

Figure 3.11: Magnetic compensation temperature T_M and Curie temperature T_c for amorphous GdFe and TbFe alloys for different concentrations of Gd and Tb respectively.

We further extended the temperature dependent magnetization studies, particularly for the $Dy_{28}Fe_{72}$ which has a compensation point just above room temperature. We simulate the $Dy_{28}Fe_{72}$ nanostructures in the form of random alloys, bilayers and core-shell whose structures are depicted in Fig. 3.13. All input parameters for Dy and Fe used were the same as previously mentioned in Tables 3.1 and 3.2. The value of the exchange integral J_{Dy-Fe} for 28 at % of Dy content, due to an additional exchange interaction among Dy-Fe atoms was calculated using the equation described by Talbot *et.al* [56] in their work for magnetization reversal in Dy/Fe multilayers:

$$\frac{J_{Fe-Dy}(A_{Fe})}{k_B} = 8 - 198(1 - A_{Fe}). \tag{3.27}$$

Here A_{Fe} presents the concentration of Fe ions. The value of J_{Fe-Dy} was calculated to be -2.49×10^{-21} J/link. It is evident from the Fig. 3.14 that no

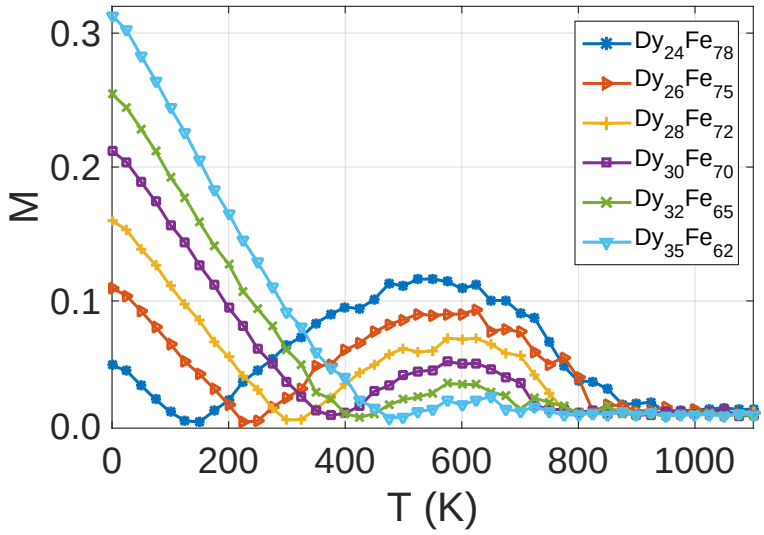

Figure 3.12: Temperature dependent magnetization curves for the DyFe alloy with different Dy ion concentrations in the host element Fe. Solid lines are only meant to be guides to the eye.

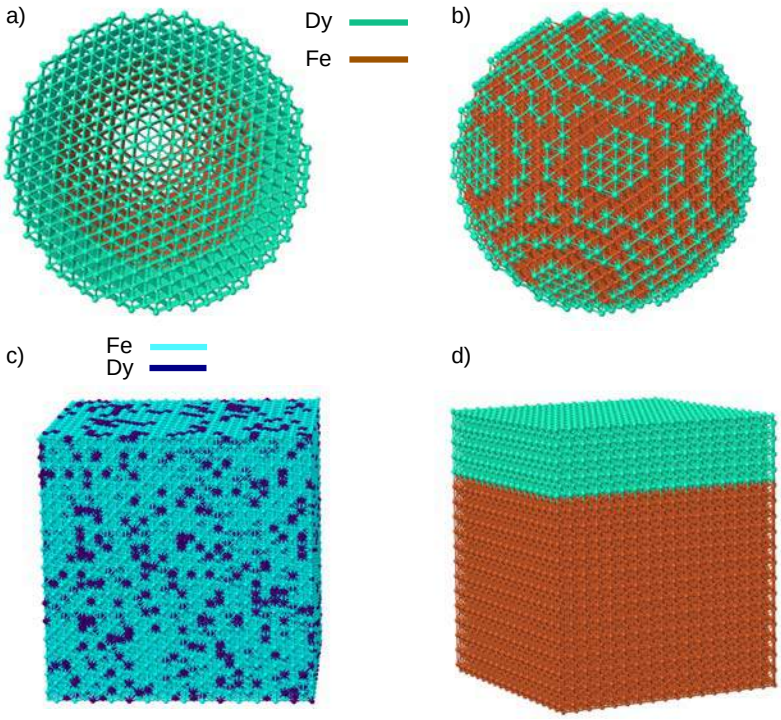

Figure 3.13: Different nanostructures of $Dy_{28}Fe_{72}$ are visualized. a) Coreshell with Fe as core, b) coreshell with Fe as shell, c) $Dy_{28}Fe_{72}$ random alloy and d) bilayer.

compensation temperature is observed for the nanostructures in case of bilayer and coreshell with Fe as core. The Curie temperature estimated from the curves are tabulated in Table 3.3.

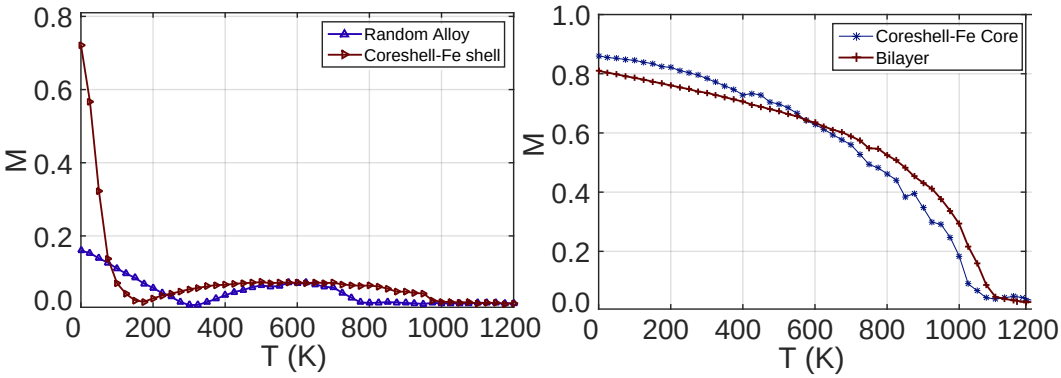

Figure 3.14: M-T curves for $Dy_{28}Fe_{72}$ magnetic nanostructures in the form of random alloy, bilayer and coreshell with Fe and Dy core. Solid lines are guide to the eye.

Table 3.3: Curie temperature estimated from M-T curves for different Dy-Fe magnetic nanostructures.

Dy-Fe	Bilayer	Coreshell- Fe Core	Coreshell-Dy Core	Alloy
T_c (K)	1040	1020	990	790

Prior to the study of ultrafast magnetic switching of these magnetic structures, we start with the preliminary analysis of demagnetization in transition metals and their alloys.

3.4.2 Sub-lattice Resolved Ultrafast Demagnetization

To study thermally induced magnetic switching and demagnetization by the femtosecond laser, a pulsed laser program with LLG-Heun integrator under two temperature profile with a time step of 0.1 fs was applied. The laser fluence for an optical pulse of 50 fs was adjusted to generate a peak electronic temperature $T_e = 1492$ K, unless stated otherwise.

As a background preparatory study, Fig. 3.15 illustrates the result of ultrafast demagnetization for Ni when subjected to thermally induced heating by the 50 fs optical pulse. In response to a femtosecond pulse, the system undergoes a thermal non-equilibrium state. The magnetization of the material follows a local minima before magnetization equilibrates to a newer value as shown in Fig. 3.15. The time taken for the magnetization to achieve this minima is known as demagnetization time τ_D whereas the time required for magnetization to adapt to the equilibrium value is referred to relaxation time τ_R. The demagnetization time constant of pure Ni is τ_D=150 fs [57] and is extracted from the non linear least square curve fitting of the following bi-exponential function [26]:

$$f = g \times \left(a - b\, e^{\left(\frac{-\tau}{\tau_R}\right)} + c e^{\left(\frac{-\tau}{\tau_D}\right)} \right) \tag{3.28}$$

where τ_R and τ_D are demagnetization and relaxation time constants and a, b, c, g are other fit parameters. It is rewarding that demagnetization time constants returned from our simulation are in well agreement with experimental results [26, 57]. Similarly, Fig. 3.16 depicts the elemental demagnetization

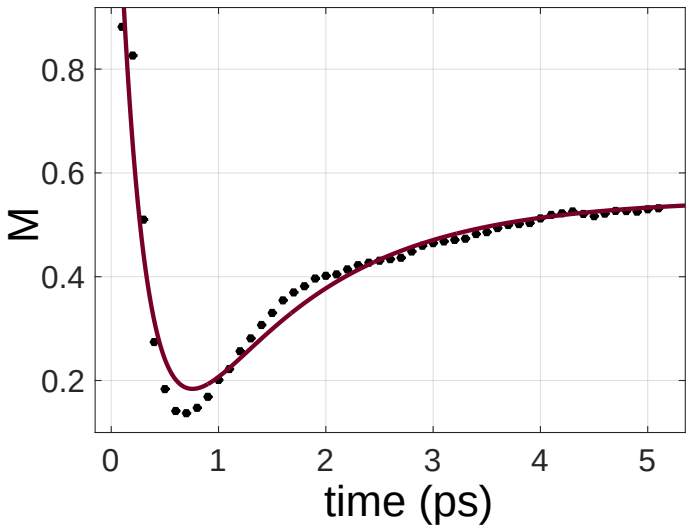

Figure 3.15: Ultrafast demagnetization of metallic Ni in response to a femtosecond laser pulse of 50 fs.

curve for Fe, Co and Ni which are ferromagnetically coupled in host permalloy ($Ni_{80}Fe_{20}$) and permendur ($Co_{35}Fe_{65}$). The data presented here is again curve

fitted using Eq. (3.28) and demagnetization time constants deduced are 180 fs for Ni and 330 fs for Co. However Fe exhibits different demagnetization rates in different host elements, 220 fs in permalloy and 330 fs in permendur. The difference arises due to different inter sublattice exchange values. Consequentially, the magnitude of demagnetization for Fe in host permalloy is smaller and demagnetization rate of Ni is faster than Fe as is evident from Fig. 3.16 (a), whereas in $Co_{35}Fe_{65}$, two sublattices decay at equal rates as shown in Fig. 3.16 (b).

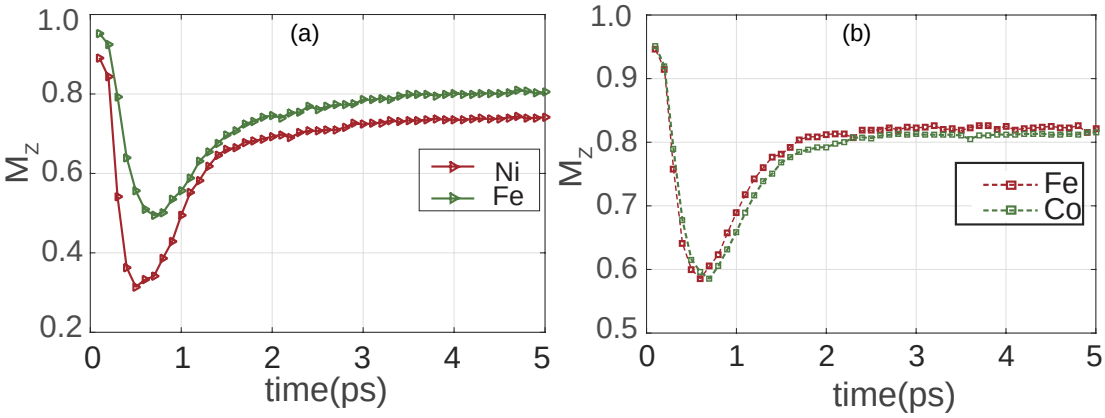

Figure 3.16: Sublattice resolved ultrafast demagnetization of metallic $Ni_{80}Fe_{20}$ and $Co_{35}Fe_{65}$.

This characteristic demagnetization time [27, 58] for each magnetic sublattice in a multi lattice structure scales with:

$$\tau_i = \frac{\mu_i}{2\lambda_i \gamma_i k_B T} \tag{3.29}$$

where μ_i is the moment at site i, γ_i is gyromagnetic ratio, λ_i is coupling to thermal bath and T is the temperature. Consequentially, if a magnetic structure with two or more sublattice with different magnetic moments $\mu_1 \neq \mu_2$ is subjected to high temperatures, despite the strong exchange coupling, two sublattice will undergo different demagnetization dynamics. In permalloy, the Ni magnetic moment is 3.6 times less than that of Fe, hence a rapid decrease in magnetization.

We conclude this section with a short note that no magnetization reversal was observed in ferromagnetic metals and alloys. For extreme electron temperatures, *i.e.*, $T_e > 2000$ K, magnetization is found to decreases sharply to zero and did not recover until for long period of time.

The next section discusses the RE-TM alloys (Gd-Fe and Tb-Fe) which are signature composites for both AOS and AO-HDS switching of magnetization [14, 16, 26, 52, 55]. Here we extend the studies with different concentration of Gd ion concentration in host Gd-Fe alloy in conjunction with different peak electron temperatures. The variation of magnetization switching time against peak electron bath temperature is also investigated for the Tb-Fe alloy. Finally, we explore the Dy-Fe magnetic nanostructures which could serve as potential candidates for ultrafast magnetization switching.

3.4.3 All-Optical Thermal Switching

The spin system for simulation was excited with a 50 fs laser pulse and was initialized at room temperature. We chose the concentration of RE element for which the compensation temperature is above room temperature, as discussed in Section 3.4.1. The anisotropy energy of Gd and Fe was neglected in the Hamiltonian and we assumed the same damping parameter $\alpha = 0.02$, for both RE and TM lattices. Only temperature effects from the laser pulse were considered and we adopted the two temperature model, discussed earlier in Section 3.3.4.

Fig. 3.17 presents the results of simulated magnetization dynamics for $Gd_{24}Fe_{76}$ with different laser fluences which correspondingly produce different peak electronic temperatures. In Fig. 3.17, all optical switching time is computed as a function of peak electron bath temperature. The selection for this particular choice of variable, *i.e.*, is twofold. One is to observe the influence of peak electron temperature or laser fluence on switching time which can be used to gauge the switching time and second is the verification of the previous findings by Chimata *et.al* [55] which suggested a minimum temperature threshold

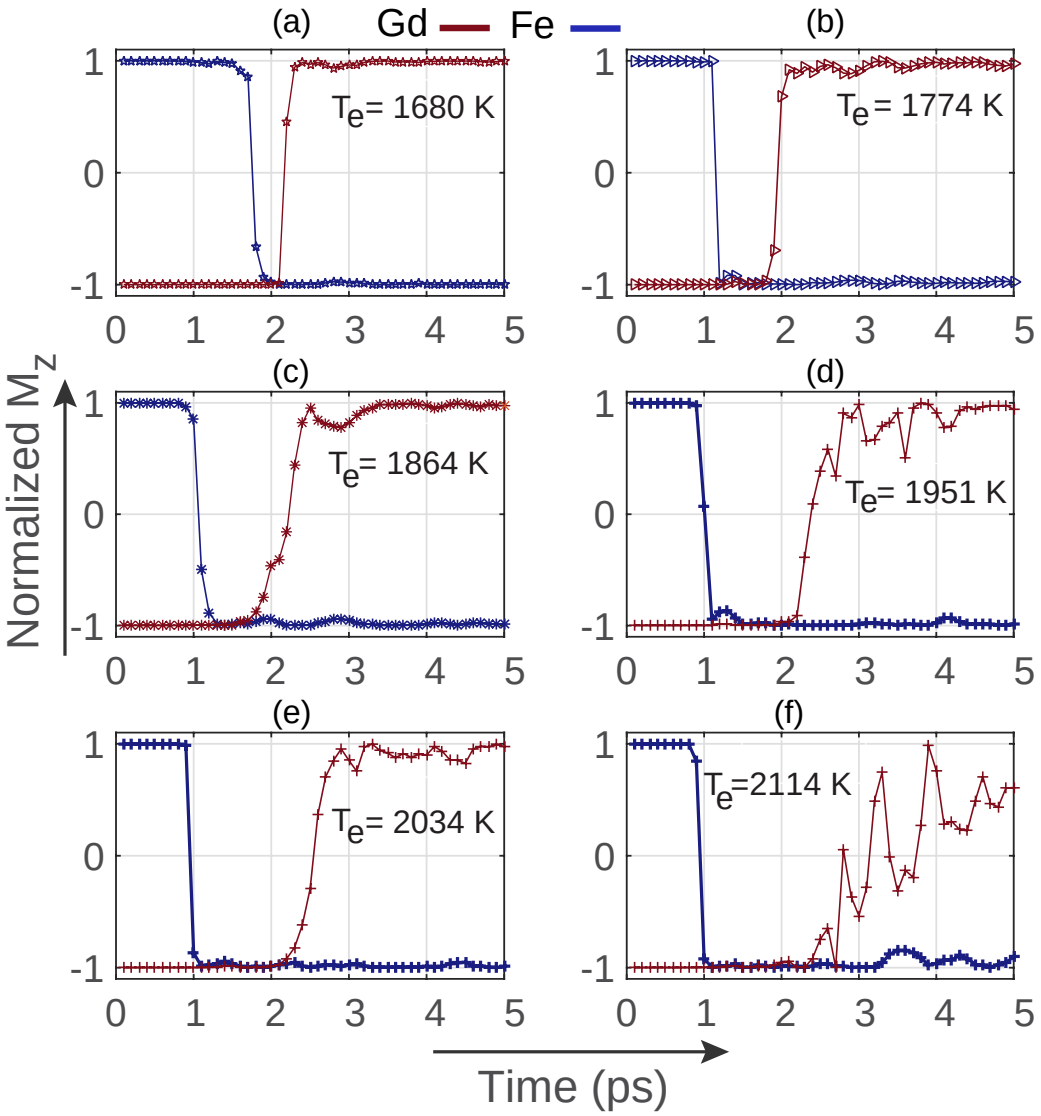

Figure 3.17: Sub-lattice resolved evolution of magnetization switching time for the $Gd_{24}Fe_{76}$ alloy at different peak electron temperature. The solid lines are visual guides.

alongwith an upper bound for all optical switching to occur. Additionally, the simulated curves depict different demagnetization rates for each magnetic sublattice which has also been verified by XMCD experiments [26, 55] and are in accordance with Eq. (3.29).

It is noticeable in Fig. 3.17 that initially both Gd and Fe sublattice demagnetizes but Fe sublattice reverses its magnetization first, so that for a short period

of time both Fe and Gd sublattice have parallel magnetization and exhibit a transient ferromagnetic state. The results also show that the magnetization for Fe immediately equilibrates in a direction opposite to the initial direction.

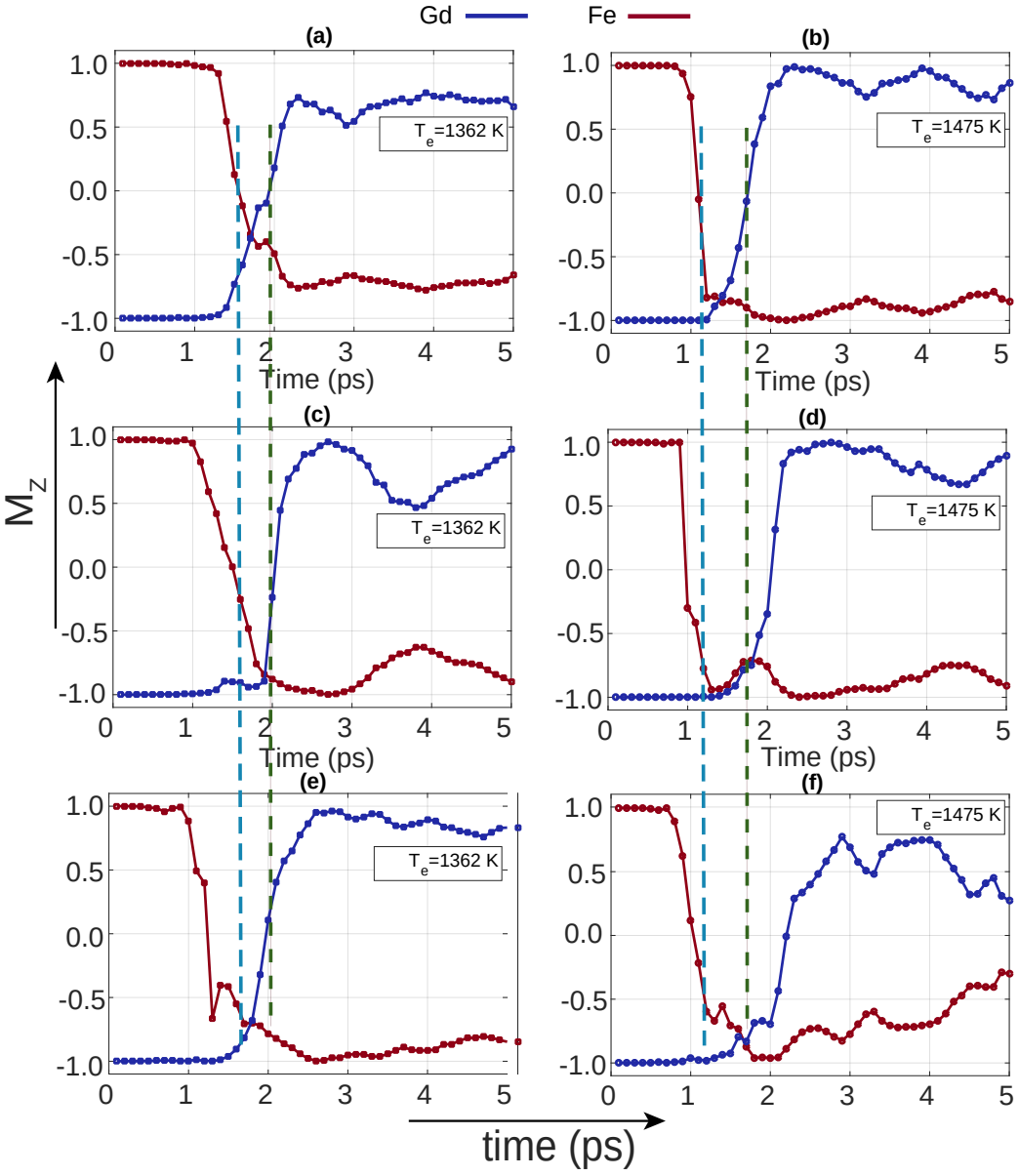

Figure 3.18: All-optical switching time dynamics for different concentration of Gd ion in host Gd-Fe alloy (a–b) $Gd_{24}Fe_{76}$, (c–d) $Gd_{27}Fe_{73}$ and (e–f) $Gd_{30}Fe_{70}$ at two different peak electron bath temperature. Dashed lines are drawn for comparison of switching time.

At higher electronic temperature, for example Fig. 3.17(d), we find excellent agreement with the previous findings [27]. It also emphasizes the role of electron temperature T_e for all optical switching of RE-TM alloys. It is worth noting that in Fig. 3.18(a–f), T_e is always greater than Curie temperatures of alloy and the constituent elements as well.

At lowest electron temperature $T_e = 1680$ K, all optical switching time T_{OS} for Gd and Fe are 2.2 ps and 1.8 ps. With further increase in T_e, T_{OS} decreases for both Gd and Fe sublattice as shown in Fig. 3.17(b). However, the switching time for Fe decreases monotonically while for Gd sublattice, it shows a decrease at first but then increases for temperature greater than 1774 K. The minimum T_{OS} observed for Fe sublattice is 0.9 ps.

Additionally, we investigated the role of Gd concentration in host Gd-Fe alloy and the results are depicted in Fig. 3.18. It is observed that increasing the Gd ion concentration, the switching time for Gd sublattice decreases and for Fe sublattice, magnetization reversal shift towards shorter times. The minimum switching time estimated for Gd is 1.8 ps for $T_e = 1472$ K as shown in Fig. 3.18(b), whereas for Fe the minimum $T_{OS} = 1$ ps as depicted in Fig. 3.18(d).

Fig. 3.19 illustrates the sub-lattice resolved magnetization switching for the $Tb_{25}Fe_{75}$ alloy. For the lowest $T_e = 1680$ K, Tb and Fe sublattice magnetizations decay approximately at the same rate and optical switching occurs at 1.85 ps for Fe and 2.1 for Tb. A further increase in electron temperature demonstrates the decrease in T_{OS} for Fe whereas for Tb, the switching time increases as shown in Fig. 3.19(b–d). The minimum T_{OS} observed for Fe and Tb sublattices are 1.2 ps and 2.0 ps respectively for a peak temperature of 2034 K. Finally we present the result of all-optical thermally induced magnetization switching for Dy-Fe magnetic nanostructures. The damping parameter was kept constant $\alpha = 0.02$ to draw a comparison of switching time among different RE-TM alloys as discussed above. Fig. 3.20 presents the

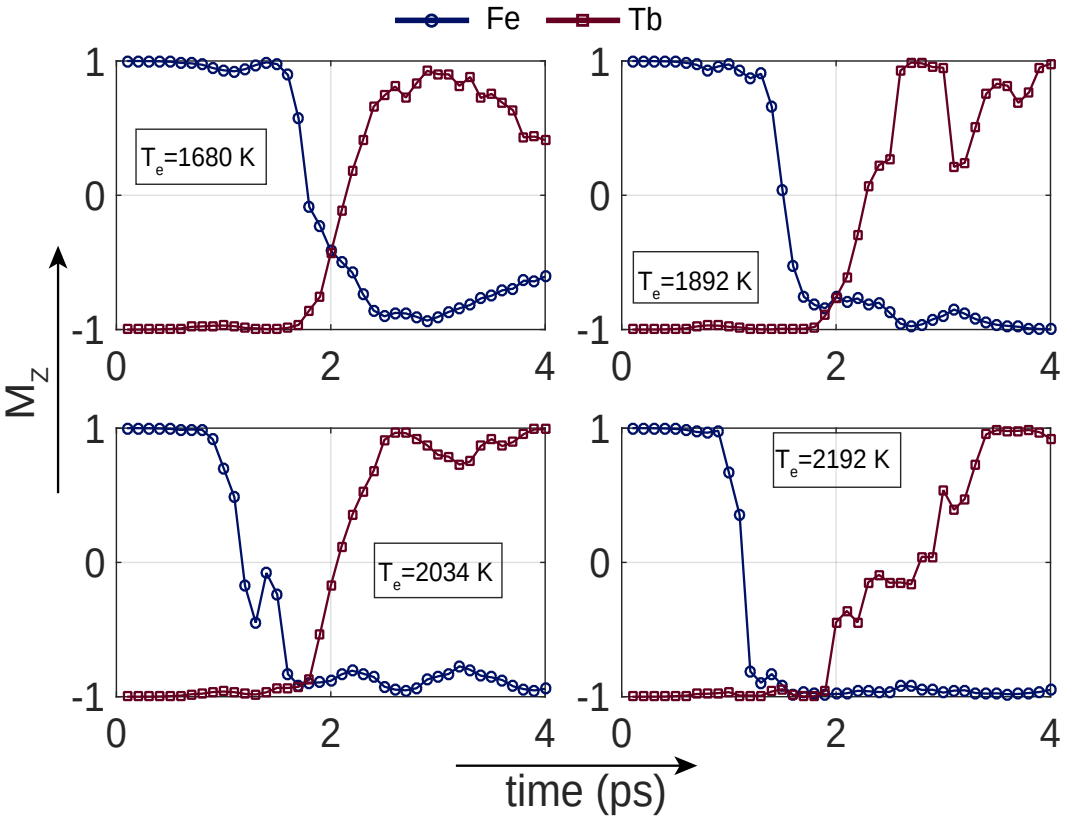

Figure 3.19: All optical switching time dynamics against different electron bath temperature for $Tb_{25}Fe_{75}$ alloy. The damping constant for this simulation was kept at $\alpha = 0.02$. The solid lines are visual guides.

results for $Dy_{28}Fe_{72}$ alloy and coreshell-Fe core. In case of $Dy_{28}Fe_{72}$ bilayer and coreshell-Dy core, no magnetization switching was observed for the entire range of electronic temperatures investigated, *i.e.*, $1000 \leq T_e \leq 2300$ K.

We observed faster switching time $T_{OS} = 1.1$ ps for Dy in host alloy as compared to switching time estimated for Gd-Fe and Tb-Fe alloys. In case of coreshell-Fe core, the magnetization switching occurs for peak electron temperature $T_e = 2034$ K, where Fe reverses its magnetization at 1 ps and Dy switches the magnetization at 3.5 ps.

The scenario of reversal can be understood as follows. An ultrashort laser pulse increases the thermal energy of the electrons in the alloy, creating a

thermal bath for spins with a temperature much higher than the Curie point. The rapid increase in thermal energy of the system leads to a very fast energy transfer into the spin system. This results in the Fe and RE sublattices demagnetizing on very different timescales mainly because of differing magnetic moments. The temperature of electronic system starts decreasing rapidly as

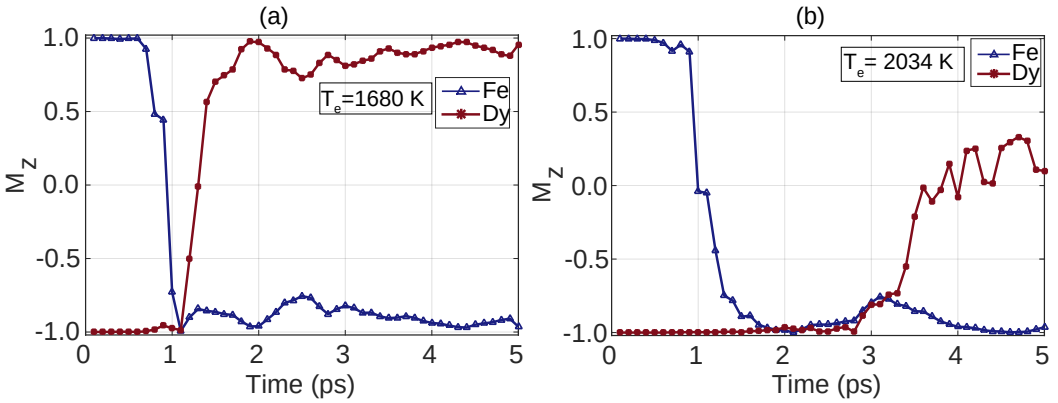

Figure 3.20: All optical switching magnetization dynamics for a) $Dy_{28}Fe_{72}$ alloy and b) coreshell-Fe core. The respective electron bath temperature are labelled in the insets.

a result of electron-lattice interaction and temperature falls below Curie temperature within 1 ps. After this the initial sharp increase of the temperature of electronic heat bath, the magnetization of the sublattices is still changing due to exchange relaxation [55]. The non-equivalence of the sublattices combined with the exchange relaxation means that Fe reaches zero magnetization before that of RE, eventually leading to the onset of the ferromagnetic like state where two sublattice align parallel. The magnetization of the Fe sublattice is then increasing while the RE is decreasing because of exchange relaxation.

The foregoing discussion elicits the complete characterization of ultrafast magnetization RE-TM alloys (RE=Tb, Gd, Dy) and DyFe nanostructures in response to femtosecond laser pulse. The ultrafast magnetization response of GdFe and TbFe alloys demonstrate different switching time as the concentration of RE ions in host TM and electronic heat bath temperatures are varied. Furthermore, DyFe magnetic nanostructures in the form of random alloy and

coreshell with Fe as core offer faster switching than traditional composites of GdFe and TbFe alloys.

This concludes our discussion on ultrafast magnetization dynamics of RE-TM alloys. We now briefly summarize the computational and experimental investigations of magnetic nanostuctures carried out as a collaborative work [59].

In this work, we proposed and actualized experimentally the synthesis of nanodimensional magnetic media consisting of patterned arrays of DyFe bilayer structure. As stated earlier, the presence of spontaneous magnetization in a composite at room temperature is essential for magnetic storage applications. In this context, we first simulated the magnetic response of the DyFe bilayer where we have assumed the input parameters as prescribed earlier in Tables. 3.1 and 3.2. The composition of DyFe nanostructures is varied by decreasing Dy thickness from 100 nm to 75 nm (Fe content increases from 0–25 nm).

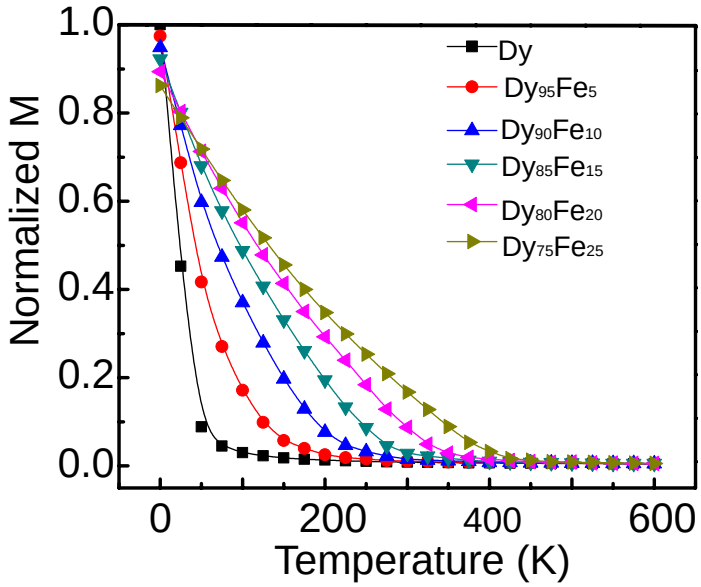

Figure 3.21: Temperature dependent magnetization curves as the thickness of Fe layer is varied in DyFe bilayer structure.

Fig. 3.21 represents the magnetization curves for different compositions of DyFe bilayers. It is obvious from M-T curves that the Curie point shifts to-

wards higher temperatures as the thickness of Fe is increased from 0–25 nm. The minimum thickness of Fe which results in a room temperature magnetization of the bilayer system is 10 nm ($Dy_{90}Fe_{10}$). This preliminary analysis helped us to choose the suitable composition and served as a commencing point for our experimental exploration.

The experiemental scheme can be stated in the following way. In the first step, nano-structures are patterened on Si substrate using E-beam lithography. The DyFe bilayer structures were deposited on E-beam exposed patterened structurral arrays through DC (Dy) and RF (Fe) magnetron sputtering. The thickness of each layer (90 nm for Dy and 10 nm afor Fe) is monitered and controlled by STM thickness monitor.

The subsequent measurements which involve structural, chemical, optical and magnetic characterizations of patterened bilayer structures, are perfromed using field emission scanning electron microscope (FE-SEM, Nova NanoSEM-450), energy dispersive X-ray spectroscopy (EDX, Oxford Instruments) and vibrating sample magnetometer (VSM, Cryogenics), respectively. We only cite here key results of our experimental study whereas the detailed optimization process for NSs and analysis can be found here [59].

We focused on the synthesis of nano-dimensional $Dy_{90}Fe_{10}$ bilayer structured arrays in cylindrical geometry using E-beam lithography. The diameter of cylindrical nanostructures is kept fixed at 100 nm with the same height while the center to center spacing between NSs is 200 nm. In order to achieve the desired size and height of patterned structured arrays, we have optimized various E-beam exposure parameters such as E-beam driving potential, dose factor *etc.* We obtain good results for 20 kV of E-beam voltage with the dose factor equals 1.

The surface morphology and structural analysis was performed using field emission scanning electron microscope (FE-SEM) and results are displayed

in Fig. 3.22. The surface of NSs appears to be round in shape and well patterned with a separation distance of 95 ± 5 nm, both vertically and horizontally. Furthermore, the diameter of these NSs was found to be 105 ± 5 nm, showing a continuous and homogeneous overall morphology. The results of

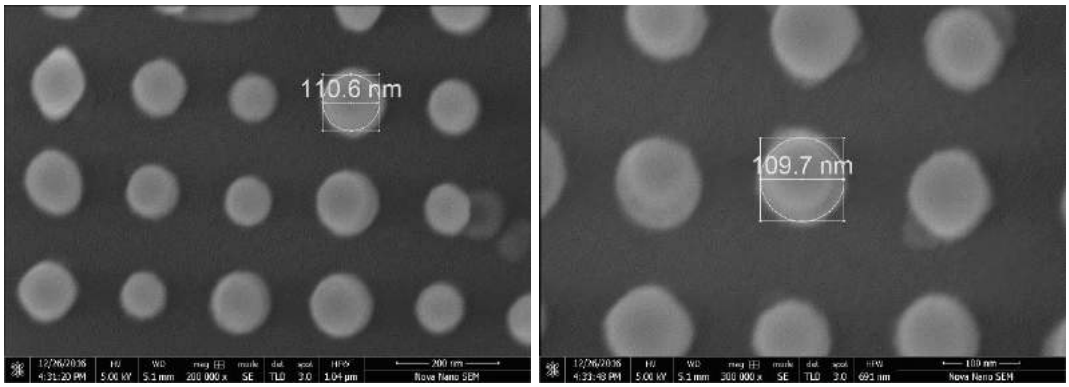

Figure 3.22: FE-SEM images of 100 nm NSs with a) magnification 200,000x and b) 300,000x, respectively.

elemental profiling using EDX are presented in the Appendix Our simulation

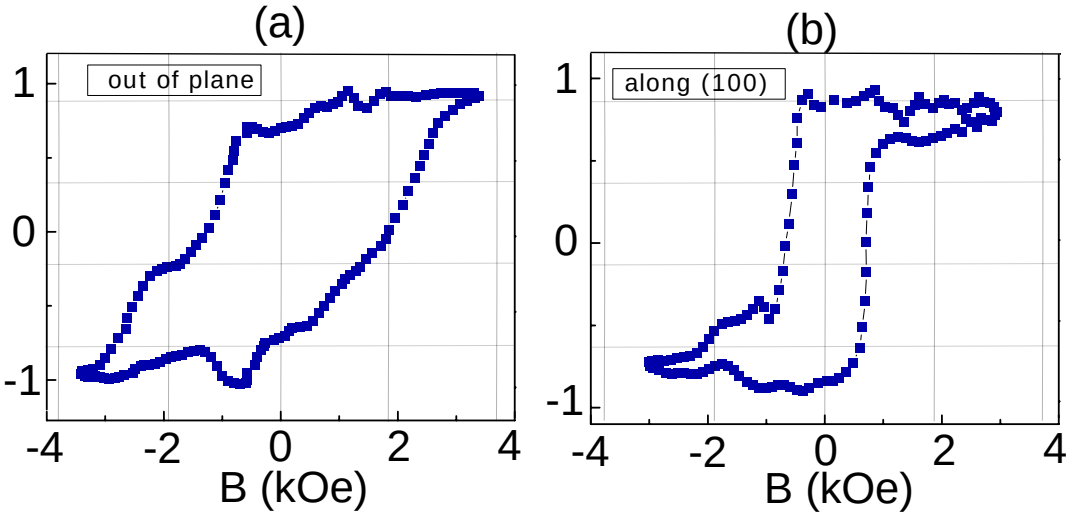

Figure 3.23: Magnetization curves of $Dy_{90}Fe_{10}$ bilayer (100 nm thickness) against magnetic field applied a) parallel and b) perpendicular to the (100) plane of Fe.

results predicted the ferrimagnetic behaviour of Dy_90Fe_10 bilayer structure at room temperature. In order to experimentally investigate the magnetic properties of these NSs, hysteresis measurements are performed for magnetic fields

B directed parallel (in-plane) and perpendicular (out-of-plane) to (100) plane. Fig. 3.23 shows the variation in normalized magnetization as a function of magnetic field.

The results clearly reveal the presence of uniaxial magnetic anisotropy as corecivity changes for different direction of applied magnetic fields. The estimated coercivities are 700 Oe and 1340 Oe for in-plane and out-of-plane applied magnetic field, respectively and easy axis lie in-plane (100) plane of the body centered cubic (bcc) Fe for the deposited NSs. The presence of uniaxial magnetic anisotropy is a highly desirable feature for a nano-composite to be used in HAMR application.

We conclude this chapter with a short note that DyFe NSs are proposed as a suitable candidate for HAMR application however these structures can be potentially investigated experimentally for the ultrafast magnetization switching as well.

References

[1] L. Liu, C.-F. Pai, Y. Li, H. Tseng, D. Ralph, and R. Buhrman, "Spin-torque switching with the giant spin Hall effect of tantalum," *Science*, vol. 336, no. 6081, pp. 555–558, 2012.

[2] J. Katine, F. Albert, R. Buhrman, E. Myers, and D. Ralph, "Current-driven magnetization reversal and spin-wave excitations in Co/Cu/Co pillars," *Physical Review Letters*, vol. 84, no. 14, p. 3149, 2000.

[3] G. E. Bauer, E. Saitoh, and B. J. Van Wees, "Spin caloritronics," *Nature Materials*, vol. 11, no. 5, pp. 391–399, 2012.

[4] N. Roschewsky, C.-H. Lambert, and S. Salahuddin, "Spin-orbit torque switching of ultralarge-thickness ferrimagnetic GdFeCo," *Physical Review B*, vol. 96, no. 6, p. 064406, 2017.

[5] S. Wienholdt, D. Hinzke, and U. Nowak, "THz switching of antiferromagnets and ferrimagnets," *Physical Review Letters*, vol. 108, no. 24, p. 247207, 2012.

[6] Y. Zhang, Y. Feng, J. Zhao, T. Jiang, and B. Zhu, "Terahertz beam switching by electrical control of graphene-enabled tunable metasurface," *Scientific Reports*, vol. 7, no. 1, pp. 1–10, 2017.

[7] K. Buschow, *Handbook of Magnetic Materials*. No. Vol. 15 in Handbook of Magnetic Materials, Elsevier Science, 2003.

[8] B. Hillebrands and K. Ounadjela, *Spin Dynamics in Confined Magnetic Structures II*. Physics and Astronomy Online Library, Springer, 2003.

[9] B. Hillebrands and K. Ounadjela, *Spin Dynamics in Confined Magnetic Structures I*. Topics in Applied Physics, Springer Berlin Heidelberg, 2003.

[10] W. A. Challener, T. W. Mcdaniel, C. D. Mihalcea, K. R. Mountfield, K. Pelhos, and I. K. Sendur, "Light delivery techniques for heat-assisted magnetic recording," *Japanese Journal of Applied Physics*, vol. 42, no. 2S, p. 981, 2003.

[11] A. M. Kalashnikova, A. V. Kimel, and R. V. Pisarev, "Ultrafast opto-magnetism," *Physics-Uspekhi*, vol. 58, no. 10, p. 969, 2015.

[12] B. Hebler, A. Hassdenteufel, P. Reinhardt, H. Karl, and M. Albrecht, "Ferrimagnetic Tb–Fe alloy thin films: composition and thickness dependence of magnetic properties and all-optical switching," *Frontiers in Materials*, vol. 3, p. 8, 2016.

[13] R. F. Evans, T. A. Ostler, R. W. Chantrell, I. Radu, and T. Rasing, "Ultrafast thermally induced magnetic switching in synthetic ferrimagnets," *Applied Physics Letters*, vol. 104, no. 8, p. 082410, 2014.

[14] J. Barker, U. Atxitia, T. Ostler, O. Hovorka, O. Chubykalo-Fesenko, and R. Chantrell, "Two-magnon bound state causes ultrafast thermally induced magnetisation switching," *Scientific Reports*, vol. 3, p. 3262, 2013.

[15] C. Spezzani, F. Vidal, R. Delaunay, M. Eddrief, M. Marangolo, V. H. Etgens, H. Popescu, and M. Sacchi, "Thermally induced magnetization switching in Fe/MnAs/GaAs (001): selectable magnetic configurations by temperature and field control," *Scientific Reports*, vol. 5, p. 8120, 2015.

[16] S. Mangin, M. Gottwald, C. Lambert, D. Steil, V. Uhlíř, L. Pang, M. Hehn, S. Alebrand, M. Cinchetti, G. Malinowski, *et al.*, "Engineered materials for all-optical helicity-dependent magnetic switching," *Nature Materials*, vol. 13, no. 3, p. 286, 2014.

[17] A. Eschenlohr, M. Battiato, P. Maldonado, N. Pontius, T. Kachel, K. Holldack, R. Mitzner, A. Föhlisch, P. M. Oppeneer, and C. Stamm, "Ultrafast spin transport as key to femtosecond demagnetization," *Nature Materials*, vol. 12, no. 4, p. 332, 2013.

[18] J.-Y. Chen, L. He, J.-P. Wang, and M. Li, "All-optical switching of magnetic tunnel junctions with single subpicosecond laser pulses," *Physical Review Applied*, vol. 7, no. 2, p. 021001, 2017.

[19] A. Stupakiewicz, K. Szerenos, D. Afanasiev, A. Kirilyuk, and A. Kimel, "Ultrafast nonthermal photo-magnetic recording in a transparent medium," *Nature*, vol. 542, no. 7639, p. 71, 2017.

[20] H. Yang, Y. Chen, S. Leong, C. An, K. Ye, and J. Hu, "Measurement of magnetic property of FePt granular media at near Curie temperature," *Journal of Magnetism and Magnetic Materials*, vol. 423, pp. 27–33, 2017.

[21] C. Stanciu, F. Hansteen, A. Kimel, A. Kirilyuk, A. Tsukamoto, A. Itoh, and T. Rasing, "All-optical magnetic recording with circularly polarized light," *Physical Review Letters*, vol. 99, no. 4, p. 047601, 2007.

[22] A. Hassdenteufel, B. Hebler, C. Schubert, A. Liebig, M. Teich, M. Helm, M. Aeschlimann, M. Albrecht, and R. Bratschitsch, "Thermally assisted all-optical helicity dependent magnetic switching in amorphous FeTb alloy films," *Advanced Materials*, vol. 25, no. 22, pp. 3122–3128, 2013.

[23] A. Hassdenteufel, C. Schubert, B. Hebler, H. Schultheiss, J. Fassbender, M. Albrecht, and R. Bratschitsch, "All-optical helicity dependent magnetic switching in Tb-Fe thin films with a MHz laser oscillator," *Optics Express*, vol. 22, no. 8, pp. 10017–10025, 2014.

[24] M. El Hadri, P. Pirro, C.-H. Lambert, N. Bergeard, S. Petit-Watelot, M. Hehn, G. Malinowski, F. Montaigne, Y. Quessab, R. Medapalli, *et al.*, "Electrical characterization of all-optical helicity-dependent switching in ferromagnetic Hall crosses," *Applied Physics Letters*, vol. 108, no. 9, p. 092405, 2016.

[25] C. Schubert, A. Hassdenteufel, P. Matthes, J. Schmidt, M. Helm, R. Bratschitsch, and M. Albrecht, "All-optical helicity dependent magnetic switching in an artificial zero moment magnet," *Applied Physics Letters*, vol. 104, no. 8, p. 082406, 2014.

[26] I. Radu, C. Stamm, A. Eschenlohr, F. Radu, R. Abrudan, K. Vahaplar, T. Kachel, N. Pontius, R. Mitzner, K. Holldack, *et al.*, "Ultrafast and

distinct spin dynamics in magnetic alloys," in *Spin*, vol. 5, p. 1550004, World Scientific, 2015.

[27] T. Ostler, J. Barker, R. Evans, R. Chantrell, U. Atxitia, O. Chubykalo-Fesenko, S. El Moussaoui, L. Le Guyader, E. Mengotti, L. Heyderman, *et al.*, "Ultrafast heating as a sufficient stimulus for magnetization reversal in a ferrimagnet," *Nature Communications*, vol. 3, p. 666, 2012.

[28] A. Khorsand, M. Savoini, A. Kirilyuk, A. Kimel, A. Tsukamoto, A. Itoh, and T. Rasing, "Role of magnetic circular dichroism in all-optical magnetic recording," *Physical Review Letters*, vol. 108, no. 12, p. 127205, 2012.

[29] M. S. El Hadri, M. Hehn, G. Malinowski, and S. Mangin, "Materials and devices for all-optical helicity-dependent switching," *Journal of Physics D: Applied Physics*, vol. 50, no. 13, p. 133002, 2017.

[30] M. Krupinski, D. Mitin, A. Zarzycki, A. Szkudlarek, M. Giersig, M. Albrecht, and M. Marszałek, "Magnetic transition from dot to antidot regime in large area Co/Pd nanopatterned arrays with perpendicular magnetization," *Nanotechnology*, vol. 28, no. 8, p. 085302, 2017.

[31] V. Sundar, X. Yang, Y. Liu, Z. Dai, B. Zhou, J. Zhu, K. Lee, T. Chang, D. Laughlin, and J.-G. Zhu, "Fabrication of bit patterned media using templated two-phase growth," *APL Materials*, vol. 5, no. 2, p. 026106, 2017.

[32] H. Yetiş and H. Denizli, "Antidot shape dependence of switching mechanism in permalloy samples," *Journal of Magnetism and Magnetic Materials*, vol. 422, pp. 181–187, 2017.

[33] T. Schneider, M. Langer, J. Alekhina, E. Kowalska, A. Oelschlägel, A. Semisalova, A. Neudert, K. Lenz, K. Potzger, M. P. Kostylev, *et al.*, "Programmability of Co-antidot lattices of optimized geometry," *Scientific Reports*, vol. 7, p. 41157, 2017.

[34] H. Yabe and T. Kuji, "Crystal structure and its magnetization of rare earth–iron alloys by mechanical alloying," *Journal of Alloys and Compounds*, vol. 408, pp. 313–318, 2006.

[35] G. Iles, C. Binns, S. Baker, and M. Roy, "Ferromagnetism of Dy films containing embedded Fe atoms and nanoparticles," *Journal of Magnetism and Magnetic Materials*, vol. 322, no. 17, pp. 2509–2515, 2010.

[36] A. Tamion, E. Cadel, C. Bordel, and D. Blavette, "Three-dimensional atom probe investigation of Fe/Dy multilayers," *Scripta Materialia*, vol. 54, no. 4, pp. 671–675, 2006.

[37] E. Talbot, P. E. Berche, and D. Ledue, "Monte Carlo investigation of the magnetic anisotropy in Fe/Dy multilayers," *Journal of Magnetism and Magnetic Materials*, vol. 320, no. 21, pp. 2814–2822, 2008.

[38] R. F. Evans, W. J. Fan, P. Chureemart, T. A. Ostler, M. O. Ellis, and R. W. Chantrell, "Atomistic spin model simulations of magnetic nanomaterials," *Journal of Physics: Condensed Matter*, vol. 26, no. 10, p. 103202, 2014.

[39] A. Akbar, M. Saleem, S. Atiq, and M. S. Anwar, "Magnetic dynamics and all-optical switching in 5 nm Dy–Fe nanostructures," *IEEE Transactions on Magnetics*, vol. 54, no. 7, pp. 1–6, 2018.

[40] N. Ashcroft and N. Mermin, *Solid State Physics*. HRW International Editions, Holt, Rinehart and Winston, 1976.

[41] N. Spaldin, *Magnetic Materials: Fundamentals and Applications*. Cambridge University Press, 2010.

[42] B. Cullity and C. Graham, *Introduction to Magnetic Materials*. Wiley, 2011.

[43] J. Coey and J. Coey, *Magnetism and Magnetic Materials*. Knovel Library, Cambridge University Press, 2010.

[44] J. Stöhr and H. Siegmann, *Magnetism: From Fundamentals to Nanoscale Dynamics*. Springer Series in Solid-State Sciences, Springer Berlin Heidelberg, 2007.

[45] S. Blundell, *Magnetism in Condensed Matter*. Oxford Master Series in Condensed Matter Physics 4, OUP Oxford, 2001.

[46] W. Hiebert, G. Ballentine, and M. Freeman, "Comparison of experimental and numerical micromagnetic dynamics in coherent precessional switching and modal oscillations," *Physical Review B*, vol. 65, no. 14, p. 140404, 2002.

[47] S. Woodford, *Ultrafast Magnetization Dynamics*. Schriften des Forschungszentrums Jülich / Reihe Schlüsseltechnologien: Reihe Schlüsseltechnologien, Forschungszentrum, Zentralbibliothek, 2008.

[48] W. Rüemelin, "Numerical treatment of stochastic differential equations," *SIAM Journal on Numerical Analysis*, vol. 19, no. 3, pp. 604–613, 1982.

[49] J. O'Brien, "Time integration schemes," in *Advanced Physical Oceanographic Numerical Modelling*, pp. 155–163, Springer, 1986.

[50] L. Jiang and H.-L. Tsai, "Improved two-temperature model and its application in ultrashort laser heating of metal films," *Journal of Heat Transfer*, vol. 127, no. 10, pp. 1167–1173, 2005.

[51] I. Hughes and T. Hase, *Measurements and Their Uncertainties: A Practical Guide to Modern Error Analysis*. OUP Oxford, 2010.

[52] W. Cheng, X. Li, H. Wang, X. Cheng, and X. Miao, "Laser induced ultrafast magnetization reversal in TbCo film," *AIP Advances*, vol. 7, no. 5, p. 056018, 2017.

[53] S. Honda and M. Yoshiyama, "Magneto-optical Kerr rotation and sublattice magnetic moments in RE-Co sputtered films," *Japanese Journal of Applied Physics*, vol. 27, no. 9R, p. 1687, 1988.

[54] R. Medapalli, I. Razdolski, M. Savoini, A. Khorsand, A. Kirilyuk, A. Kimel, T. Rasing, A. Kalashnikova, A. Tsukamoto, and A. Itoh, "Efficiency of ultrafast laser-induced demagnetization in GdFeCo alloys," *Physical Review B*, vol. 86, no. 5, p. 054442, 2012.

[55] R. Chimata, L. Isaeva, K. Kádas, A. Bergman, B. Sanyal, J. H. Mentink, M. I. Katsnelson, T. Rasing, A. Kirilyuk, A. Kimel, *et al.*, "All-thermal switching of amorphous Gd-Fe alloys: Analysis of structural properties and magnetization dynamics," *Physical Review B*, vol. 92, no. 9, p. 094411, 2015.

[56] E. Talbot, D. Ledue, and P.-E. Berche, "Magnetization reversal in amorphous Fe/Dy multilayers: A Monte Carlo study," *Journal of Applied Physics*, vol. 106, no. 2, p. 023901, 2009.

[57] E. Beaurepaire, J.-C. Merle, A. Daunois, and J.-Y. Bigot, "Ultrafast spin dynamics in ferromagnetic nickel," *Physical Review Letters*, vol. 76, no. 22, p. 4250, 1996.

[58] N. Kazantseva, D. Hinzke, U. Nowak, R. W. Chantrell, U. Atxitia, and O. Chubykalo-Fesenko, "Towards multiscale modeling of magnetic materials: Simulations of FePt," *Physical Review B*, vol. 77, no. 18, p. 184428, 2008.

[59] S. K. Abbas, A. Akbar, S. Atiq, M. Saleem, M. Iftikhar, H. M. Rafiq, S. Naseem, and M. S. Anwar, "Optimization of dyfe nanostructures using e-beam lithography for magneto-optical applications," *Journal of Magnetism and Magnetic Materials*, vol. 469, pp. 196–202, 2019.

Chapter 4

Faraday Rotation and Ellipticity of the Single Photon

The first three chapters revolved around the interaction of magnetism and light where light is considered as wave—*classical* light. Though this notion was never spelled out explicitly yet the rationale for this assumption developed through Maxwell's equations which led us to the wave equation, together with the material properties, become the defining principle for phenomena that were observed.

The present chapter focuses on Faraday rotation for polarized *quantum* light. Though the magnitude of Faraday rotation for light remains the same for both classical and quantum light (conditioned to the same wavelength), yet the demonstration of Faraday rotation with quantum light throws light on the peculiar and non-intuitive picture painted in the quantum realm and necessitate the need to invoke quantum mechanics for a satisfactory explanation.

The theory of quantum mechanics owes itself to many distinct efforts by physicists spanned over the time of over century [1]. With the quantum body of knowledge, has the emerging fields of quantum optics, quantum information, quantum cryptography [2] and quantum computing [3, 4], to name a few.

The concept of polarization is generally understood as the confinement of the electric field vector of light in a certain plane which reinforces the wave picture

of light. However for single photons, often realized as particle or granular in nature, it is extremely difficult to imagine or comprehend the concept of polarized photon. Furthermore, Faraday rotation which is defined as the plane of polarization of rotation, one is driven to viewing light as a classical wave. But a single photon, quantum field does have polarization and it can be manipulated through Faraday rotation. This chapter aims to demonstrate this very facet.

To further our discussion, it is useful to differentiate between *classical* and *quantum* light. The definition of classical light stems from the Maxwell's equations and was discussed in detail in Chapter 1. Formally, the distinction between quantum light and classical light is based on different criteria. For example the distinction may be defined on the basis of the statistics of photons [5], writing states in Galuber-Sudarshan basis weighted by quasi-probability distribution functions [6] and the degree of second order coherence [7].

Generally, there are certain states which fulfills one of the above mentioned criteria and qualifies as quantum light. Fock states, squeezed light and single photons are all termed quantum whereas the light from thermal sources (blackbody, discharge lamps or laser) are deemed classical. In summary, quantum light shows sub-Poissonian statistics whereas classical light shows Poissonian or chaotic statistics [8]. Quantum light's signature is antibunched photons, whereas classical light exhibits bunching of photons [9]. Finally. for the quantum light, the second-order degree of coherence $g^2(0) < 1$ whereas it is ≥ 1 for classical light [10]. Therefore, non locality tests dubbed as Bell's tests are unequivocal proofs of non-classical signatures [11]. This is not a thesis on quantum optics, yet our work [12] shows that the light source used in these experiments has the full quantum signatures.

It is noteworthy that unlike classical optics experiments, visualized in the earlier chapters, the quantum light requires an altogether new approach and special tools for both the experimental and theoretical investigations. Keeping

this in mind, the current chapter is structured into three major parts. First part presents a brief overview of quantum mechanics which encompasses the introduction to state representation, operators and measurements aspect of quantum state.

The second part will lay down the theoretical background for characterization of polarization state of single photons, *i.e.*, quantum state tomography. In the third part, we demonstrate the generation of single photons through spontaneous parametric downconversion (SPDC) and subsequently their detection. Finally, we present the experimental results and analysis for extracting the variable of interest—the Faraday rotation angle θ.

4.1 Mathematical Preliminaries

This section is not meant to be an exhaustive review of the mathematical foundations of quantum mechanics, rather it is a collection of tools which will be required for understanding quantum state tomography which is the basis of our measurement scheme for the Faraday rotation of single photons.

4.1.1 Quantum State Vector, Qubits and the Density Matrix

In quantum mechanics, a physical system can sometimes be completely characterized by a state vector $|\psi\rangle$ defined in a complex vector space (Hilbert space) [13]. In general, any state vector can be expanded as a linear combination of basis vectors $\{|u_i\rangle\}$

$$|\psi\rangle = \sum_i a_i \, |u_i\rangle$$

where a_i's are complex amplitudes and can be evaluated by the inner product (signifies the overlap between two vectors) of the state vectors as $a_i = \langle u_i|\psi\rangle$ [14]. The inner product of a state vector with itself is always real and positive and the state vector is said to be normalized if

$$\langle\psi|\psi\rangle = 1.$$

The orthonormality condition for basis vectors is defined by

$$\langle u_m | u_n \rangle = \delta_{mn}, \tag{4.1}$$

where δ_{mn} is the Kronecker delta function. The superposition of states, (say $|\psi_1\rangle$ and $|\psi_2\rangle$) is also an admissible state of the same Hilbert space and can be expressed as [15]

$$|\psi\rangle = a\,|\psi_1\rangle + b\,|\psi_2\rangle\,. \tag{4.2}$$

Here a and b are the probability amplitudes but more physically meaningful quantities are $|a|^2$ and $|b|^2$ which present probabilities of finding the system in states $|\psi_1\rangle$ and $|\psi_2\rangle$, respectively. Furthermore, $|a|^2 + |b|^2 = 1$ which is simply interpreted as the sum of all probabilities must be equal to unity. The conjugate counterpart of the state $|\psi\rangle$ is represented by $\langle\psi|$ and is known as a dual vector, which lives in the dual space.

Note that the state vector $|\psi\rangle$ only describes a limited set of states, called pure states. Most states achieved or measured in real experiments are 'non-pure' or mixed. They are described by density matrices as we'll explain shortly. In our context, the polarization of a qubit is the relevant degree of freedom qualifying to define the quantum state.

With this brief partial introduction of state representation, we now like to introduce the reader to the concept of a qubit which will be employed frequently throughout this chapter.

4.1.2 Qubit

The idea of a bit surfaced in the previous chapter where we utilized the notion of magnetization to describe the 1 and 0 states of the magnetic system which form the basic unit of classical information. Similarly a quantum bit (qubit) is the basic unit for quantum information [16]. However, unlike the classical bit which could only assume one of the two possible states (0 or 1, written as $|0\rangle$ and $|1\rangle$ in state vector representation), a coherent superposition of states

($|0\rangle$ and $|1\rangle$) is also an admissible state for a qubit.

$$|\psi\rangle = \alpha\,|0\rangle + \beta\,|1\rangle\,. \tag{4.3}$$

A qubit is simply a two level quantum system and could be realized in many different physical systems. For example, the electron spin has two levels, conventionally called spin up and spin down, the polarization encoding of light with horizontal and vertical polarization or a 2-level artificial atom [16]. Table 4.1 illustrates few examples of qubits. Here we are interested in using the

Table 4.1: Few examples of qubit states realized in physical systems with characteristic properties which is being utilized for quantum information.

Physical system	Property	$\|0\rangle$	$\|1\rangle$
Photon	Polarization	$\|H\rangle$	$\|V\rangle$
	Fock states	vacuum	single photon
	Path after a beamsplitter	$\|$reflected$\rangle$	$\|$transmitted$\rangle$
Electron	Spin	$\|\uparrow\rangle$	$\|\downarrow\rangle$
Atomic nucleus	Spin	$\|\uparrow\rangle$	$\|\downarrow\rangle$
Superconducting charge qubit	Charge	$\|$absent$\rangle$	$\|$present$\rangle$

photon polarization for the description of qubit and therefore Eq. (4.3) can be relabeled as [17]

$$|\psi\rangle = \alpha\,|H\rangle + \beta\,|V\rangle\,, \tag{4.4}$$

where $|0\rangle$ and $|1\rangle$ basis representation is replaced by horizontal $|H\rangle$ and vertical $|V\rangle$ polarization states of photon, respectively. From a mathematical perspective, this is merely a relabeling. The basis states $\{|H\rangle\,, |V\rangle\}$ can be written in the matrix form as [17]

$$|\psi\rangle = \alpha \begin{pmatrix} 1 \\ 0 \end{pmatrix} + \beta \begin{pmatrix} 0 \\ 1 \end{pmatrix} = \begin{pmatrix} \alpha \\ \beta \end{pmatrix}. \tag{4.5}$$

The matrix representation of Eq. (4.5) seems similar to the Jones vector discussed earlier in Chapter 1, yet the elements of two matrices elicit an altogether different meaning. In case of the Jones vector, α and β contains the amplitude and phase information for horizontally and vertically polarized light [18] whereas, in the case of single photons, the relevant quantity is squared modulus of $|\alpha|^2$ or $|\beta|^2$, which determines the probability of finding the horizontal or vertical state as a result of some measurement which can sort out the photon into horizontal and vertical channels. In most labs, a polarizing beam splitter achieves this.

4.1.3 The Density Matrix

The alternative to the state vector representation is the density operator (or matrix) formalism. In order to understand the concept of the density matrix, we consider an example of an apparatus which randomly prepares a quantum system in particular states, say horizontally and vertically polarized photons. We also assumes that the apparatus is imperfect and it does not always produce the same state, *i.e.*, horizontal polarization $|H\rangle$ is produced with a probability q_1 and vertical polarization $|V\rangle$ with probability q_2. For this particular case where the system is a statistical mixture of two possible states and assuming that there are no interference effects, the density matrix can be written as

$$\rho = q_1 |H\rangle \langle H| + q_2 |V\rangle \langle V| = \begin{pmatrix} q_1 & 0 \\ 0 & q_2 \end{pmatrix}. \tag{4.6}$$

The above expression implies that the density matrix is a sum of the probabilistic weighting (called the convex sum) of pure states. This definition can further be generalized for two or more states leading to the mathematical form

$$\rho = \sum_i q_i |\phi_i\rangle \langle \phi_i| \tag{4.7}$$

where q_i's are the classical probabilities, $0 \leq q_i \leq 1$ for preparing the system in the normalized $|\phi_i\rangle$. Moreover, the sum of all probabilities must equal unity, *i.e.*, $\sum_i q_i = 1$. The density operator for a pure state is given by

$$\rho = |\psi\rangle \langle \psi|. \tag{4.8}$$

Furthermore, a legitimate density matrix must obey the following properties.

1. The density operator must be Hermitian *i.e.*, $\rho = \rho^{\dagger}$.

2. $Tr(\rho) = 1$ *i.e.*, the sum of all diagonal elements must equal unity.

3. For any state vector $|\psi\rangle$, ρ is a positive operator $\langle\psi|\rho|\psi\rangle \geq 0$.

The off diagonal terms of a density matrix ($\rho_{mn}, m \neq n$) are called coherences which originate from the interference effects among different states and diagonal terms are called populations. The distinction between a mixed and a pure state is made clearer by invoking the trace property of the density matrix. This leads to the definition that for a pure state $Tr(\rho^2) = 1$, whereas for a mixed state $Tr(\rho^2) < 1$.

These preliminaries acquaint the reader to the various representations of a quantum system. How the information of physical quantities can be extracted from these states and how these states will evolve with time or when they are subjected to various transformations, is now discussed.

4.1.4 Observables, Operators and Measurements

In quantum mechanics, any measurable physical quantity is represented by an observable [15]. For any observable A, there exists a mathematical object $\hat{A}$ which maps one state vector (say $|\psi\rangle$) into another state vector $|\phi\rangle$ which is described by $\hat{A}\,|\psi\rangle = |\phi\rangle$. For any state $|\psi\rangle$, if

$$\hat{A}\,|\psi\rangle = a\,|\psi\rangle$$

then $|\psi\rangle$ is said to be an eigenstate of $\hat{A}$ and a is known as the eigenvalue of $\hat{A}$ [14]. This mathematical object $\hat{A}$ is called an operator. An eigenvalue is the outcome of a measurement on a physical system, so for an observable, it must be real. Additionally, a linear operator $\hat{A}$ can also be represented by a matrix and the matrix elements A_{ij} for a given operator $\hat{A}$ in the basis state $\{|\psi_j\rangle\}$ are given by the expression [19]

$$A_{ij} = \langle\psi_i|\hat{A}|\psi_j\rangle\,. \tag{4.9}$$

An operator when transported to the dual space becomes a Hermitian adjoint:

$$\hat{A}\,|\psi\rangle \rightarrow \langle\psi|\,\hat{A}^{\dagger}. \tag{4.10}$$

For a state vector chosen to be its own dual vector, we can define the projection operator in the following way

$$\hat{\mathcal{P}} = |\psi\rangle\,\langle\psi|\,, \tag{4.11}$$

where $\hat{\mathcal{P}}$ obeys the property

$$\hat{\mathcal{P}}^2 = |\psi\rangle\,\underbrace{\langle\psi|\psi\rangle}_{1}\,\langle\psi| = |\psi\rangle\,\langle\psi| = \hat{\mathcal{P}}.$$

The action of the projection operator can be realized by placing a polarizer in the path of a beam of photons followed by detection or counting with a photodetector. Such measurement is classified as a projective measurement.

Suppose we have a single photon polarized at 45°, for which we write the quantum state as

$$|\psi\rangle = \frac{1}{\sqrt{2}}\big(\,|H\rangle + |V\rangle\,\big). \tag{4.12}$$

The action of a polarizer oriented parallel to the horizontal axis will collapse the superposition state. The act of projective measurement can be described mathematically as

$$\hat{\mathcal{P}_H}\,|\psi\rangle = |H\rangle\,\langle H|\psi\rangle = \frac{1}{\sqrt{2}}\big(\,|H\rangle\,\langle H|H\rangle + |H\rangle\,\langle H|V\rangle\,\big) = \frac{1}{\sqrt{2}}\,|H\rangle\,. \tag{4.13}$$

Now if we apply $\langle\psi|$ from left to obtain the expectation value, we obtain

$$\langle\psi|H\rangle\,\langle H|\psi\rangle = |\,\langle H|\psi\rangle\,|^2 = \frac{1}{2}. \tag{4.14}$$

Eq. (4.14) is narrated as the probability of finding the state $|H\rangle$ when $|\psi\rangle$ is being subjected to a horizontally oriented polarizer—the Born's probability rule [13]. In other words, a detection placed after the polarizer will click with a probability, on average, of one-half! A similar argument for the polarizer with transmission axis oriented along the vertical axis also holds. Prior to the measurement, the system was in state $|\psi\rangle$ and the act of measurement

collapsed the state to $|H\rangle$, a scheme known as the Von Neumann measurement postulate [14]. Now if the same measurement is repeated on the basis state $|H\rangle$, the probability of observing the state $|H\rangle$ will be

$$P_i' = |\langle H|H\rangle|^2 = 1.$$

We now would like to introduce the reader to another important class of operators, *i.e.*, unitary operators which become extremely important and useful while discussing operations on a qubit. Unitary operators are defined as [15]

$$\hat{U}\hat{U}^\dagger = \hat{U}^\dagger\hat{U} = \hat{I} \tag{4.15}$$

where $\hat{I}$ represents the identity operator and $\hat{U}^\dagger$ is the adjoint of the operator $\hat{U}$. Unitary operators are special kind of operators which preserve the norm of the state vector. Assume that $|\psi'\rangle$ is obtained by the action of unitary operator on state $|\psi\rangle$, then we can write

$$|\psi'\rangle = \hat{U}|\psi\rangle\,. \tag{4.16}$$

Taking the dual state, we have

$$\langle\psi'| = \langle\psi|\,\hat{U}^\dagger, \tag{4.17}$$

and therefore

$$\langle\psi'|\psi'\rangle = \langle\psi|\hat{U}^\dagger\hat{U}|\psi\rangle = \langle\psi|\psi\rangle\,, \tag{4.18}$$

showing that the norm for the states $|\psi\rangle$ and $\hat{U}|\psi\rangle$ remains unchanged by a unitary operation. For a polarization encoded photon qubit system, the unitary operations is realized by waveplates which rotate the polarization of the quantum state. Table 4.2 enlists the waveplates commonly used in an experiment setting [20].

So far we have surveyed the mathematical description of a quantum system for a single qubit. The following section extends the description of a quantum state for a two qubit system. We will revisit these operators when we discuss qubits being represented on the Bloch sphere.

Table 4.2: Operators for commonly used waveplates for manipulation of the polarization state of light. Waveplates perform a unitary operation.

Optical Element	Operator
Rotation of polarization through an angle θ	$\begin{pmatrix} \cos\theta & -\sin\theta \\ \sin\theta & \cos\theta \end{pmatrix}$
Quarter waveplate (fast axis at θ w.r.t horizontal)	$\begin{pmatrix} \cos\theta^2 + i\sin\theta^2 & (1-i)\sin 2\theta \\ (1-i)\sin\theta\cos\theta & \sin\theta^2 + i\cos\theta^2 \end{pmatrix}$

4.1.5 Composite Systems

We extend the discussion of single particles to two particles in terms of photon polarization states. In order to describe a two particle system, it is necessary to construct a Hilbert space $\mathcal{H}$ which is a composite of independent Hilbert spaces $\mathcal{H}_1$ and $\mathcal{H}_2$ of individual particles [21]. Let $|\phi_1\rangle \in \mathcal{H}_1$ and $|\phi_2\rangle \in \mathcal{H}_2$ be two state vectors, then a new vector $|\psi\rangle \in \mathcal{H}$ can be constructed by the tensor product and be represented as [22]

$$|\psi\rangle = |\phi_1\rangle \otimes |\phi_2\rangle = |\phi_1\phi_2\rangle \tag{4.19}$$

where $|\psi\rangle \in \mathcal{H}$. Furthermore, the dimension of the composite Hilbert space $\mathcal{H}$ would be the product of dimensions of the individual Hilbert spaces [16]. In case of photon polarization states, the two vectors are usually two beams of photons and the composite states may take the form $|HH\rangle$, $|HV\rangle$, $|VH\rangle$ or $|VV\rangle$ and the density matrix for such a system would be a 4×4 matrix. The state $|HV\rangle$ means that one photon is in state $|H\rangle$ whereas the second photon is in the state $|V\rangle$.

Similar to the single qubit case, the superposition principle also holds true for the two qubit system. It is the superposition of the two qubit system which in fact brings the bizarre nature of quantum world to the surface for the presence of correlation—*entanglement*, between different states of a superposition state is purely a quantum mechanical phenomenon which has no classical counterpart [16, 22]. States which cannot be expressed as a product state are

entangled states. For completeness, we only cite here the four famous Bell's entangled states as extent of this chapter would be insufficient to capture the entirety of the subject. For a two qubit system realized as two beam of photons generated through SPDC and considering their polarization degrees of freedom, Bell states are given by [16]

$$|\phi^+\rangle = \frac{1}{\sqrt{2}}\big(\,|HH\rangle + |VV\rangle\,\big), \tag{4.20}$$

$$|\phi^-\rangle = \frac{1}{\sqrt{2}}\big(\,|HH\rangle - |VV\rangle\,\big), \tag{4.21}$$

$$|\psi^+\rangle = \frac{1}{\sqrt{2}}\big(\,|HV\rangle + |VH\rangle\,\big), \tag{4.22}$$

$$|\psi^-\rangle = \frac{1}{\sqrt{2}}\big(\,|HV\rangle - |VH\rangle\,\big). \tag{4.23}$$

The density matrix for one of the Bell's state is given by [17]

$$\begin{aligned}\rho &= |\phi^+\rangle\,|\phi^+\rangle \\ &= \frac{1}{2}\big(\,|HH\rangle\,\langle HH| + |HH\rangle\,\langle VV| + |VV\rangle\,\langle HH| + |VV\rangle\,\langle VV|\,\big) \\ &= \frac{1}{2}\begin{pmatrix} 1 & 0 & 0 & 1 \\ 0 & 0 & 0 & 0 \\ 0 & 0 & 0 & 0 \\ 1 & 0 & 0 & 1 \end{pmatrix}.\end{aligned} \tag{4.24}$$

The entangled state $|\phi^+\rangle$ represents that the two photons are in a superposition state. Now if a measurement is performed and the first photon is found in state $|H\rangle$, it can be instantly known that the other photon is in state $|H\rangle$ as well. In other words, knowing the polarization state of one photon determines the state the other photon. This violates the classical world view of local realism [11] and has far reaching consequences, philosophically as well as technologically.

This concludes our discussion and brings us to the next section which gives a brief overview of the process for measuring the density matrix, known as quantum state tomography. As stated earlier, in the case of incomplete information about the quantum system (mixed state), we resolve to the density matrix formalism for the description of the state. The following discussion will

explore the working of the tomographic method for the construction of density matrix from unitary and projective measurements.

4.2 Quantum State Tomography

In order to experimentally determine the density matrix, we need to perform several measurement in different bases to completely characterize the polarization state of the photons. Furthermore, if a quantum state has a single copy, it is impossible to construct the density matrix with a single measurement. This in turns necessitates to perform the measurement in successive stages on many identical ensembles of the quantum state. Since there can never be an infinite supply of particles, so we can only make an informed guess of the quantum state. Different approaches are outlined by several authors for such an estimation [23–26].

Quantum state tomography is a method for the complete characterization of a quantum state of a particle or particles through successive measurements on many identical copies of the quantum system. Tomographic methods have been widely employed for measurements in diverse and complex quantum systems. One of the successful adaptation of the tomographic method is for qubit based on polarization entangled beams of single photons generated through SPDC.

The main focus of this section is to introduce the reader with the basics of tomographic method we employed in our work to characterize and consequently analyzed to extract the variable of interest—the Faraday rotation, as well as the ellipticity acquired by the single photon as it negotiates with the magneto-optic element.

In Chapter 2, we demonstrated the complete characterization of classical light with the Stokes polarimetry based on the Fourier decomposition of intensity measurements. However, for quantum light, we deal with the probabilities of a particular measurement—photon counts. In the next section, we will see how

these Stokes parameters emerge naturally while discussing the measurement perspective of tomography process.

4.2.1 Single Qubit in the Bloch Sphere Picture

In Chapter 2, we mapped different polarization states of classical light on a unit radius sphere known as the Poincare sphere. The polarization was also described by the Stokes parameters $\{I,\ M,\ C,\ S\}$. However, for a two level quantum system or qubit, the geometrical representation of quantum states as points on a unit sphere is traditionally given by the Bloch sphere which is isomorphic (totally equivalent to the Poincare picture).

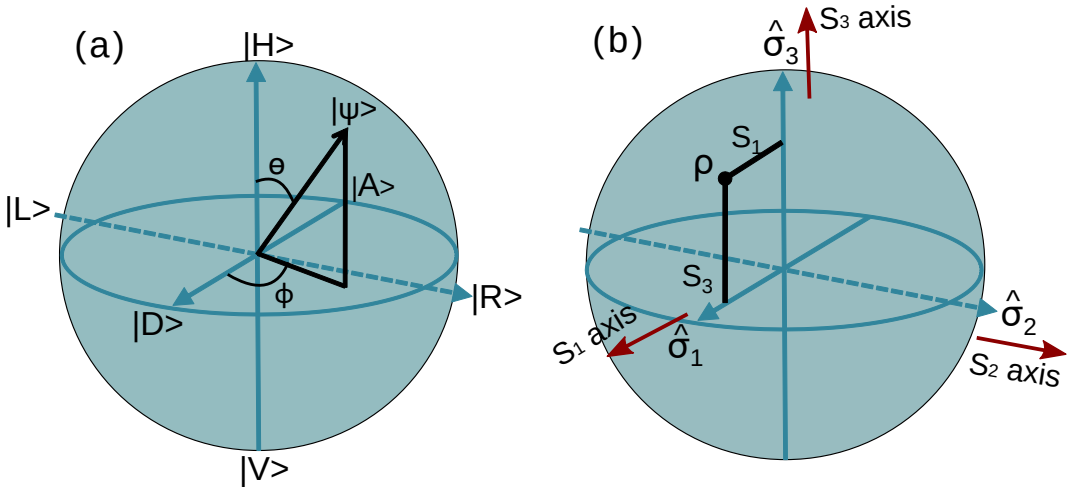

Figure 4.1: (a) Geometrical representation of an arbitrary state $|\psi\rangle$ on the Bloch sphere. (b) An arbitrary mixed state, represented by density matrix ρ can be located merely by projection along each axis of the Bloch sphere. The axes are relabeled as Pauli matrices.

Fig. 4.1 shows the representation of an arbitrary state $|\psi\rangle$ on the surface of Bloch sphere where $\{|H\rangle, |V\rangle\}$ basis states are assigned to the poles. This arbitrary pure quantum state $|\psi\rangle$ can be characterized by the angle θ, ϕ (suppressing the global phase factor) and is given by

$$|\psi\rangle = \cos\frac{\theta}{2}|H\rangle + e^{i\phi}\sin\frac{\theta}{2}|V\rangle\,. \tag{4.25}$$

These angles are defined in the Bloch sphere and later in the chapter will also be designated as θ_B and ϕ_B. The other two axes of the Bloch sphere are iden-

tified as $|D\rangle = 1/2\big(|H\rangle + |V\rangle\big)$ and $|R\rangle = 1/2\big(|H\rangle + i\,|V\rangle\big)$. The antipodal points on these axes represent their orthogonal counterpart polarization denoted by $|A\rangle$ and $|L\rangle$, respectively. It is important to mention here that the polarization states along each axis $|H\rangle, |D\rangle, |R\rangle$ are not mutually orthogonal yet they are represented by orthogonal axes only in the geometry of the Bloch sphere picture.

This particular visualization of the pure state is more intuitive and becomes useful when a unitary rotation is performed on a qubit. Another important set of unitary operators which become imperative while discussing the rotation of single qubit on the Bloch sphere is the set of Pauli matrices. Pauli matrices along with the identity matrix are defined as

$$\hat{\sigma}_\circ = \begin{pmatrix} 1 & 0 \\ 0 & 1 \end{pmatrix}, \quad \hat{\sigma}_1 = \begin{pmatrix} 0 & 1 \\ 1 & 0 \end{pmatrix}, \quad \hat{\sigma}_2 = \begin{pmatrix} 0 & -i \\ i & 0 \end{pmatrix}, \quad \hat{\sigma}_3 = \begin{pmatrix} 1 & 0 \\ 0 & -1 \end{pmatrix}. \tag{4.26}$$

In the canonical basis $\{|H\rangle, |V\rangle\}$, it can be readily seen that Pauli matrices take the form

$$\hat{\sigma}_\circ = |H\rangle\langle H| + |V\rangle\langle V|, \tag{4.27}$$

$$\hat{\sigma}_1 = |D\rangle\langle D| - |A\rangle\langle A|, \tag{4.28}$$

$$\hat{\sigma}_2 = |R\rangle\langle R| - |L\rangle\langle L|, \tag{4.29}$$

$$\hat{\sigma}_3 = |H\rangle\langle H| - |V\rangle\langle V|. \tag{4.30}$$

Note that in each of the latter three equations, we have the difference of two projection operators, *e.g.*, $\hat{\sigma_1} = \hat{\mathcal{P}}_D - \hat{\mathcal{P}}_A$ *etc.* Therefore each Pauli operator is called a polarization operator, showing whether a state is pointing in one direction or its antipodally opposite direction. We will also use $\hat{\sigma}_1 = \hat{\sigma}_x$, $\hat{\sigma}_2 = \hat{\sigma}_y$ and $\hat{\sigma}_3 = \hat{\sigma}_z$.

4.2.2 Rotation on the Bloch Sphere

Pauli operators are useful in another way too. Unitary rotations are generated by taking the exponential of Pauli matrices. A rotation about the $\hat{\sigma}_i$ axis on the Bloch sphere through an angle θ is defined as

$$e^{i\theta\frac{\hat{\sigma}_i}{2}} = \cos\frac{\theta}{2}\hat{\sigma}_\circ + i\sin\frac{\theta}{2}\hat{\sigma}_i \tag{4.31}$$

For instance, the rotation about y and z-axis can be written in matrix form as

$$R_y(\theta) = e^{-i\theta\frac{\hat{\sigma_y}}{2}} = \cos\frac{\theta}{2}\hat{\sigma}_\circ - i\sin\frac{\theta}{2}\hat{\sigma}_y = \begin{pmatrix} \cos\frac{\theta}{2} & -\sin\frac{\theta}{2} \\ \sin\frac{\theta}{2} & \cos\frac{\theta}{2} \end{pmatrix}, \tag{4.32}$$

whereas

$$R_z(\theta) = e^{-i\theta\frac{\hat{\sigma_z}}{2}} = \cos\frac{\theta}{2}\hat{\sigma}_\circ - i\sin\frac{\theta}{2}\hat{\sigma}_z = \begin{pmatrix} e^{-i\frac{\theta}{2}} & 0 \\ 0 & e^{i\frac{\theta}{2}} \end{pmatrix} = e^{-i\frac{\theta}{2}}\begin{pmatrix} 1 & 0 \\ 0 & e^{i\theta} \end{pmatrix}. \tag{4.33}$$

It is noticeable that Eq. (4.32) is similar to the expression (though not exactly equal) for an arbitrary rotation defined earlier in Table 4.2. The rotation in Table 4.2 has an argument θ whereas in the Bloch sphere description, a rotation through θ about the y-axis yields an angle $\theta/2$ in the matrix. Therefore a physical rotation through θ is equal to a rotation through 2θ about the y-axis in the Bloch sphere picture.

Furthermore, the HWP and QWP also perform unitary operations If the angle of the HWP or QWP is θ in the lab frame, the HWP or QWP performs rotation about the axis which is aligned at 2θ with the north pole of the Bloch sphere. For HWP, the amount of rotation is π and for QWP the amount of rotation is $\pi/2$. For completeness, the expressions for quarter and half waveplates can also be rewritten in terms of Pauli matrices as

$$\hat{U}_{HWP} = \exp\Big(- i\pi\big(\frac{\hat{\sigma}_z}{2}\cos 2\theta + \frac{\hat{\sigma}_x}{2}\sin 2\theta\big)\Big), \quad \text{and} \tag{4.34}$$

$$\hat{U}_{QWP} = \exp\Big(- i\frac{\pi}{2}\big(\frac{\hat{\sigma}_z}{2}\cos 2\theta + \frac{\hat{\sigma}_x}{2}\sin 2\theta\big)\Big). \tag{4.35}$$

4.2.3 Towards Tomography

For a single qubit arbitrary mixed state, the expression for the density matrix is given by Eq. (4.7) and in general has the following form

$$\rho = \begin{pmatrix} a & b+ic \\ b-ic & 1-a \end{pmatrix}, \tag{4.36}$$

where a, b and c are real and non-negative numbers. The Pauli matrices alongwith the identity matrix, span the space for 2×2 Hermitian operators.

Table 4.3: Correspondence between definitions of Stokes parameters from Ch. 2 and 4.

Notation from Ch. 2	Notation from Ch.4
I	$S_\circ$
M	S_3
C	S_1
S	S_2

Hence, any density matrix for a single qubit can also be decomposed into the linear combination of Pauli matrices and Eq. (4.36) can be rewritten as

$$\rho = \frac{1}{2}\sum_{i=0}^{3} S_i\sigma_i, \tag{4.37}$$

where the coefficients S_i are given by

$$S_i = Tr(\sigma_i\rho). \tag{4.38}$$

We have previously learned that for a pure state $Tr(\rho^2) = Tr(\rho) = 1$. Using the definition of density matrix in (4.37), it can be readily seen that

$$Tr(\rho^2) = \frac{1}{2}\left(1 + S_1^2 + S_2^2 + S_3^2\right) \tag{4.39}$$

where $S_0 = 1$ due to normalization. By invoking the trace property for a legitimate density operator, it can be clearly seen that $S_1^2 + S_2^2 + S_3^2 = 1$ for a pure state whereas, for a mixed state $S_1^2 + S_2^2 + S_3^2 < 1$. Note that definitions similar to these, *i.e.*, $\sum_{i=1}^{3} S_i^2 \leq 1$ have been previously used in Chapter 2 while discussing the Stokes parameters. Indeed the coefficients S_i's are the Stokes parameters. Furthermore, $S_1^2 + S_2^2 + S_3^2 = 0$ refers the center of sphere which represents the maximally entangled state.

This chapter uses an alternate description of Stokes parameters $\{S_0, S_1, S_2, S_3\}$ instead of $\{I, M, C, S\}$, introduced in Chapter 1, since we like to conform to the quantum picture traditionally used in the form of the Bloch sphere. The correspondence is highlighted in Table 4.3.

Fig. 4.1(b) represents the Bloch sphere where each axis is relabeled in terms of Pauli matrices or the "Stokes axes". Density matrices can also be mapped to the Bloch sphere. A point represented by ρ for example, lies in the $\hat{\sigma}_1$-$\hat{\sigma}_3$ plane inside the Bloch sphere. The projection along axes σ_1 and σ_3 will result in the respective Stokes parameters S_1 and S_3. For this particular choice of state, $S_2 = 0$.

In Chapter 2, the Stokes parameters are related with the measurement of intensity of *classical* light whereas for *quantum* light or in the case of single photons, intensities are replaced by the photon-counts. Here we need a reconciliation of previous definitions for Stokes parameters $\{I,\, M,\, C,\, S\}$ with the new definitions $\{S_0, S_1, S_2, S_3\}$ and this can be summarized as

$$\begin{aligned} & S_0 = P_{|H\rangle} + P_{|V\rangle} \qquad I = \left\langle E_x^2 \right\rangle + \left\langle E_y^2 \right\rangle, \\ & S_1 = P_{|D\rangle} - P_{|A\rangle} \qquad C = \left\langle E_d^2 \right\rangle - \left\langle E_a^2 \right\rangle, \\ & S_2 = P_{|R\rangle} - P_{|L\rangle} \qquad S = \left\langle E_r^2 \right\rangle - \left\langle E_l^2 \right\rangle \\ \text{and} \quad & S_3 = P_{|H\rangle} - P_{|V\rangle} \qquad M = \left\langle E_x^2 \right\rangle - \left\langle E_y^2 \right\rangle. \end{aligned} \tag{4.40}$$

Here $P_{|\psi\rangle}$ represents the probability of measuring the photon in the polarization state $|\psi\rangle$ and can be evaluated as

$$P_{|\psi\rangle} = \langle\psi|\rho|\psi\rangle = Tr(|\psi\rangle\langle\psi|\,\rho) = Tr(\hat{\mathcal{P}}_{|\psi\rangle}\rho). \tag{4.41}$$

Furthermore, the expression for the Stokes parameters given by Eq. (4.38) can also be restated using equations (4.30) and (4.41)

$$S_1 = Tr(\rho\sigma_1) = Tr\big(\rho\,|D\rangle\langle D| - |A\rangle\langle A|\,\big) = P_{|D\rangle} - P_{|A\rangle} \tag{4.42}$$

$$S_2 = Tr(\rho\sigma_2) = Tr\big(\rho\,|R\rangle\langle R| - |L\rangle\langle L|\,\big) = P_{|R\rangle} - P_{|L\rangle} \tag{4.43}$$

$$S_3 = Tr(\rho\sigma_1) = Tr\big(\rho\,|H\rangle\langle H| - |V\rangle\langle V|\,\big) = P_{|H\rangle} - P_{|V\rangle}. \tag{4.44}$$

The expressions above demonstrate the correlation between the Stokes parameters and density matrix elements. Hence, quantum state tomography is in fact the measurement of the Stokes parameters which enables us to reconstruct the density matrix.

The next section will discuss the process of determination of density matrix. We set up the discussion with the simple case of single qubit and assume the measurement process exhibit no errors and has perfect experimental conditions.

4.2.4 Single Qubit Tomography

The current Section is built upon the pioneering work of Kwiat *et.al* [27]. The description of quantum state tomography described here also runs parallel to the upcoming work soon to be published by our research group [12]. Quantum state tomography is in fact the measurement of the Stokes parameters (S_1, S_2, S_3). Prior to measurement, we have no knowledge of the quantum state, yet it can be said with certainty that the any single qubit state represents a point on the Bloch sphere and must lie somewhere on or inside the sphere. The act of measurement of Stokes parameters is precisely to locate the point where it is located on the Bloch sphere.

Figure 4.1(a) presents an unknown state inside the Bloch sphere. Similar to the projection of a point on a sphere along three spherical coordinates (r, θ, ϕ), a set of three independent measurement isolate a single quantum state in the Bloch sphere. The first projection measurement along $\{|H\rangle, |V\rangle\}$ basis will isolate the state in a plane. Further measurements along $\{|D\rangle, |A\rangle\}$ and $\{|R\rangle, |L\rangle\}$ basis will restrict the unknown state to a line and then to a point, respectively.

It is obvious from Eqns. (4.42)–(4.44) that we need six probabilities $P_{|H\rangle}$, $P_{|V\rangle}$, $P_{|D\rangle}$, $P_{|A\rangle}$, $P_{|R\rangle}$ and $P_{|L\rangle}$ in order to determine the Stokes parameters. These probabilities are experimentally determined by projecting a state onto a beam splitter (2-detector scheme) in respective basis $\{|H\rangle, |V\rangle\}$, $\{|D\rangle, |A\rangle\}$ and $\{|R\rangle, |L\rangle\}$. The outcome of these measurements are utilized to determine the Stokes parameters and consequentially, the estimation of density matrix.

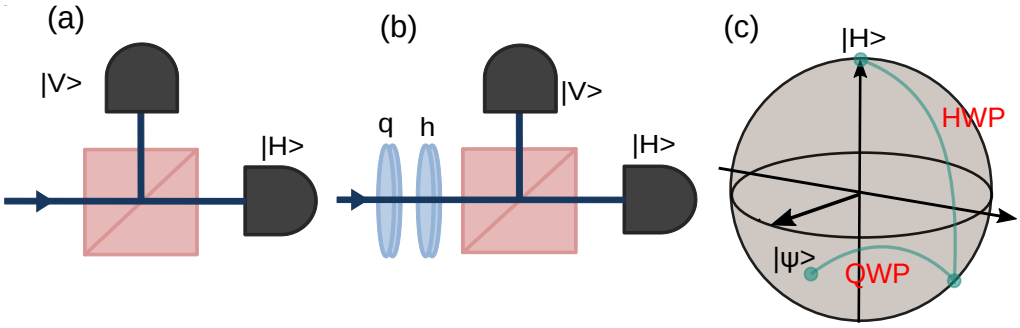

Figure 4.2: The projective measurement is performed along (a) $\{|H,|V\rangle\rangle\}$. (b) Measurement along $\{|R,|L\rangle\rangle\}$ and $\{|D,|A\rangle\rangle\}$ basis are realized by transforming the state into $\{|H,|V\rangle\rangle\}$ basis using different setting (q, h) of quarter- and half wave-plates whereas (c) depicts the action of QWP and HWP on an arbitrary state in the Bloch sphere.

The projection of state on the canonical basis $\{|H\rangle, |V\rangle\}$ is straightforward by placing a polarizing beam splitter (HV polarizer) in the path of light. A polarizing beam splitter either reflects ($|V\rangle$) or transmits photons ($|H\rangle$) depending upon the polarization state of the incoming light.

However the projections along the bases $\{|D\rangle, |A\rangle\}$ and $\{|R\rangle, |L\rangle\}$ need a somewhat different strategy as it's extremely difficult to manufacture a PBS which splits light into respective set of orthogonal states $\{|D\rangle, |A\rangle\}$ and $\{|R\rangle, |L\rangle\}$.

The workaround this problem is to rotate the incoming state by unitary operation. These unitary operations can be performed by waveplates (QWP, HWP) with suitable orientations which will project the states $|D\rangle \rightarrow |H\rangle$, $|A\rangle \rightarrow |V\rangle$, $|R\rangle \rightarrow |H\rangle$ and $|L\rangle \rightarrow |V\rangle$. See Fig. 4.2(b) which shows the placement of QWP and HWP with orientation angles q and h. For analysis along $\{|D\rangle, |A\rangle\}$, we require $q = 45°$, $h = 22.5°$ whereas for $\{|R\rangle, |L\rangle\}$ basis, the setting is $q = 45°$, $h = 0$. This concludes our discussion on single qubit tomography. The next Section will extend the single qubit description to two qubit tomography.

4.2.5 Two Qubit Tomography

It is generally straightforward to extend the idea of single qubit tomography to two qubit or multiple qubit tomography. In the context of our experimental needs, we'll restrict our discussion only to the two qubit tomography. A two qubit system can be realized in terms of photon pairs generated through spontaneous parametric downconversion (SPDC, we will discuss this shortly). The two photon system lives in a four dimensional space and the state vector representation for a pure state is given by

$$|\psi\rangle = a_1 |HH\rangle + a_2 |HV\rangle + a_3 |VH\rangle + a_4 |VV\rangle = \begin{pmatrix} a_1 \\ a_2 \\ a_3 \\ a_4 \end{pmatrix} \tag{4.45}$$

with a_i being a complex number and $\sum_i |a_i|^2 = 1$. However in case of a mixed state, the density matrix has the following general form for two qubit system

$$\rho = \begin{pmatrix} A_1 & B_1 e^{i\phi_1} & B_2 e^{i\phi_2} & B_3 e^{i\phi_3} \\ B_1 e^{-i\phi_1} & A_2 & B_4 e^{i\phi_4} & B_5 e^{i\phi_5} \\ B_2 e^{-i\phi_2} & B_4 e^{-i\phi_4} & A_3 & B_6 e^{i\phi_6} \\ B_3 e^{-i\phi_3} & B_5 e^{-i\phi_5} & B_6 e^{-i\phi_6} & A_4 \end{pmatrix}, \tag{4.46}$$

where ρ follows the characteristics of a legitimate density matrix. Here we have 16 unknown parameters $(A_1, \cdots, A_4, B_1, \cdots, B_6, \phi_1, \cdots, \phi_6)$ however with unit trace property, *i.e.*, $A_1 + A_2 + A_3 + A_4 = 1$, we are left with 15 parameters to be determined for complete characterization of the state. Moreover, the relationship between the Stokes parameters and density matrix, analogous to Eq. (4.37), in case of two qubit will take the form

$$\rho = \frac{1}{4} \sum_{i,j=0}^{3} S_{ij} \sigma_i \otimes \sigma_j, \tag{4.47}$$

where the S_{ij} coefficients are given by the tensor product of single qubit Stokes parameters and

$$S_{ij} = S_i \otimes S_j = (P_{|\psi_i\rangle} \pm P_{|\psi_{i\perp}\rangle}) \otimes (P_{|\psi_j\rangle} \pm P_{|\psi_{j\perp}\rangle}). \tag{4.48}$$

Here $P_{|\psi_i\rangle}$ denote the probability for projecting the single qubit state along different basis. For normalization, $S_{00} = 1$ and hence we need $16 - 1 = 15$ real

parameters are needed for locating the point in the two qubit, four dimensional space. The tensor product notation in the expression (4.48) can be further spelled out

$$
\begin{aligned}
S_{00} &= (P_{|H\rangle} + P_{|V\rangle}) \otimes (P_{|H\rangle} + P_{|V\rangle}) = P_{|HH\rangle} + P_{|HV\rangle} + P_{|VH\rangle} + P_{|VV\rangle} \\
S_{01} &= (P_{|H\rangle} + P_{|V\rangle}) \otimes (P_{|D\rangle} - P_{|A\rangle}) = P_{|HD\rangle} - P_{|HA\rangle} + P_{|VD\rangle} - P_{|VA\rangle} \\
S_{02} &= (P_{|H\rangle} + P_{|V\rangle}) \otimes (P_{|R\rangle} - P_{|L\rangle}) = P_{|HR\rangle} - P_{|HL\rangle} + P_{|VR\rangle} + P_{|VL\rangle} \\
S_{03} &= (P_{|H\rangle} + P_{|V\rangle}) \otimes (P_{|H\rangle} - P_{|V\rangle}) = P_{|HH\rangle} - P_{|HV\rangle} + P_{|VH\rangle} - P_{|VV\rangle} \\
S_{10} &= (P_{|D\rangle} - P_{|A\rangle}) \otimes (P_{|H\rangle} + P_{|V\rangle}) = P_{|DH\rangle} + P_{|DV\rangle} - P_{|AH\rangle} - P_{|AV\rangle} \\
S_{11} &= (P_{|D\rangle} - P_{|A\rangle}) \otimes (P_{|D\rangle} - P_{|A\rangle}) = P_{|DD\rangle} - P_{|DA\rangle} - P_{|AD\rangle} + P_{|AA\rangle} \\
S_{12} &= (P_{|D\rangle} - P_{|A\rangle}) \otimes (P_{|R\rangle} - P_{|L\rangle}) = P_{|DR\rangle} - P_{|DL\rangle} - P_{|AR\rangle} + P_{|AL\rangle} \\
S_{13} &= (P_{|D\rangle} - P_{|A\rangle}) \otimes (P_{|H\rangle} - P_{|V\rangle}) = P_{|DH\rangle} - P_{|DV\rangle} - P_{|AH\rangle} + P_{|AV\rangle} \\
S_{20} &= (P_{|R\rangle} - P_{|L\rangle}) \otimes (P_{|H\rangle} + P_{|V\rangle}) = P_{|RH\rangle} + P_{|RV\rangle} - P_{|LH\rangle} - P_{|LV\rangle} \\
S_{21} &= (P_{|R\rangle} - P_{|L\rangle}) \otimes (P_{|D\rangle} - P_{|A\rangle}) = P_{|RD\rangle} - P_{|RA\rangle} - P_{|LD\rangle} + P_{|LA\rangle} \\
S_{22} &= (P_{|R\rangle} - P_{|L\rangle}) \otimes (P_{|R\rangle} - P_{|L\rangle}) = P_{|RR\rangle} - P_{|RL\rangle} - P_{|LR\rangle} + P_{|LL\rangle} \\
S_{23} &= (P_{|R\rangle} - P_{|L\rangle}) \otimes (P_{|H\rangle} - P_{|V\rangle}) = P_{|RH\rangle} - P_{|RV\rangle} - P_{|LH\rangle} + P_{|LV\rangle} \\
S_{30} &= (P_{|H\rangle} - P_{|V\rangle}) \otimes (P_{|H\rangle} + P_{|V\rangle}) = P_{|HH\rangle} + P_{|HV\rangle} - P_{|VH\rangle} - P_{|VV\rangle} \\
S_{31} &= (P_{|H\rangle} - P_{|V\rangle}) \otimes (P_{|d\rangle} - P_{|a\rangle}) = P_{|HD\rangle} - P_{|HA\rangle} - P_{|VD\rangle} + P_{|VA\rangle} \\
S_{32} &= (P_{|H\rangle} - P_{|V\rangle}) \otimes (P_{|R\rangle} - P_{|L\rangle}) = P_{|HR\rangle} - P_{|HL\rangle} - P_{|VR\rangle} + P_{|VL\rangle} \\
S_{33} &= (P_{|H\rangle} - P_{|V\rangle}) \otimes (P_{|H\rangle} - P_{|V\rangle}) = P_{|HH\rangle} - P_{|HV\rangle} - P_{|VH\rangle} + P_{|VV\rangle}. \quad (4.49)
\end{aligned}
$$

In this notation, $P_{|HR\rangle}$ determines the joint probability of first photon in $|H\rangle$ basis and second photon in the $|R\rangle$ basis. This is true for all other definitions in the above expression.

In order to construct the density matrix, we need to measure 16 Stokes parameters. For four detector scheme where two detectors are reserved for each qubit, we can use three settings corresponding to the projections along the three bases $\{|H\rangle,|V\rangle\}$, $\{|D\rangle,|A\rangle\}$ and $\{|R\rangle, |L\rangle\}$. This implies that there are total $3 \times 3 = 9$ settings and in each setting, we measure four ($2^2 = 4$) probabilities at the output channels $|HH\rangle$, $|HV\rangle$, $|VH\rangle$ and $|VV\rangle$. Hence $9 \times 4 = 36$

measurements will suffice to construct the density matrix. This means that we have more measurements, precisely 36, than unknown parameters which account to 15. It is obvious that we have an over-determined system.

Conventionally, the estimated density matrix can be used as a measure of purity of a state, or the degree of mixedness and also utilized to quantify the magnitude of entanglement [27]. In our case, we will use the estimated density matrix to quantify the magnitude of the Faraday rotation θ.

This concludes our discussion on quantum state tomography where we have assumed exact measurements, *i.e.*, no errors associated and perfect experimental conditions. However, it goes without saying that no experimental investigation is imperceptible to the errors which needed to be accounted for while analyzing the outcome of a particular experiment. The next section will discuss briefly about the types of errors which could lead to non-physical outcome while performing the quantum state tomography.

4.2.6 Errors and Compensation

The estimated density matrix from the tomographic measurement must be semi-definite positive, Hermitian and has unit trace [26]. However, in a physically realizable system, as an outcome to a measurement it is not necessary that these conditions are met.

The errors propagating in the density matrix are categorized into three types: errors in the measurement basis, errors originating from the counting statistics and errors due to lack of experimental stability [27]. The first and third type of errors are systematic in nature which could be minimized by using accurate apparatus and by modifying detection scheme ($2n$ detector), respectively. A more detailed discussion about the use of $2n$ detector scheme can be found here [27]. Meanwhile, the second type of errors can be reduced by taking measurements (detection of photo-counts) for a longer period of time.

Moreover, there are additional errors which need to be compensated. For example, accidental coincidence counts due to background light. Dark counts which are present even in the absence of light. These errors can be compensated by subtraction from the total measured counts. With all these errors been compensated, it is still possible that the estimated density matrix is not legit. This leads us to our next topic of discussion—maximum likelihood estimation.

4.2.7 Maximum Likelihood Estimation

The current section closely follows the description of maximum likelihood estimation made by Kwiat *et.al* [27]. Maximum likelihood estimation is an effective technique which accommodates for imperfect measurements. The problem of illegal density matrix is resolved by searching for the density matrix which most likely has returned the experimentally measured coincidence counts. In practice, the analytical calculations for this maximally likely state is non-trivial and requires a numerical search. Three elements required for MLE are the parameterization of density matrix, a likelihood function which could be maximized and a numerical method which searches for the maximum over the space of density matrix's parameters. Any matrix written in the form $T^\dagger T$ fulfills the criteria for a legitimate density matrix, *i.e.*, the inner product of $\langle\psi|T^\dagger T|\psi\rangle \geq 0$ is positive, $T^\dagger T$ is Hermitian and for normalization, we can divide by the trace. Thus a physically realizable density matrix is parameterized and is given by

$$\rho = \frac{T^\dagger T}{Tr\big(T^\dagger T\big)} \tag{4.50}$$

where T defined for a two qubit system has the following form

$$T = \begin{pmatrix} t_1 & 0 & 0 & 0 \\ t_5 + it_6 & t_2 & 0 & 0 \\ t_7 + it_8 & t_9 + it_1 0 & t_3 & 0 \\ t_1 1 + it_1 2 & t_1 3 + it_1 4 & t_1 5 + it_1 6 & t_4 \end{pmatrix}. \tag{4.51}$$

For a four detector scheme, total number of measurements for complete characterization account to 36 coincidences counts whose expectation values are given by $\bar{n_i} = N\langle\psi_i|\rho_p|\psi_i\rangle$ (for $i = 1, 2, \cdots, 36$) and N is a normalization

factor equal to the size of ensemble per measurement. Now, if we assume the a Gaussian distribution for the coincidences counts, the problem is reduced to finding the minimum of the log likelihood function [27]

$$\mathcal{L} = \sum_{i=1}^{36} \frac{\left[N \langle\psi_i|\rho|\psi_i\rangle - n_i\right]^2}{2N \langle\psi_i|\rho|\psi_i\rangle} \tag{4.52}$$

where n_i represents the result of i'th measurement, N is for normalization. The final piece in the puzzle is to define an optimization routine. The maximum likelihood estimation technique for a two qubit photon system is implemented by Kwiat *et.al* [27] which utilizes non linear least square quadratic function implemented in Matlab (*lsqnonlin*). In our experiments, we have explicitly utilized the online interface developed by Kwiat[1] for estimation of density matrices. The preceding discussion completes the theoretical background imperative to our experimental investigation. The next section will lay down the details of our experimental investigation.

4.3 Experimental Details

The current Section will present brief details of our experiments which aim at finding the Faraday rotation and ellipticity of a single photon. The following section will discuss and analyze results. The source of single photons is a non linear crystal which generates two non-collinear beam of single photons (named as signal and idler). One of the photon beam (idler) is allowed to pass through an isotropic medium (TGG crystal) which acts as our Faraday rotator, placed between the poles of an electromagnet. As the magnetic field is turned on, medium becomes birefringent and manifests as the change in polarization state of idler beam—the famous Faraday rotation.

Meanwhile the other photon beam (signal) passes through optical elements and registers a detection at the respective detector. If both photons register a detection at their respective detectors simultaneously within a specific time window, a coincidence count is observed. Hence the registration of one idler

[1] http://tomography.web.engr.illinois.edu/TomographyDemo.php

photon coincident with the signal photon is the fiducial signature of a single photon. This scheme of generating single photons is dubbed as heralded [28].

The workflow of our subsequent analysis is simple. These counts are in fact probabilities of observing this composite system in certain state as mentioned earlier. For example, these are the terms ($P_{|HV\rangle}$, $P_{|DA\rangle}$) etc. in Eq. (4.49). We further use these counts (probabilities) to extract the Stokes parameters according to equation (4.48). Finally the density matrix is estimated from the Stokes parameters given by Eq. (4.47) in conjunction with maximum likelihood technique (4.52) which ensures the legitimacy of the received density matrix.

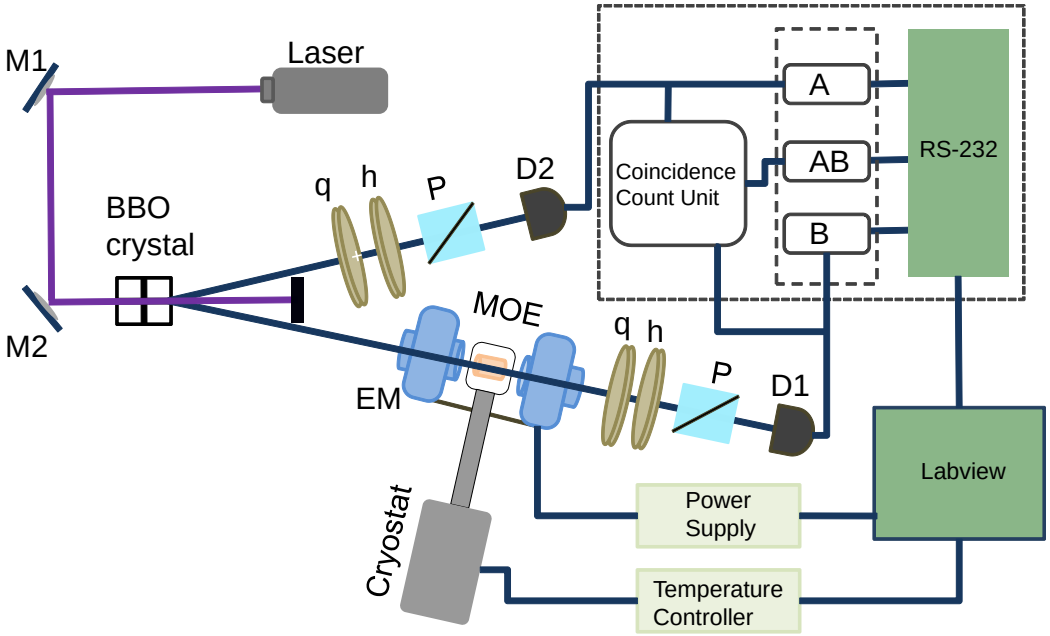

Figure 4.3: The schematic illustration of the experiment involving spontaneous parametric down conversion (SPDC) in BBO crystal, optical elements, single photon count detectors, coincidence counting unit, cryostat and temperature controller interfaced with the computer in Labview environment. Here **q**= quarter waveplates, **h**= half waveplate, **P**= polarizer, **EM**= electromagnet, **MOE**= magneto-optic element and $\mathbf{D_i}$= avalanche photodetectors.

As stated earlier in Chapter 1, Faraday rotations are usually minuscule and can be measured with phase sensitive detection in conjunction with lowering

the temperature of birefringent medium. We will make use of both of these methods in our experimental investigation.

4.3.1 Experimental Methods

Figure 4.3 gives a comprehensive view of the equipment involved in the experiment. We divide the experimental setup into two major aspects: optical setup and mechanical setup for achieving cryogenic temperatures which is already described in Chapter 2 in detail. Prior to the discussion of the details of optical setup, we would like to present the phenomenological description of spontaneous parametric downconversion process which is of paramount importance in experiments related to quantum light as being the element generating single photons from a pump laser beam.

4.3.2 Spontaneous Parametric Down Conversion

Spontaneous parametric downconversion, schematically illustrated in Fig. 4.4, is a non linear optical process where a high energy photon of frequency ω_p annihilates, creating two low energy photons (signal) ω_s and (idler) ω_i under the laws of conservation of energy $\omega_p = \omega_s + \omega_i$ and momentum $\mathbf{k}_p = \mathbf{k}_s + \mathbf{k}_i$ [29]. The process is said to be spontaneous as there is no signal or idler field to stimulate the process [29]. Furthermore, SPDC is parametric in nature as it depends on electric fields rather than the light intensities. This also implies that there exists a phase relationship between input and output beams. Downconversion is referred to the fact that output beams have lower frequency than the incident beam.

The direction of propagation of signal and idler beams depends upon many key factor such as their respective frequencies, conservation laws and most importantly the angle between the crystal optic axis and direction of pump beam, known as the phase matching angle θ_m [30].

The phenomenon of SPDC is categorized into type-I and type-II, based on the polarization state of the signal and idler beams. If both the outgoing

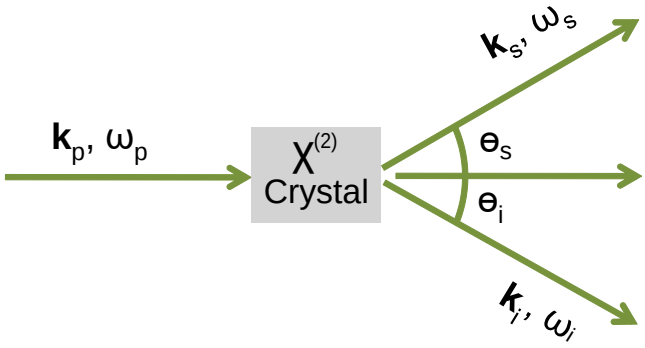

Figure 4.4: An illustration of spontaneous parametric downconversion of light where $\hbar$ times the $(\mathbf{k_j}, \omega_j)$ denotes the momentum and energy of the incoming and outgoing light whereas θ_j signifies angle between the pump beam and outgoing photon beam. The subscripts p, s and i are attributed to the pump, signal and idler and $\chi^{(2)}$ presents the non-linear electric susceptibility.

photons are produced with linear parallel polarization but perpendicular to the incident pump beam, the process is deemed as type-I, whereas in type-II downconversion, the outgoing photon beams are orthogonal to each other [31]. The definition could be restated in terms of ordinary and extraordinary polarization of signal and idler. In type-I downconversion, both the photons are ordinarily polarized whereas in Type-II, one photon is polarized extraordinarily while other is ordinary[2].

In type-I SPDC, signal and idler are ordinarily polarized. This means that they are polarization correlated but they do not exhibit any entanglement. For the generation of entangled photons, two type-I crystals can be utilized placed back to back [29].

In our case, we used two stacked β-Barium Borate (BBO, BaB_2O_4) crystals mounted in a kinematic mount such that the optic axis of one of the crystal is orthogonal relative to the other. This particular arrangement of crystal allows for the conversion of both horizontally and vertically polarized photons. The BBO crystal are cut for type-I parametric down conversion to produce photon pairs of parallel polarization but perpendicular to the pump beam polarization.

[2]Light rays polarized along the optic axis of uniaxial crystal is termed extraordinary ray and perpendicular to the optic axis as ordinary ray

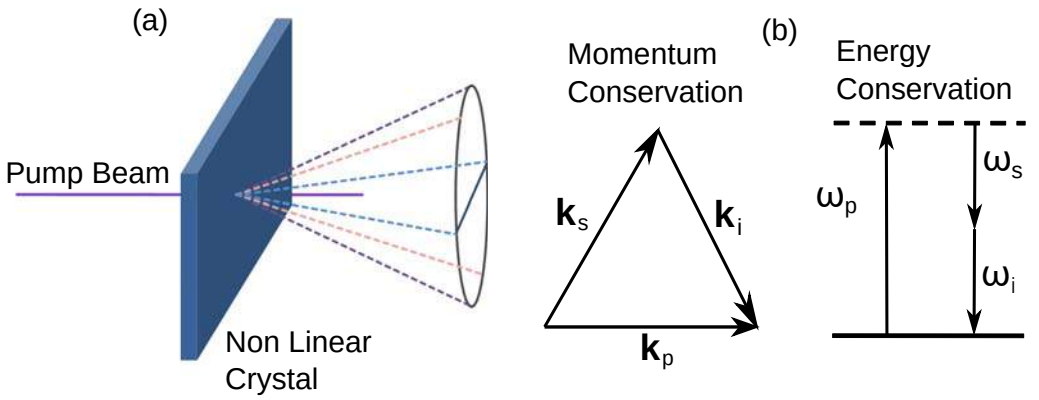

Figure 4.5: (a) An illustration of type-I spontaneous parametric downconversion. The downconverted photons are emitted at different range of angles distributed over the cross-section of a cone. Different pair of colors are used to represent the fact that each photon pair appear at antipodal points of the cone. (b) The description of momentum and energy conservation in SPDC process where $\mathbf{k_j}$, ω denotes the wavevector and frequencies.

We can summarize this scenario mathematically as

$$|H\rangle \rightarrow |VV\rangle\,,$$

$$|V\rangle \rightarrow |HH\rangle\,,$$

where the two transformations are achieved by one crystal of the pair. For an input state polarized at 45°, we get one of the Bell's states and the transformation can be written as

$$\frac{|H\rangle + |V\rangle}{\sqrt{2}} \rightarrow \frac{|HH\rangle + |VV\rangle}{\sqrt{2}}.$$

4.3.3 Phase Matching the Downconversion Process

For the signal and idler photons making angles θ_s and θ_i with the pump beam, respectively, as shown in Fig. 4.4, the resolution of wavevectors into rectangular components and applying the law of conservation of momentum will yield

$$n_p\omega_p = n_s\omega_s\cos\theta_s + n_i\omega_i\cos\theta_i \tag{4.53}$$

$$0 = n_s\omega_s\sin\theta_s + n_i\omega_i\sin\theta_i \tag{4.54}$$

The downconverted photons are emitted from the crystal at range of wavelengths and angles. However, for our case where we consider the photons for which $\omega_s = \omega_i = \omega_p/2$ and $\theta_s = \theta_i = \theta_c$, Eq. (4.53) will be simplified as

$$n_p \omega_p = n_s \cos\theta_c \tag{4.55}$$

For an isotropic medium, it is not possible to satisfy the equation (4.55) as $n_p > n_s$ when $\lambda_p < \lambda_s$. However the problem can be overcome in case of uniaxial birefringent crystal which offers two different refractive indices for light parallel or perpendicular to the optic axis (ordinary $n_\circ$ and extraordinary n_e). For light beam polarized along the optic axis, the effective index of refraction n_{eff} depends upon the phase matching angle θ_m and given by

$$n_{\text{eff}}(\theta_m) = \left(\frac{\cos\theta_m{}^2}{n_\circ^2} + \frac{\sin\theta_m{}^2}{n_e^2} \right)^{-\frac{1}{2}} \tag{4.56}$$

In case of type-I SPDC, the pump photon has the effective index of refraction n_{eff} and down-converted photons have the ordinary index of refraction $n_\circ$. In order to make the signal and idler beam to form a laboratory angle (θ_L) with the pump beam outside the crystal, we can use Snell's law ($\sin\theta_L = n_\circ \sin\theta_c$) to obtain θ_c and extract the phase matching angle θ_m which satisfies Eq. (4.55). In our case $\theta_L = 3^\circ$ and the phase matching angle calculated is 29.24°. This phase matching angle is as communicated to the manufacturer while ordering the crystal.

The next section will present a brief description of optical components of our experimental setup employed to execute quantum state tomography.

4.3.4 Optical Setup

Figure 4.3 depicts the arrangement of optical components involved in the experiment. As stated earlier that special tools and instruments are required for the generation, measurement and detection of the quantum light, here we present a brief introduction of these components.

The idea is to generate single photons. These photon beams are routed through

two physical paths with half wave and quarter wave plates manipulating the polarization of photons in each path. Additionally, the MOE is placed in one beam. It is the change in properties of photons while traversing through MOE, we are interested in determining. The photon beam's polarization states are measured by letting them fall on single photon counting modules (SPCM). The SPCM's accept photons coupled through an optic fiber. Hence somewhere along the line, the photon beams propagating in free space need to be efficiently focused into the fiber. The electronic signals from the SPCM are then digitally analyzed on a field programmable-gate array (FPGA) and a computer. Coincidence counts are measured from which the analysis work flow, described earlier, launches off.

A beam of vertically polarized light (pump beam, $\lambda = 405$ nm) passes through a half wave plate (HWP) before falling on a downconversion crystals β-Barium Borate (BBO, BaB_2O_4). The half waveplate controls the polarization of the pump beam. Down converted photon pairs (signal and idler) of wavelength 805 nm are generated by the two stacked BBO crystals, cut for type-I downconversion. Thereafter, signal and idler beams passes through optical components (HWP, QWP) before getting collected at the fibre coupling lenses coupled with multimode fibre optic cables. In front of the fibre coupling lens, long pass filters RG-780 filters are mounted to block the light of wavelength shorter than 780 nm. They also serve the purpose of blocking the ambient light which not only alters the photon statistics but can also cause damage to the single photon counting modules (SPCM).

The other end of the optical fibre is connected to a fibre to fibre coupler which couples the light into another fibre as shown in Fig. 4.6(a). This particular arrangement is useful for swapping the connection between the coupling lenses and different detectors. Finally, the distal end of this second optical fibre is connected to the single photon counting module (SPCM) where photons are detected.

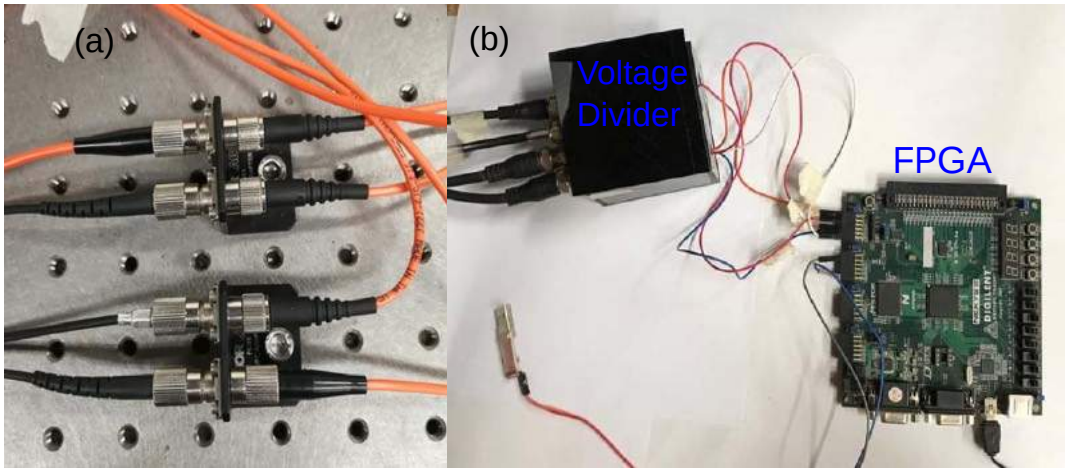

Figure 4.6: (a) Fiber to fiber coupler receives light from collection lenses and couples to the input of SPCM. (b) FPGA based coincidence counting unit with the capability of four single count detections and four coincident photon detection. The potential divider steps down the 5 V signal from SPCM to 3.3 V. The FPGA read out is achieved through RS-232 communication protocol.

We used SPCM (SPCM-AQ4C) with four independent channels of avalanche photodiodes (APDs). APDs can detect the photons in wavelength range of 400–1060 nm. They produce an output pulse (TTL, 5 V) of about 20–25 ns for each photodetection. The APDs also have dead time of $\approx$ 50 ns between pulses and are powered by three power supplies of 2 V, 5 V and 30 V, which are meant for powering the in-built Peltier coolers, providing high voltage to the detectors and biasing the electronic circuitry.

The pulses generated by APDs in response to photon beams (signal and idler) detection are ANDed together, producing an output only if the two pulses overlap in time. Such a single output is known as coincidence count, *i.e.*, detection of two or more particles simultaneously at two different detectors (APDs). A coincidence counting unit based on FPGA (Nexys 2) is used for counting of pulses generated by APDs and is shown in Fig. 4.6(a). FPGA has an internal clock of 50 MHz which provides an effective coincidence window of (2×20 ns). The FPGA was programmed by my colleague Hamza Waseem working in our research group [12].

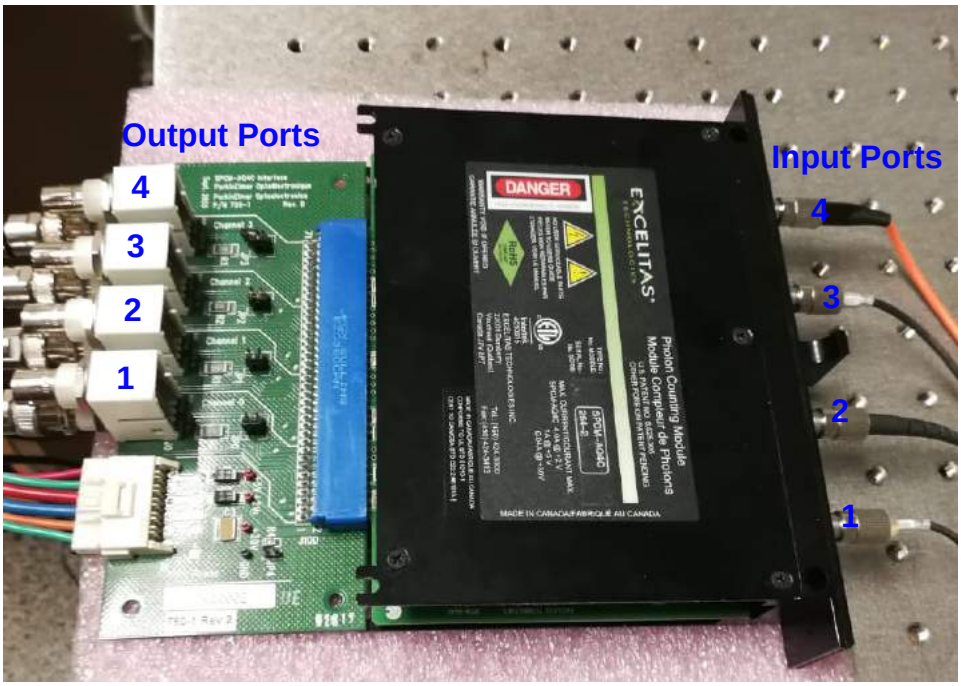

Figure 4.7: Single photon counting module (SPCM-$AQ4C$). single photons are coupled to the SPCM through input ports and 5 V pulses from output ports are transmitted via BNC couplers.

Furthermore, the two pulses from APDs can overlap only if one pulse arrives after the other within the width of first pulse. This also means that coincidence window is directly proportional to the width of pulses. However, coincidence window is independent of which pulse arrives first, hence the true coincidence window is twice the pulse width.

Coincidence counting calculations are performed by hardware logic on FPGA which is further communicated to the computer through RS-232 communication protocol and all the counters are being reset every 0.1 s which is the minimum update period limited by the read-out-rate of the FPGA. The coincidence and single counts are then monitored on computer within a Labview based interface. The preceding discussion introduces the reader with all the essential ingredients of the setup and we now are ready to discuss the experimental actualization.

4.3.5 The Experimental Setting for Quantum State Tomography

Fig. 4.8 presents the schematics for the tomographic setup where the detection unit is excluded for clarity. The light from pump laser ($\lambda = 405$ nm) is allowed

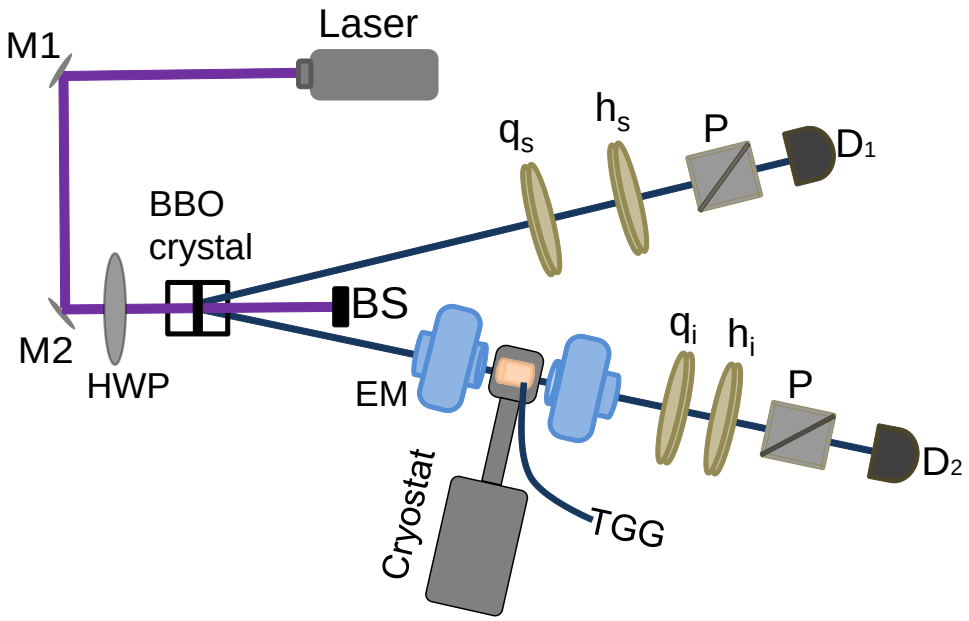

Figure 4.8: The schematic for two qubit tomography measurement setup where detection unit and mechanical setup has been excluded for convenience. The optical elements **(M1,M2)**= mirrors installed in kinematic mounts, **BS**= beam stopper, **HWP**= half waveplate, **P**= Glan-Thompson polarizers, **D1,D2**= detectors and ($\mathbf{q_{s,i}}$, $\mathbf{h_{s,i}}$)=quarter and half waveplates where subscripts s and i represent signal and idler beam.

to pass through the SPDC crystal which generates non-collinear photon pairs through spontaneous parametric downconversion. The signal beam is collected at detector D_1 after passing through quarter (q_s) wave, half (h_s) waveplates and polarizer P.

The magneto-optical element (TGG-terbium gallium garnet crystal) is mounted inside the cryostat which is placed between the electromagnet (GMW-3470). The axial holes through electromagnet poles allow the light to pass through the TGG crystal. The choice of placing the MOE in idler beam is completely arbitrary. The idler beam is first aligned to navigate through the axial hole

of electromagnet prior to pass through the cryostat optical window and subsequently the magneto optical element. The light then exits through the opposite hole of electromagnet and travels through QWP (q), HWP (h) and polarizer (P) to reach the detector D_2.

Instead of four detectors (two detectors after a PBS in each photon beam), we use only two detectors (with a polarizer in each path). We will explain shortly how this setting can still achieve the intended probabilities required for tomography.

The idler beam encounters more optical elements on its path to detector (D_2), therefore the individual counts at detector D_2 decreases drastically due to loss caused by back reflections from the optical elements and optical window of cryostat. This decrease is apparent in the reduced coincidence counts. Consequentially, we adapted the two detector scheme by replacing the polarizing beam splitters with Glan-Thompson polarizers as back reflections from PBS would have further reduced the counts. In this revised scheme we need 16 tomographic settings instead of the 9 required with four detectors.

The various tomographic settings are realized by different orientation of quarter and half waveplates which will project the incoming state ρ along different polarization bases. The waveplates are mounted in motorized stages whose control is managed through a Labview based interface. The sixteen measurement settings along with the various orientation of waveplates are tabulated in Table 4.4. It is worth mentioning that prior to the aligning of complete optical setup, the magnetic field produced by the electromagnet has been measured by a Gaussmeter (410-SCT, LakeShore) against the input current. The magnetic field calibration is measured 59 mT/A. Throughout this chapter, we'll mention the current through coils explicitly instead of magnetic field produced.

Table 4.4: Different settings of waveplates for complete determination of Stokes parameters. The $h_s(h_i)$ and $q_s(q_i)$ denote the quarter and half waveplates angles of signal (idler), respectively

Measurement Basis	$h_s(^\circ)$	$q_s(^\circ)$	$h_i(^\circ)$	$q_i(^\circ)$
$\|HH\rangle$	0	0	0	0
$\|HV\rangle$	0	0	45	0
$\|HD\rangle$	0	0	22.5	45
$\|HL\rangle$	0	0	0	45
$\|VH\rangle$	45	0	0	0
$\|VV\rangle$	45	0	45	0
$\|VD\rangle$	45	0	22.5	45
$\|VL\rangle$	45	0	0	45
$\|DH\rangle$	22.5	45	0	0
$\|DV\rangle$	22.5	45	45	0
$\|DD\rangle$	22.5	45	22.5	45
$\|DL\rangle$	22.5	45	0	45
$\|LH\rangle$	0	45	0	0
$\|LV\rangle$	0	45	45	0
$\|LD\rangle$	0	45	22.5	45
$\|LL\rangle$	0	45	0	45

4.4 Measurement of Faraday Rotation of a Single Photon

We performed tomographic measurements for two different polarization states: $|HH\rangle$ and Bell's states $\phi^+ = (|HH\rangle + |VV\rangle)/\sqrt{2}$. The generation of these states is controlled by placing a half waveplate before the BBO crystal as shown in Fig. 4.8. The procedural steps for the experiment can be enumerated in the following way.

For a particular state ($|HH\rangle$ or $|\phi^+\rangle = (|HH\rangle + |VV\rangle)/\sqrt{2}$), we first perform the tomographic measurements in the absence of magnetic field. This is achieved by performing sixteen measurements by setting different angles of QWP and HWP. At each measurement setting, the individual (also called sin-

Table 4.5: Tomographic data obtained for $|HH\rangle$ state at 15 K with zero applied field where channel A (B) represent the individual counts from signal (idler) beam, respectively and channel AB enumerates coincidence counts.

Measurement Basis	Single Counts Channel A	Single Counts Channel B	Coincidence Counts (AB)
$\|HH\rangle$	61278	17518	809
$\|HV\rangle$	5473	17393	76
$\|HD\rangle$	37493	17741	648
$\|HL\rangle$	29223	17355	669
$\|VH\rangle$	61231	2600	71
$\|VV\rangle$	5400	2550	2
$\|VD\rangle$	37547	2580	46
$\|VL\rangle$	29218	2545	66
$\|DH\rangle$	61348	8150	261
$\|DV\rangle$	5411	8139	32
$\|DD\rangle$	37507	8171	214
$\|DL\rangle$	29250	8253	199
$\|LH\rangle$	61167	9904	163
$\|LV\rangle$	5334	9970	12
$\|LD\rangle$	37654	9627	109
$\|LL\rangle$	29153	9973	111

gles) and coincidence counts are measured for a period of 10 s. The measured counts are then averaged to give one value for single and coincidence counts. This step is then repeated for all the remaining settings, hence completing the tomography measurement for a particular state.

In the second step, the magnetic field is turned on gradually from minimum to a maximum value and the above mentioned step is repeated at each value of the magnetic field. In order to capture the temperature dependence of the change in polarization state of photons, the aforementioned steps are performed at different temperatures (8 K, 15 K, 30 K and 100 K). The registered data, as presented in Table 4.5, is then processed using the toolbox developed by Kwiat[3] which employs maximum likelihood estimation for the construction of legitimate density matrix which is described in Section 4.2.7.

[3] http://research.physics.illinois.edu/QI/Photonics/Tomography/

Figures 4.9 and 4.10 visualizes density matrices at two distinct temperatures (8 K and 15 K) for the nominal input state $\rho_\circ = |HH\rangle\langle HH|$ and illustrate the change in magnitude of different elements of density matrices as the magnetic field is varied. The estimated density matrices at 8 K and 15 K are given by

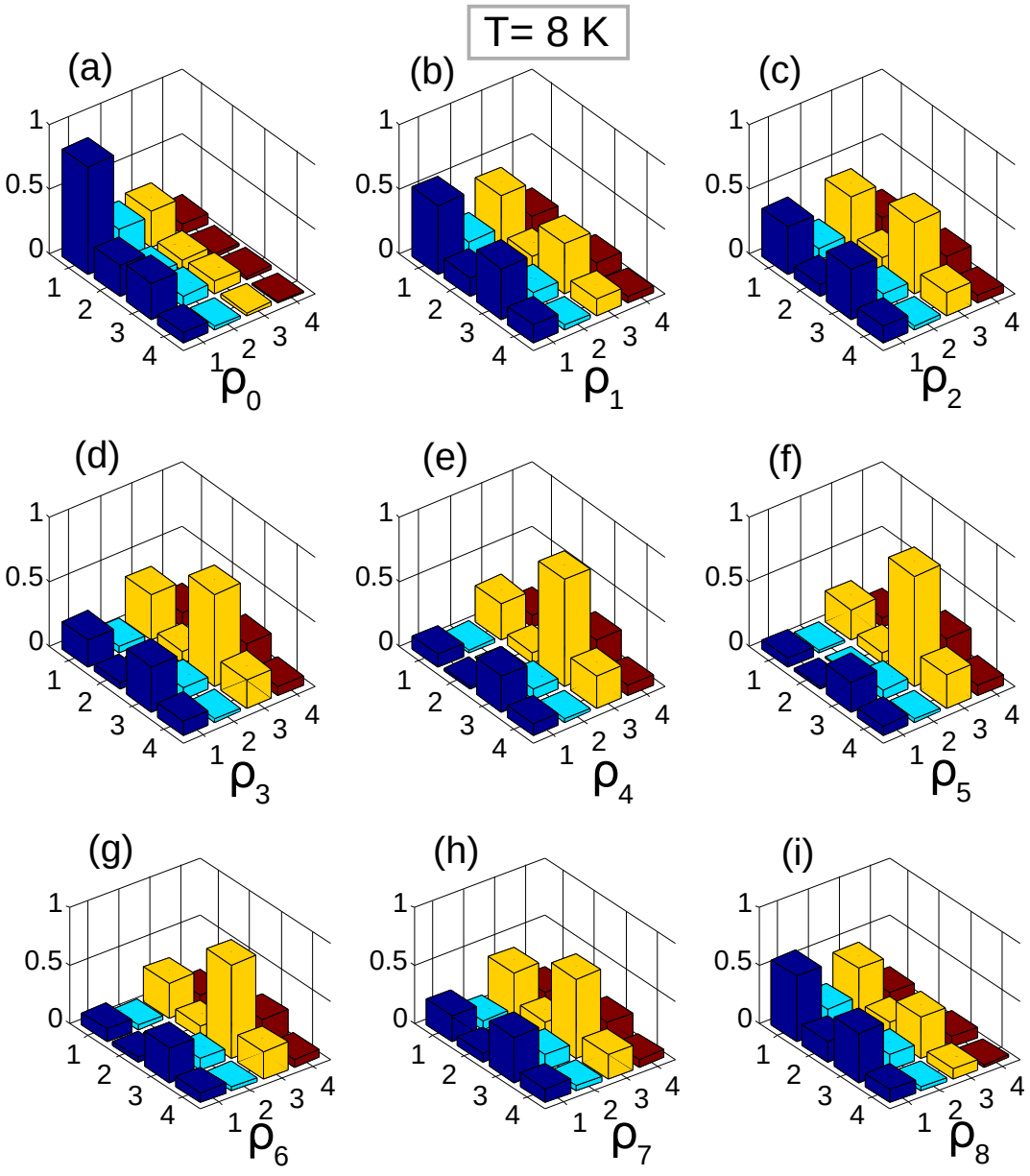

Figure 4.9: Experimentally estimated density matrices for different strength of applied magnetic field. The density matrix (a) $\rho_\circ$ corresponds to zero magnetic field whereas (b)–(i) are the density matrices for magnetic field range (1–3 A) with a step size of 0.25 A. The nominally generated input state is $\rho_\circ = |HH\rangle\langle HH|$.

$$\{\rho_{|HH\rangle}\}_{(8\mathrm{K})} = \begin{pmatrix} 0.83 & 0.17-0.17i & -0.13+0.25i & 0.03+0.07i \\ 0.17+0.17i & 0.07 & -0.08+0.02i & -0.01+0.02i \\ -0.13-0.25i & -0.08-0.02i & 0.09 & 0.02-0.02i \\ 0.03-0.07i & -0.01-0.02i & 0.02+0.02i & 0.01 \end{pmatrix}, \tag{4.57}$$

and

$$\{\rho_{|HH\rangle}\}_{(15\mathrm{K})} = \begin{pmatrix} 0.82 & 0.17-0.19i & -0.14+0.24i & 0.05+0.07i \\ 0.17+0.19i & 0.08 & -0.08+0.02i & -0.01+0.03i \\ -0.14-0.24i & -0.08-0.02i & 0.10 & 0.01-0.03i \\ 0.05-0.07i & -0.01-0.03i & 0.01+0.03i & 0.01 \end{pmatrix}, \tag{4.58}$$

respectively. The density matrices and plots for higher temperatures (50 K and 100 K) are provided in the supplementary information 4.5.1 and 4.25.

Similarly, we employed the tomography process for Bell's state $\phi^+ = (|HH\rangle + |VV\rangle/\sqrt{2})$ at different temperatures under the action of different strengths of applied magnetic field. The estimated density matrices are plotted and are shown in Figs. 4.11 and 4.12 for two temperature (8 K and 15 K) and respective density matrices are given by

$$Re\{\rho_{\phi^+}\}_{(8\mathrm{K})} = \begin{pmatrix} 0.37 & 0.04 & -0.06 & -0.11 \\ 0.04 & 0.10 & -0.08 & 0.04 \\ -0.06 & -0.08 & 0.13 & -0.13 \\ -0.11 & 0.04 & -0.13 & 0.40 \end{pmatrix} \tag{4.59}$$

$$Re\{\rho_{\phi^+}\}_{(15\mathrm{K})} = \begin{pmatrix} 0.45 & 0.06 & -0.04 & 0.24 \\ 0.06 & 0.08 & -0.06 & 0.07 \\ -0.04 & -0.06 & 0.06 & -0.03 \\ 0.24 & 0.07 & -0.03 & 0.42 \end{pmatrix} \tag{4.60}$$

It is evident from the figures that elements of the density matrix changes in response to the variation in current through coils. Furthermore, comparing Fig. 4.11(a) with (i) also depicts the oscillatory behavior of the polarization state, showing the cyclic evolution of the density operator as a result of the magneto-optic rotation, providing justification to the largely coherent and unitary process involved.

However, the quantification of θ is not straightforward as different elements of density matrix exhibit different magnitude of rotation due to dissimilar dependence on trigonometric functions. We approach this problem in two distinct ways: an exhaustive search approach and a non-linear Levenberg-Marquardt based optimization.

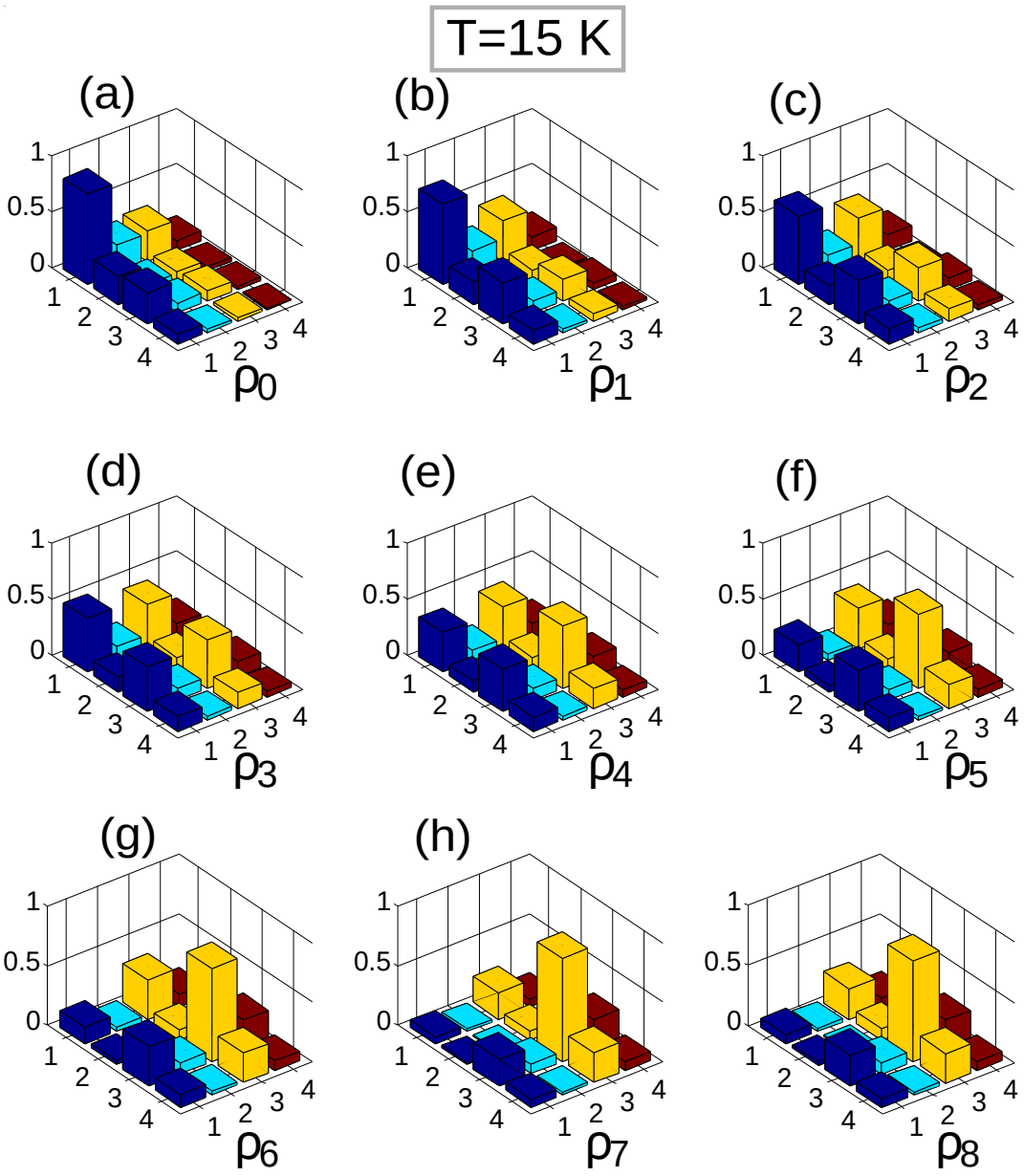

Figure 4.10: The density matrices reconstructed from tomography measurements at 15 K as a function of magnetic field. The density matrix (a) $\rho_\circ$ corresponds to zero magnetic field whereas (b)–(i) are the density matrices for magnetic field range (1–3 A) with a step size of 0.25 A. The nominally generated input state is $\rho_\circ = |HH\rangle\langle HH|$.

4.4.1 Estimating Faraday Rotation by Exhaustive Search

The first method employs an exhaustive search methodology for the task at hand. To understand this, let's assume that the measured density matrices as a result of tomography measurement are represented by $\rho_\circ^{exp}$ and ρ_i^{exp}, where

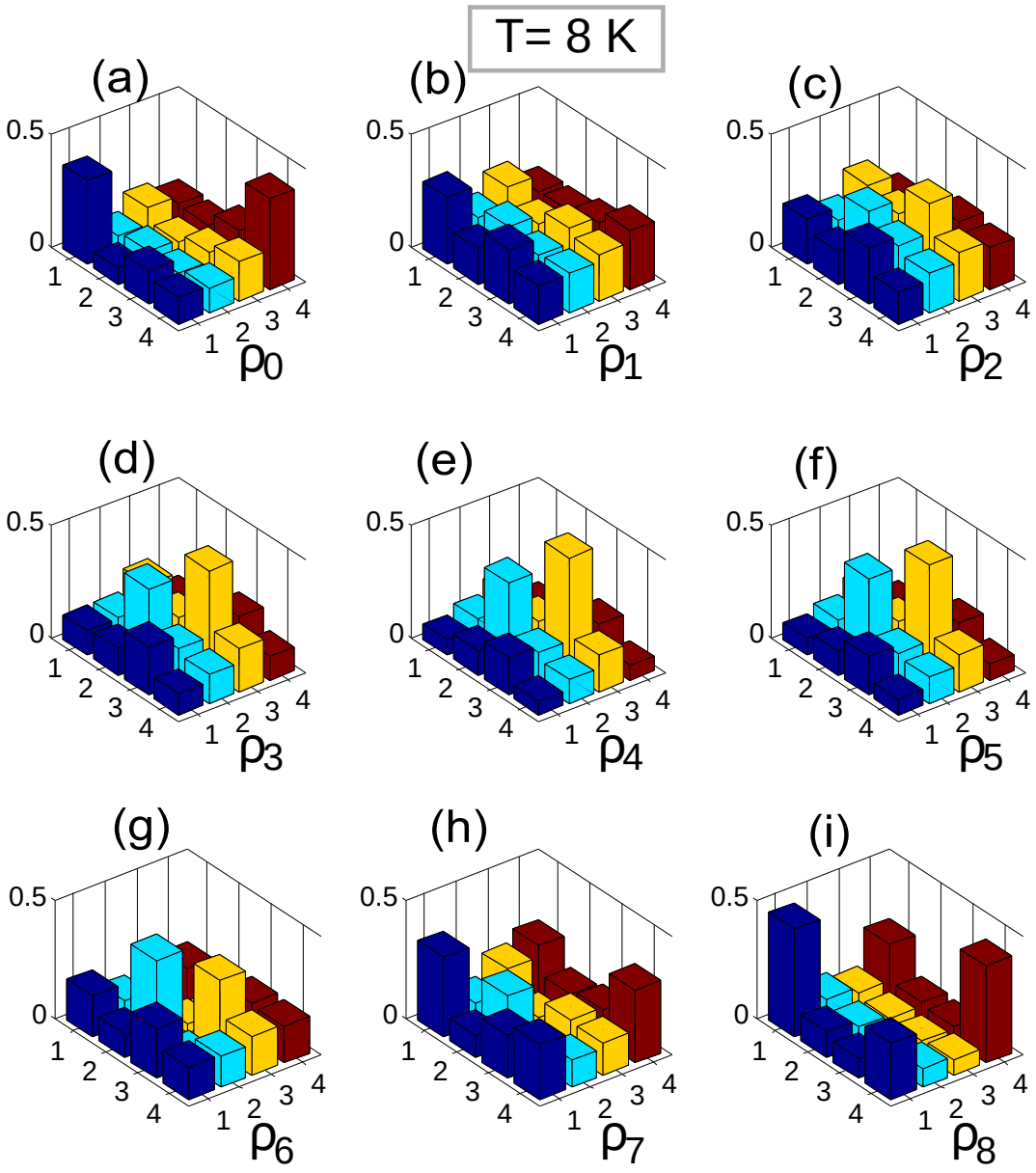

Figure 4.11: 3D plots of density matrices for Bell's state $|\phi^+\rangle$ with different applied current through electromagnet's coils. The density matrix a) $\rho_\circ$ corresponds to the original state generated through SPDC in the absence of magnetic field whereas for (b)–(i), the magnitude of applied current are 1 A, 1.25 A, 1.50 A, 1.75 A, 2.0 A, 2.5 A, 3.0 A, 3.5 A and 4.0 A, respectively.

$\rho_\circ^{exp}$ is the density matrix at zero magnetic field and ρ_i^{exp} at some particular value of magnetic field. As a first step, the density matrix $\rho_\circ^{exp}$ is subjected to an arbitrary rotation θ by a rotation operator $\mathcal{R}(2\theta)$ which satisfies the property of unitary operator, *i.e.*, $\mathcal{R}\mathcal{R}^\dagger = \hat{I}$. The unitary state evolution will

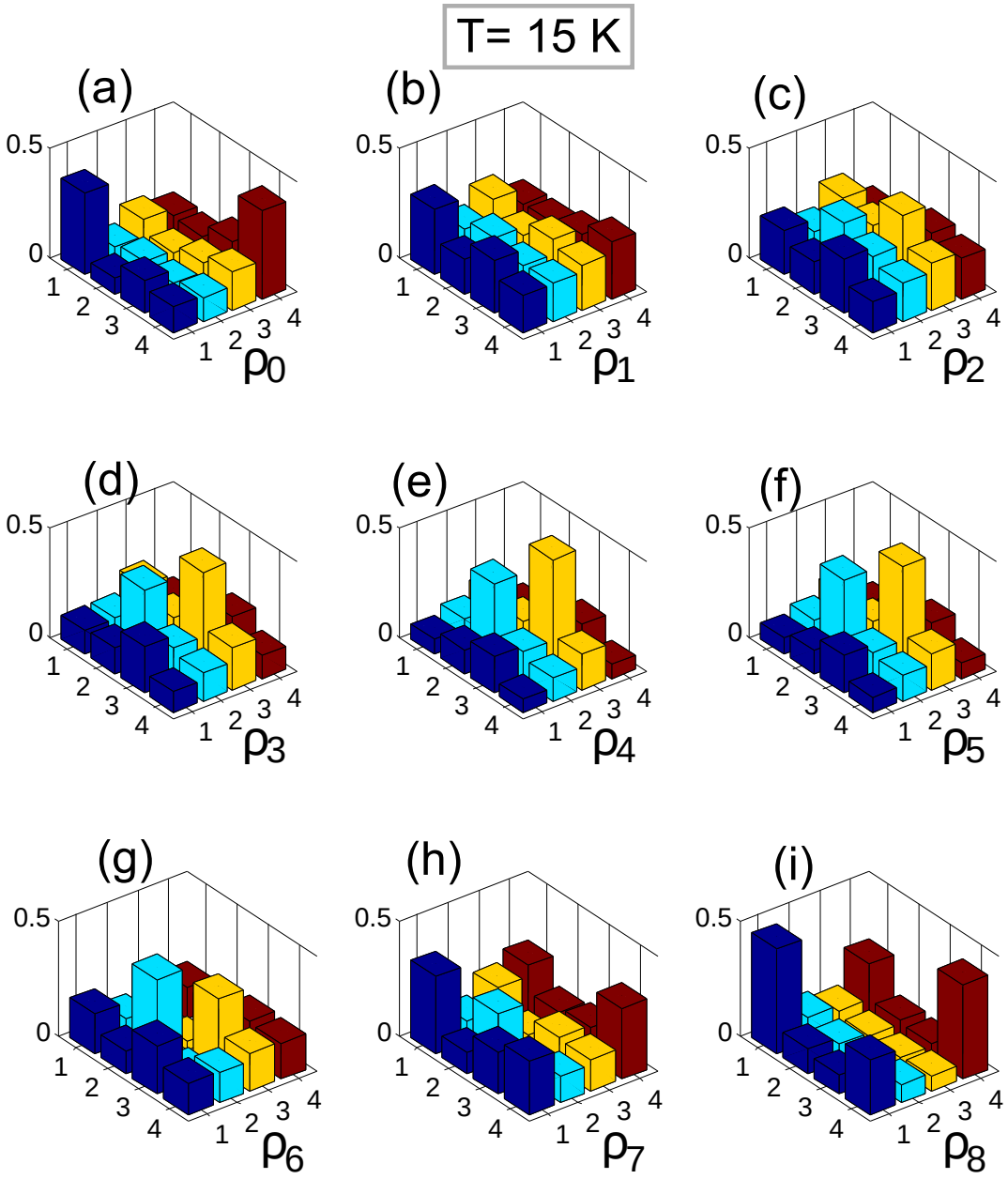

Figure 4.12: 3D plots of Bell's state $|\phi^+\rangle$ at T= 015 K where (a) $\rho_\circ$ corresponds to zero magnetic field whereas for (b)–(i), the current through the EM coils is varied from 1–5 A with a step size of 0.5 A.

have the mathematical form

$$\rho_i^{th} = \mathcal{R}_i(2\theta)\rho_0^{exp}\mathcal{R}_i^\dagger(2\theta) \tag{4.61}$$

where the index i refers to the distinct magnetic fields (currents). Please note that $\mathcal{R}_i(2\theta) = \mathcal{R}(2\theta_i)$. Equation (4.61) follows naturally from the Schrodinger

equation

$$|\psi'\rangle = \hat{U}\,|\psi\rangle\,,$$

which leads to

$$|\psi'\rangle\,\langle\psi'| = \hat{U}\,|\psi\rangle\,\langle\psi|\,\hat{U}^{\dagger}.$$

The rotation operator $\mathcal{R}$ is defined in the four dimensional Hilbert space and is constructed in the following way

$$R_i(2\theta)\otimes 1 = \exp(-i2\theta\frac{\hat{\sigma}_y}{2})\otimes\hat{I}, \tag{4.62}$$

where θ is the purported Faraday rotation. In the Bloch sphere picture, this means that the idler photon is subjected to a rotation 2θ about the $\hat{\sigma}_y$-axis, leading to a physical rotation of the plane of polarization of the single photon by θ in the lab frame. The tensor product $\otimes\hat{I}$ indicates that, nominally, no operation happens in the Hilbert space of the signal photon. The matrix expression for the idealized unitary operator is therefore given by

$$\mathcal{R}_i(2\theta) = \begin{pmatrix}\cos\theta & -\sin\theta\\ \sin\theta & \cos\theta\end{pmatrix}\otimes\begin{pmatrix}1 & 0\\ 0 & 1\end{pmatrix} = \begin{pmatrix}\cos\theta & 0 & -\sin\theta & 0\\ 0 & \cos\theta & 0 & -\sin\theta\\ -\sin\theta & 0 & \cos\theta & 0\\ 0 & \sin\theta & 0 & -\cos\theta\end{pmatrix} \tag{4.63}$$

Now if the rotation angle θ is varied from 0°–180° with a step size of 1°, this in turn will generate 181 candidate density matrices ρ^{th} corresponding to different rotations. We search the space of ρ^{th}'s for the one whose overlap with ρ_i^{exp} is the maximum or whose difference from ρ_i^{exp} is minimum. Therefore the Faraday rotation angle can be estimated by finding the minimum of the following function.

$$\theta_i = min\sum_{j,k}\left(|\rho_i^{th}-\rho_i^{exp}|^2\right)_{j,k} \tag{4.64}$$

where the subscript i signifies the magnetic field and the notation means that we subtract ρ_i^{th} and ρ_i^{exp}, then square each term in the matrix and find the sum of all these squares. We identify where the sum hits the minimum. Note than in Eq. (4.64), ρ_i^{th} is given by Eq. (4.61) and ρ_i^{exp} is the experimental data returned by tomography for the i'th magnetic field. We will use θ_i and θ interchangeably, depending on the context.

This numerical search for both states is performed in Matlab for the complete range of magnetic fields. The extracted Faraday rotation angles θ_i for different temperatures are plotted as a function of current through electromagnet coils in Fig. 4.13. These tomographic results show excellent agreement with the prediction of a linear dependence on the magnetic field and match our trends observed for TGG with classical light; only that now we are probing Faraday rotation of truly the single photon.

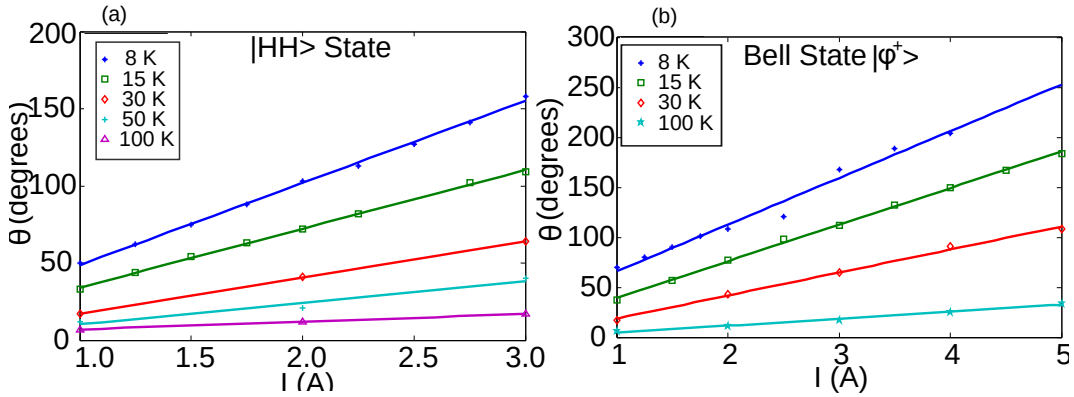

Figure 4.13: The Faraday rotation angles are plotted as a function of change in current through coils for two different input states. The input states are a) $|HH\rangle$ and b) $|\phi^+\rangle$. Solid lines represent linear curve fit of the data.

Furthermore, Fig. 4.14 shows the variation in the magnitude of the Faraday rotation angle θ at a particular magnetic field as the temperature of the TGG crystal is varied. The curves presented in Fig. 4.14 captures accurately the paramagnetic nature of TGG crystal where the magnetization increase as the temperature of the material is lowered.

4.4.2 Estimating Faraday Rotation by Constrained Optimization

The second method involves the least squares non-linear search for minima which utilizes the interior point algorithm [32] for estimating the Faraday rotation angle (θ). The key idea in this scheme is to find the minimum of difference among density matrices, occurring as a result of birefringence induced by the

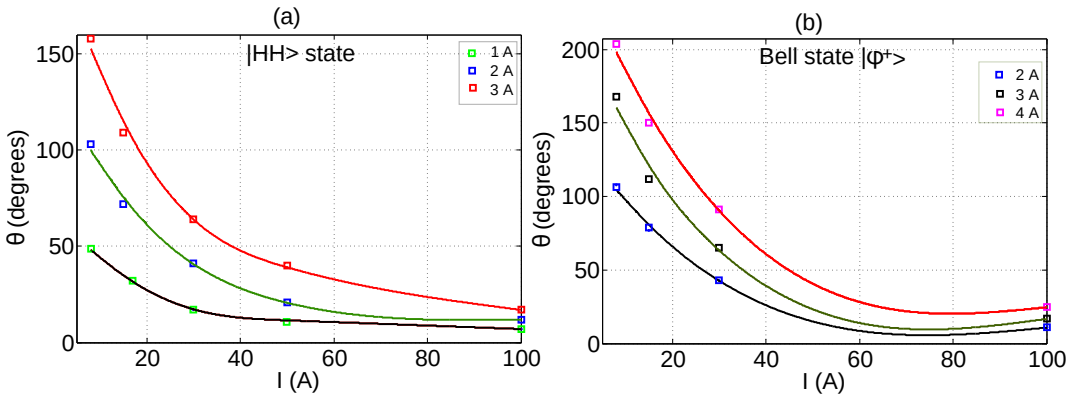

Figure 4.14: The change in Faraday rotation angle θ as a function temperature for different amplitude of current through magnet coils. The two input states are a) $|HH\rangle$ and b) $|\phi^+\rangle$. Solid lines are spline fit to the data.

magnetic field. The first step is similar to what was employed in the previous section, *i.e.*, density matrix $\rho_\circ^{exp}$ being rotated by the unitary operator $R_i(2\theta)$. In the second step, we measure the change in density matrices which is given as

$$\Delta\rho_i^{th} = \rho_i^{th} - \rho_\circ^{exp} \tag{4.65}$$

where ρ_i^{th} is given by Eq. 4.61 and $\rho_\circ^{exp}$ is the experimental estimated density matrix at zero magnetic field. Similarly, the change in experimentally estimated density matrices can be written as

$$\Delta\rho_i^{exp} = \rho_i^{exp} - \rho_\circ^{exp}. \tag{4.66}$$

The rationale for measuring these changes in density matrices ($\Delta\rho_i^{th}$ and $\Delta\rho_i^{exp}$) is that the difference will now reflect purely the change in density matrix in response to varying magnetic field and eliminates the unwanted noise in off-diagonal terms which does not contribute to Faraday rotation. Finally, the Faraday rotation angles can be extracted by minimization of the following function

$$\begin{aligned}\theta_i &= min \sum_{j,k} \left(|\Delta\rho_i^{th} - \Delta\rho_i^{exp}|^2 \right), \\ &= min(f_i(\theta)).\end{aligned} \tag{4.67}$$

We employed the Matlab optimization toolbox which utilizes the function *fmincon* with interior point algorithm for this particular task. The extracted

rotation angles are plotted as a function of current through coils in Fig. 4.15(a). To give a comprehensive picture of data processing, we also plotted $f(\theta)$ as a function of θ for different values of field at a particular temperature (T=15 K).

A typical $f_i(\theta)$ for a field of 3 A is given by

$$\begin{aligned}\frac{f_i(\theta)}{10^{-3}} =&(31\sin 2\theta - 8\cos 2\theta + 41)^2 + (370\cos 2\theta + 130\sin 2\theta + 74)^2 \\ &+ (75\cos 2\theta + 23\sin 2\theta + 1)^2 + (31\cos 2\theta + 8\sin 2\theta + 5)^2 \\ &+ (370\cos 2\theta + 130\sin 2\theta + 61)^2 + (75\sin 2\theta - 23\cos 2\theta \\ &+ 150)^2 + (31\cos 2\theta + 8\sin 2\theta - 7)^2 + (75\sin 2\theta - 23 \\ &\times \cos 2\theta + 14)^2 + (75\cos 2\theta + 23\sin 2\theta - 8)^2 + (370 \\ &\times \sin 2\theta - 130\cos 2\theta + 410)^2.\end{aligned} \quad . \quad (4.68)$$

The minimum for this one-dimensional function can also be found from a simple minimization routine or by analytical differentiation and is given by

$$\theta_{f_i|_{min}} = 150^\circ.$$

Furthermore, Table 4.6 draws a comparison between density matrices ρ_i^{exp} and ρ^F at the same magnitude of applied current through coils (3 A). Here ρ_i^{exp} is experimentally measured density matrix and ρ^F is the density matrix evaluated at a particular value of θ and i obtained after the minimization algorithm. The overlap between the density matrices ρ^{exp} and ρ^F in terms of fidelity is also presented in Table 4.6. Fidelity between two density matrices ρ_1 and ρ_2 is defined as $Tr(\rho_1\rho_2)$. This concludes our discussion for tomographic measurement of the Faraday rotation for single photon. [h!]

4.4.3 Faraday Rotation of Single Photons by Phase Sensitive Detection

In another version of the experiment, we made use of phase sensitive detection of the coincidence counts. In the experiments described hitherto, the signal-to-noise ratio were large. For example, the coincidence counts were in the range 39 to 700 counts per second. Hence, the variations were significant as the magnetic field is varied. This is because Faraday rotations are relatively large

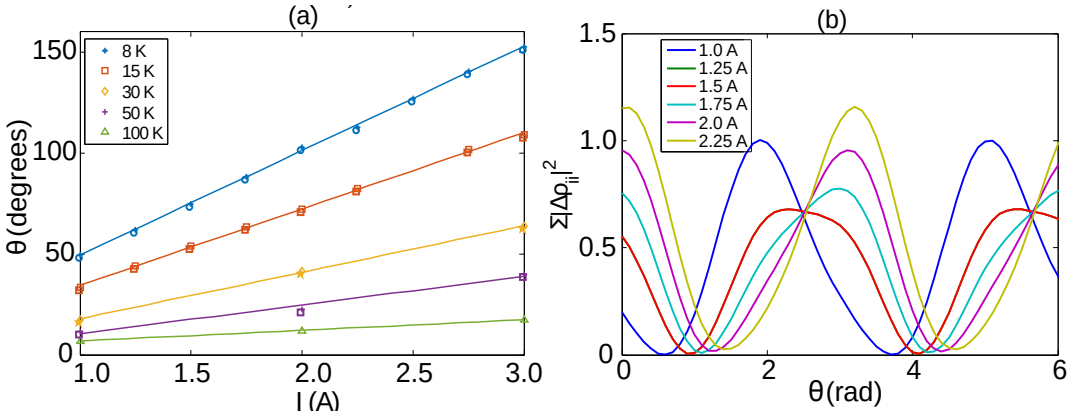

Figure 4.15: Temperature dependent Faraday rotation angles as a function of applied current through electromagnet coils determined by constrained optimization whereas (b) depicts the minimization function $f(\theta)$ at $T = 15$ K.

Table 4.6: Density matrices for $|HH\rangle$ state at two distinct temperatures where ρ^{exp} represents the experimentally measured and ρ_F describes the density matrix evaluated at a particular value of θ extracted from (4.73).

T(K)	$\rho_{\|HH\rangle}$(3 A)	Fidelity
8 K	$Re(\rho^{exp}) = \begin{pmatrix} 0.56 & 0.11 & -0.42 & -0.04 \\ 0.11 & 0.06 & -0.09 & -0.03 \\ -0.42 & -0.09 & 0.35 & 0.04 \\ -0.04 & -0.03 & 0.04 & 0.02 \end{pmatrix}$	0.79
	$Re(\rho^{F}) = \begin{pmatrix} 0.56 & 0.11 & -0.37 & -0.01 \\ 0.11 & 0.04 & -0.12 & -0.03 \\ -0.37 & -0.12 & 0.35 & 0.06 \\ -0.01 & -0.03 & 0.06 & 0.02 \end{pmatrix}$	
	$Im(\rho^{exp}) = \begin{pmatrix} 0 & -0.17 & 0.24 & 0.07 \\ 0.17 & 0 & 0.02 & 0.02 \\ -0.24 & -0.02 & 0 & -0.02 \\ -0.07 & -0.02 & 0.02 & 0 \end{pmatrix}$	
	$Im(\rho^{F}) = \begin{pmatrix} 0 & -0.10 & 0.25 & -0.03 \\ 0.10 & 0 & 0.13 & 0.02 \\ -0.25 & -0.13 & 0 & -0.09 \\ 0.03 & -0.02 & 0.09 & 0 \end{pmatrix}$	

T(K)	$\rho_{\|HH\rangle}$(3 A)	Fidelity
15 K	$Re(\rho^{exp}) = \begin{pmatrix} 0.08 & 0.02 & -0.12 & -0.07 \\ 0.02 & 0.01 & 0.03 & -0.02 \\ -0.12 & 0.03 & 0.84 & 0.15 \\ -0.07 & -0.02 & 0.15 & 0.07 \end{pmatrix}$	0.77
	$Re(\rho^{F}) = \begin{pmatrix} 0.08 & 0.01 & -0.11 & 0.03 \\ 0.01 & 0.01 & -0.1 & -0.01 \\ -0.1 & -0.1 & 0.83 & 0.17 \\ 0.03 & -0.01 & 0.17 & 0.07 \end{pmatrix}$	
	$Im(\rho^{exp}) = \begin{pmatrix} 0 & -0.19 & 0.24 & 0.07 \\ 0.19 & 0 & 0.01 & 0.02 \\ -0.24 & -0.01 & 0 & -0.02 \\ -0.07 & -0.02 & 0.02 & 0 \end{pmatrix}$	
	$Im(\rho^{F}) = \begin{pmatrix} 0 & -0.03 & 0.24 & 0.08 \\ 0.03 & 0 & 0.01 & 0.02 \\ -0.24 & -0.01 & 0 & -0.18 \\ -0.08 & -0.02 & 0.18 & 0 \end{pmatrix}$	

at cryogenic temperatures. One may also like to measure these rotations using some phase sensitive detection (PSD) technique, which can possibly allow measurements of even small Faraday rotations of single photons. This section prescribes how one could do that.

The schematic for PSD in conjunction with measuring coincidence counts is illustrated in Fig. 4.16. An optical chopper placed just before the BBO crystal modulates the light at the rate of $f = 20$ Hz. The output signal from the optical chopper also serves as a reference signal to the lockin amplifier. The experiment is made simpler by removing the quarter and half waveplates from signal and idler beam paths which are required for tomographic measurement.

Furthermore, the polarizer axis in both arms (signal and idler) is oriented along the horizontal (lab frame). A key element is a digital-to-analog converter that converts digital counts from the FPGA based coincidence counter

to an analog signal which serves as input to the lockin amplifier. This amplifier is described in Section 1.3.5. The procedural steps and underlying principle for the measurement is as follows.

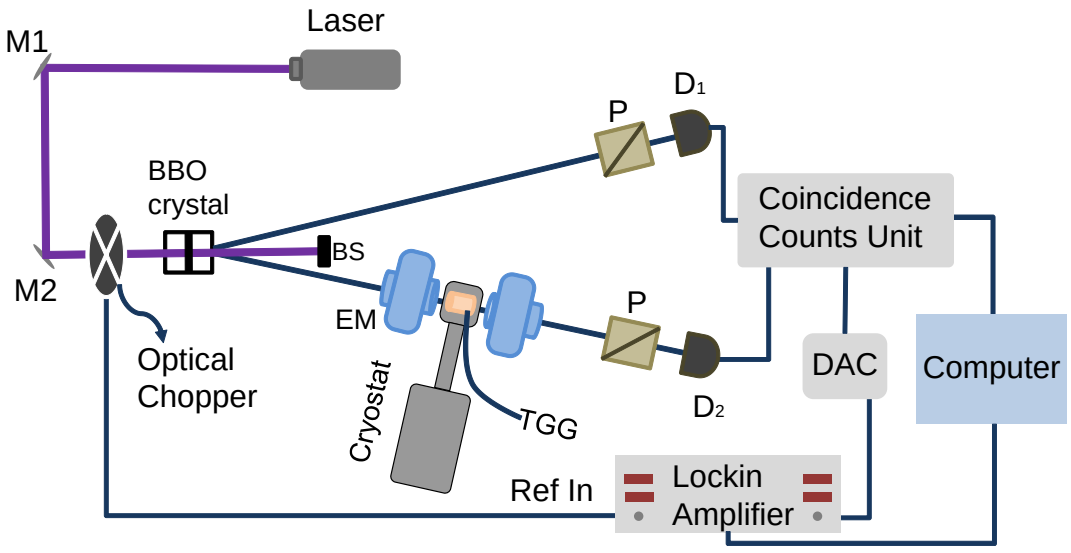

Figure 4.16: The schematic illustration of phase sensitive detection of single photons where **M**= mirrors, **BS**= beam stopper, **EM**= electromagnet, **P**= polarizer, **D**= photodetectors and **DAC**= digital to analog converter.

The idler beam passes through the axial hole of the electromagnet and subsequently through TGG crystal placed inside the cryostat. The idler beam then exits through other hole of the electromagnet and travels through the polarizer before getting collected at the detector D_2. However, the signal beam encounters only polarizer before registering the counts at detector D_1. The coinciding counting unit registers the singles as well as the coincidence counts.

In the detection part of the single photons, a minimal modification enabled us to utilize the phase sensitive detection. Prior to read out in the computer, the digital output of coincidence count signal is converted to an analog signal through digital to analog converter (DAC). This analog signal is then fed to the input of lockin amplifier. The lockin amplifier reads the rms value of analog signal which is proportional to the number of coincidence counts.

We performed this experiment for $|HH\rangle$ state over a wide temperature range 8–250 K. At each temperature, we measured the coincidences counts and lockin output for zero magnetic field for a period of 20 s. The magnitude of field is then increased gradually from minimum to a maximum value and the preceding steps are repeated. At each value of applied magnetic field, the recorded data is averaged to give a single value of coincidence count and voltage.

The change in the number of coincidence counts against the varying current through electromagnet coils is depicted in Fig 4.17. Similar curves are obtained for intensity as a result from lockin measurement and are presented in the supplementary information 4.23.

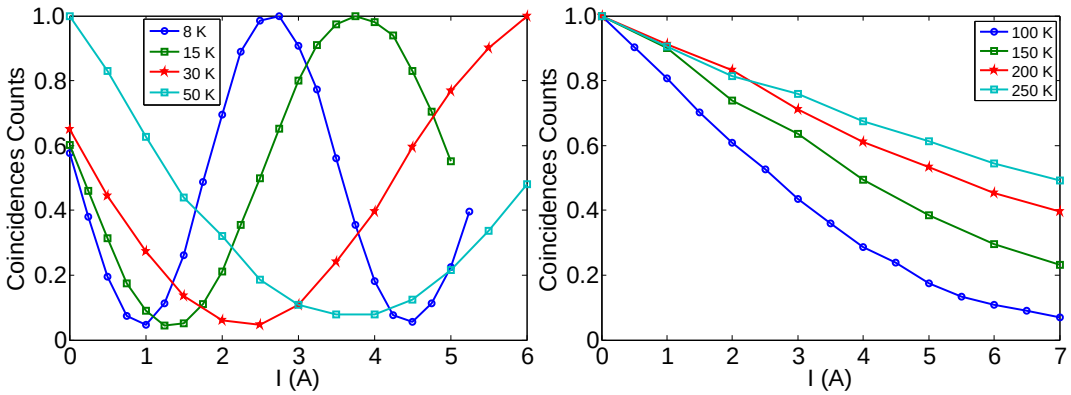

Figure 4.17: Normalized coincidence counts as function of applied current through EM coils. Subfigures (a) and (b) show low and high temperature ranges.

It is worth remembering that single photons are generated in a particular polarization state and projection of these states results in coincidence counts. To put it simply, in our experimental arrangement, each coincidence count is a representative of a particular polarization state and as the magnetic field is varied, the change in polarization state is reflected through the change in coincidence counts. This in turns manifests the Faraday rotation of single photons. In order to quantify the magnitude of Faraday rotation, one can fit these oscillating curves with the following function

$$y = a\cos^2(bI + c) + d \tag{4.69}$$

where a, b, c and d are fitting parameters, I is the current and y represents the coincidence counts. Finally, the Faraday rotation angle can be estimated from the time period of cosine function. The time period for the curve at 8 K is estimated to be 3.5 A which corresponds to a 2π rotation. Subsequently, the Faraday rotation angle at a magnetic field corresponding to the current of 5 A is estimated and yields $\theta \approx 462°$.

At low temperatures (8–50 K), the magnitude of rotation is large and exhibit an oscillatory behavior which perfectly corroborates our theoretical description of Faraday effect explained in Chapter 1 (see, for example Fig. 1.6). The variation in the coincidence counts is also apparent in the high temperature data 4.17(b).

In phase sensitive detection scheme, the signal beam does not undergo any rotation yet it serves as a conditioning element for the idler beam. It is this conditioning which transcribes photons as quantum light. In the absence of signal beam conditioning, the light will be deemed as classical and the subsequent rotation as the conventional classical Faraday effect. Our experimental results show that it is perfectly possible to measure Faraday rotation of single photons which comprise the quantum light.

4.4.4 Ellipticity Measurement of Single Photon as an Off-Resonant Rotation on the Bloch Sphere

In the preceding discussion for estimation of rotation angles, we have assumed the *pure* Faraday rotation is captured by a rotation operator $\mathcal{R}(2\theta)$. However, theoretical investigation and experimental results in Chapters 1 and 2 demonstrates the presence of another important parameter, *i.e.*, ellipticity χ. The current Section investigates the ellipticity acquired by a single photon as it traverses through the isotropic magneto-optic medium (TGG) in the presence of a magnetic field.

In the Bloch sphere picture, the Faraday effect is the rotation of an input state

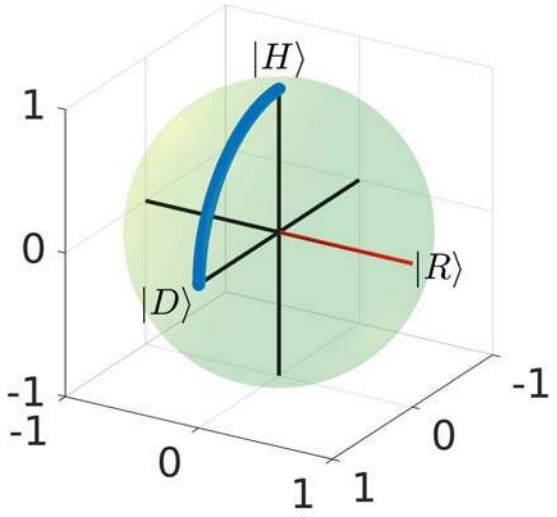

Figure 4.18: The action of pure Faraday rotator in the Bloch sphere diagram is visualized where an input state $|H\rangle$ is rotated about the $\hat{\sigma}_y$-axis (highlighted as red) through an angle of $\theta_B = \pi/2$ on the Bloch sphere.

about the $\hat{\sigma}_y$-axis (denoted as $|R\rangle$-axis on the Bloch sphere). This scenario is presented in Fig. 4.18 where input state $\rho_\circ$ is rotated through an angle $\pi/2$. Note the evolution of input state which remains on the surface of the Bloch sphere (pure state) while traversing through $|H\rangle$ to $|D\rangle$ axis.

Now in order to incorporate the effect of ellipticity, we can modify the expression (4.62) for rotation operator as following

$$R_i(2\theta) = \exp\left(-i2\theta\left(\frac{\hat{\sigma}_y \cos\xi}{2} + \frac{\hat{\sigma_z} \sin\xi}{2}\right)\right) \otimes \hat{I}, \tag{4.70}$$

which implies that the input state will now rotate about a new axis which is tilted at an angle ξ with respect to the $\hat{\sigma}_y$ axis. The above expression in the matrix form is then given by

$$\mathcal{R}(2\theta,\xi) = \begin{pmatrix} \cos\theta - i\sin\theta\sin\xi & 0 & -\sin\theta\cos\xi & 0 \\ 0 & \cos\theta - i\sin\theta\cos\xi & 0 & -\sin\theta\cos\xi \\ \sin\theta\cos\xi & 0 & \cos\theta + i\sin\theta\cos\xi & 0 \\ 0 & \sin\theta\cos\xi & 0 & \cos\theta + i\sin\theta\cos\xi \end{pmatrix}. \tag{4.71}$$

The rotation through a tilted axis can account for ellipticity in the following way. The state nominally initiating as $|H\rangle\langle H|$ will now rotate not along the large circle at the $\phi_B = 0^\circ$ meridian, rather it will traverse the upper

quadrant away from the $\hat{\sigma}_2$-$\hat{\sigma}_3$ plane and tilt towards the $\hat{\sigma}_y$-axis. The state will end up at some point whose polar coordinates are (θ_B, ϕ_B) from which the Faraday rotation and ellipticity can subsequently be extracted!. In NMR literature, such a single qubit rotation is often called an off-resonant pulse [33].

The recipe for extracting the Faraday rotation angle and off-resonant axis angle ξ with respect to $\hat{\sigma}_y$-axis is similar to the previous estimation routines and is redefined here with minimal modification of the rotation operator

$$\Delta\rho_i^{th} = \rho_i^{th} - \rho_\circ^{exp}, \tag{4.72}$$

where

$$\rho_i^{th} = \mathcal{R}(\theta, \xi)\rho_\circ^{exp}\mathcal{R}^\dagger(\theta, \xi)$$

is now function of two variables, θ and ξ. These angles can be estimated from the minimization of the following function

$$\begin{aligned}\theta_i &= min \sum_{j,k} \left(|\Delta\rho_i^{th} - \Delta\rho_i^{exp}|^2 \right), \\ &= min(f_i(\theta, \xi)),\end{aligned} \tag{4.73}$$

where the minimization routine is similar to what were used in Section 4.4.2.

Using this technique, the extracted Faraday rotation and off-resonant axis angles ξ's are plotted in Fig. 4.19. The Faraday rotation angles θ's obtained from minimization corroborates with the previous findings in Section 4.4.2. For instance, the Faraday rotation angle for temperature 8 K at a field of 3 A is $\approx 10^\circ$ less than what was observed previously (4.15). Moreover, the angle ξ of axis of rotation with respect to $\hat{\sigma}_y$ does not vary much with the applied field and equals $\approx 45^\circ \pm 0.6^\circ$.

Furthermore, in order to highlight the minimization process, we have plotted the function $Re\{f_i(\theta, \xi)\}$ at a particular temperature (15 K) and magnetic field (2 A) and is displayed in Fig. 4.20. Moreover, we also plot the trajectory of the input state for the idler photon only $\rho_\circ^{idler} = |H\rangle\langle H|$ on the Bloch

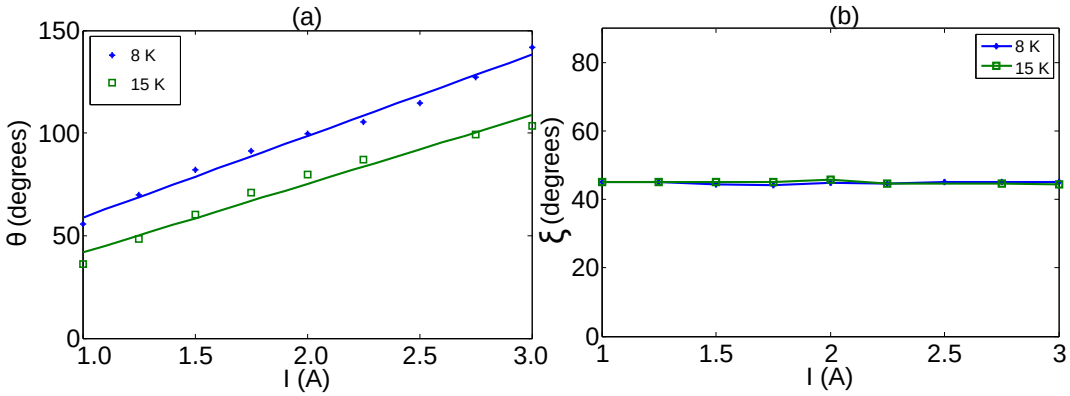

Figure 4.19: The estimated Faraday rotation angles as a function of applied current through coils at two different temperatures (T= 8 and 15 K). Solid lines represent the least square curve fit of the data for subfigure (a).

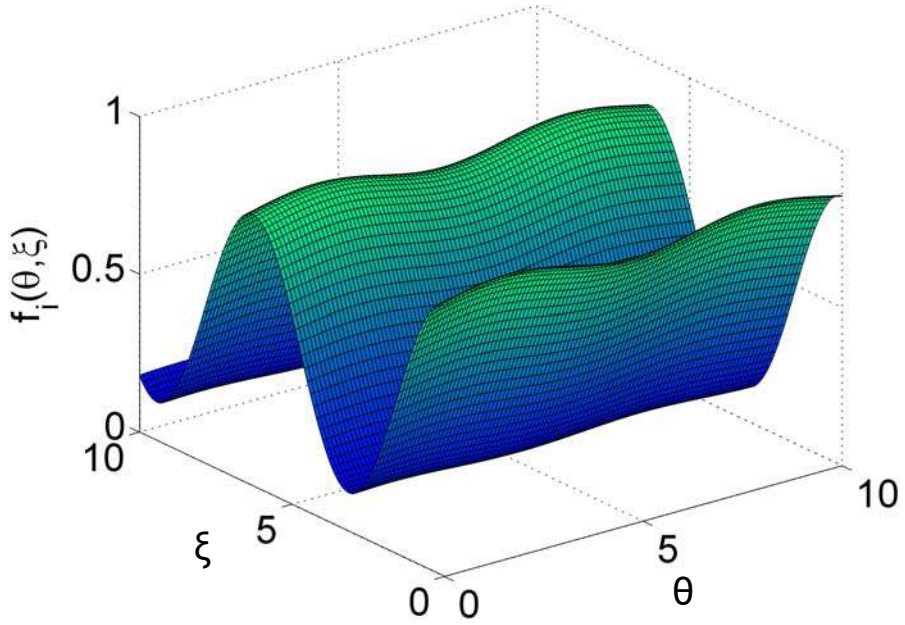

Figure 4.20: The function $Re\{f_i(\theta,\xi)\}$ is plotted for arbitrary values of θ and ξ.

sphere for different magnetic fields in Fig. 4.21. Each subfigure illustrates the evolution of input state, being rotated about an axis making an angle ξ with $\hat{\sigma}_y$-axis. We are justified in choosing $\rho_{\circ}^{idler} = |H\rangle\langle H|$ as the input state for the argument for the following reasons. First, the tomography shows that for a

nominal $|HH\rangle\langle HH|$ input state, we obtain

$$\rho_\circ = \begin{pmatrix} 0.83 & 0.17-0.17i & -0.13+0.25i & 0.03+0.07i \\ 0.17+0.17i & 0.07 & -0.08+0.02i & -0.01+0.02i \\ -0.13-0.25i & -0.08-0.02i & 0.09 & 0.02-0.02i \\ 0.03-0.07i & -0.01-0.02i & 0.02+0.02i & 0.01 \end{pmatrix}. \tag{4.74}$$

If we take the reduced density matrix [16] for the idler photon, this yields

$$\rho_\circ^{reduced} = \begin{pmatrix} 0.90 & -0.14+0.26i \\ -0.14-0.26i & 0.10 \end{pmatrix} \tag{4.75}$$

which has a high degree of fidelity (overlap) with

$$|H\rangle\langle H| = \begin{pmatrix} 1 & 0 \\ 0 & 0 \end{pmatrix}.$$

Our single photon, two qubit states are separable, so we are justified in taking the reduced density matrices without loss of description. For the estimation of ellipticity angles, we first need to establish the correlation among Faraday rotation angle θ, off-resonant axis angle ξ and Bloch sphere coordinates θ_B, ϕ_B. For this, let's assume we have the single qubit pure input state $|H\rangle$ which is being rotated by two dimensional unitary operator $\mathcal{R}_r$ given by

$$\mathcal{R}_r(2\theta,\xi) = \begin{pmatrix} \cos\theta - i\sin\theta\sin\xi & -\sin\theta\cos\xi \\ \sin\theta\cos\xi & \cos\theta + i\sin\theta\sin\xi \end{pmatrix}. \tag{4.76}$$

The transformation of the input state $|H\rangle$ under the action of this unitary operation can be summarized as

$$\begin{aligned} |p\rangle &= \mathcal{R}_r|H\rangle \\ &= (\cos\theta - i\sin\theta\sin\xi)|H\rangle + (\sin\theta\cos\xi)|V\rangle, \end{aligned} \tag{4.77}$$

which can be further simplified with trigonometric manipulations and rewritten as

$$|p\rangle = \sqrt{\cos^2\theta + \sin^2\theta\sin^2\xi}\,|H\rangle + e^{\tan^{-1}(\tan\theta\sin\xi)}(\sin\theta\cos\xi)|V\rangle. \tag{4.78}$$

We also know that any arbitrary pure state $|\psi\rangle$ on the Bloch sphere can be characterized by angles θ_B, ϕ_B and has the following form [34]

$$|\psi\rangle = \cos\frac{\theta_B}{2}|H\rangle + e^{i\phi_B}\sin\frac{\theta_B}{2}|V\rangle \tag{4.79}$$

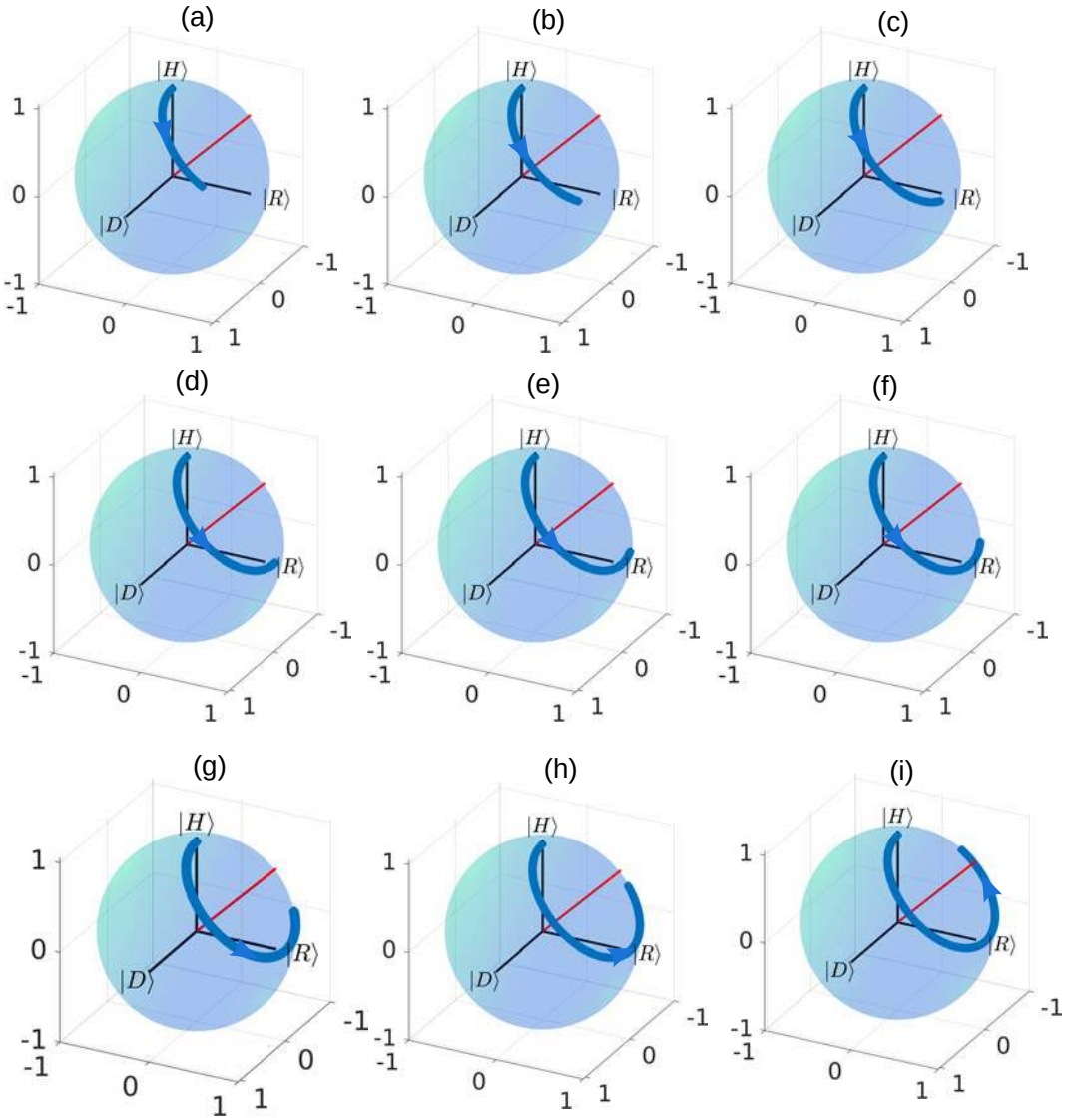

Figure 4.21: The trajectory of input state $\rho_\circ = |H\rangle\langle H|$ rotated about the off-resonant axis (represented by red line) which makes an angle ξ w.r.t $\hat{\sigma}_y$-axis. In each subfigure, the state rotates from an initial point $\theta = 0$ (along $|H\rangle$-axis) to a final position θ_i which is estimated from minimization of function $f_i(\theta, \xi)$, where i refers to different magnetic fields varied from 1–3 A with a step size of 0.25 A.

where subscript B is merely to differentiate the Bloch sphere parameters. Comparing Eqns. (4.79) and (4.78), the following relations can be readily obtained

$$\theta_B = 2\tan^{-1}\left(\frac{\cos\xi\sin\theta}{\sqrt{\cos^2\theta + \sin^2\theta\sin^2\xi)}}\right), \tag{4.80}$$

$$\phi_B = \tan^{-1}\big(\tan\theta\sin\xi\big). \tag{4.81}$$

Finally, comparing the polarization states description in two pictures pre-

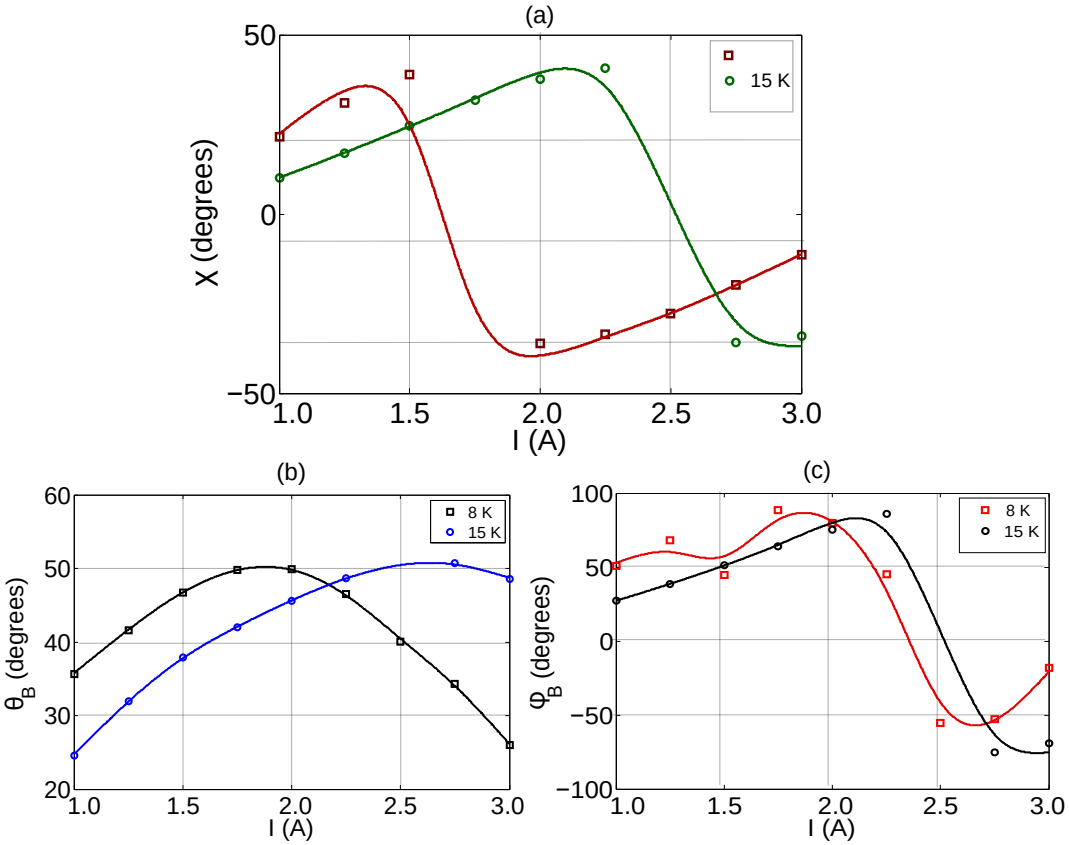

Figure 4.22: (a) The variation of ellipticity angles against the current through coils. b) and c) depict the plots for Bloch sphere coordinates (θ_B), (ϕ_B) as magnetic field is varied from minimum to a maximum value. Solid lines are cubic spline fit to the data.

sented by Poincare sphere in Section 2.2.4 and Bloch sphere, the following relationship can be obtained to estimate the parameters f the polarization ellipse [35]

$$\psi = \tan^{-1}\left(\frac{\cos\xi \sin\theta}{\sqrt{\cos^2\theta + \sin^2\theta \sin^2\xi)}}\right), \tag{4.82}$$

$$2\chi = \sin^{-1}(\sin\psi \sin\phi), \tag{4.83}$$

where ψ represents the rotation of the polarization ellipse and χ is the ellipticity. The ellipticity acquired by the single photon as it traverses through TGG are plotted as a function of magnetic field in Fig. 4.22. For completeness, the polar coordinates of the resulting nominal pure idler photon quantum state

are also shown in the same Figure.

It is clear that ellipticity is a strong function of the magnetic field and the temperature. Our model with a tilted rotation axis allows an interesting method to determine the ellipticity acquired by the polarization state of a single photon qubit. The ellipticity χ whose value is constrained to lie in the range $[-\pi/4,\pi/4]$ is seen to traverse the full range available. Our description based on the Bloch sphere of the photon polarization offers unique and interesting perspective on magneto-optic rotations.

4.5 Supplementary Information

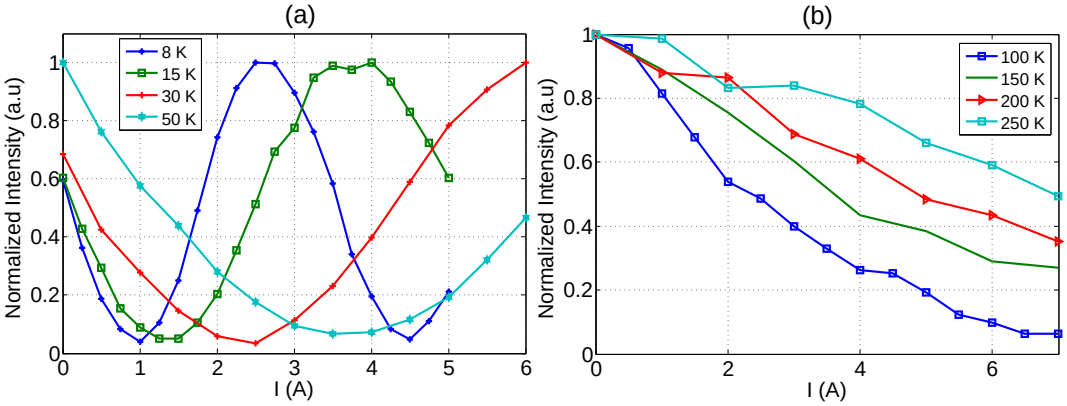

Figure 4.23: Normalized intensity measured by lockin amplifier as function of applied current through EM coils. Subfigures (a) and (b) show low and high temperature ranges and solid lines are guide to the eyes.

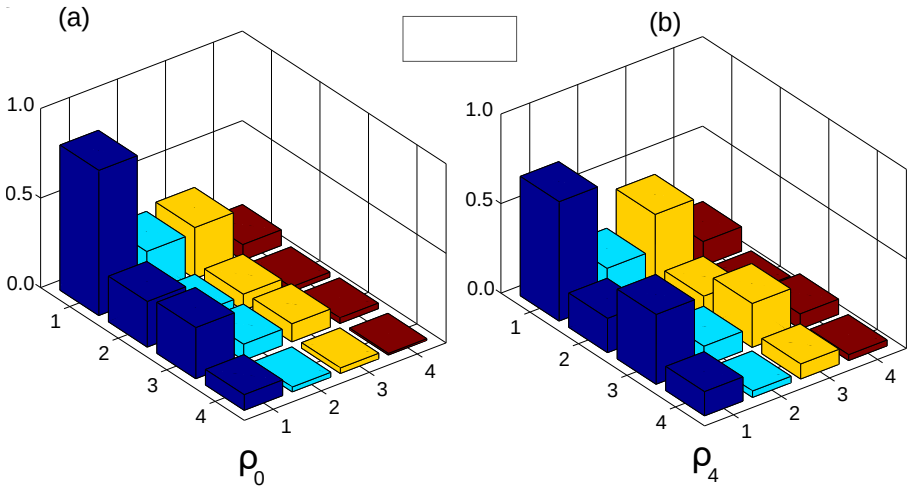

Figure 4.24: The absolute value of density matrix is plotted for $|HH\rangle$ state. a) $\rho_\circ$ corresponds to zero magnetic field and ρ_1 to a maximum current (3 A) through the coils.

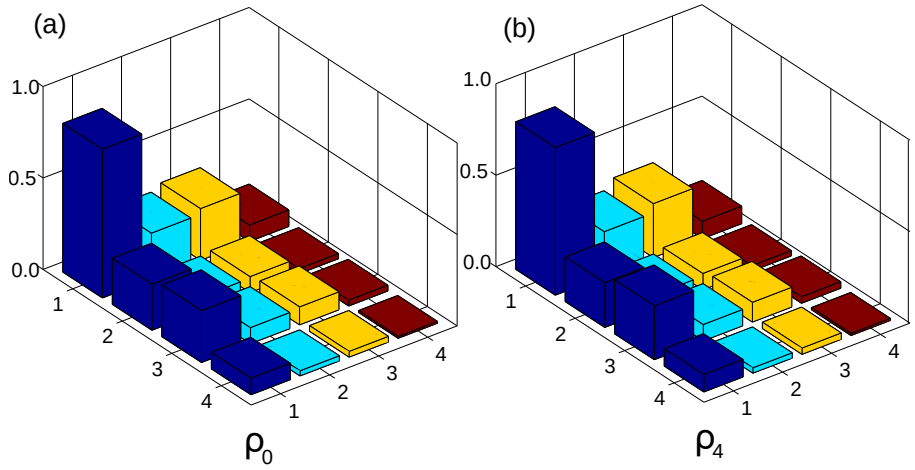

Figure 4.25: The absolute value of density matrix is plotted for $|HH\rangle$ state at T= 100 K. a) $\rho_\circ$ corresponds to zero magnetic field and ρ_1 to a maximum current (3 A) through the coils.

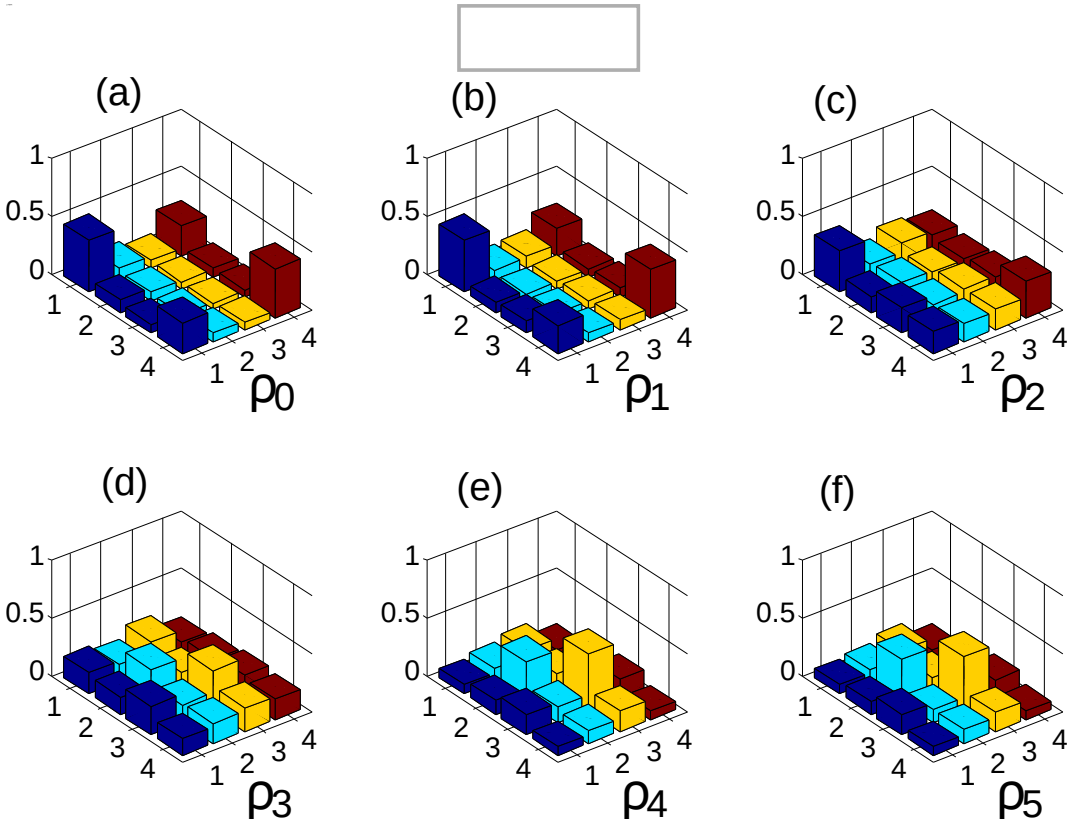

Figure 4.26: Bell's state $|\psi^+\rangle$ density matrix plots for different applied magnetic fields. a) corresponds to zero magnetic field whereas for (b)–(f) the current through coils is varied from 1–5 A in a step size of 1 A.

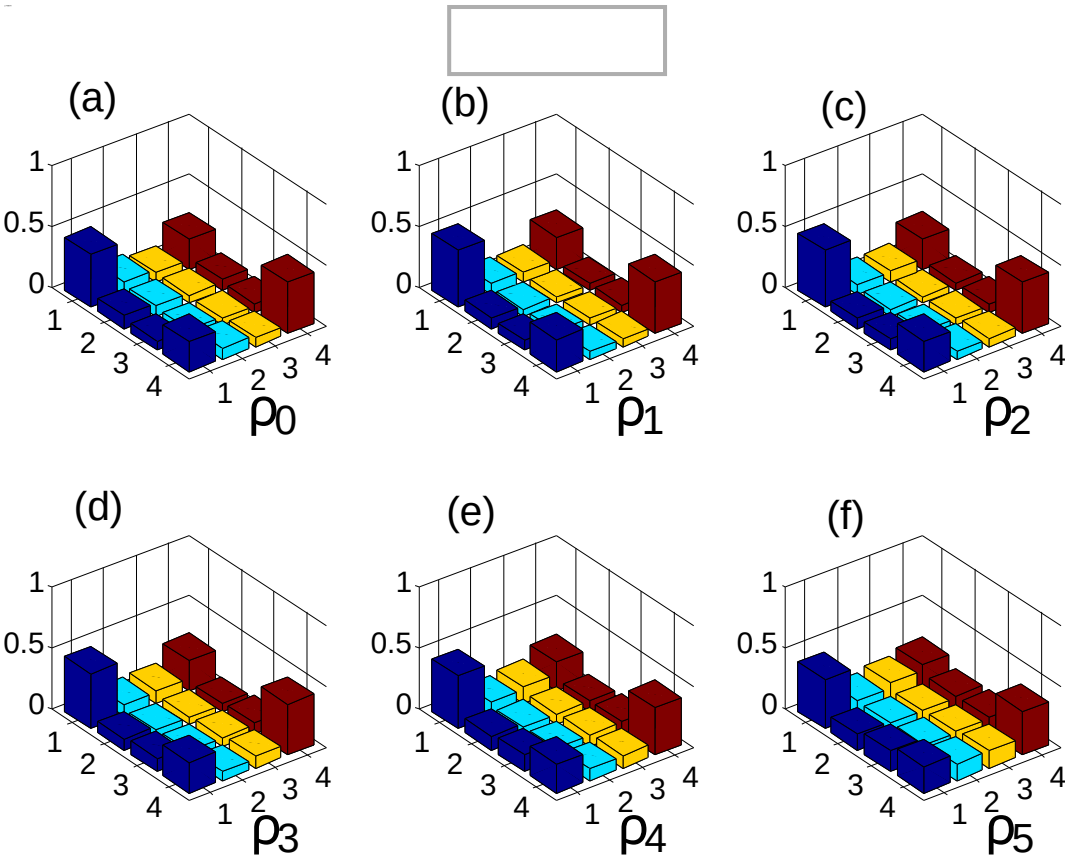

Figure 4.27: Bell's state $|\psi^+\rangle$ density matrix plots at T=100 K for different applied magnetic fields. a) $\rho_\circ$ corresponds to zero magnetic field whereas for (b)–(f) the current through coils is varied from 1–5 A in a step size of 1 A.

4.5.1 Density Matrices for $|HH\rangle$ States at 8 K

$$Re\{\rho_2\} = \begin{pmatrix} 0.37 & 0.06 & 0.39 & 0.08 \\ 0.06 & 0.03 & 0.07 & 0.03 \\ 0.39 & 0.07 & 0.55 & 0.12 \\ 0.08 & 0.03 & 0.12 & 0.06 \end{pmatrix} \tag{4.84}$$

$$Re\{\rho_3\} = \begin{pmatrix} 0.21 & 0.03 & 0.31 & 0.02 \\ 0.03 & 0.01 & 0.08 & 0.02 \\ 0.31 & 0.08 & 0.71 & 0.15 \\ 0.02 & 0.02 & 0.15 & 0.07 \end{pmatrix} \tag{4.85}$$

$$Re\{\rho_4\} = \begin{pmatrix} 0.10 & 0.02 & 0.16 & -0.02 \\ 0.02 & 0.01 & 0.08 & 0.01 \\ 0.16 & 0.08 & 0.82 & 0.16 \\ -0.02 & 0.01 & 0.16 & 0.08 \end{pmatrix} \tag{4.86}$$

$$Re\{\rho_5\} = \begin{pmatrix} 0.07 & 0.01 & -0.05 & -0.06 \\ 0.01 & 0.01 & 0.06 & 0.00 \\ -0.05 & 0.06 & 0.85 & 0.17 \\ -0.06 & 0.00 & 0.17 & 0.08 \end{pmatrix} \tag{4.87}$$

$$Re\{\rho_6\} = \begin{pmatrix} 0.11 & 0.03 & -0.16 & -0.09 \\ 0.03 & 0.01 & 0.02 & -0.02 \\ -0.16 & 0.02 & 0.81 & 0.14 \\ -0.09 & -0.02 & 0.14 & 0.07 \end{pmatrix} \tag{4.88}$$

$$Re\{\rho_7\} = \begin{pmatrix} 0.22 & 0.05 & -0.32 & -0.11 \\ 0.05 & 0.03 & -0.02 & -0.04 \\ -0.32 & -0.02 & 0.68 & 0.13 \\ -0.11 & -0.04 & 0.13 & 0.07 \end{pmatrix} \tag{4.89}$$

$$Re\{\rho_8\} = \begin{pmatrix} 0.39 & 0.09 & -0.41 & -0.09 \\ 0.09 & 0.05 & -0.07 & -0.04 \\ -0.41 & -0.07 & 0.52 & 0.08 \\ -0.09 & -0.04 & 0.08 & 0.04 \end{pmatrix} \tag{4.90}$$

4.5.2 Density Matrices for Bell's State at 8 K

$$\rho_1 = \begin{pmatrix} 0.30 & -0.15+0.04i & 0.24+0.02i & 0.15+0.08i \\ -0.15-0.04i & 0.20 & -0.17-0.00i & -0.17+0.03i \\ 0.24-0.02i & -0.17+0.00i & 0.23 & 0.20+0.06i \\ 0.15-0.08i & -0.17-0.03i & 0.20-0.06i & 0.26 \end{pmatrix} \tag{4.91}$$

$$\rho_2 = \begin{pmatrix} 0.20 & -0.15-0.02i & 0.23+0.10i & 0.08+0.12i \\ -0.15+0.02i & 0.27 & -0.21-0.01i & -0.17-0.02i \\ 0.23-0.10i & -0.21+0.01i & 0.34 & 0.19+0.10i \\ 0.08-0.12i & -0.17+0.02i & 0.19-0.10i & 0.19 \end{pmatrix} \tag{4.92}$$

$$\rho_3 = \begin{pmatrix} 0.11 & -0.10-0.06i & 0.12+0.17i & -0.02+0.09i \\ -0.10+0.06i & 0.33 & -0.15-0.02i & -0.11-0.07i \\ 0.12-0.17i & -0.15+0.02i & 0.45 & 0.10+0.16i \\ -0.02-0.09i & -0.11+0.07i & 0.10-0.16i & 0.11 \end{pmatrix} \tag{4.93}$$

$$\rho_4 = \begin{pmatrix} 0.07 & -0.05-0.10i & 0.01+0.16i & -0.06+0.02i \\ -0.05+0.10i & 0.36 & -0.14+0.01i & -0.04-0.10i \\ 0.01-0.16i & -0.14-0.01i & 0.51 & 0.02+0.16i \\ -0.06-0.02i & -0.04+0.10i & 0.02-0.16i & 0.06 \end{pmatrix} \tag{4.94}$$

$$\rho_5 = \begin{pmatrix} 0.08 & -0.00 - 0.11i & -0.06 + 0.16i & -0.06 - 0.03i \\ -0.00 + 0.11i & 0.38 & -0.13 + 0.02i & 0.01 - 0.12i \\ -0.06 - 0.16i & -0.13 - 0.02i & 0.47 & -0.04 + 0.16i \\ -0.06 + 0.03i & 0.01 + 0.12i & -0.04 - 0.16i & 0.07 \end{pmatrix} \tag{4.95}$$

$$\rho_6 = \begin{pmatrix} 0.17 & 0.06 - 0.08i & -0.19 + 0.09i & 0.02 - 0.14i \\ 0.06 + 0.08i & 0.36 & -0.03 + 0.02i & 0.07 - 0.11i \\ -0.19 - 0.09i & -0.03 - 0.02i & 0.31 & -0.13 + 0.10i \\ 0.02 + 0.14i & 0.07 + 0.11i & -0.13 - 0.10i & 0.15 \end{pmatrix} \tag{4.96}$$

$$\rho_7 = \begin{pmatrix} 0.34 & 0.09 + 0.00i & -0.18 + 0.00i & 0.18 - 0.15i \\ 0.09 - 0.00i & 0.21 & -0.06 + 0.02i & 0.11 - 0.01i \\ -0.18 - 0.00i & -0.06 - 0.02i & 0.15 & -0.14 + 0.01i \\ 0.18 + 0.15i & 0.11 + 0.01i & -0.14 - 0.01i & 0.31 \end{pmatrix} \tag{4.97}$$

$$\rho_8 = \begin{pmatrix} 0.46 & 0.06 + 0.09i & -0.02 - 0.08i & 0.22 - 0.08i \\ 0.06 - 0.09i & 0.08 & -0.06 - 0.00i & 0.05 + 0.06i \\ -0.02 + 0.08i & -0.06 + 0.00i & 0.06 & -0.02 - 0.06i \\ 0.22 + 0.08i & 0.05 - 0.06i & -0.02 + 0.06i & 0.41 \end{pmatrix} \tag{4.98}$$

References

[1] R. H. Brown and R. Q. Twiss, "Correlation between photons in two coherent beams of light," *Nature*, vol. 177, no. 4497, pp. 27–29, 1956.

[2] C. H. Bennett, F. Bessette, G. Brassard, L. Salvail, and J. Smolin, "Experimental quantum cryptography," *Journal of Cryptology*, vol. 5, no. 1, pp. 3–28, 1992.

[3] D. Deutsch, "Quantum theory, the Church–Turing principle and the universal quantum computer," *Proceedings of the Royal Society of London. A. Mathematical and Physical Sciences*, vol. 400, no. 1818, pp. 97–117, 1985.

[4] R. P. Feynman, "Quantum mechanical computers.," *Found. Phys.*, vol. 16, no. 6, pp. 507–532, 1986.

[5] H. J. Kimble, M. Dagenais, and L. Mandel, "Photon antibunching in resonance fluorescence," *Physical Review Letters*, vol. 39, no. 11, p. 691, 1977.

[6] E. Sudarshan, "Equivalence of semiclassical and quantum mechanical descriptions of statistical light beams," *Physical Review Letters*, vol. 10, no. 7, p. 277, 1963.

[7] E. Bocquillon, C. Couteau, M. Razavi, R. Laflamme, and G. Weihs, "Coherence measures for heralded single-photon sources," *Physical Review A*, vol. 79, no. 3, p. 035801, 2009.

[8] R. Short and L. Mandel, "Observation of sub-Poissonian photon statistics," *Physical Review Letters*, vol. 51, no. 5, p. 384, 1983.

[9] A. Pathak and A. Ghatak, "Classical light vs. nonclassical light: characterizations and interesting applications," *Journal of Electromagnetic Waves and Applications*, vol. 32, no. 2, pp. 229–264, 2018.

[10] G. Scarcelli, V. Berardi, and Y. Shih, "Can two-photon correlation of chaotic light be considered as correlation of intensity fluctuations?," *Physical Review Letters*, vol. 96, no. 6, p. 063602, 2006.

[11] J. S. Bell, "On the Einstein Podolsky Rosen paradox," *Physics Physique Fizika*, vol. 1, no. 3, p. 195, 1964.

[12] H. Waseem, F. Ilahi, and M. S. Anwar, *Quantum Mechanics in a Single Photon Laboratory*. to be published by the Institute of Physics Publishing, London, to appear (2020).

[13] D. Griffiths, *Introduction to Quantum Mechanics*. Cambridge University Press, 2017.

[14] R. Shankar, *Principles of Quantum Mechanics*. Springer US, 2012.

[15] J. Townsend, *A Modern Approach to Quantum Mechanics*. International series in pure and applied physics, University Science Books, 2000.

[16] M. Nielsen and I. Chuang, *Quantum Computation and Quantum Information: 10th Anniversary Edition*. Cambridge University Press, 2010.

[17] M. Beck, *Quantum Mechanics: Theory and Experiment*. Oxford University Press, 2012.

[18] E. Hecht, "Optics, ed," *MA: Addison-Wesley Publishing Company*, 1998.

[19] N. Zettili, *Quantum Mechanics: Concepts and Applications*. Wiley, 2009.

[20] N. Kolmakova, R. Levitin, A. Popov, N. Vedernikov, A. Zvezdin, and V. Nekvasil, "Magnetic linear birefringence in rare-earth garnets: Crystal-field effects and the Judd-Ofelt approximation," *Physical Review B*, vol. 41, no. 10, p. 6170, 1990.

[21] A. Lvovsky, *Quantum Physics: An Introduction Based on Photons*. Undergraduate Lecture Notes in Physics, Springer Berlin Heidelberg, 2018.

[22] D. McMahon, *Quantum Computing Explained*. Wiley - IEEE, Wiley, 2007.

[23] D. Xia *et al.*, "Estimation of low rank density matrices by Pauli measurements," *Electronic Journal of Statistics*, vol. 11, no. 1, pp. 50–77, 2017.

[24] M. Paris and J. Rehacek, *Quantum state estimation*, vol. 649. Springer Science & Business Media, 2004.

[25] Y. Sun, Y. Li, A. Kuceyeski, and S. Basu, "Large spectral density matrix estimation by thresholding," *arXiv preprint arXiv:1812.00532*, 2018.

[26] Z. Hradil, "Quantum-state estimation," *Physical Review A*, vol. 55, no. 3, p. R1561, 1997.

[27] J. B. Altepeter, E. R. Jeffrey, and P. G. Kwiat, "Photonic state tomography," *Advances in Atomic, Molecular, and Optical Physics*, vol. 52, pp. 105–159, 2005.

[28] S. Barz, G. Cronenberg, A. Zeilinger, and P. Walther, "Heralded generation of entangled photon pairs," *Nature Photonics*, vol. 4, no. 8, pp. 553–556, 2010.

[29] S. Karan, S. Aarav, H. Bharadhwaj, L. Taneja, G. Kulkarni, and A. K. Jha, "Phase matching in spontaneous parametric down conversion," *arXiv preprint arXiv:1810.01184*, 2018.

[30] A. B. U'Ren, C. Silberhorn, R. Erdmann, K. Banaszek, W. P. Grice, I. A. Walmsley, and M. G. Raymer, "Generation of pure-state single-photon wavepackets by conditional preparation based on spontaneous parametric downconversion," *arXiv preprint quant-ph/0611019*, 2006.

[31] C. Hong and L. Mandel, "Experimental realization of a localized one-photon state," *Physical Review Letters*, vol. 56, no. 1, p. 58, 1986.

[32] H. Yamashita, "A globally convergent primal-dual interior point method for constrained optimization," *Optimization Methods and Software*, vol. 10, no. 2, pp. 443–469, 1998.

[33] W.-K. Rhim, D. Elleman, and R. Vaughan, "Analysis of multiple pulse nmr in solids," *The Journal of Chemical Physics*, vol. 59, no. 7, pp. 3740–3749, 1973.

[34] E. Collett, *Field Guide to Polarization*. Field Guide Series, SPIE Press, 2005.

[35] E. Collett and B. Schaefer, "Visualization and calculation of polarized light. i. the polarization ellipse, the poincaré sphere and the hybrid polarization sphere," *Applied Optics*, vol. 47, no. 22, pp. 4009–4016, 2008.

Appendices

Appendix A

A.1 SEM Images of Permalloy Thin Films

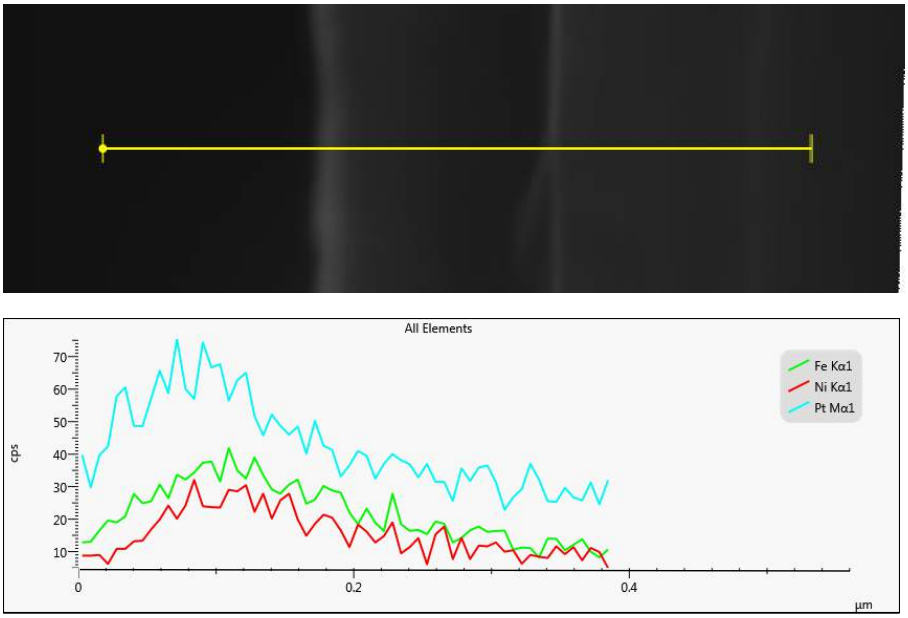

Figure A.1: SEM image and corresponding energy dispersive x-ray spectroscopic linescan along the yellow line of Si/Pt/NiFe thin film deposited by mangetron sputtering.

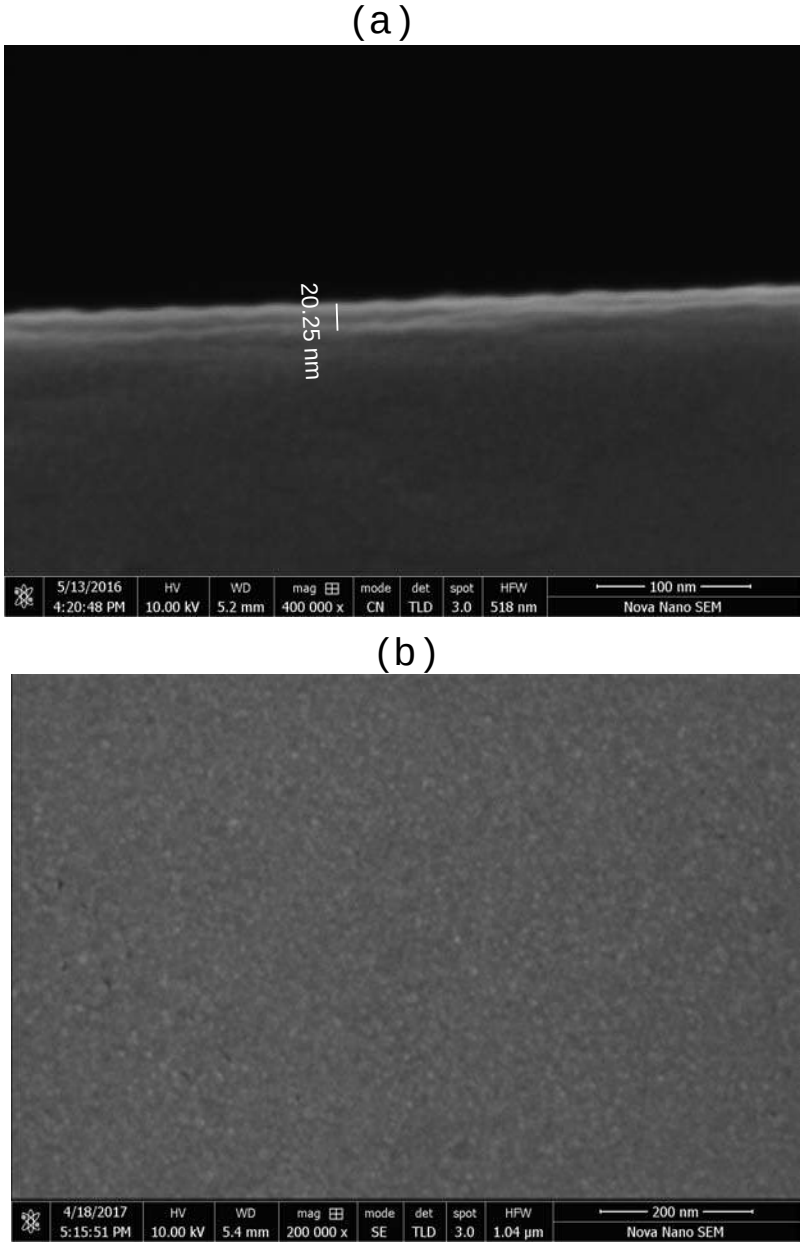

Figure A.2: Permalloy thin film images viewed under a scanning electron microscope (SEM) where a) presents cross-sectional image of thin film for thickness measurement and b) depicts the uniform surface morphology of sputtered thin film.

A.1.1 Labview Interface for MOKE Setup

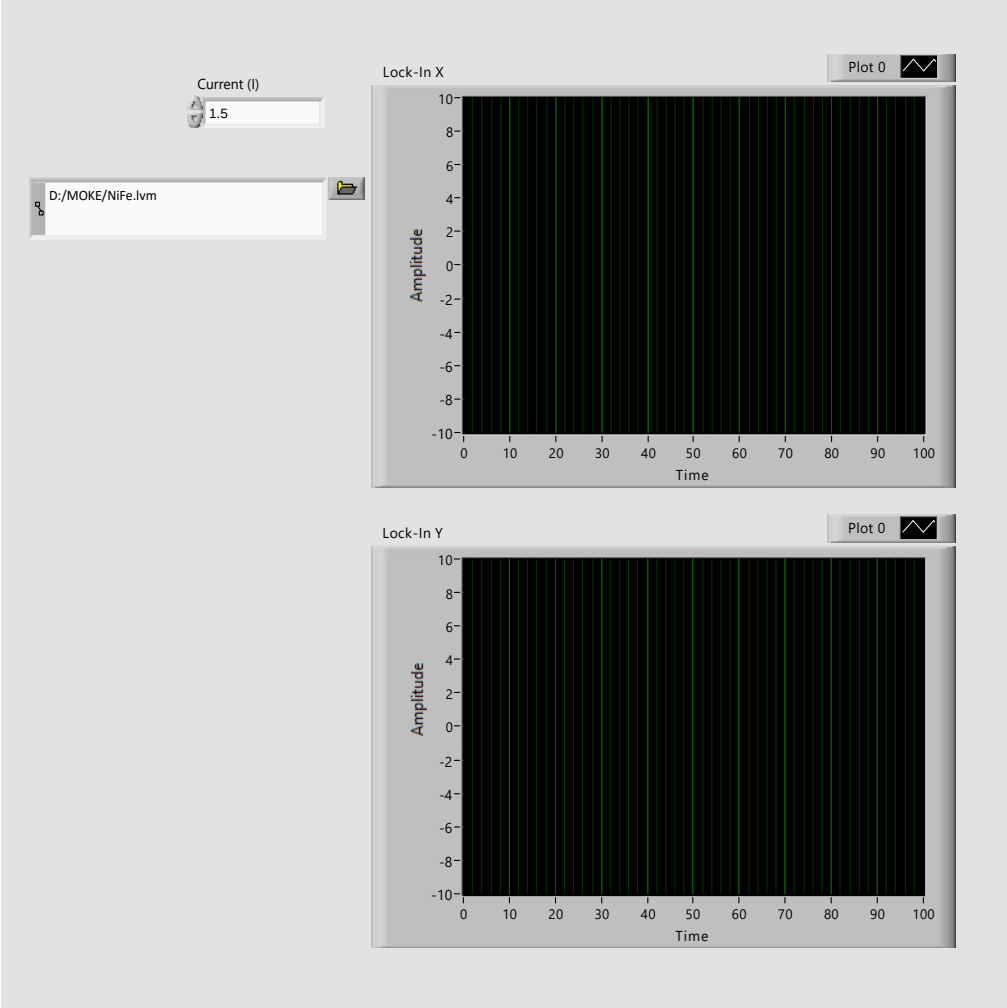

Figure A.3: Front panel of the MOKE setup visualized in labview environment. The graphical VI's display the real time output voltages from lockin channels (X and Y) with time whereas the current (I) tab controls the input current to the bipolar power supply.

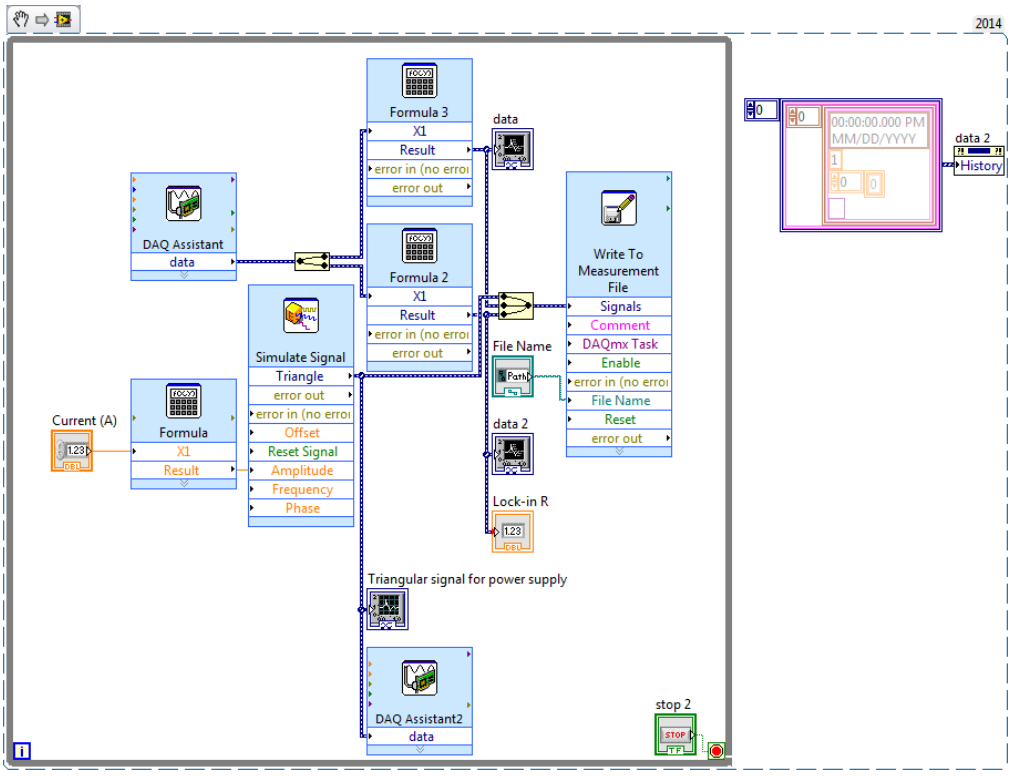

Figure A.4: Block diagram of the virtual elements of the labview program for MOKE setup. **Simulate Signal** VI generates a triangular wave of frequency f and amplitude A and is fed to the data acquisition device **DAQ** which drives the bipolar power supply. The other DAQ assistant receives the input from lockin channels and stores in the measurement file assigned by the user.

Appendix B

B.1 Labview Interface for Stokes Polarimetry

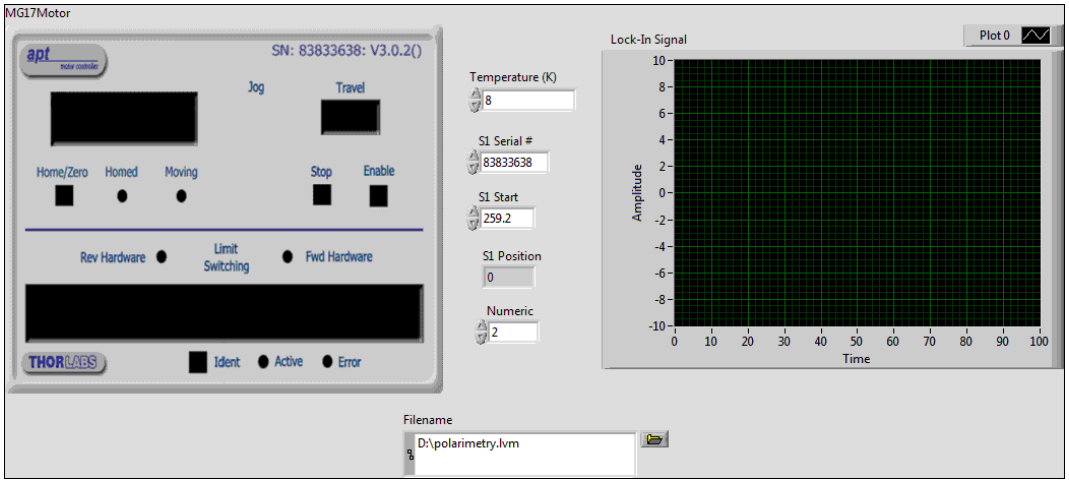

Figure B.1: Front panel of the Stokes polarimetry labview program. The graphical VI displays the output from the lockin channel whereas **MG17Motor** control shows the angular position of quarter waveplate which is being rotated in a step size of 5°.

B.1.1 Stokes Polarimetry Code

```
1 field=[0:0.25:5]*0.0493;
2 temperatures=[8 10 15 20 30 40 50 60 80 100 125 150];
4 shapes={'b-o','b-^','b-*','b-x','b-s','b->','b-p','b-v',
   'b-h','b-d','b-<'};
5 lol=2;
6 lol2=[1 3 5 7 9 ];
7 colors={[1 0 0 ],[0 1 0 ],[0 0 1 ],[0.5 0.5 0 ],[0.5 0 0.5 ],
```

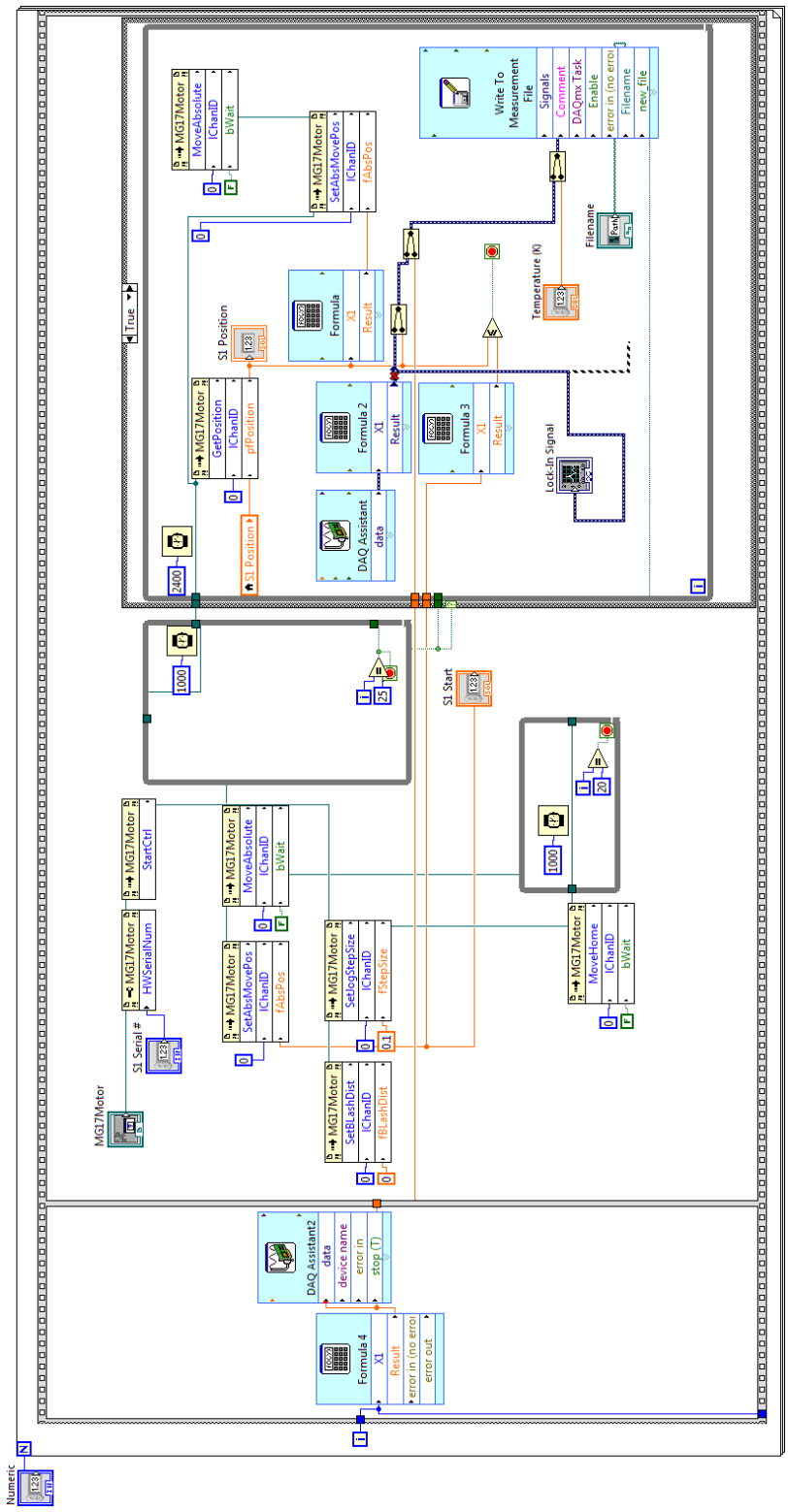

Figure B.2: Block diagram for the polarimetry setup where **DAQ Assistant**= data acquistion, **MG17Motor**= controls for the rotation stages and **write to mesaurement**= element for storing data.

```
    [0 0.5 0.5],[0.25 0.75 0 ],[0.25 0 0.75 ],[0 0.25 0.75],
    [0.75 0.25 0 ],[0.75 0 0.35 ],[0 0.75 0.25]};
8   names={'8K_' ,'10K_','15K_','20K_','30K_','40K_','50K_','60K_',
    '80K_','100K_','125K_','150K_'};
9   for count=1:1:lol  %temperature values
10      flag=0;
11      signal=0;
12      nishani=0;
13      alamat=0;
14      N=36;
15      L=18;
16  %% retardance and zero error for alpha=0
17  retardance = 86.2571;
18  zeroerror = 3.6828;
19  %% Code Continue
20      deltabeta=(5*pi/180);
21      del = (retardance*pi/180); %retardance
22      alpha=(0*pi/180); %analyzer angle
23      beta0=zeroerror*pi/180; % zero error
24  for num=1:1:21   %field values
25  %defining variables
26     filename=char([names{count} num2str(num) '.xlsx']);
27     A=xlsread(filename);
28     current_applied(num) = A(1,4); %reading values of current
29  %% Fourier Series Calculation
30          Beta(1,:)=(A(1,3) - A(:,3))*(pi/180);
31          It(1,:)= A(:,2);
32
33          for k=1:(L+1) %calculating fourier coefficeints
34              w=((2*pi)/(N*deltabeta))*(k-1);
35              if((k==1)||(k==L+1))
36                  Co(k) = (2/N)*(1/2)*sum(It.*cos(w*Beta));
```

```
37              Si(k) = (2/N)*(1/2)*sum(It.*sin(w*Beta));
38          else
39              Co(k) = (2/N)*(1)*sum(It.*cos(w*Beta));
40              Si(k) = (2/N)*(1)*sum(It.*sin(w*Beta));
41          end
42      end
43      w=0:((2*pi)/(N*deltabeta)):((2*pi)/(N*deltabeta))*L;
44  %calculating stokes parameters
45  M(count,num)=(2/(1-cos(del)))*(Co(3)*cos(2*alpha + 4*beta0)
      + Si(3)*sin(2*alpha + 4*beta0));
46  C(count,num)=(2/(1-cos(del)))*(Si(3)*cos(2*alpha + 4*beta0)
      - Co(3)*sin(2*alpha + 4*beta0));
47  S(count,num)= (Co(2)^2+Si(2)^2)^0.5/(sin(del)^2);
48  S1(count,num)=-Si(2)/(sin(del)*cos(2*alpha+4*beta0));
49  S2(count,num)= Co(2)/(sin(del)*sin(2*alpha+4*beta0));
50  I(count,num)=Co(1)- ((1+cos(del))/(1-cos(del)))
      *(Co(3)*cos(4*alpha + 4*beta0) + Si(3)*sin(4*alpha + 4*beta0));
51  Ip(count,num) = (M(count,num)^2 + C(count,num)^2
      + S1(count,num)^2)^0.5;
52  M(count,num)=M(count,num)/I(count,num);
53  C(count,num)=C(count,num)/I(count,num);
54  S1(count,num)=S1(count,num)/I(count,num);
55  Ip(count,num)=Ip(count,num)/I(count,num);
56  I(count,num)=I(count,num)/I(count,num);
57  %% Ellipticity
58  Eta1(count,num) = (1*(2*Ip(count,num))+ ((((2*Ip(count,num))^2)
      - 4*abs(S1(count,num))
      *abs(S1(count,num)))^0.5))/(2*abs(S1(count,num)));
59  Eta2(count,num) = (1*(2*Ip(count,num))- ((((2*Ip(count,num))^2)
      - 4*abs(S1(count,num))
      *abs(S1(count,num)))^0.5))/(2*abs(S1(count,num)));
60  ellipticity(count,num)= ((1/2)
```

```
    *atand(((S1(count,num)))/(norm([M(count,num), C(count,num)])));
61 if(S1(count,num)<0)
62  Eta2(count,num)=-1*Eta2(count,num);
63 end
64 %% Rotation
65 basic_angle(count,num) = ((1/2)
    *atand((abs(C(count,num)))/(abs(M(count,num)))));
66 if ((C(count,num)>=0)&&(M(count,num)>=0))
67         Zeta(count,num) = basic_angle(count,num);
68            else if((C(count,num)<=0)&&(M(count,num)<=0))
69 Zeta(count,num) = 90 + basic_angle(count,num);
70              else if ((C(count,num)>=0)&&(M(count,num)<=0))
71   Zeta(count,num) = 90 - basic_angle(count,num);
72     else if ((C(count,num)<=0)&&(M(count,num)>=0))
73      Zeta(count,num) = -1*basic_angle(count,num);
74                    end
75                end
76             end
77         end
78 if((Zeta(count,num)>=0)&&(Zeta(count,num)<=180)&&(num>1))
79     Zeta(count,num)= Zeta(count,num) - 180;
80 end
81 if (Zeta(count,num)<=-90)
82      flag=1;
83 end
84 if ((flag==1)&&(Zeta(count,num)<=0)&&(Zeta(count,num)>=-90))
85     Zeta(count,num) = Zeta(count,num) - 180;
86 end
87 if ((flag==1)&&(Zeta(count,num)<=0)&&(Zeta(count,num)>=-90))
88     Zeta(count,num) = Zeta(count,num) - 180;
89 end
90 if(Zeta(count,num)<=-180)
```

```
91      signal = 1;
92  end
93  if ((signal==1)&&(Zeta(count,num)<=-90)&&(Zeta(count,num)>=-180))
94      Zeta(count,num) = Zeta(count,num) - 180;
95  end
96  if(Zeta(count,num)<=-270)
97      nishani = 1;
98  end
99  if ((nishani==1)&&(Zeta(count,num)<=-180)&&(Zeta(count,num)>=-270))
100     Zeta(count,num) = Zeta(count,num) - 180;
101 end
102 if(Zeta(count,num)<=-360)
103     alamat = 1;
104 end
105 if ((alamat==1)&&(Zeta(count,num)<=-270)&&(Zeta(count,num)>=-360))
106     Zeta(count,num) = Zeta(count,num) - 180;
107 end
108 end
109 end
110 %% Plotting Rotation
111 figure(2)
112 hold on
113 xlabel('Magnetic Field (T)','FontSize', 20)
114 ylabel('Ellipticity (degrees)','FontSize', 20)
115 title('Ellipticity','FontSize', 40)
116 for k=1:lol
117
118     if k> length(shapes)
119         temp=k-length(shapes);
120     else
121         temp=k;
122     end
```

```
123
124     if k> length(colors)
125         temp11=k-length(colors);
126     else
127         temp11=k;
128     end
129  set(gca,'fontsize',20)
130  plot(field.^2,ellipticity(k,:)-ellipticity(k,1),
       shapes{temp},'Color',colors{temp11},
       'MarkerFaceColor',colors{temp11})
131  end
132  legend('8K','10K','15K','20K','30K','40K','50K','60K','80K'
       ,'100K','125K','150K')
133  %% Plotting Rotation
134  figure(1)
135  hold on
136  xlabel('1/B^2(1/T^2)','FontSize', 20)
137  ylabel('tan(2\theta)','FontSize', 20)
138  title('Rotation','FontSize', 40)
139  for k=1:lol
140   if k> length(shapes)
141         temp=k-length(shapes);
142   else
143       temp=k;
144   end
145   if k> length(colors)
146      temp11=k-length(colors);
147   else
148     temp11=k;
149   end
150  set(gca,'fontsize',20)
151  theta(k,:)=(basic_angle(k,:)-basic_angle(k,1)+45);
```

```
152 plot(field,((basic_angle(k,:)-basic_angle(k,1)+45)),shapes{temp},
    'Color',colors{temp11},'MarkerFaceColor',colors{temp11})
153 end
154 legend('8K','10K','15K','20K','30K','40K','50K','60K','80K',
    '100K','125K','150K');
```

B.1.2 Sample Holder Drawing

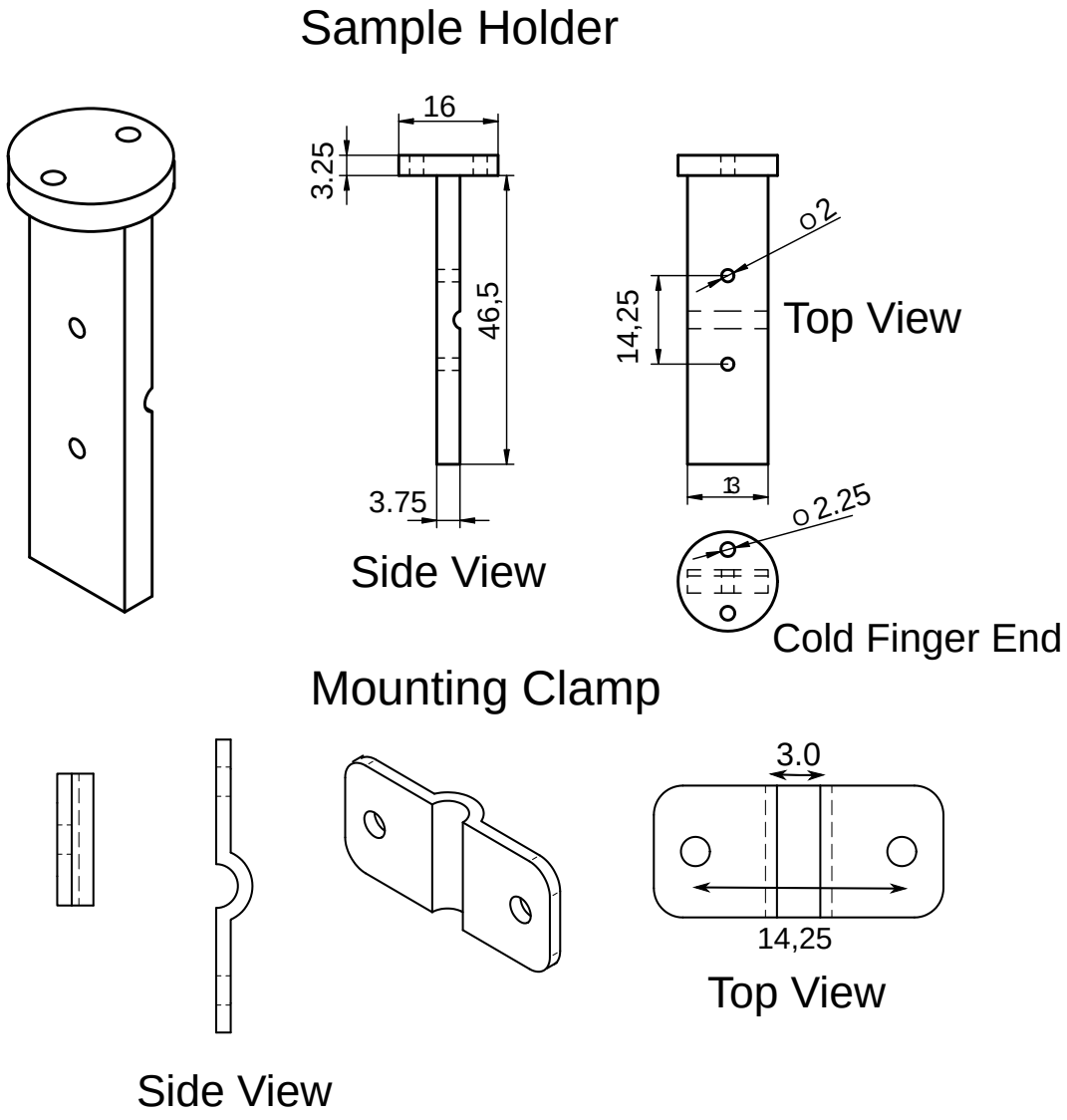

Figure B.3: Design and drawings of sample holder and mounting clamp. All the dimensions are in millimeters.